Spectral properties of semiconductor lasers

Yee, Wai Mun

Award date:
1994

Awarding institution:
University of Bath

SPECTRAL PROPERTIES OF SEMICONDUCTOR LASERS

Submitted by Yee Wai Mun, B. Eng. (Hons)

for the degree of

Doctor of Philosophy

of the University of Bath

1994

ProQuest LLC
789 East Eisenhower Parkway
P.O. Box 1346
Ann Arbor, MI 48106-1346

To my Father, Mother and Sister

Summary

In this thesis, several aspects of the spectral properties of semiconductor lasers are studied theoretically, including self-locking frequency-modulation (FM) laser operation, nearly degenerate four-wave mixing (NDFWM), all-optical frequency conversion and tuning, and infrared intersubband lasing. A multimode semiconductor laser model is developed, based on the Lamb semiclassical laser theory, to study the multi-longitudinal mode spectral behaviours of semiconductor lasers. Intrinsic multiwave mixing nonlinearities occurring in the presence of gain saturation are shown to give rise to self-locking in semiconductor lasers, resulting in FM longitudinal-mode spectrum. Calculated values of output power and FM modulation index in the self-locked state are in agreement with experimental evidence. A model for cavity-enhanced NDFWM in laser diodes with nonuniform gain distribution is developed. Enhancements of conjugate wave generation and NDFWM bandwidth are shown to be achievable in laser diodes with low and unequal (asymmetric) facet reflectivities. The NDFWM model is also used to investigate the all-optical frequency conversion characteristics of asymmetric-facet two-section laser diodes. It is demonstrated that, under appropriate biasing conditions, such devices exhibit a uniform and an enhanced-efficiency frequency conversion properties. A theoretical model is also developed to study the wavelength tuning characteristics of asymmetric gain-levered Fabry-Perot laser diodes. Enhancement of wavelength tunability in asymmetric two-section laser diodes is revealed. The feasibility of achieving infrared lasing based on intersubband transitions in quantum well (QW) structures is also studied. A carrier transport model is developed which demonstrates the opportunity for the achievement of intersubband population inversion in resonant tunnelling coupled QW structures. The incorporation of optical loss analysis into the carrier transport model provides a complete formulation for the calculation of threshold current density. Reasonably low threshold currents of 1–5 kA/cm^2 are achievable for room-temperature lasing at wavelength of 60 μm. Significantly higher threshold currents are required for lasing at 10 μm wavelength.

Acknowledgements

I would like to express my deep gratitude to Dr. K. A. Shore for his excellent supervision throughout the course of this work.

Helpful discussions with Dr. J. Sarma, Dr. P. S. Spencer, Dr. I. Middlemast, Dr. L. N. Langley and M. Green are gratefully acknowledged.

I would also like to thank the University of Bath and the Committee of Vice Chancellors and Principals for providing financial support for this project.

Contents

List of Figures

Chapter 1

General Introduction

Since its invention in 1962, the semiconductor laser has attracted considerable research and development effort, resulting in its emergence as an important component in optoelectronic systems. Because "conventional" semiconductor lasers rely on stimulated *interband* electron–hole recombination to provide the optical gain, the emission spectra of semiconductor lasers are limited to frequencies corresponding to the semiconductor bandgap energy. With advances in material processing and epitaxial growth techniques, a variety of semiconductor materials have been found and demonstrated to exhibit interband lasing action with emission wavelengths covering the optical spectrum from the visible to the near-infrared. The development of GaAs semiconductor lasers emitting in the near-infrared wavelength region of 0.8–0.9 μm during the 1970s led to their deployment in the first generation of optical fiber communication systems. However, long-wavelength InGaAsP semiconductor lasers emitting in the wavelength range of 1.1–1.6 μm are currently of particular interest for long-haul optical fiber communications. This is due to the availability of low-loss dispersion-free fibers at 1.3 μm, and ultra-low-loss fibers at 1.55 μm wavelength. Considerable efforts continue to develop further the performance characteristics of semiconductor lasers for specialized applications. Recently, in view of the enormous potential applications

in such diverse fields as medicine, free-space communications and spectroscopy, some effort has been devoted to extending the emission spectrum of semiconductor lasers to the far-infrared wavelength regime. Particular attention is focused on developing far-infrared semiconductor lasers based on *intersubband transitions* in multiple quantum well (MQW) structures fabricated using the III–V material systems, such as GaAs and InGaAs, because of their well-developed technologies.

The operation and overall performance of optoelectronic systems are critically dependent on the spectral properties of the semiconductor laser source. Semiconductor media are optical materials of significant nonlinearity. Undesirable spectral effects, such as multi-longitudinal mode operation, frequency chirping (frequency spread of the single dominant lasing mode), and mode-hopping (spontaneous change of dominant lasing mode), may arise because of gain and refractive index nonlinearities in semiconductor lasers, and can severely degrade the system performance. In optical fiber communications, for example, frequency chirping and spectral broadening (multi-longitudinal-mode lasing) effects place a severe penalty on the optical signal bit-rate achievable in long-haul transmission because of fiber dispersion. Therefore, the study of the spectral properties of semiconductor lasers is of fundamental importance both for improving the device performance and for the understanding of the nonlinear physical processes in semicondctor media.

On the other hand, nonlinearity-induced spectral properties of semiconductor lasers have recently attracted considerable interest for device applications in view of the possibility of realizing *optical functional devices* based on nonlinear operations of semiconductor lasers. Chinn and Swanson have studied self-induced frequency-modulation (FM) spectral characteristics in Fabry-Perot (FP) laser diodes and have demonstrated optical short pulse generation at high repet-

itive rates (up to 233 GHz) by converting the self-induced FM oscillation to amplitude modulation (AM) pulses [1]. The generation of new spectral components via external optical injection induced four-wave mixing (FWM) nonlinearities in FP semiconductor lasers has been extensively studied (see, for example, Refs. [2, 3]) and exploited in nonlinear operations such as optical phase conjugation [4] and all-optical frequency conversion [5]. Furthermore, electronically frequency-tunable FP semiconductor lasers, generally known as *frequency-agile optical sources*, which are expected to be key components in future coherent communication systems, have been demonstrated [6]. The above discussion clearly shows that different aspects of the spectral properties of semiconductor lasers can be utilized for realizing a multitude of applications.

In this thesis, the study of the spectral properties of semiconductor lasers is divided into four main areas, namely self-locking FM laser operation, nearly degenerate four-wave mixing (NDFWM), optical frequency conversion and tuning, and far-infrared intersubband lasing. These aspects of the spectral properties of semiconductor lasers are briefly introduced in the following and the organisation of the thesis is outlined.

1.1 Self-Locking FM Laser Operation

Long-wavelength (typically 1.3–1.55 μm) InGaAsP index-guided FP semiconductor lasers are usually observed to operate in multi-longitudinal mode at moderately high injection currents above threshold. Tiemeijer *et al.* [7] were the first to propose that the multi-longitudinal mode spectra are actually frequency components of a *self-induced* FM supermode. This phenomenon is known as *self-locking FM laser operation*, which was originally observed in gas lasers.

In this thesis, a theoretical model originally developed for gas lasers by Lamb [8] is adapted to account for the properties of semiconductor lasers and is used to analyse the multi-longitudinal mode spectral behaviours of semiconductor lasers. In chapter 2, a three-mode laser model based on the Lamb semiclassical laser theory is developed [9]. The three-mode semiconductor laser rate equations are then numerically integrated to determine the conditions under which self-locking FM operation occurs in the presence of multiwave mixing and gain saturation nonlinearities. Output powers in the self-locked state are computed and compared with available experimental results. Nonlinear gain diagnostics is carried out to establish the role of nonlinearities of the medium in effecting self-locking FM spectral behaviours.

The three-mode semiconductor laser model is generalized in chapter 3 to include five, seven and nine modes in the description of self-locking FM operation in semiconductor lasers [10]. In particular, FM modulation index is computed in the five-mode self-locked state and comparison is made with experimentally determined values.

1.2 Nearly Degenerate Four-Wave Mixing

The effects of external optical-signal injection on the spectral characteristics of semiconductor lasers are studied in chapter 4. When the frequency of the externally injected "probe" signal is slightly detuned from that of the lasing "pump" signal, an additional spectral component, the "conjugate signal", is generated. The process through which the conjugate signal is generated is referred to as *nearly degenerate four-wave mixing* (NDFWM).

A travelling-wave model of cavity-enhanced NDFWM in FP laser diodes with

nonuniform longitudinal gain distribution is described in chapter 4 [11]. Probe and conjugate output characteristics are studied. Particular emphasis is given to the enhancement of conjugate signal generation in laser diodes with low and/or unequal (asymmetric) facet reflectivities.

1.3 Optical Frequency Conversion and Tuning

The nonlinearity-induced spectral characteristics of semiconductor lasers can be utilized constructively in device applications. This is illustrated in chapter 5 where all-optical *frequency conversion* and *wavelength tuning* in two-section laser diodes are investigated.

An all-optical frequency converter is a nonlinear optical functional device whose role is to transform an incoming data signal at a given optical carrier frequency into an output image signal at a different carrier frequency. All-optical frequency converters are expected to be key components in future optical coherent multicarrier transmission systems. In chapter 5, all-optical frequency conversion using NDFWM in two-section laser diodes is investigated using the FWM model developed in chapter 4. Enhanced uniform all-optical frequency conversion may be realized using NDFWM in two-section laser diodes [12].

In addition, the effects of carrier density variations on spectral shift in laser diodes are studied in chapter 5. The carrier-dependent spectral shift is utilized in wavelength tuning, which is important for the construction of wavelength- (or frequency-) agile laser sources. A travelling-wave formulation is presented in chapter 5 to investigate wavelength tuning characteristics, which takes into account the longitudinal variations of carrier density in the laser cavity. Enhancement of wavelength tunability may be obtained in asymmetric-facet two-section

FP laser diodes.

1.4 Infrared Intersubband Semiconductor Lasers

The possibility of extending the emission spectra of semiconductor lasers to the mid- and far-infrared wavelength range using *intersubband transitions* in MQW structures was first proposed more than twenty years ago [13]. The principal challenges in obtaining lasing action in such an intersubband QW structure are difficulties in achieving intersubband population inversion and obtaining sufficient gain to overcome the high losses at infrared wavelengths.

In chapter 6, the issue of achieving intersubband population inversion in coupled QW structures is addressed. A carrier transport model incorporating the relevant physical mechanisms of resonant tunnelling and intersubband absorption–emission processes is described [14]. Based on this carrier transport model, the injection current densities needed for the achievement of intersubband population inversion at the emission wavelengths of 10 μm and 60 μm are calculated.

The prescription of lasing conditions in the coupled QW laser structures is described in chapter 7. In this respect, optical loss analysis is carried out which takes into account the configuration of the coupled QW laser devices. The incorporation of optical loss analysis into the carrier transport model described in chapter 6 provides a complete formulation [15] to calculate the lasing threshold current densities needed for room-temperature operation of the infrared intersubband semiconductor lasers.

References

[1] S. R. Chinn and E. A. Swanson, "Passive FM locking and pulse generation from 980-nm strained-quantum-well Fabry-Perot lasers," *IEEE Photon. Technol. Lett.*, vol. 5, pp. 969–971, 1993.

[2] R. Nietzke, P. Panknin, W. Elsässer, and E. O. Göbel, "Four-wave mixing in GaAs/AlGaAs semiconductor lasers," *IEEE J. Quantum Electron.*, vol. 25, pp. 1399–1406, 1989.

[3] M. P. van Exter, C. Biever, and J. P. Woerdman, "Effect of optical injection on bias voltage and spectrum of a semiconductor laser," *IEEE J. Quantum Electron.*, vol. 29, pp. 2771–2779, 1993.

[4] G. P. Agrawal, "Four-wave mixing and phase conjugation in semiconductor laser media," *Opt. Lett.*, vol. 12, pp. 260–262, 1987.

[5] L. Li and K. Petermann, "Characteristics of optical frequency conversion in a semiconductor laser," *IEEE J. Quantum Electron.*, vol. 29, pp. 2793–2798, 1993.

[6] M. J. Chawki, R. Auffret, L. Berthou, and L. Demeure, "1.5 Gbit/s FSK transmission system using two-electrode Fabry-Perot buried heterostructure laser," *Electron. Lett.*, vol. 27, pp. 417–418, 1991.

[7] L. F. Tiemeijer, P. I. Kuindersma, P. J. A. Thijs, and G. L. J. Rikken, "Passive FM locking in InGaAsP semiconductor lasers," *IEEE J. Quantum Electron.*, vol. 25, pp. 1385–1391, 1989.

[8] W. E. Lamb, "Theory of an optical maser," *Phys. Rev.*, vol. 134, pp. A1429–A1450, 1964.

[9] K. A. Shore and W. M. Yee, "Theory of self-locking FM operation in semiconductor lasers," *IEE Proc. Part J*, vol. 138, pp. 91–96, 1991.

[10] W. M. Yee and K. A. Shore, "Multimode analysis of self locked FM operation in laser diodes," *IEE Proc. Part J*, vol. 140, pp. 21–25, 1993.

[11] W. M. Yee and K. A. Shore, "Nearly degenerate four-wave mixing in laser diodes with nonuniform longitudinal gain distribution," *J. Opt. Soc. America B*, vol. 11, pp. 1221–1228, 1994.

[12] W. M. Yee and K. A. Shore, "Enhanced uniform phase conjugation in two-section asymmetric laser diodes," *Opt. Lett.*, accepted for publication.

[13] R. F. Kazarinov and R. A. Suris, "Possibility of the amplification of electromagnetic waves in a semiconductor with a superlattice," *Sov. Phys. Semicond.*, vol. 5, pp. 707–709, 1971.

[14] W. M. Yee, K. A. Shore, and E. Schöll, "Carrier transport and intersubband population inversion in coupled quantum wells," *Appl. Phys. Lett.*, vol. 63, pp. 1089–1091, 1993.

[15] W. M. Yee and K. A. Shore, "Threshold current density calculations for far-infrared semiconductor lasers," *Semicond. Sci. Technol.*, vol. 9, pp. 1190–1197, 1994.

Chapter 2

Theory of Self-Locking FM Laser Operation

2.1 Introduction

The use of amplitude modulation (AM) and phase or frequency modulation (FM) to achieve mode-locking is very well known in several laser systems [1]. Particular emphasis has been given to developing active and passive *AM mode-locking* techniques with a view to the production of ultra-short (picosecond and subpicosecond) repetitive optical pulses. For semiconductor lasers, *active* AM mode-locking is effected by directly modulating the injection current, and thus the gain, at a frequency equal to the frequency spacing between the longitudinal modes [2]. The gain modulation causes the longitudinal modes to interact with one another, thereby locking them in phase. In *passive* AM mode-locking, a saturable absorber is placed in the laser cavity to achieve the same effect. Since the typical length of a semiconductor laser is about 300 μm corresponding to an intermodal frequency spacing of over 100 GHz, it is very difficult to modulate the gain of the laser, either actively or passively, at these frequencies. Hence almost all AM mode-locking configurations of semiconductor lasers used an external cavity to reduce the intermodal frequency spacing to below a few gigahertz.

On the other hand, rather less effort has been given over to the study and application of *FM mode-locking* properties of lasers. FM mode-locking of lasers is typically effected through the use of an intracavity phase perturbative element (intracavity phase modulator), which allows the path length of the optical resonator to be modulated. FM mode-locking of lasers may be used for optical short pulse generation if the intracavity phase modulator is driven at the intermodal spacing frequency. However, when the intracavity phase modulator is driven at a modulation frequency close to, but not exactly equal to, the intermodal frequency spacing, a pronounced increase in the FM modulation depth is realized. This phenomenon was first reported in gas lasers by Harris and Targ [3], which is now widely known as "*FM laser oscillation*" or "*FM laser operation*". The classical theory of FM laser oscillation [4] shows that the signal envelope of an FM laser oscillation is constant, but a periodic change of frequency is swept across the signal.

For semiconductor lasers, in particular, the possibilities of achieving FM locking have received relatively little attention. Although Saito *et al.* [5] reported FM laser operation in an external cavity semiconductor laser some time ago, there has not been a sustained attempt to explore this topic using semiconductor lasers. Lately, however, a number of workers have begun to address important issues related to the FM locking phenomenon in semiconductor lasers. Recent interest in FM locking properties of semiconductor lasers arises because of the possibility of using frequency modulation in optical fibre communications, and the possible utilization of FM laser diodes as sources in sensors and in optical radar. The relationship between FM laser operation and threshold of instability in directly modulated single-carrier external-cavity semiconductor lasers has been investigated by Schremer and coworkers [6]. Schremer and Tang [7] have also studied FM locking properties in external cavity AlGaAs laser diodes and

have shown a phase reversal effect in this configuration. Bösl and coworkers have demonstrated the generation of stable *active* FM mode-locked optical pulses with a repetition rates of up to 7.7 Gbit/s using an intracavity phase modulator in AlGaAs laser diodes [8]. Nietzke *et al.* [9] have studied the generation of near-FM oscillation sidebands by *external optical injection* cascade four-wave mixing. Furthermore, optical pulse generation using FM mode-locking in an extended-cavity semiconductor laser containing a tunable distributed Bragg reflector gain medium operating near 1.5 μm has been reported by Nagar *et al.* [10].

In this chapter, it is shown that nonlinear optical properties intrinsic to semiconductor lasers may, in contrast, give rise to self-locking FM behaviour in semiconductor lasers. It is emphasised that the FM locking phenomenon studied here arises because of the *intrinsic* properties of nonlinear multimode interactions in the solitary semiconductor laser (ie., without external cavity), and does not result from any external modulation (of either the amplitude or the frequency) of the semiconductor laser.

In section 2, fundamental concepts of mode-locking are discussed. Particular emphasis is given to differentiating FM laser operation from other forms of beat frequency locking phenomenon. In section 3, the experimental basis of self-locking FM operation in semiconductor lasers is reviewed. A formalism is developed [11] in section 4 based on Lamb's semiclassical laser theory [12] to model three-mode operation in semiconductor lasers. The characteristics of self-locking FM operation are theoretically studied in section 5. Nonlinear gain diagnostics is carried out in section 6 based on the concept of three-mode self-locking FM operation in laser diodes in order to map out regions in the nonlinear coefficient parameter-space where self-locking phenomenon is expected to occur. Finally, conclusions are drawn in section 7.

2.2 Mode-Locking of Semiconductor Lasers

In the literature, mode-locking of lasers is almost synonymous with the generation of optical pulses at a repetitive frequency equal to the frequency spacing between longitudinal modes. In this thesis, however, the term mode-locking is used in the more general sense to refer to the *locking of beat frequencies* between adjacent longitudinal modes. The beat frequency locking results in fixed (time invariant) phase relations between the modes. Mode-locked lasers produce optical signals which are periodically modulated including repetitive short pulses and frequency-swept (FM operation) signals, depending on the exact phase relations of the mode-locked longitudinal modes.

In multi-longitudinal mode free-running lasers, the phases $\phi_n(t)$ of the oscillating modes vary randomly with time. The field E can be written as

$$E(t) = \sum_n E_n \exp\{i[\omega_n t + \phi_n(t)]\} , \tag{2.1}$$

where E_n is the amplitude coefficient and ω_n is the oscillation frequency of the n-th mode, which is not necessarily equal to the passive cavity frequency Ω_n because of dispersion of the active medium. The beat frequencies between adjacent modes are not generally equal to one another.

In mode-locked lasers, on the other hand, some mechanism exists (either actively or passively applied or intrinsic to the lasers) which couples the beat frequencies between the modes. As a result, modes which were otherwise nearly equally spaced become exactly equally spaced in frequency. In this case,

$$\omega_n = \omega_q + (n - q)\omega , \tag{2.2}$$

where n and q are integers and ω is the locked beat frequency between adjacent longitudinal modes. Furthermore, the phases become fixed (time independent)

in mode-locking. The field is then given by

$$E(t) = \sum_n E_n \exp\{i[(\omega_0 + n\omega)\, t + \phi_n]\} \,, \tag{2.3}$$

where ω_0 is taken as the central mode.

It can be shown that $E(t)$ is periodic with a period $T = 2\pi/\omega$, ie.,

$$\begin{aligned} E(t+T) &= \sum_n E_n \exp\{i[(\omega_0 + n\omega)(t + \frac{2\pi}{\omega}) + \phi_n]\} \\ &= \sum_n E_n \exp\{i[(\omega_0 + n\omega)\, t + \phi_n]\} \ \exp\{i[2\pi(\frac{\omega_0}{\omega} + n)]\} \\ &= E(t) \,, \end{aligned} \tag{2.4}$$

because (ω_0/ω) is an integer from Eq. (2.2).

It is thus shown that for a set of longitudinal modes in which the modes are exactly equally spaced in frequency, regardless of their relative amplitudes and phases, the output signal will be periodic in time, with a fundamental period equal to the inverse of the intermodal frequency spacing.

2.2.1 Mode-Locked Short Pulse Generation

If all the equally spaced longitudinal modes have the *same phase*, regardless of their amplitudes, periodic short pulse output will be obtained. To simplify the analysis, it is assumed that there are N oscillating modes with equal amplitude E_0 and equal phase ϕ. The field equation becomes

$$\begin{aligned} E(t) &= E_0 \exp[i(\omega_0 t + \phi)] \sum_n \exp(i\, n\omega t) \\ &= E_0 \exp[i(\omega_0 t + \phi)] \, \frac{\sin(N\omega t/2)}{\sin(\omega t/2)} \,. \end{aligned} \tag{2.5}$$

The average laser output power is proportional to $|E(t)|^2$, and in this case is given by

$$P(t) \propto \frac{\sin^2(N\omega t/2)}{\sin^2(\omega t/2)} \,. \tag{2.6}$$

The output power waveform of a nine-mode mode-locked short-pulse laser is shown in Fig. 2.1. The power is emitted in the form of a train of pulses with period $T = 2\pi/\omega$, and pulse width $\tau = T/N$. Extensive research effort has been given to developing various mode-locking techniques with a view to the production of compact, reliable optical sources of short pulses for electro-optic sampling systems, soliton transmission systems, and high bit-rate telecommunications applications.

2.2.2 FM Laser Oscillation

On the other hand, mode-locking can also result in an output signal in which the signal envelope is constant, but a periodic change of frequency is swept across the signal. This is referred to as *FM laser operation.* In FM operation, each of the previously free-running longitudinal modes is modulated (either actively by using an intracavity phase modulator or spontaneously by mechanisms intrinsic to the laser diode), so that sidebands are generated at frequencies which nearly coincide with other lasing modes. Each of the longitudinal mode regards itself as the carrier of an FM signal and others as its FM sidebands. The resulting multiple FM oscillations then compete with each other for the carrier population. Under appropriate conditions, the strongest FM carrier is able to quench all other, thus establishing a single FM laser supermode signal.

In pure FM operation, the field of the FM supermode has a constant amplitude E_0 and is of the form

$$E(t) = E_0 \cos(\omega_0 t + \beta \cos \omega t) , \tag{2.7}$$

where β is the FM modulation index, ω is the beat frequency between adjacent modes, and ω_0 is the frequency of the dominant mode, taken as the central mode.

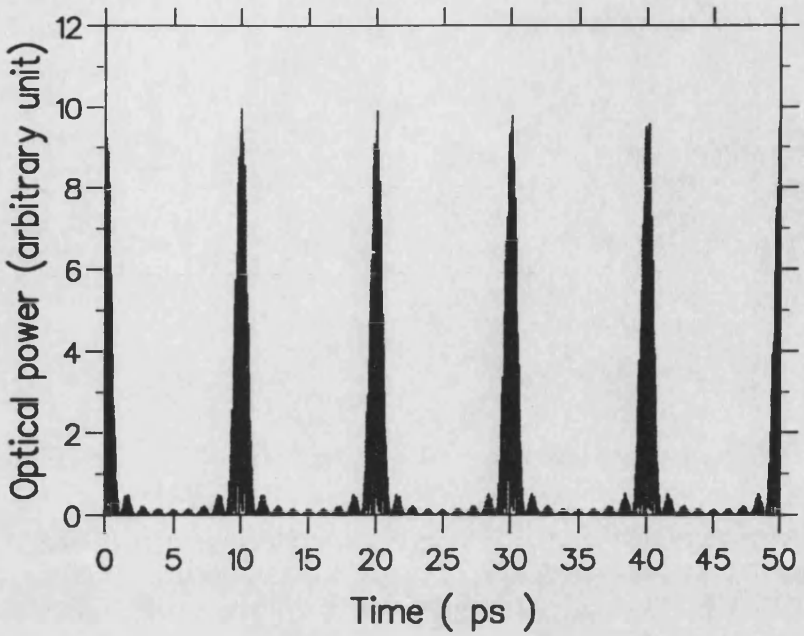

Figure 2.1: Nine-mode short pulse generation by mode-locking in a semiconductor laser.

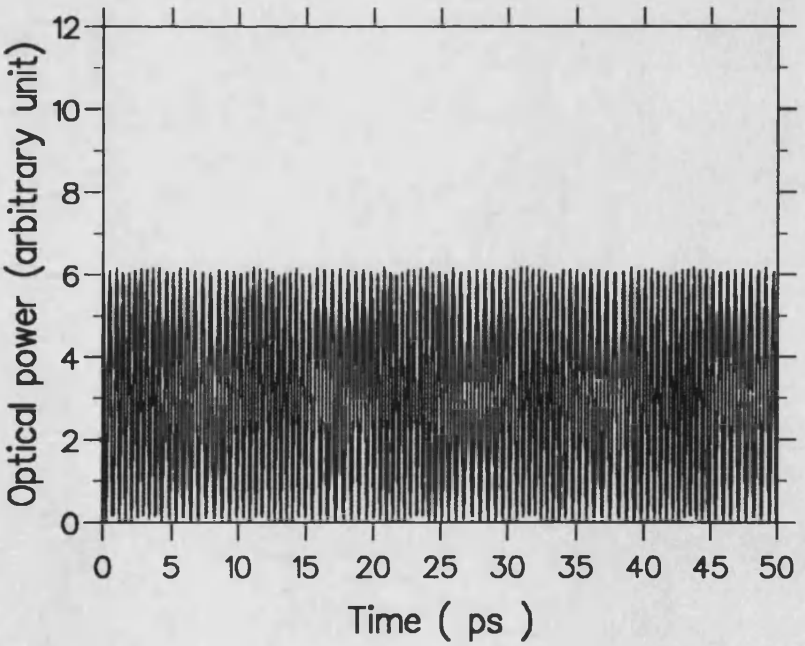

Figure 2.2: Nine-mode FM laser oscillation in a semiconductor laser.

The relative amplitudes of the cavity modes are defined by the Bessel functions:

$$E(t) = E_0 \sum_n J_n(\beta) \cos\left[(\omega_0 + n\omega)\, t - |n|\frac{\pi}{2}\right] . \tag{2.8}$$

Fig. 2.2 shows the time waveform for an FM operation signal involving nine longitudinal modes.

2.3 Experimental Basis of Self-Locking FM Operation

The motivation for the present theoretical treatment is the experimental work of Tiemeijer *et al.* who first demonstrated self-induced (passive) FM locking in multi-longitudinal-mode Fabry-Perot (FP) InGaAsP laser diodes [13]. In this section, the evolution of the longitudinal mode spectrum towards self-locking FM oscillation with increasing current pumping, as observed by Tiemeijer, is discussed. The approach by Tiemeijer to verify the observation of self-locking FM oscillation is outlined. Other recent reports on the observation of self-locking FM oscillation are cited.

2.3.1 Longitudinal Mode Spectra of Laser Diodes

Fig. 2.3 shows a typical CW light versus current curve recorded at room temperature for an InGaAsP FP laser diode, together with a few longitudinal mode spectra at different output powers (from Ref. [13]).

In semiconductor lasers, a large spontaneous emission exists because of high injected carrier density and a wide gain-spectrum bandwidth arising from interband transitions. The large spontaneous emission can be considered as a noise source in the gain medium. The longitudinal modes can thus be considered as

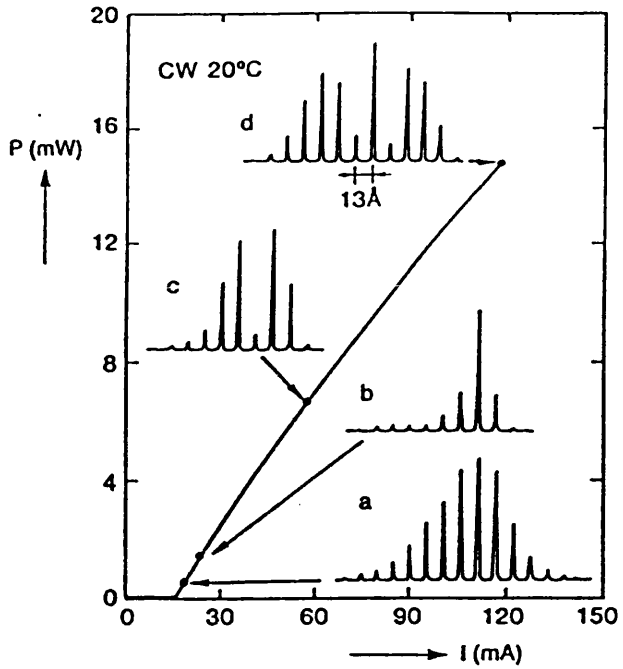

Figure 2.3: Typical CW power versus injection current curve for an InGaAsP laser (from Ref. [13]). Inset are longitudinal mode spectra recorded at (a) 0.5 mW: amplified spontaneous emission, (b) 1.5 mW: near single-mode operation, (c) 7 mW: self-locking FM oscillation with $\beta = 2.4$, and (d) 15 mW: self-locking FM oscillation with $\beta = 3.9$.

selectively amplified spontaneous emission at frequencies for which the cavity resonant conditions are satisfied. Therefore, at injection current levels near lasing threshold, the output spectrum (a) of the laser diode consists of a broad-band amplified spontaneous emission as shown in Fig. 2.3.

The evolution towards near single longitudinal mode operation with increasing injection current is observed in the FP laser diode (spectrum (b)). This observation is consistent with the classical theory of amplified spontaneous emission with a linear gain. In this theory, the gain saturates at a value slightly below the loss because of a finite continuous input of spontaneous emission noise in the laser oscillator. This saturation of the spectral gain implies that the quasi-Fermi level separation is locked, and hence the side-mode amplitudes remain saturated with excess excitation going into stimulated emission of the dominant mode (which is usually the mode nearest to the peak of the gain spectrum).

At injection current levels well above threshold, the near single mode spectral envelope begins to rebroaden and multi-longitudinal mode operation is observed, as shown in spectra (c) and (d) in Fig. 2.3. The multimode behaviours of FP laser diodes at high injection currents cannot be explained using the simple linear gain model. Various nonlinear gain models (see Refs. [14, 15] for recent reviews) have been proposed to explain the observed multimode characteristics of FP laser diodes [16]–[18]. Particular attention has been focused on elucidating the nonlinear mechanisms that give rise to the observed multimode behaviours [19]–[22] (and references therein). In contrast, rather less effort has been given to the study of the spectral characteristics of the multimode oscillation, and no systematic analysis describing the multimode spectrum of a semiconductor laser has yet been presented. Specifically, it is of considerable interest to ascertain whether the multi-longitudinal modes are lasing independently (free running) or whether specific frequency or phase relations exist between the modes, indicating frequency-locked operation.

2.3.2 Experimental Verification of Self-Locking FM Operation

Tiemeijer proposed that the multimode spectra (c) and (d) (Fig. 2.3) observed at high injection currents represent sidebands of self-locked FM laser oscillation. The Tiemeijer approach was to measure the fundamental and the second harmonic (SH) spectra of the laser diodes at high injection current levels. Then using the measured fundamental multimode spectrum, calculation was made of the SH spectrum expected in the cases of

(i) free-running,

(ii) mode-partitioned behaviour, and

(iii) FM laser oscillation behaviour.

Comparison was then made between the measured SH spectrum and the calculated SH spectra of the above mentioned cases. On this basis, it was concluded that FM operation was indeed occurring in the devices.

Self-locking FM operation in strained quantum well (QW) InGaAs ridge-waveguide lasers operating at 980 nm wavelength was recently reported by Chinn and coworkers [23]. Chinn reached the conclusion that FM self-locking was occurring in their devices based on the general agreement between the calculated FM-locked SH spectrum and the measured SH spectrum. Moreover, Chinn and Swanson have used optical fibre dispersion to convert the coherent self-locking FM oscillation output to a AM pulse train at multiples of the laser round-trip frequency [24]. This latter work produced AM optical pulses at repetitive frequencies of up to 233 GHz from a single self-induced FM-locked laser diode with no external modulation, and demonstrated that self-locking FM operation is of considerable interest both for device applications and for the understanding of the physical mechanisms that give rise to this phenomenon.

By measuring the beat spectra between adjacent longitudinal modes of long-cavity (2500 μm) InGaAs single QW lasers, Sharfin *et al.* have observed a dramatic narrowing of the beat spectrum between the dominant and adjacent modes at high output powers [25]. The narrowing of the beat spectrum was accompanied by a transition from nearly single-mode behaviour to a highly structured, multi-mode spectrum. Sharfin attributed these observations as self-induced beat-frequency locking, and interpreted the results in terms of three-mode coupling interactions involving self-induced FM laser oscillation and AM effects at the beat frequency between two neigbouring modes.

Although some analysis of self-locking behaviour has been carried out by Tiemeijer *et al.* [13] to explain their experimental results, the analysis was predicated on the assumption that an FM-locked state had been attained. The objective of the present work is to show, via an integration of multimode laser rate equations, that the occurrence of self-locking FM operation in semiconductor lasers may indeed be attributed to nonlinear mechanisms intrinsic to these devices. In particular, it is demonstrated that the strength of nonlinearity required to obtain self-locking FM operation is in accordance with values of gain saturation and multiwave mixing coefficients typically encountered in long-wavelength semiconductor lasers.

2.4 Formalism

Intrinsic FM locking was examined in gas lasers many years ago [4, 26] and theoretical analysis was performed in that context based on Lamb's semiclassical laser theory [12]. An important conclusion from these earlier work is that the inclusion of three cavity modes is adequate to establish the criteria for mode-locking [27]. In the present analysis, the three-mode Lamb model is adapted to account for the properties of semiconductor lasers.

In multi-longitudinal mode lasers, the electric field can be written as

$$E(t) = \sum_n E_n(t) \exp\{-i[\nu_n t + \phi_n(t)]\} , \tag{2.9}$$

where the amplitude coefficient $E_n(t)$ and phase $\phi_n(t)$ vary little in an optical frequency period, and $(\nu_n + \dot{\phi}_n)$ is the oscillation frequency of the n-th mode. In general this oscillation frequency is not necessarily equal to the passive cavity frequency Ω_n because of dispersion of the active medium. Three modes are considered in the present analysis and it is assumed that mode 2 is nearest to the

gain peak.

2.4.1 Semiclassical Laser Equations

The amplitude- and frequency-determining equations given by Lamb [12] in the case of three modes are

$$\dot{E}_1 = E_1\left(\alpha_1 - \sum_{m=1}^{3}\theta_{1m}E_m^2\right) - E_2^2E_3(\eta_{23}\cos\Psi + \xi_{23}\sin\Psi)\,, \tag{2.10}$$

$$\dot{E}_2 = E_2\left(\alpha_2 - \sum_{m=1}^{3}\theta_{2m}E_m^2\right) - E_1E_2E_3(\eta_{13}\cos\Psi - \xi_{13}\sin\Psi)\,, \tag{2.11}$$

$$\dot{E}_3 = E_3\left(\alpha_3 - \sum_{m=1}^{3}\theta_{3m}E_m^2\right) - E_2^2E_1(\eta_{21}\cos\Psi + \xi_{21}\sin\Psi)\,, \tag{2.12}$$

$$\nu_1 + \dot{\phi}_1 = \Omega_1 + \sigma_1 + \sum_{m=1}^{3}\tau_{1m}E_m^2 - (E_2^2E_3/E_1)(\eta_{23}\sin\Psi - \xi_{23}\cos\Psi)\,, \tag{2.13}$$

$$\nu_2 + \dot{\phi}_2 = \Omega_2 + \sigma_2 + \sum_{m=1}^{3}\tau_{2m}E_m^2 + E_1E_3(\eta_{13}\sin\Psi + \xi_{13}\cos\Psi)\,, \tag{2.14}$$

$$\nu_3 + \dot{\phi}_3 = \Omega_3 + \sigma_3 + \sum_{m=1}^{3}\tau_{3m}E_m^2 - (E_2^2E_1/E_3)(\eta_{21}\sin\Psi - \xi_{21}\cos\Psi)\,, \tag{2.15}$$

where $\dot{E}_n$ and $\dot{\phi}_n$ represent time rate of change of the mode amplitude and the phase, respectively, and

α_m is the linear net (amplitude) gain (see Eq. (2.27) for its relation to conventional semiconductor laser gain),

θ_{nm} is the self/cross saturation coefficient describing the effect of gain suppression on mode n because of the presence of mode m,

η_{nm} and ξ_{nm} arise because of multiwave mixing and describe the phase dependent coupling between modes, produced by combination tones in the active medium,

σ_m is the power independent pulling coefficient arising from the dispersive nature of the active medium,

τ_{nm} is the self/cross pushing coefficient which takes into account the power dependent 'mode repulsion' effects between the various modes, and

Ψ is the relative phase angle defined as

$$\Psi(t) = (2\nu_2 - \nu_1 - \nu_3)\,t + 2\phi_2 - \phi_1 - \phi_3\,. \tag{2.16}$$

Differentiating Eq. (2.16) with respect to time, the equation of motion for Ψ is obtained as

$$\dot{\Psi} = 2(\nu_2 + \dot{\phi}_2) - (\nu_1 + \dot{\phi}_1) - (\nu_3 + \dot{\phi}_3)\,, \tag{2.17}$$

Substituting the frequency-determining equations (2.13)–(2.15) into Eq. (2.17), we obtain

$$\dot{\Psi} = S + A\sin\Psi + B\cos\Psi\,, \tag{2.18}$$

where

$$S = 2\sigma_2 - \sigma_1 - \sigma_3 + E_1^2(2\tau_{21} - \tau_{11} - \tau_{31}) + E_2^2(2\tau_{22} - \tau_{12} - \tau_{32}) + E_3^2(2\tau_{23} - \tau_{13} - \tau_{33})\,, \tag{2.19}$$

$$A = 2E_1E_3\eta_{13} + (E_2^2E_3/E_1)\eta_{23} + (E_2^2E_1/E_3)\eta_{21}\,, \tag{2.20}$$

$$B = 2E_1E_3\xi_{13} - (E_2^2E_3/E_1)\xi_{23} - (E_2^2E_1/E_3)\xi_{21}\,. \tag{2.21}$$

Hence it is seen that the frequency- and the amplitude-determining equations do not depend on the phases individually, but on the combination as the relative phase angle.

Eqs. (2.10)–(2.12) and (2.18) are the four basic working equations in this analysis. These simultaneous differential equations are solved numerically (using the Kutta-Merson method of integration within a standard library routine) to obtain the mode amplitudes and the relative phase angle.

2.4.2 Estimation of Parameter Values

The amplitude- and frequency-determining equations introduced above were originally developed for gas lasers [27]. As such it is necessary to identify the semiconductor laser analogues of the various terms contributing to the nonlinear dynamics. It is apparent that the coupled mode equations used to analyze multimode semiconductor laser operation are very similar to the equations given above. It is straight forward then to obtain the corresponding values of the self/cross saturation coefficients from typical semiconductor parameter values.

Consider the amplitude-determining equation (2.10):

$$\dot{E}_n = E_n \alpha_n \left[1 - \frac{1}{\alpha_n} \sum_{m=1}^{3} \theta_{nm} E_m^2 \right] + \ldots . \tag{2.22}$$

Letting

$$I_n = E_n^2 , \tag{2.23}$$

and differentiating with respect to time, we obtain

$$\dot{I}_n = 2 E_n \dot{E}_n . \tag{2.24}$$

It follows from Eq. (2.22) that

$$\dot{I}_n = 2 \alpha_n I_n \left[1 - \frac{1}{\alpha_n} \sum_{m=1}^{3} \theta_{nm} I_m \right] + \ldots . \tag{2.25}$$

This equation is compared with the coupled-mode photon density equations for multimode lasers [19] given by

$$\dot{P}_n = v_g g_n^L P_n \left[1 - \sum_{m=1}^{3} \beta_{nm} P_m \right] - \gamma P_n + R_{sp} , \tag{2.26}$$

where β_{nm} is the self/cross saturation coefficient (in unit of cm^3), $v_g = c/n_g$ is the group velocity, c is the velocity of light in vacuum, n_g is the group index, g_n^L is the linear gain coefficient of mode n (per-unit length), γ is the cavity loss (inverse time), and R_{sp} is the spontaneous emission coefficient.

Comparing Eqs. (2.25) and (2.26), it is noted that the photon density P (inverse volume) is given by $P_n = I_n = E_n^2$. Here the field amplitude E_n has been normalized to include the factor $\sqrt{2\epsilon_0 n_r n_g/(\hbar\nu_0)}$ so that $\sum E_m^2$ gives the total photon density, where ϵ_0 is the permittivity of free space, n_r is the refractive index, $\hbar$ is the Planck's constant divided by 2π, and ν_0 is the reference frequency. It follows that

$$\alpha_n = v_g g_n^L/2 \,, \tag{2.27}$$

$$\theta_{nm} = \alpha_n \beta_{nm} \,. \tag{2.28}$$

Using parameter values appropriate to InGaAsP laser diodes operating at 1.55 μm [19]: $n_g = 4$, $\beta \approx 6.7 \times 10^{-17}$ cm^3, $g^L = 60$ cm^{-1}, it is found that

$\alpha_n = 2.25 \times 10^{11}$ s^{-1} and

$\theta_{nm} = 1.51 \times 10^{-5}$ cm^3 s^{-1} .

The values of other parameters such as τ_{nm}, η_{nm} and ξ_{nm} are assumed to have the same order of magnitudes as θ_{nm}. The power independent pulling coefficient is assumed to be of the order of the inverse of the cavity round trip time, $\sigma_n \approx 1.0 \times 10^{12}$ s^{-1}. With these values, the amplitude- and frequency-determining equations are adapted to model semiconductor laser multimode operation and then may be solved numerically.

2.5 Self-Locking FM Laser Operation

As explained by Sayers and Allen [26], to determine the conditions under which locking occurs it is necessary to integrate the field amplitude and phase rate equations allowing the relative phase angle to become either constant (self beat-frequency locked state) or monotonically increasing with time (unlocked state). For the present work, it is shown that for nonlinear gain parameters appropriate

to long-wavelength semiconductor lasers, a self-locked state may be obtained in this way.

From the preceding section, it was estimated that all the nonlinear coupling parameters required for the present analysis are of the order 10^{-5} cm^3s^{-1}. Then, for example, using the value 1.5×10^{-5} cm^3s^{-1} for all the nonlinear coupling coefficients, it was found that the three-mode semiconductor laser evolved to a self-locking state. The dynamical behaviours of the field amplitudes and relative phase angle are shown in Figs. 2.4(a) and 2.4(b), respectively.

It must be stressed that this is a highly nontrivial result. It has been demonstrated here that gain nonlinearities typical of InGaAsP lasers are indeed sufficient to cause self-locking to occur in multimode devices.

Fig. 2.5 illustrates the time development of the mode amplitudes and relative phase angle when self-locking does not occur. It is observed from Fig. 2.5(b) that in an unlocked state the relative phase angle increases monotonically with time. In this case, side-mode suppression arising from a large nonlinear gain is evident, and leads to a near single-mode operation of the semiconductor laser.

2.5.1 Output Power in Self-Locked State

To make comparison with experimental observations of self-locking FM operation, it is necessary to calculate the output power of the laser in the self-locked state. It is possible to relate the output power per-facet P_{out} to the photon density in the laser cavity P by way of the relationship [28]

$$P_{out} = \frac{1}{2}\hbar\nu_0 v_g \frac{1}{L}\ln\left(\frac{1}{R}\right)VP \tag{2.29}$$

where L is the laser cavity length, R is the power facet reflectivity and V is the laser active region volume. Considering InGaAsP laser diodes operating at 1.55

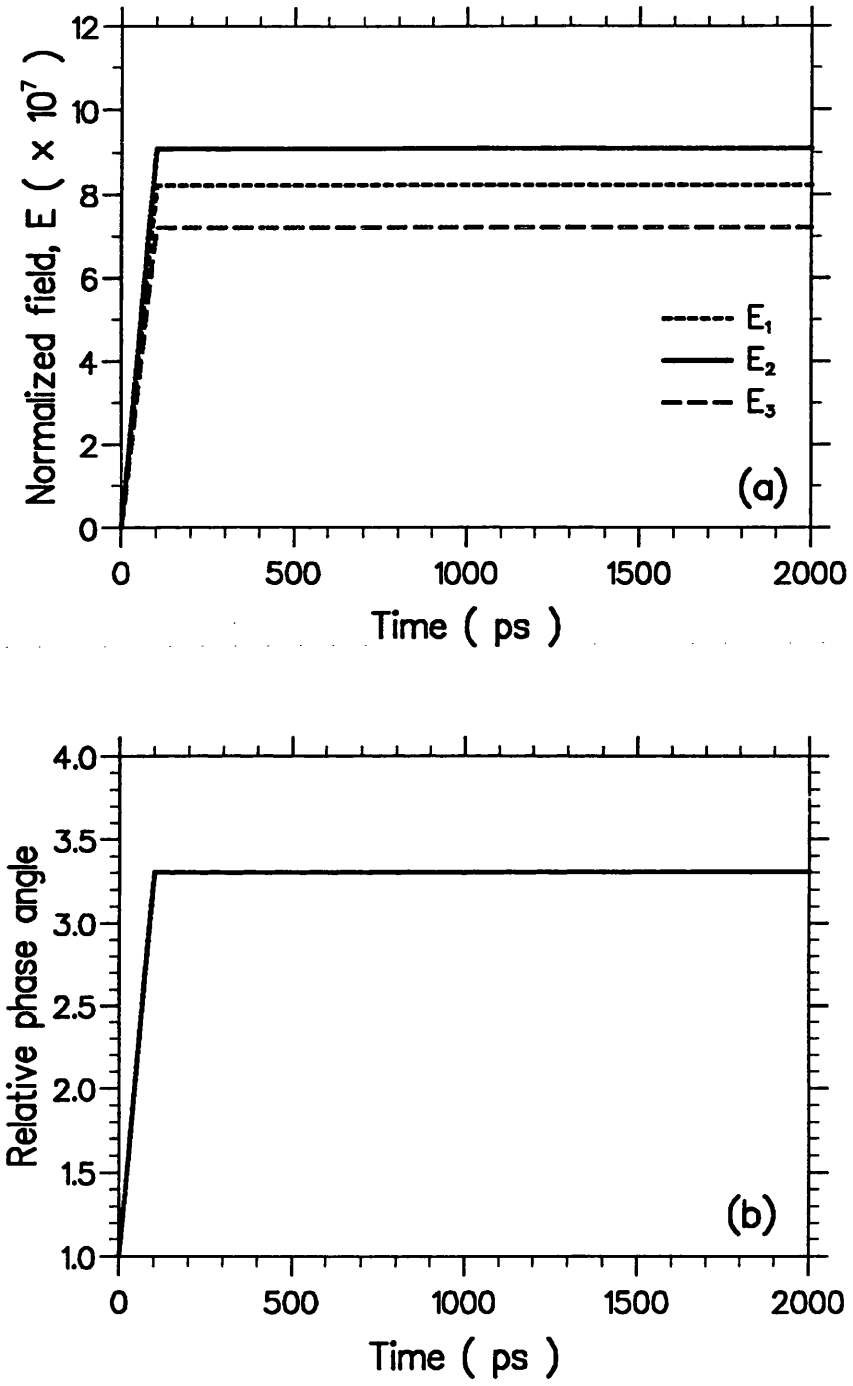

Figure 2.4: Time evolution of (a) mode amplitudes and (b) relative phase angle in a self-locked state. The normalized field amplitude is in units of $cm^{-3/2}$ throughout the analysis. Gain saturation nonlinearities are of the order of 1.5×10^{-5} cm^3s^{-1} in a self-locked state.

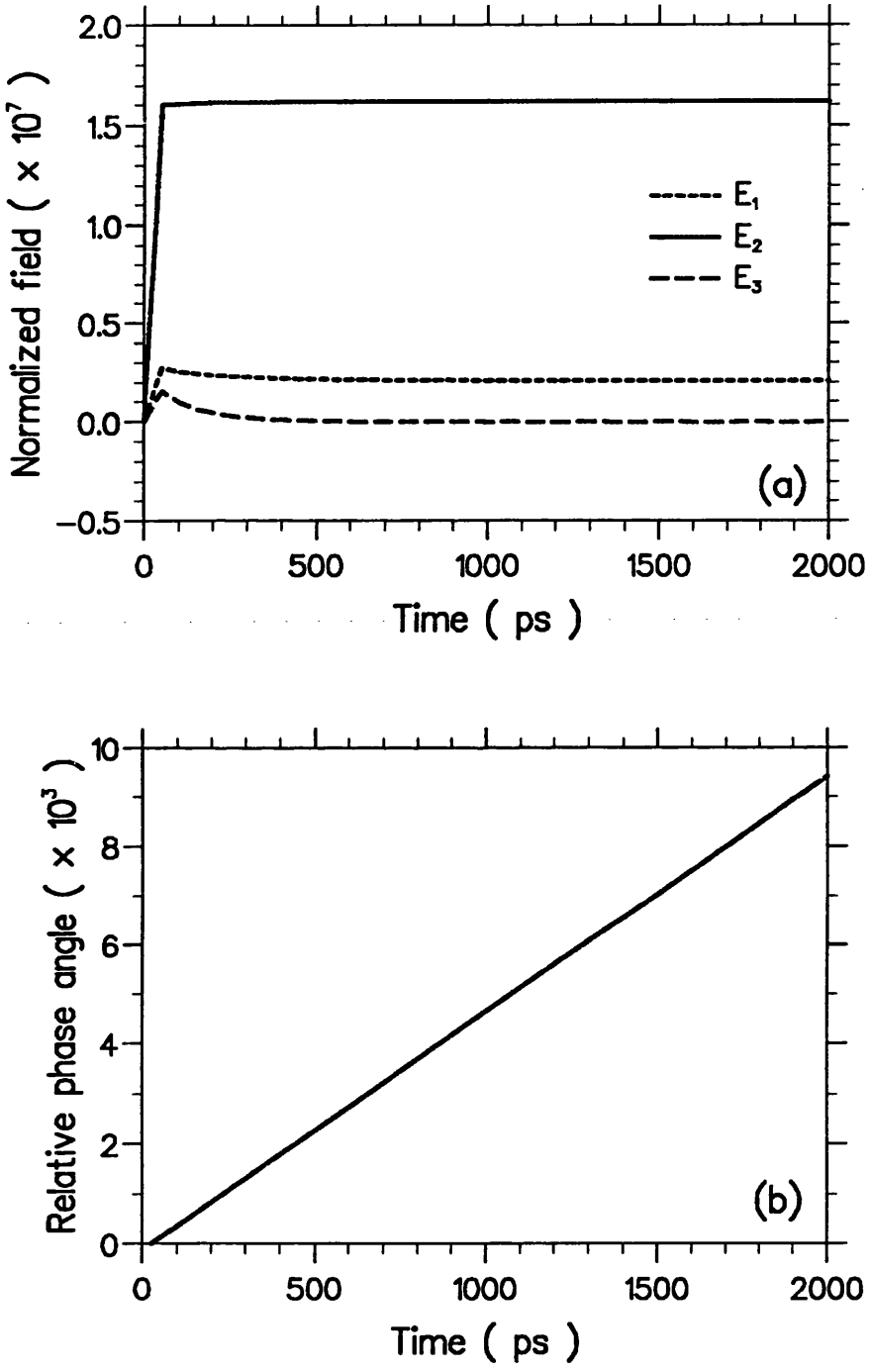

Figure 2.5: Time evolution of (a) mode amplitudes and (b) relative phase angle when self-locked state is not achieved. Gain saturation nonlinearities are in the order of 10×10^{-5} cm^3s^{-1} in this case.

μm and taking typical values: $R = 0.32$ and $V = 0.15\ \mu\text{m} \times 1.5\ \mu\text{m} \times 250\ \mu\text{m}$, it is found that the output power per-facet can be written as

$$P_{out} = 1.23 \times 10^{-15} P\ , \tag{2.30}$$

where P is the photon density in cm^{-3} and P_{out} is in mW.

For the self-locked state shown in Fig. 2.4, it is found that the laser output power per-facet is about 12.2 mW. This estimate is in excellent agreement with the experimental results reported by Tiemeijer *et al.* [13], where FM operation was observed at output powers in the range of 5 mW to 15 mW.

In contrast, using parameters appropriate to GaAs lasers, where the nonlinear self saturation coefficent is about one order of magnitude smaller than that of InGaAsP lasers (see for example Ref. [15]), the present calculation predicts that self-locking may only be achieved at output powers of the order of 200 mW to 300 mW. Hence these effects would not be anticipated in GaAs lasers under normal operating conditions. This result is again well supported by experimental evidence that GaAs lasers operating at 0.8 μm have not shown any self-locking FM behaviour [13, 24].

It should be noted that the self-locked state (Fig. 2.4) and the unlocked state (Fig. 2.5) both represent stable states of the three-mode laser operation [27]. However, under certain conditions (as discussed in Ref. [27]), the laser enters an unstable regime whereby the relative phase angle increases with time and the mode amplitudes oscillate in time. This situation is depicted in Fig. 2.6. The unstable state may be obtained if mode 1 or mode 3 is tuned towards the gain peak. Because of the asymmetric nature of the mode interactions, the linear pulling (as characterized by σ_n) and the nonlinear pushing (τ_{nm}) mechanisms give rise to unbalanced dispersion effects in the mode coupling dynamics, thereby resulting in unstable operation of the laser. It is therefore noted from Fig. 2.6(a)

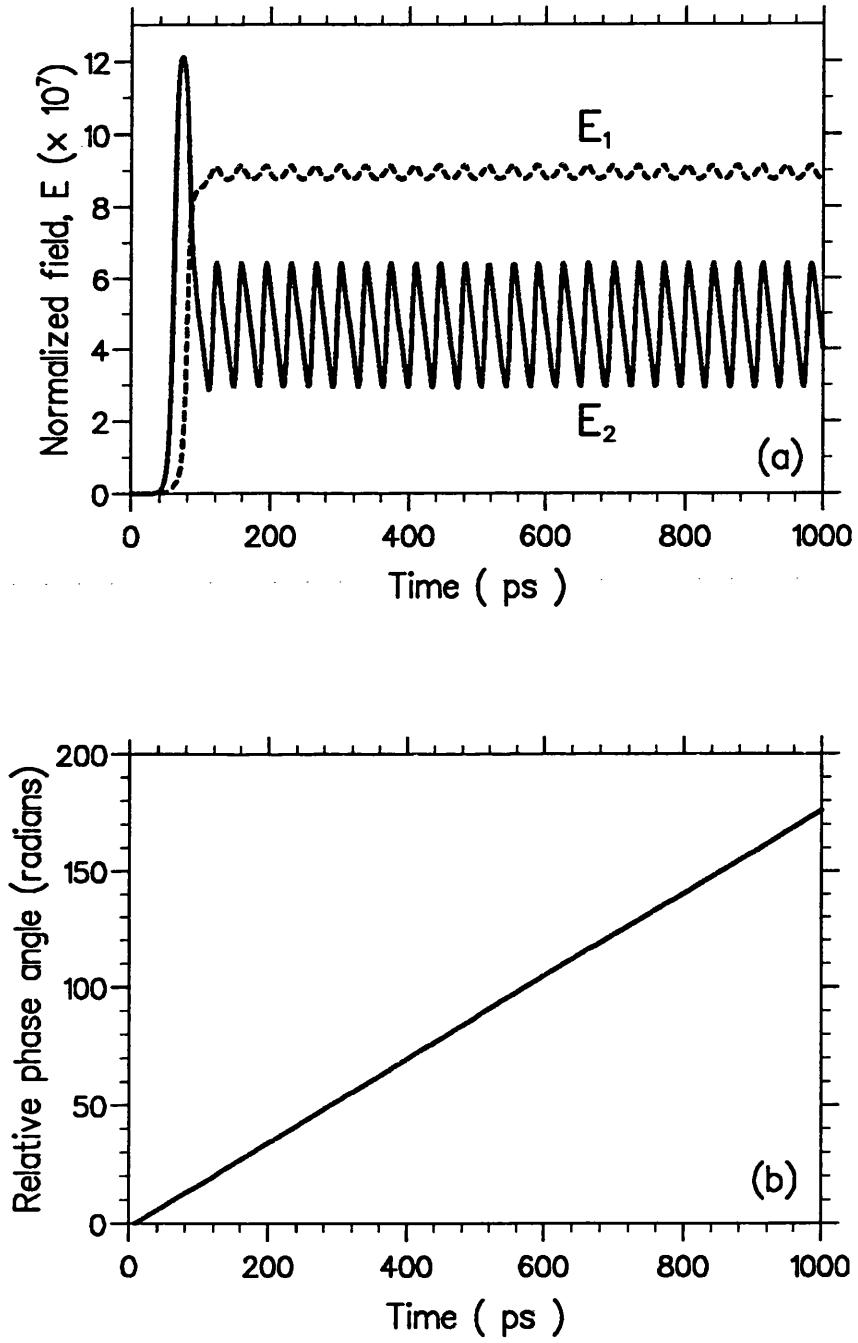

Figure 2.6: Time evolution of mode amplitudes and relative phase angle in an unstable state of the three-mode laser operation. The mode amplitude E_3 has a similar oscillatory nature as E_2, and has been omitted in the figure for clarity.

that E_1 becomes the dominant mode in the unstable state of the three-mode laser operation.

2.5.2 Nature of the Self-Locking FM Laser Operation

The above consideration of the output power in the self-locked state provides strong support for the assertion that gain nonlinearities account for the observations of Tiemeijer *et al.* [13]. Qualitative interpretation of the results obtained for a three-mode self-locked state, as illustrated in Fig. 2.4, is discussed in the following in order to gain an insight into the nature of the self-locking FM laser operation. It is also important to consider the phase information obtained from the simulations described above. In particular, the purity or otherwise of the FM operation may be assessed from the calculated value of the relative phase angle.

Since Ψ is constant (time-independent) in a self-locked state, it follows from Eq. (2.16) that

$$2\nu_2 - \nu_1 - \nu_3 = 0 \,, \tag{2.31}$$

$$2\phi_2 - \phi_1 - \phi_3 = \Psi \,. \tag{2.32}$$

Physically, Eq. (2.31) can be interpreted as follows: The beating between frequencies ν_2 and ν_1 modulates the carrier population in the semiconductor laser at the difference frequency $\nu_2 - \nu_1$. The carrier modulation (called the *population pulsations*) creates both dynamic gain and index gratings [29], which, in turn, interact with mode 2 to give the tone

$$2\nu_2 - \nu_1 \equiv \nu_3' \,, \tag{2.33}$$

which is very nearly equal to ν_3 and contributes in third-order to the complex polarization for mode 3. The process through which tones such as ν_3' (called *combination tones* in semiclassical laser theory) are generated is known as "*multiwave*

mixing". The existence of the combination tone ν_3' tempts mode 3 to oscillate at frequency ν_3'. In the presence of gain nonlinearities, beat-frequency locking occurs so that

$$\nu_3 \equiv \nu_3' = 2\nu_2 - \nu_1 \,. \tag{2.34}$$

This condition can be written as

$$\nu_2 - \nu_1 = \nu_3 - \nu_2 \,, \tag{2.35}$$

that is, the beat notes between adjacent modes are equal.

Analysis of three-mode laser operation based on Lamb's semiclassical theory [27] shows that stable self-locked state is achieved when $\Psi = 0$ or $\Psi = \pi$. The value $\Psi = 0$ implies, from Eq. (2.32), that

$$\phi_2 - \phi_1 = \phi_3 - \phi_2 \,. \tag{2.36}$$

Since one phase angle is arbitrary and another one is determined by the choice of time origin [27], it can be chosen here that $\phi_1 = \phi_2$, so that

$$\phi_1 = \phi_2 = \phi_3 \,, \tag{2.37}$$

that is, all the phases have the same value. This situation is referred to as AM locking and is the same as the case of mode-locked short pulse generation as discussed in Sec. 2.2.1. The second value $\Psi = \pi$ leads to the phase relation

$$\phi_1 = \phi_2 = \pi + \phi_3 \,, \tag{2.38}$$

which is termed 'FM locking', similar to the case as discussed in Sec. 2.2.2.

In the three-mode self-locking calculations described in this chapter, Ψ is found to lie in the range of 3 to 4 radians. For example, in the case shown in Fig. 2.4, the value of Ψ is 3.312. In order to compare the nature of the three-mode self-locking operation with both mode-locked pulsing operation (see Fig. 2.1) and

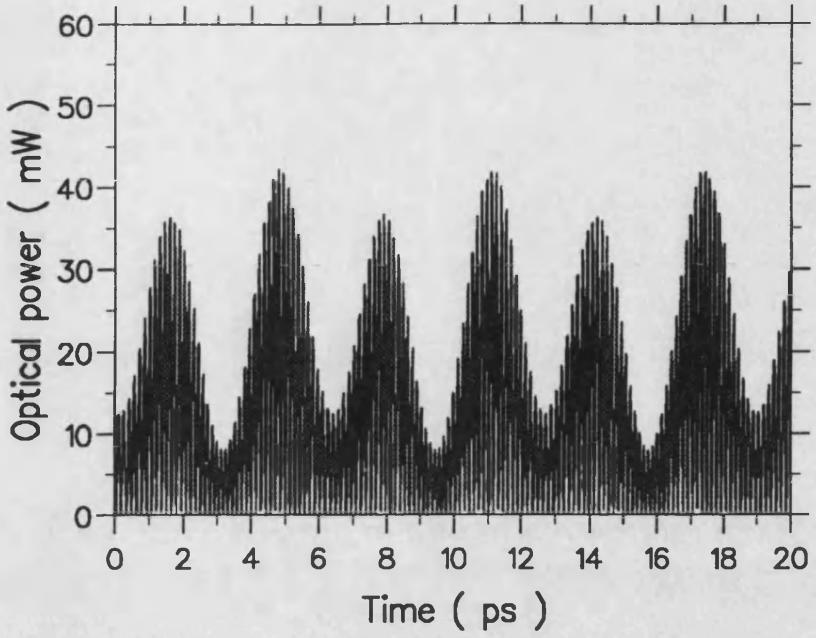

Figure 2.7: Output waveform of three-mode self-locking FM laser operation of semiconductor lasers.

pure FM laser oscillation (Fig. 2.2), the output waveform of the self-locked laser corresponding to the case in Fig. 2.4 is shown in Fig. 2.7. It is observed from Fig. 2.7 that periodic variation in the signal power envelope is present, with a period T equal to the inverse of the intermodal frequency spacing, and is given by $T = 2n_r L/c \approx 5.8$ ps. However, sharp pulsing associated with mode-locked AM operation is not evident. From the calculated value of the relative phase angle Ψ and the output waveform of the three-mode self-locked laser, it is clear that AM locking does not occur here, but also it is apparent that pure FM locking is not predicted within the present formalism. However, since the simulations described here consider only three oscillating modes, it is clear that the full set of Bessel-function sidebands contained in Eq. (2.8) are not included in the present treatment. For this aspect, in particular, there is a need to generalize the analysis in this chapter to a multimode formalism. This extension to a multimode analysis

is the subject of the next chapter.

2.6 Nonlinear Gain Diagnostics

In this section, the results obtained from an investigation of the parameter dependence of three-mode self-locked operation are presented and discussed. Within the acknowledged limitation of this model, it is sought to map out regions in the nonlinear coefficient parameter space where self-locking FM operation is expected to occur. It is suggested that this procedure may be useful as a means of calibrating nonlinear gain saturation in semiconductor lasers. A considerable effort has been directed at elucidating the mechanisms for gain nonlinearities in semiconductor lasers (see Refs. [14, 15] for reviews). In particular, the role of multiwave mixing processes has been emphasized recently [29]–[31]. It is argued, therefore, that the results given below may be used to give quantitative tests for theories of nonlinear gain in semiconductor lasers.

2.6.1 Self and Cross Saturation Effects

The dependence of the mode amplitudes and the relative phase angle on the gain saturation coefficient, θ_{nm}, is illustrated in Figs. 2.8(a) and 2.8(b), respectively. It is found that increasing the value of θ_{nm} (other things being held constant) will decrease the amplitudes of the various modes, but will increase the steady-state value of the relative phase angle, in self-locking operation.

The reduction in mode amplitudes for increasing θ_{nm} can be explained as follows. Consider the amplitude-determining equation for mode 1 as given by

$$\dot{E}_1 = E_1 \left[\alpha_1 - \theta_{12}E_2^2 - \theta_{13}E_3^2\right] - \theta_{11}E_1^3 + \ldots \ . \tag{2.39}$$

In the absence of any interaction between the modes, the single mode equation

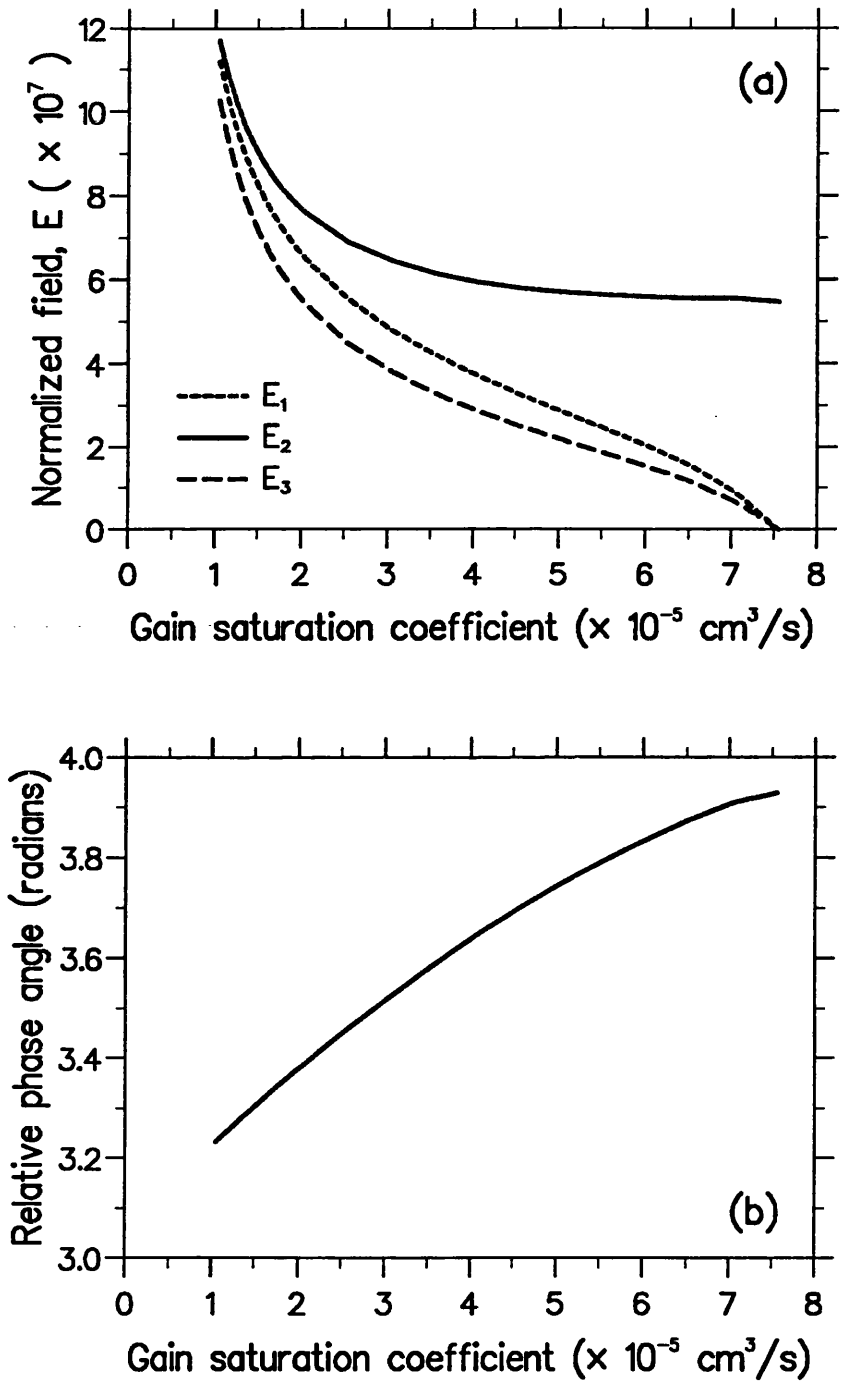

Figure 2.8: Dependence of (a) normalized field amplitudes and (b) relative phase angle on gain saturation coefficient in the self-locked state. The normalized field is in units of $cm^{-3/2}$ throughout the analysis.

would be

$$\dot{E}_1 = \alpha E_1 - \beta_1 E_1^3 \,, \tag{2.40}$$

where $\beta_1 = \theta_{11}$ is the self saturation coefficient for mode 1. Comparing these two equations, it is concluded that the effect of the interaction terms θ_{12} and θ_{13} is to reduce the effective gain of mode 1. α in Eq. (2.40) is effectively replaced by terms in brackets in Eq. (2.39). Hence, increasing θ_{nm} will decrease the effective gain of the various modes, resulting in reduced steady-state amplitudes.

It is also observed that the rate of decrease of amplitude with respect to θ_{nm} is smallest in the central mode compared with the side-modes. For $\theta_{nm} > 7.5 \times 10^{-5}$ $\mathrm{cm^3 s^{-1}}$, the amplitudes of the two side-modes reduce to zero rapidly leaving only mode 2 in oscillation, and self-locking ceases to occur. It is thus found that there is an upper limit to the value of θ_{nm} above which no-locking is observed. Because θ_{nm} is inversely related to mode amplitudes and thus optical power, as discussed above, it is concluded that self-locking FM operation occurs only when the laser optical power exceeds a threshold value. In addition, increasing θ_{nm} will increase the deviation of Ψ from the value π radians, as shown in Fig. 2.8(b). The resulting FM intensity waveform will be highly distorted because of the increase in the AM component in the self-locking FM optical wave.

Fig. 2.9 shows the output power (per-facet) versus gain saturation coefficient curve for the three-mode self-locking laser. From Fig. 2.9, it is found that the threshold output power (minimum power) for self-locking FM operation to occur is about 2 mW (corresponding to $\theta_{nm} = 7.5 \times 10^{-5}$ $\mathrm{cm^3 s^{-1}}$). This estimate of the self-locking threshold output power agrees excellently with experimental evidence from Ref. [13], in which the threshold *internal power* for the occurrence of self-locking FM oscillation was extrapolated from experimental data to be 4 mW. Below the estimated self-locking threshold output power of 2 mW (right-hand

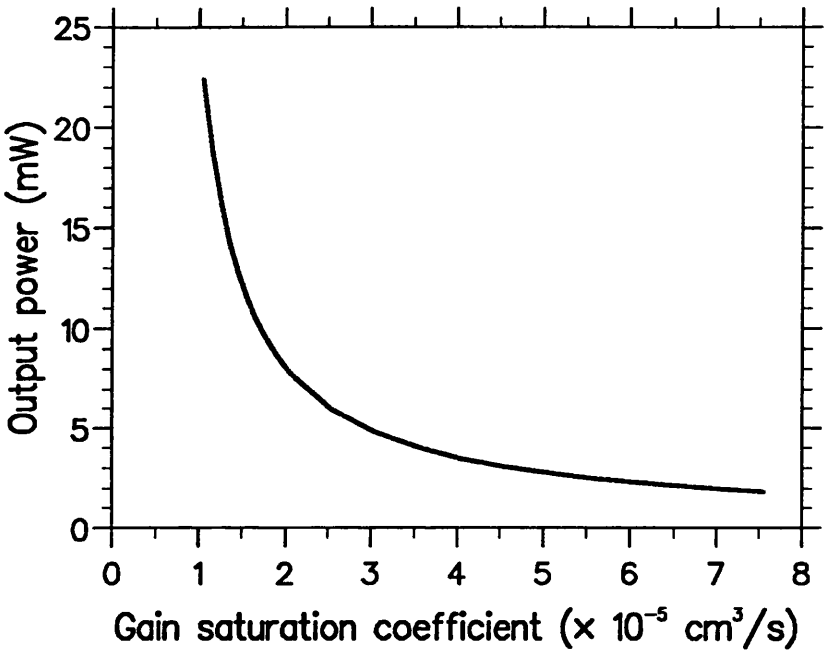

Figure 2.9: Output power versus gain saturation coefficient curve for three-mode self-locked operation in a semiconductor laser.

limit of the curve in Fig. 2.9), the laser diode operates in single longitudinal mode, as shown in Fig. 2.8(a), in accordance with experimental observation (see Fig. 2.3).

Furthermore, the output power increases rapidly for $\theta_{nm} < 1.0 \times 10^{-5}$ cm^{3}s^{-1}. Because self-locking FM operation was observed in InGaAsP lasers at powers below 20 mW, it can be deduced from Fig. 2.9 that under normal operating conditions, the value of the gain saturation coefficient θ_{nm} is likely to be greater than 1.0×10^{-5} cm^{3}s^{-1} (corresponding to $\beta \approx 4.4 \times 10^{-17}$ cm^3 from Eq. (2.28)).

2.6.2 Multiwave Mixing Effects

The parameter η_{nm} and ξ_{nm} represent the general saturation terms (multiwave mixing coefficients), which take into account the phase-coupling "combination

tones" interaction of the three-mode laser. Figs. 2.10(a) and 2.10(b) illustrate the dependence of the mode amplitudes and the relative phase angle upon the multiwave mixing coefficient η_{nm}, respectively. It is observed that the amplitudes of the side modes increase monotonically with η_{nm}, whereas the amplitude of the central mode decreases at first and then increases after passing through a minimum point. For values of $\eta_{nm} > 2.5 \times 10^{-5}$ cm^3s^{-1}, the output power is found to be greater than 20 mW and this output power increases exponentially for further increase in η_{nm}. Since observation of self-locking FM oscillation in semiconductor lasers was reported for output powers below 20 mW, the value of multiwave mixing coefficient is estimated to be smaller than 2.5×10^{-5} cm^3s^{-1} under normal operating conditions.

From Fig. 2.10(a), it is also noted that the amplitudes of the side modes decay to zero for value of $\eta_{nm} < 0.3 \times 10^{-5}$ cm^3s^{-1}, and that the laser diode goes into no-locking below this value of η_{nm}. This demonstrates that multiwave mixing processes are critical in effecting self-locking FM operation in laser diodes, and that multiwave mixing values in the range of 0.3×10^{-5} to 2.5×10^{-5} cm^3s^{-1} may give rise to self-locking FM oscillation in semiconductor lasers in the presence of gain nonlinearities.

The parameter σ_n and τ_{nm} describe the linear pulling and the nonlinear pushing effects of the three-mode laser interactions, respectively. It is found that self-locking operation is critically dependent upon the relative magnitudes of all the nonlinear gain and coupling coefficients, as will be discussed in the following paragraphs.

Because the mode amplitudes always settle to constant values in the *stable* operating regime (see Figs. 2.4 and 2.5), regardless of whether or not self-locking is achieved, the parameters S, A and B in the frequency-determining equation

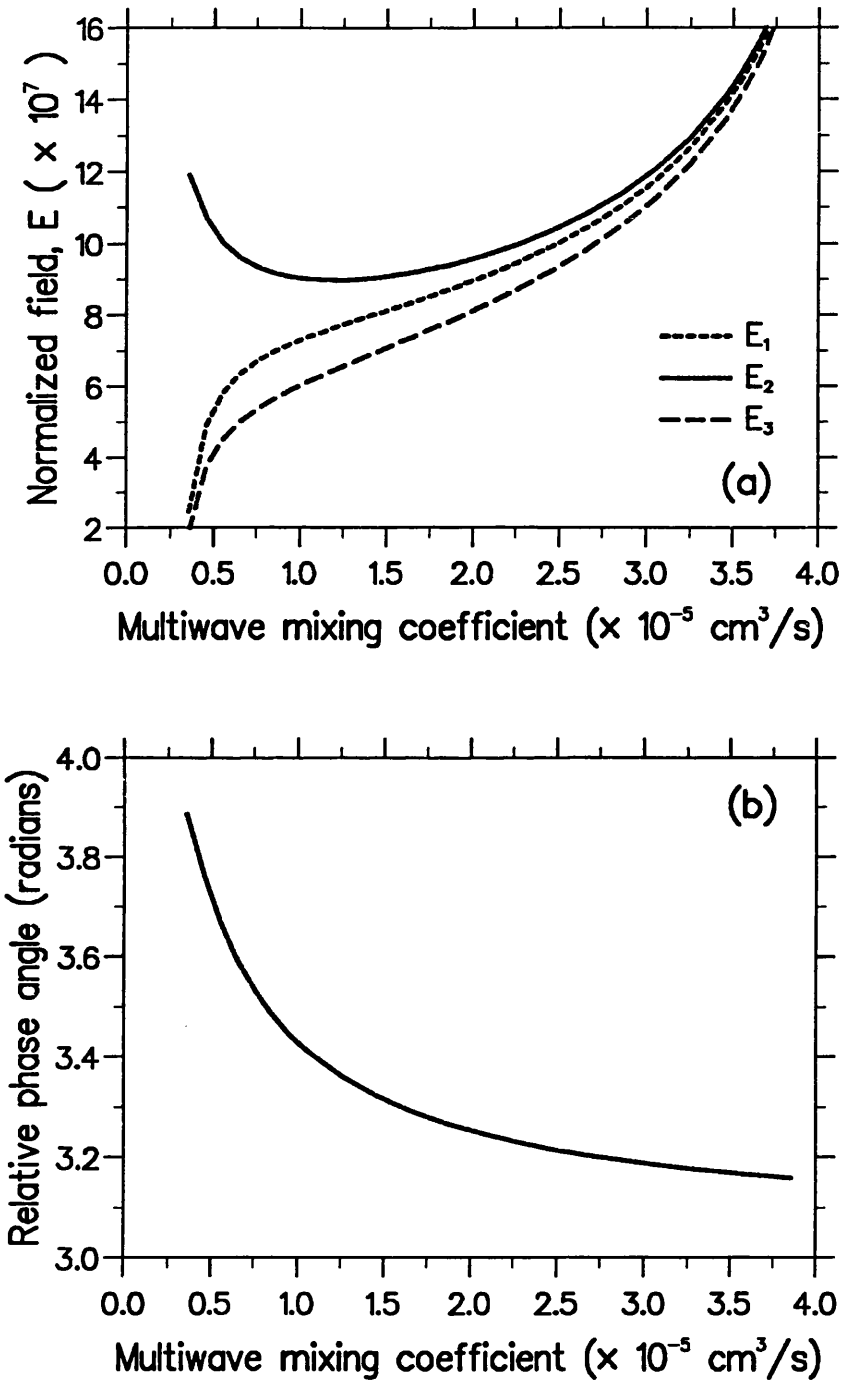

Figure 2.10: Dependence of (a) mode amplitudes and (b) relative phase angle on multiwave mixing coefficient for three-mode self-locking FM operation in a semiconductor laser.

(2.18) can be taken as constants. Hence, the frequency-determining equation can be treated independently from the amplitude-determining equations (2.10)–(2.12). This is called the "decoupled approximation" [27]. Eq. (2.18) can be expressed as

$$\dot{\Psi} = S + C\sin(\Psi - \Psi_0)\,, \tag{2.41}$$

where

$$C = \sqrt{A^2 + B^2}\,, \tag{2.42}$$

$$\Psi_0 = -\tan^{-1}(B/A)\,. \tag{2.43}$$

From Eq. (2.41), two situations exist. If $A^2 + B^2 < S^2$, $\dot{\Psi}$ is always positive and hence Ψ is monotonically changing with time, and thus the modes are not locked. On the other hand, if $A^2+B^2 \geq S^2$, $\dot{\Psi} = 0$ in some instances. This implies that Ψ is independent of time and thus, by definition, $\nu_2 - \nu_1 = \nu_3 - \nu_2$ and the relative phase angle rapidly approaches a constant value, the actual value being dependent on S and other parameters in the amplitude-determining equations. The modes are therefore locked in this latter situation. Hence, the necessary criterion for self-locking operation to occur is given by

$$A^2 + B^2 \geq S^2\,. \tag{2.44}$$

Since A and B (as given by Eqs. (2.20) and (2.21), respectively) are dependent upon η_{nm} and ξ_{nm}, whereas S (given by Eq. (2.19)) is a function of σ_n and τ_{nm}, from Eq. (2.44), it is deduced that self-locking may be achieved if the values of η_{nm} and ξ_{nm} (multiwave mixing coefficients) are large compared to σ_n and τ_{nm}. On the other hand, Eq. (2.44) is a necessary, but not sufficient, condition for self-locking: to achieve self-locking, it is also essential that the optical power of the laser exceeds a threshold value at which the nonlinear gain effect is significant. Since the optical power, and hence the mode amplitudes are dependent upon

θ_{nm}, α_n, η_{nm} and ξ_{nm}, there is no explicit relationship to determine when, and at what values of the various parameters, self-locking take place. It is found that, generally, self-locking is critically dependent on the relative magnitudes of η_{nm} and ξ_{nm} with respect to α_n and θ_{nm}. It is also established that self-locking is more sensitive to the multiwave mixing parameters, η_{nm} and ξ_{nm}, than the mode pulling/pushing coefficients, σ_n and τ_{nm}.

In summary, it has been shown that

(i) For gain saturation parameter greater than $\approx 7.5 \times 10^{-5}$ cm^3s^{-1}, side-mode suppression effect is such that the laser operates in a single longitudinal mode (at the central mode frequency) and hence FM self-locking cannot occur.

(ii) For multiwave mixing nonlinearities less than 0.3×10^{-5} cm^3s^{-1}, the central frequency again dominates because of insufficient population pulsation interactions to effect combination tone coupling, thereby inhibits self-locking operation.

(iii) For gain saturation parameter less than 1.0×10^{-5} cm^3s^{-1}, self-locking occurs at output powers greater than 20 mW. The self-locked output power is inversely related to the gain saturation parameter.

(iv) For multiwave mixing greater than $\approx 2.5 \times 10^{-5}$ cm^3s^{-1}, self-locking requires laser output power in excess of 20 mW. The self-locked output power increases with increased multiwave mixing nonlinearities.

(v) The value of the linear gain parameter α_n does not significantly affect the behaviours described above. The value of the linear gain does, of course, help determine the powers in the self-locked state.

The results summarized in (i) and (ii) delimit regions in the nonlinear parameter space for which self-locking is sustained. Specifically, it has been shown that self-locking occurs because of intrinsic multiwave mixing effects in semiconductor lasers in the presence of nonlinear gain. Furthermore, the determination of optical output powers in the self-locked state, indicated in (iii) to (v), provide further indications of the magnitude of gain nonlinearities present in semiconductor lasers.

2.7 Conclusion

A three-mode model has been used to demonstrate the role of gain nonlinearities in effecting self-locked FM oscillation in semiconductor lasers. The requisite gain nonlinearities and output power levels have been shown to be consistent with experimental observations. Specifically, self-locking FM oscillation occurs in long-wavelength InGaAsP lasers because of intrinsic multiwave mixing interactions occurring in the presence of large gain saturation nonlinearities in these devices. To demonstrate intensity-invariant FM oscillation and to establish the depth of the FM modulation in the self-locked state, it is necessary to take more than three modes into account. An extension of the formalism presented in this chapter to include a larger number of oscillating modes will be considered in the next chapter.

References

[1] A. E. Siegman, *Lasers*, University Science Books, pp. 1041–1049, 1986.

[2] K. Y. Lau, "Short-pulse and high frequency signal generation in semiconductor lasers," *J. Light. Technol.*, vol. 7, pp. 400–419, 1989.

[3] S. E. Harris and R. Targ, "FM oscillation of the He–Ne laser," *Appl. Phys. Lett.*, vol. 5, pp. 202–204, 1964.

[4] S. E. Harris and O. P. McDuff, "Theory of FM laser oscillation," *IEEE J. Quantum Electron.*, vol. QE-1, pp. 245–263, 1965,

[5] S. Saito, O. Nilsson, and Y. Yamamoto, "Oscillation center frequency tuning, quantum FM noise, and direct frequency modulation characteristics in external grating loaded semiconductor lasers," *IEEE J. Quantum Electron.*, vol. QE-18, pp. 961–970, 1982.

[6] A. Schremer, T. Fujita, C. F. Lin, and C. L. Tang, "Instability threshold resonances in directly modulated external-cavity semiconductor lasers," *Appl. Phys. Lett.*, vol. 52, pp. 263–265, 1988.

[7] A. Schremer and C. L. Tang, "Abrupt phase reversal in frequency-modulated external-cavity semiconductor lasers," *Appl. Phys. Lett.*, vol. 55, pp. 1832–1834, 1989.

[8] J. Bösl, R. Bauer, H. Rauch, U. Penning, G. Weimann, and W. Schlapp, "Modelocking of AlGaAs laser diode by intracavity AlGaAs phase-modulator," *Electron. Lett.*, vol. 25, pp. 864–866, 1989.

[9] R. Nietzke, P. Panknin, W. Elsässer, and E. O. Göbel, "Four-wave mixing in GaAs/AlGaAs semiconductor lasers," *IEEE J. Quantum Electron.*, vol. 25, pp. 1399–1406, 1989.

[10] R. Nagar, D. Abraham, N. Tessler, A. Fraenkel, and G. Eisenstein, "Frequency-modulation mode locking of semiconductor laser," *Opt. Lett.*, vol. 16, pp. 1750–1752, 1991.

[11] K. A. Shore and W. M. Yee, "Theory of self-locking FM operation in semiconductor lasers," *IEE Proc. Part J*, vol. 138, pp. 91–96, 1991.

[12] W. E. Lamb, "Theory of an optical maser," *Phys. Rev.*, vol. 134, pp. A1429–A1450, 1964.

[13] L. F. Tiemeijer, P. I. Kuindersma, P. J. A. Thijs, and G. L. J. Rikken, "Passive FM locking in InGaAsP semiconductor lasers," *IEEE J. Quantum Electron.*, vol. 25, pp. 1385–1391, 1989.

[14] K. A. Shore and M. W. McCall, "Nonlinear and quantum optics in semiconductor lasers," *Prog. Quantum Electron.*, vol. 14, pp. 63–129, 1990.

[15] J. Huang and L. W. Casperson, "Gain and saturation in semiconductor lasers," *Opt. Quantum Electron.*, vol. 25, pp. 369–390, 1993.

[16] B. Zee, "Broadening mechanism in semiconductor (GaAs) lasers: limitations to single mode power emission," *IEEE J. Quantum Electron.*, vol. QE-14, pp. 727–736, 1978.

[17] J. Manning, R. Olshansky, D. M. Fye and W. Powazinik, "Strong influence of nonlinear gain on spectral and dynamic characteristics of InGaAsP lasers," *Electron. Lett.*, vol. 21, pp. 496–497, 1985.

[18] G. P. Agrawal, "Effect of nonlinear gain on single-frequency behaviour of semiconductor lasers," *Electron. Lett.*, vol. 22, pp. 696–697, 1986.

[19] G. P. Agrawal, "Gain nonlinearities in semiconductor lasers: theory and application to distributed feedback lasers," *IEEE J. Quantum Electron.*, vol. QE-23, pp. 860–868, 1987.

[20] M. Yamada, "Theoretical analysis of nonlinear optical phenomena taking into account the beating vibration of the electron density in semiconductor lasers," *J. Appl. Phys.*, vol. 66, pp. 81–89, 1989.

[21] R. Frankenberger and R. Schimpe, "Origin of nonlinear gain saturation in index-guided InGaAsP laser diodes," *Appl. Phys. Lett.*, vol. 60, pp. 2720–2722, 1992.

[22] K. Kikuchi, M. Amano, C. E. Zah, and T. P. Lee, "Analysis of origin of nonlinear gain in 1.5 μm semiconductor active layers by highly nondegenerate four-wave mixing," *Appl. Phys. Lett.*, vol. 64, pp. 548–550, 1994.

[23] S. R. Chinn, C. A. Wang, and G. A. Evans, "Frequency modulation locking in 980 nm strained quantum well lasers," *Electron. Lett.*, vol. 29, pp. 646–648, 1993.

[24] S. R. Chinn and E. A. Swanson, "Passive FM locking and pulse generation from 980-nm strained-quantum-well Fabry-Perot lasers," *IEEE Photon. Technol. Lett.*, vol. 5, pp. 969–971, 1993.

[25] W. F. Sharfin, J. Schlafer, and E. S. Koteles, "Observation of mode beating and self-frequency locking in a nearly single-mode semiconductor laser," *IEEE J. Quantum Electron.*, vol. 30, pp. 1709–1712, 1994.

[26] M. D. Sayers and L. Allen, "Amplitude, competition, self-locking, beat frequency, and time development in a three-mode gas laser," *Phys. Rev. A*, vol. 1, pp. 1730–1746, 1970.

[27] M. Sargent III, M. O. Scully, and W. E. Lamb, Jr., *Laser Physics*, London: Addition-Wesley Publishing Company, chapter 8 and 9, 1974.

[28] K. Petermann, *Laser Diode Modulation and Noise*, Netherlands: Kluwer Academic Publishers, chapter 2, 1991.

[29] G. P. Agrawal, "Population pulsations and nondegenerate four-wave mixing in semiconductor lasers and amplifiers," *J. Opt. Soc. America B,* vol. 5, pp. 147–159, 1988.

[30] A. P. De Fonzo and B. Gomatam, "Gain nonlinearities in semiconductor lasers and amplifiers," *Appl. Phys. Lett.*, vol. 56, pp. 611-613, 1990.

[31] G. R. Gray and G. P. Agrawal, "Importance of self-induced carrier-density modulation in semiconductor lasers," *IEEE Photon. Technol. Lett.*, vol. 4, pp. 1216–1219, 1992.

Chapter 3

Multimode Analysis of Self-Locking FM Laser Operation

3.1 Introduction

The first reported observation of self-locking FM laser operation in multimode InGaAsP Fabry-Perot (FP) lasers by Tiemeijer *et al.* [1] has generated significant interest in the properties of FM oscillation in semiconductor lasers. The study of self-locking FM behaviours in semiconductor lasers is important both for the understanding of nonlinear physical mechanisms in semiconductor active medium [2, 3], and for possible device applications. Self-locking FM effects have also been observed recently in strained quantum well InGaAs FP lasers operating at 0.98 μm wavelength [4, 5]. Furthermore, Chinn and Swanson have demonstrated optical short pulse generation at repetitive frequencies of up to 233 GHz by converting the self-locked FM oscillation output of a solitary diode laser to an AM pulse train by use of optical fiber dispersion [6].

In chapter 2, it has been established, using a three-mode model, that *intrinsic multiwave mixing* occurring together with nonlinear gain may account for

self-locking FM laser operation in semiconductor lasers [7]. The requisite gain saturation and multiwave mixing nonlinearities have been shown to be consistent with experimental observations of Ref. [1]. Although a three-mode model is sufficient to demonstrate the occurrence of self-locking FM laser operation, it is necessary to extend the model to take more than three modes into account in order to calculate the modulation depth of the FM laser oscillation.

In this chapter, a multimode formalism is developed for the analysis of self-locking FM operation, incorporating five, seven and nine modes in semiconductor lasers [8]. An FM index of 1.3 has been found for the case of a five mode FM supermode. This calculated modulation index is in agreement with available experimental evidence.

3.2 Formalism

In this section, a generalization of the three-mode laser model presented in the previous chapter to include more than three oscillating modes is described. An odd number of modes, N, is considered in the analysis. The oscillating modes have frequencies ν_n where $n = 1, 2, \ldots, N$, and $\nu_{(1+N)/2}$ is the central-mode frequency which is assumed to be nearest to the gain peak. The modes are defined by field phasors of amplitudes E_n and phases ϕ_n. The amplitude- and frequency-determining equations given by Lamb [9] for a multimode laser are

$$\dot{E}_n = \alpha_n E_n - \sum_{\mu}\sum_{\rho}\sum_{\sigma} E_\mu E_\rho E_\sigma \, \mathrm{Im}\{\vartheta_{n\mu\rho\sigma} \exp(i\Psi_{n\mu\rho\sigma})\} \,, \tag{3.1}$$

$$\nu_n + \dot{\phi}_n = \Omega_n + \sigma_n - \sum_{\mu}\sum_{\rho}\sum_{\sigma} E_\mu E_\rho E_\sigma E_n^{-1} \, \mathrm{Re}\{\vartheta_{n\mu\rho\sigma} \exp(i\Psi_{n\mu\rho\sigma})\} \,, \tag{3.2}$$

where $\Psi_{n\mu\rho\sigma}$ is the relative phase angle defined as

$$\Psi_{n\mu\rho\sigma} = (\nu_n - \nu_\mu + \nu_\rho - \nu_\sigma)\, t + \phi_n - \phi_\mu + \phi_\rho - \phi_\sigma \,, \tag{3.3}$$

and $i = \sqrt{(-1)}$, Im and Re denote the imaginary and the real parts of the complex quantity in the curly braces, respectively, and α_n prescribes the linear gain of the laser. Multiwave mixing nonlinearities are described by the coefficient $\vartheta_{n\mu\rho\sigma} \exp(i\Psi_{n\mu\rho\sigma})$. σ_n is the power independent pulling coefficient arising from the dispersive nature of the medium and Ω_n is the passive-cavity resonance frequency of the n-th mode.

In deriving the Lamb equations (3.1) and (3.2), it is noted that the field E_n cannot respond to frequency variations much larger than the cavity bandwidth, so that only terms that satisfy the following equation are retained,

$$\nu_n - \nu_\mu + \nu_\rho - \nu_\sigma \simeq 0 \,, \tag{3.4}$$

or equivalently

$$n = \mu - \rho + \sigma \,. \tag{3.5}$$

In the three-mode case, it is found that there are four non-zero relative phase angles satisfying Eq. (3.5), which are Ψ_{2123}, Ψ_{2321}, Ψ_{1232} and Ψ_{3212}. Using Eq. (3.3), it is found that these relative phase angles are related to one another. If it is assumed that $\Psi_{2123} = \Psi$, then all of the other relative phase angles can be written in terms of Ψ, that is, $\Psi_{2321} = \Psi$ and $\Psi_{1232} = \Psi_{3212} = -\Psi$. Hence only one independent $\Psi_{n\mu\rho\sigma}$ can be determined in a three-mode laser. This is because one phase angle is arbitrary and another is determined by the choice of time origin [9]. In the N-mode problem, therefore, there are in fact $(N-2)$ linearly independent relative phase angles, which are taken to have the form

$$\Psi_{j+1,j,j+1,j+2} = (2\nu_{j+1} - \nu_j - \nu_{j+2})\,t + 2\phi_{j+1} - \phi_j - \phi_{j+2} \,, \tag{3.6}$$

where $j = 1, \ldots, (N-2)$.

To determine the initial conditions of the phases, consider time $t = 0$. From

Eq. (3.6),

$$2\phi_{j+1} - \phi_j - \phi_{j+2} = \Psi_{j+1,j,j+1,j+2} \cdot \tag{3.7}$$

If the time origin is chosen such that $\phi_1 = \phi_2 = \phi$, where ϕ is an arbitrary constant, then $\phi_3 = \phi - \Psi_{2123}$, and, in general,

$$\phi_m = 2\phi_{m-1} - \phi_{m-2} - \Psi_{m-1,m-2,m-1,m} \ , \quad m = 3, \ldots, N \ . \tag{3.8}$$

Hence by specifying the initial values of $(N-2)$ number of independent $\Psi_{n\mu\rho\sigma}$ and $\phi_1 = \phi_2 = \phi$, ϕ being an arbitrary constant, all the phases are defined. Furthermore, other dependent $\Psi_{n\mu\rho\sigma}$ in the amplitude- and frequency-determining equations which satisfy Eq. (3.5) are properly and completely defined at $t = 0$ by

$$\Psi_{n\mu\rho\sigma} = \phi_n - \phi_\mu + \phi_\rho - \phi_\sigma \ , \tag{3.9}$$

since all ϕ_n are defined.

In order to identify the semiconductor laser analogues of the various nonlinear terms contributing to the multimode laser interaction, the cross/self saturation coefficient θ_{nm} and the cross/self pushing coefficient τ_{nm} are introduced:

$$\theta_{nm} = \mathrm{Im}\left\{\vartheta_{nnmm} + \vartheta_{nmmn}\right\} \ , \tag{3.10}$$

$$\tau_{nm} = \mathrm{Re}\left\{\vartheta_{nnmm} + \vartheta_{nmmn}\right\} \ . \tag{3.11}$$

The amplitude- and frequency-determining equations then become

$$\dot{E}_n = \alpha_n E_n - \sum_{m=1}^{N} \theta_{nm} E_m^2 E_n + \text{ multiwave mixing terms} \ , \tag{3.12}$$

$$\nu_n + \dot{\phi}_n = \Omega_n + \sigma_n - \sum_{m=1}^{N} \tau_{nm} E_m^2 + \text{ multiwave mixing terms} \ . \tag{3.13}$$

Using the procedures as described in Sec. (2.4.2), the linear gain and the nonlinear gain saturation parameters are obtained as follows,

$\alpha_n = 2.25 \times 10^{11}$ s^{-1}, and

$\theta_{nm} = 1.51 \times 10^{-5}$ cm^{3}s^{-1}.

The values of other nonlinear parameters such as $\vartheta_{n\mu\rho\sigma}$ and τ_{nm} are assumed to have the same order of magnitude as θ_{nm}. The linear mode pulling coefficient is assumed to be $\sigma_{nm} \approx 1.0 \times 10^{12}$ s^{-1}. With all these parameter values and initial conditions for the mode amplitudes and the relative phase angles, the N-mode amplitude- and frequency-determining equations (3.1) and (3.2) can then be solved numerically to obtain the time evolutions of the mode amplitudes and the relative phase angles.

3.3 Multimode Self-Locking FM Laser Operation

An integration of the amplitude- and frequency-determining equations shows that a self-locked state may indeed occur for nonlinear gain parameter values appropriate to InGaAsP lasers operating at an emission wavelength of 1.55 μm. In the self-locked state, the mode amplitudes and the relative phase angles all settle to stable, constant (time-invariant) values, as described in the previous chapter.

3.3.1 Frequency Modulation Index

In pure FM operation, the field of the FM supermode has a constant amplitude, E_0 and is of the form

$$E(t) = E_0 \cos(\omega_0 t + \beta \cos \omega t) , \tag{3.14}$$

where β is the FM index, ω is the beat frequency between adjacent modes, and ω_0 is the frequency of the dominant mode, taken as the central mode. The relative amplitudes of the cavity modes are defined by the Bessel functions:

$$E(t) = E_0 \sum_n J_n(\beta) \cos\left\{(\omega_0 + n\omega)t - |n|\frac{\pi}{2}\right\} , \tag{3.15}$$

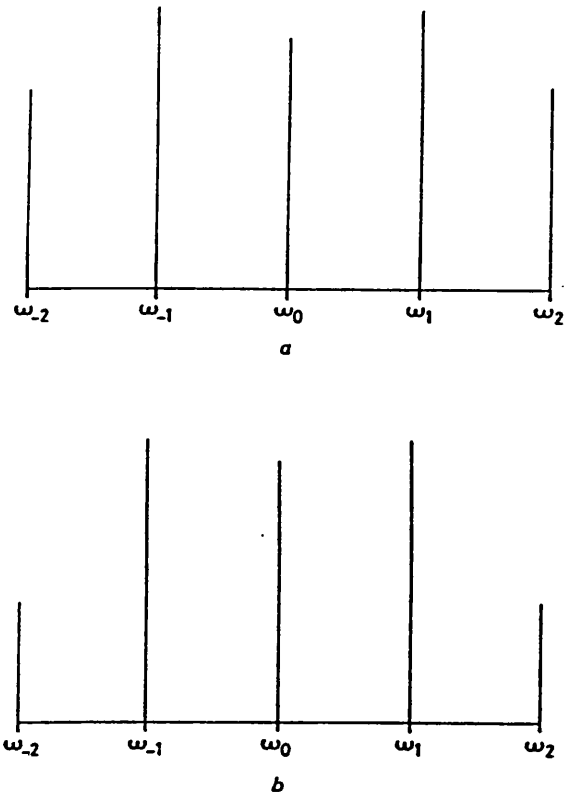

Figure 3.1: Comparison between (a) calculated longitudinal mode spectrum of five-mode self-locking oscillation and (b) ideal Bessel function sideband spectrum.

where n is an integer. The FM index, β for the self-locking FM oscillation may then be deduced from the calculated mode amplitudes by making use of the standard Bessel function identity

$$\frac{2n}{\beta}J_n(\beta) = J_{n+1}(\beta) + J_{n-1}(\beta)\,. \tag{3.16}$$

Using a five-mode model, the steady-state mode amplitudes are computed and plotted against frequency as shown in Fig. 3.1(a). This calculated amplitude spectrum is compared with the theoretical ideal FM sidebands as shown in Fig. 3.1(b). The general agreement between the calculated and the theoretical FM sideband spectra suggests that the self-locking oscillation approaches pure FM operation.

Using typical mode amplitudes of a five-mode self-locked laser oscillation computed using the present model, the FM index β is calculated using Eq. (3.16). An

FM index of ≈ 1.3 is obtained for parameter values appropriate to InGaAsP laser diodes. This calculated FM index is in good agreement with values determined experimentally [1].

3.3.2 Limitations to Pure FM Laser Operation

The time-domain representations of the self-locking FM laser oscillation with five, seven and nine frequency components are shown in Fig. 3.2. It is evident from the observation of the output intensity waveforms that a small periodic variation in the signal intensity envelope is present and pure FM operation is inhibited. This indicates an admixture of AM component in the self-locked FM supermode. The periodic nature of the intensity envelope variation is due to the locking of the longitudinal modes at the same beat frequency. The period of the signal envelope variation is given by the inverse of the intermodal frequency spacing, which is $T = 2n_r L/c \approx 5.8$ ps, where n_r is the refractive index, L is the cavity length, and c is the velocity of light in vacuum. Thus, instead of a pure FM oscillation (with the field as given by Eq. (3.14)), the field of the self-locked oscillation can be written in the form

$$E(t) = E_0 [1 + f(t)] \cos[\omega_0 t + \beta \cos(\omega t + \varphi)] , \tag{3.17}$$

where $f(t)$ denotes a time function describing the variation of the signal envelope, which is not explicitly specified in the present multimode context, and is a result of the residue amplitude modulation, and φ is the relative phase between the FM and AM components.

It is found that self-locking FM operation, caused by medium nonlinearities, is always accompanied by a small AM component for nonlinear parameters associated with semiconductor lasers. A qualitative explanation for the admixture of AM and FM components in the self-locked FM supermode is given below which

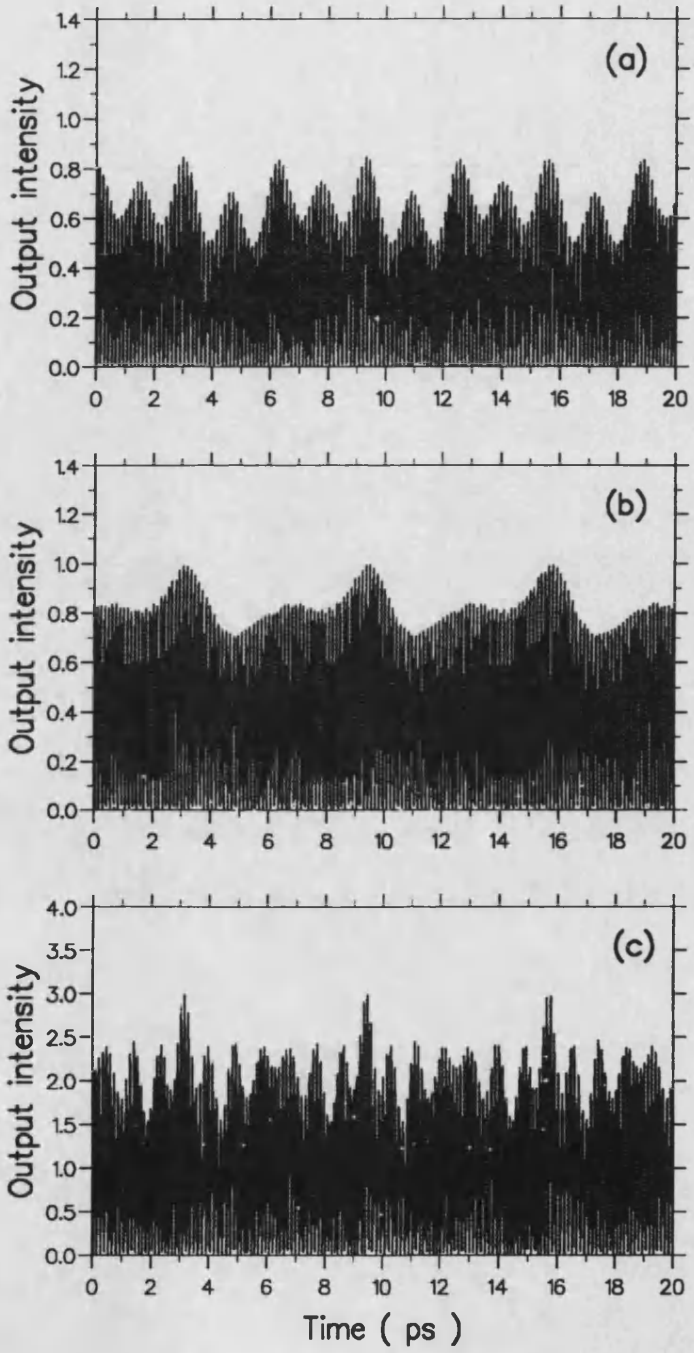

Figure 3.2: Output intensity waveforms of self-locking FM laser operation with (a) five (P_{out} = 7.5 mW, β = 1.27), (b) seven (P_{out} = 9.3 mW, β = 0.80), and (c) nine (P_{out} = 18.3 mW, β = 1.76) longitudinal mode components. Output intensity is in units of $\times 10^{11}$ Wm^{-2}.

involves a consideration of the contributions of various nonlinearities.

There is still a considerable debate on the origin of gain nonlinearities in semiconductor lasers. Physical mechanisms that are believed to play a significant role in effecting gain nonlinearities include spectral hole burning, carrier heating, spatial hole burning, and carrier density modulation. It has been established in the previous chapter that FM self-locking is critically sensitive to multiwave mixing nonlinearities. The term $\Psi_{n\mu\rho\sigma}$ represents the phase dependent coupling between modes and arises because of the *beating of beat frequencies* between lasing modes. The beat-frequency coupling generates frequency components, which in semiclassical laser theory are often referred to as *combination tones* [9], through intrinsic multiwave mixing processes. The physical mechanism which gives rise to intrinsic multiwave mixing is the modulation of the carrier population of the active medium at the beat frequency between the oscillating modes. This carrier density modulation (called *population pulsations*) translates to a modulation of the refractive index because of the free-carrier contribution to the refractive index. The modulation of the refractive index in turn causes the *optical length* of the laser cavity to be modulated, thereby modulating the eigenfrequency of the Fabry-Perot resonator. Thus self-locking FM operation is effected. On the other hand, owing to the carrier dependence of medium gain, the carrier modulation also leads to gain/loss modulation of the active medium. This gain/loss modulation results in the mode amplitude variation and thus produces an AM component in the self-locked FM supermode.

3.4 Effects of Medium Nonlinearities on FM Index

In this section, the dependence of FM index on medium nonlinearities is investigated using a five-mode laser model. Comparison of the calculated output power with experimentally determined output power of semiconductor lasers under which self-locking FM operation was observed provides a quantitative test of the magnitudes of the various nonlinear parameters.

3.4.1 Self and Cross Saturation Nonlinear Effects

The presence of self/cross gain saturation in multimode semiconductor laser operation causes the mode amplitudes to be suppressed. Figs. 3.3 and 3.4 illustrate the effects of self and cross saturation nonlinearities on FM index and output optical power, respectively. Both the FM index and the output power decrease as the self/cross saturation coefficient is increased. In particular, for $\theta_{nm} < 1.5 \times 10^{-5}$ cm^3s^{-1}, self-locking FM operation requires output powers in excess of 30 mW. However, self-locking FM oscillation was observed in laser diodes for output powers below 20 mW [1]. It can thus be deduced that, under normal operating circumstances, the gain saturation parameter of InGaAsP lasers is likely to be greater than $\approx 1.5 \times 10^{-5}$ cm^3s^{-1} for a five-mode laser operation.

It is also observed from Fig. 3.4 that the FM index drops off sharply and FM-locking ceases to occur for cross saturation parameter $\theta_{nm} > 4.0 \times 10^{-5}$ cm^3s^{-1}. Comparing Figs. 3.3 and 3.4, it is noted that self-locking is more sensitive to the cross saturation parameter than the self saturation gain parameter. For values of θ_{nm} in the range of 1.5×10^{-5} to 4.0×10^{-5} cm^3s^{-1}, the FM index of the self-locking FM oscillation is found to be $\approx$ 1.2–1.32 for a five-mode laser operation.

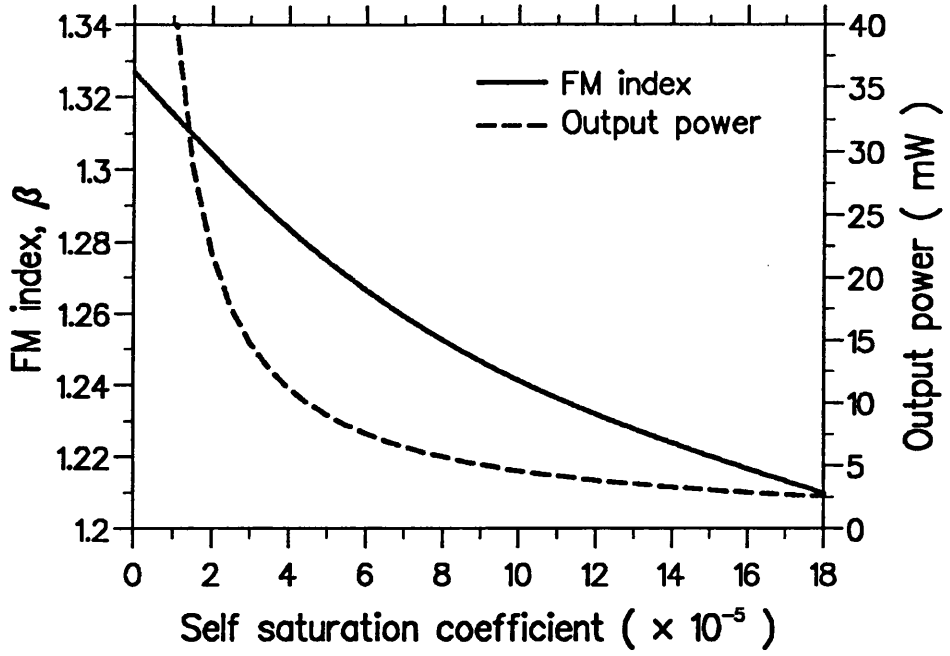

Figure 3.3: Effects of self saturation nonlinearities on FM index and output power for a five-mode self-locking FM laser diode. The nonlinear gain coefficient is in units of cm^3s^{-1} throughout the analysis.

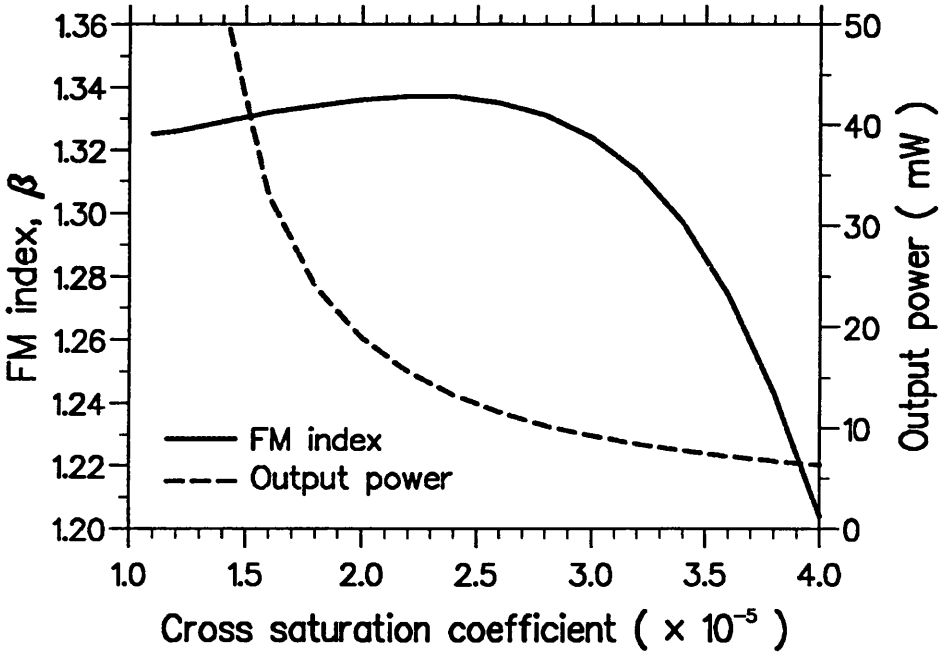

Figure 3.4: Effects of cross saturation nonlinearities on FM index and output power for a five-mode self-locking FM laser diode.

This estimate of the FM index compares favourably with experimentally determined values [1], in which $\beta = 1.9$–3.9 have been obtained. The slightly smaller calculated value of β compared to experiment may be due to the the limited number of modes considered (where $N = 5$ in this case). When seven and nine modes are taken into account in the analysis, the output power increases for a fixed value of linear gain compared to the five-mode case, and higher values of β are obtained.

Tiemeijer *et al.* showed that the spectral width of the longitudinal-mode emission spectrum is proportional to the FM index of the self-locked laser diode. Fig. 3.5 shows the recorded spectral width as a function of single-facet output power of a laser diode (from Ref. [1]). At low output power, the reduction of the spectral width towards near single-mode operation of the laser diode is consistent with the "classical" linear gain model. However, the subsequent increase of the spectral width at higher output power levels cannot be explained using the linear gain model. Tiemeijer proposed that the increase of the spectral width is a result of self-locking FM oscillation with increasing FM index. To compare with this experimental observation, the FM index versus output power (per-facet) characteristics for the five-mode self-locked laser diode calculated using the present formalism is shown in Fig. 3.6. The increase in output power is a result of decreasing the value of the self saturation coefficient (from Fig. 3.3). Comparing Figs. 3.5 and 3.6, it is found that the experimentally observed rebroadening of the spectrum at high output power is very well explained by the model of self-locking FM laser operation as described in this thesis. In particular, the observed saturation of the spectral width at higher power levels is consistent with the present calculated results. In addition, the threshold output power for self-locking FM operation to occur can be inferred from the experimental and the calculated curves. Self-locking threshold output power of (4 ± 1) mW is obtained from both

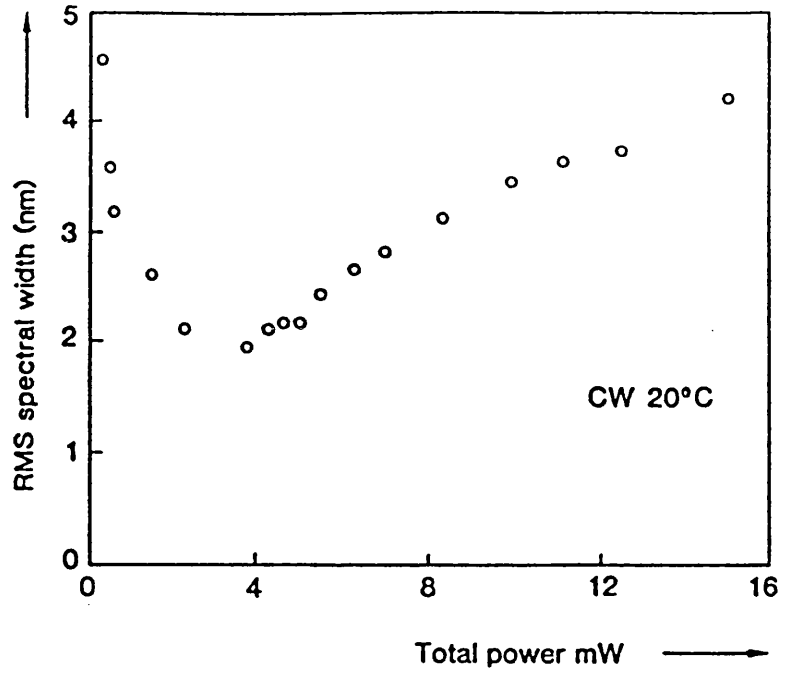

Figure 3.5: Experimental plot of spectral width versus single-facet output power of a semiconductor laser.

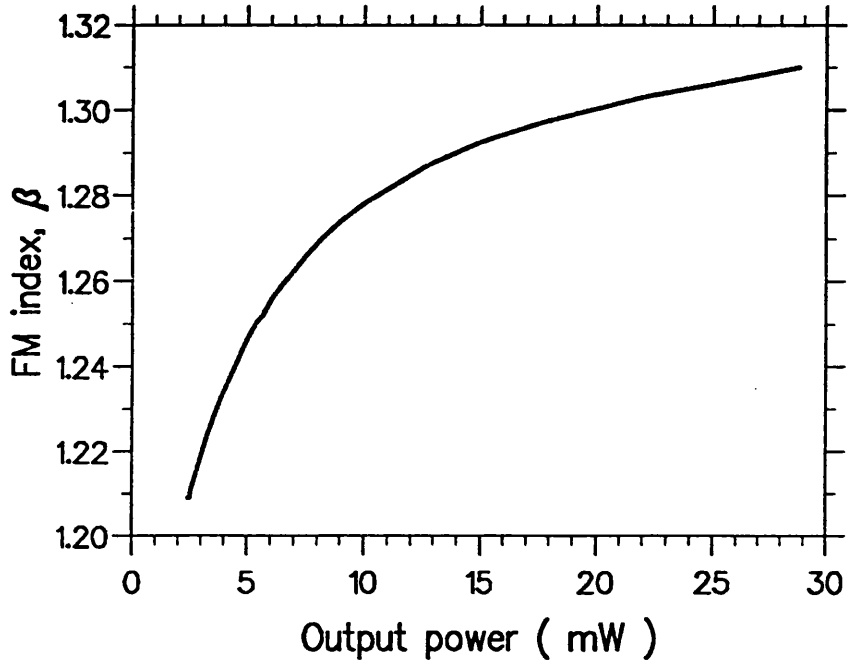

Figure 3.6: Calculated FM index versus single-facet output power of a semiconductor laser.

the experimental and the calculated results.

3.4.2 Multiwave Mixing Nonlinear Effects

The general saturation term $\vartheta_{n\mu\rho\sigma}$ is a complex quantity arising from the polarization of the active medium due to the interaction of the medium with an electromagnetic field. The complex polarization $\mathcal{P}$ can be related to the electric field component E by a complex susceptibility χ, that is

$$\begin{aligned} \mathcal{P} &= \epsilon_0 \chi E \\ &= \epsilon_0 (\chi' + i\chi'') E \,, \end{aligned} \tag{3.18}$$

where ϵ_0 is the permittivity of free space. $\mathrm{Re}\{\vartheta_{n\mu\rho\sigma}\}$ is proportional to χ' which is associated with the refractive index of the medium, whereas $\mathrm{Im}\{\vartheta_{n\mu\rho\sigma}\}$ is directly related to χ'' which gives the medium gain of semiconductor lasers [10]. The term $\vartheta_{n\mu\rho\sigma} \exp(i\Psi_{n\mu\rho\sigma})$ describes the multiwave mixing nonlinear effects on the mode-interaction and affects both the refractive index and the gain of the active medium.

The variations of FM index with the real and the imaginary parts of $\vartheta_{n\mu\rho\sigma}$ are depicted in Figs. 3.7 and 3.8, respectively. It is noted that the FM index increases as $|\mathrm{Re}\{\vartheta_{n\mu\rho\sigma}\}|$ is increased and saturates at the value of 1.332. The output power does not seem to have a significant correlation with $\mathrm{Re}\{\vartheta_{n\mu\rho\sigma}\}$ since $\mathrm{Re}\{\vartheta_{n\mu\rho\sigma}\}$ is related to the refractive index of the active medium.

On the other hand, both the FM index and the output power increase with increasing $\mathrm{Im}\{\vartheta_{n\mu\rho\sigma}\}$. This is due to the fact that higher values of $\mathrm{Im}\{\vartheta_{n\mu\rho\sigma}\}$ mean higher medium gain. Consideration of the experimentally determined output power for which self-locking FM operation occurs, suggests that the value of $\mathrm{Im}\{\vartheta_{n\mu\rho\sigma}\}$ is likely to be smaller than 1.5×10^{-5} $\mathrm{cm^3 s^{-1}}$. However there is

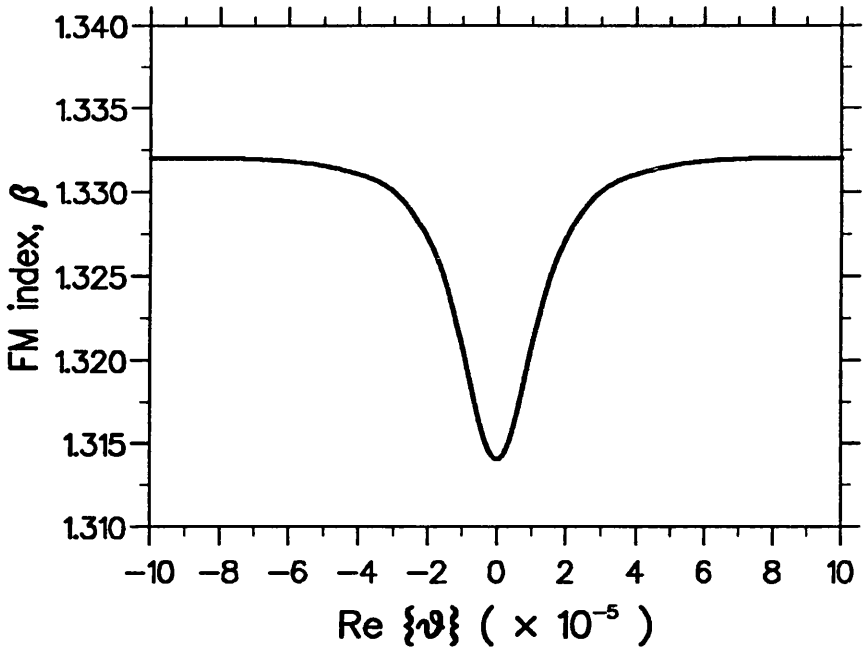

Figure 3.7: Dependence of FM index on the real part of the general saturation coefficient.

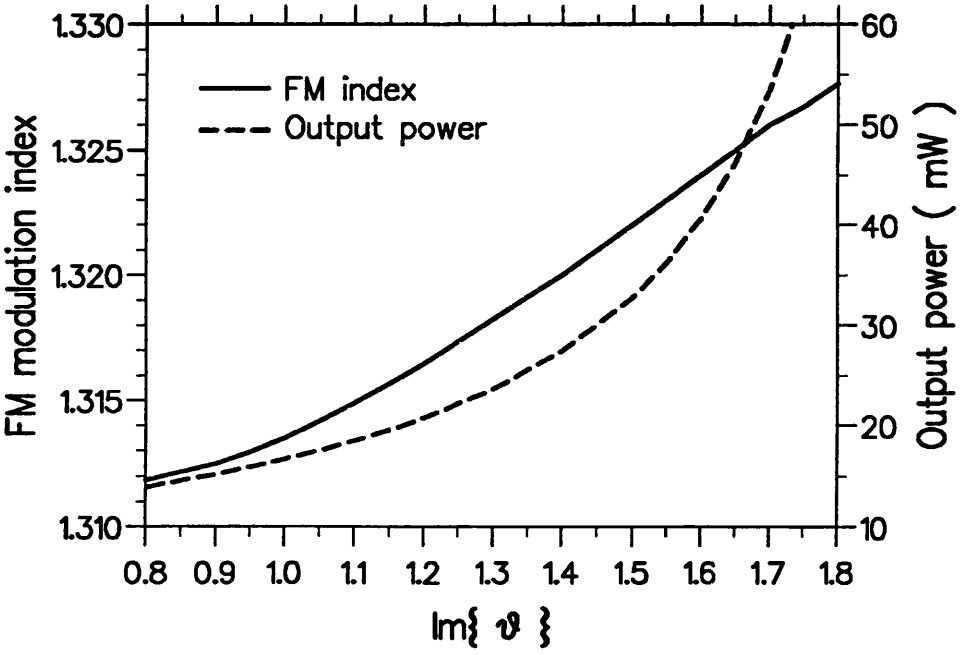

Figure 3.8: Dependence of FM index on the imaginary part of the general saturation coefficient.

a threshold value of $\mathrm{Im}\{\vartheta_{n\mu\rho\sigma}\}$, and therefore a minimum output power, below which the self-locking oscillation ceases to occur.

In summary, the semiconductor laser analogues of the various terms contributing to the nonlinear dynamics of multimode laser operation have been identified by suitably adapting the Lamb amplitude-determining equation, and comparing it with the well-known semiconductor coupled-mode photon rate equation. By integrating the multimode amplitude- and frequency-determining equations, it is shown that the mode amplitudes and, more significantly, the relative phase angles evolve to stable and constant (time invariant) values, thereby indicating self-locking operation. It has thus been established that self-locking FM laser operation may indeed be attributed to intrinsic multiwave mixing nonlinearities occurring in the presence of gain saturation, using nonlinear parameter values appropriate to InGaAsP laser diodes.

It has been shown, in particular, that the FM index increases with optical output power, which in turn is determined by the various nonlinear parameters. Self and cross saturation nonlinearities cause gain suppression and hence reduce the output power and the FM index. On the other hand, $\mathrm{Im}\{\vartheta_{n\mu\rho\sigma}\}$ is proportional to the medium gain, and therefore increasing $\mathrm{Im}\{\vartheta_{n\mu\rho\sigma}\}$ enhances the optical output power and the FM index. For a five mode laser, FM index in the range of 1.15 to 1.32 at output powers of less than 20 mW is obtained for nonlinear parameters appropriate to semiconductor lasers. These values are in good agreement with experimental evidence. When seven and nine modes are taken into account in the analysis, the output power increases for a fixed linear gain value compared to the five mode case, and the FM index increases correspondingly with the optical output power.

A general dynamical theory of semiconductor lasers would require a self-

consistent treatment of the coupled multimode rate equations not only for the field amplitudes and the relative phase angles, but also for the total carrier density. However, it has been shown that significant insight can be gained into the nature of self-locking FM operation in semiconductor lasers by using the simpler formalism presented here. More elaborate theoretical treatments utilizing the "density matrix" formalism [11]–[13] may be required in order to account in detail for the different contributions of the gain saturation nonlinearities, such as spectral hole burning, carrier heating and self-induced carrier modulation [14]–[16], in the self-locking FM process.

3.5 Conclusion

In this chapter, a multimode analysis of self-locking FM operation of laser diodes has been reported. Calculation of the FM index using this multimode semiconductor laser model gives $\beta \approx 1.3$, which is in good agreement with experimental values. A small AM component that gives rise to slight amplitude envelope variations is shown to be present in the FM supermode and inhibits pure FM operation. The contributions of various nonlinearities on the self-locking FM operation characteristics have also been established.

The present chapter has concentrated on the effects of intrinsic multiwave mixing and nonlinear gain saturation on the spectral properties of semiconductor lasers. Wave mixing may also be effected by externally injecting an optical signal into a semiconductor laser operating in a single-longitudinal mode. If the frequency difference between the injected field and the lasing field is sufficiently large so that injection locking does not occur, additional spectral components may be generated through wave mixing process (generally known as *four-wave mixing* in this case). This latter aspect of the spectral properties of semiconductor

lasers is studied in the next chapter.

References

[1] L. F. Tiemeijer, P. I. Kuindersma, P. J. A. Thijs, and L. J. Rikken, "Passive FM locking in InGaAsP semiconductor lasers," *IEEE J. Quantum Electron.*, vol. 25, pp. 1385–1391, 1989.

[2] L. F. Tiemeijer, "Effects of nonlinear gain on four-wave mixing and asymmetric gain saturation in a semiconductor laser amplifier," *Appl. Phys. Lett.*, vol. 59, pp. 499-501, 1991.

[3] S. R. Chinn, "Measurement of nonlinear gain suppression and four-wave mixing in quantum well lasers," *Appl. Phys. Lett.*, vol. 59, pp. 1673–1675, 1991.

[4] S. R. Chinn, C. A. Wang, and G. A. Evans, "Frequency modulation locking in 980 nm strained quantum well lasers," *Electron. Lett.*, vol. 29, pp. 646–648, 1993.

[5] W. F. Sharfin, J. Schlafer, and E. S. Koteles, "Observation of mode beating and self-frequency locking in a nearly single-mode semiconductor laser," *IEEE J. Quantum Electron.*, vol. 30, pp. 1709–1712, 1994.

[6] S. R. Chinn and E. A. Swanson, "Passive FM locking and pulse generation from 980-nm strained-quantum-well Fabry-Perot lasers," *IEEE Photon. Technol. Lett.*, vol. 5, pp. 969–971, 1993.

[7] K. A. Shore and W. M. Yee, "Theory of self-locking FM operation in semiconductor lasers," *IEE Proc. Part J*, vol. 138, pp. 91–96, 1991.

[8] W. M. Yee and K. A. Shore, "Multimode analysis of self-locked FM operation in laser diodes," *IEE Proc. Part J*, vol. 140, pp. 21–25, 1993.

[9] M. Sargent III, M. O. Scully, and W. E. Lamb, Jr., *Laser Physics*, London: Addition-Wesley, chapter 8 and 9, 1974.

[10] G. P. Agrawal and N. K. Dutta, *Long-Wavelength Semiconductor Lasers*, New York: Van Nostrand Reinhold, 1986.

[11] M. Asada and Y. Suematsu, "Density-matrix theory of semiconductor lasers with relaxation broadening model – gain and gain-suppression in semiconductor lasers," *IEEE J. Quantum Electron.*, vol. QE-21, pp. 434–441, 1985.

[12] G. P. Agrawal, "Gain nonlinearities in semiconductor lasers: theory and application to distributed feedback lasers," *IEEE J. Quantum Electron.*, vol. QE-23, pp. 860–868, 1987.

[13] W. W. Chow, S. W. Koch, and M. Sargent III, *Semiconductor-Laser Physics*, Berlin: Springer-Verlag, 1994.

[14] G. R. Gray and G. P. Agrawal, "Importance of self-induced carrier-density modulation in semiconductor lasers," *IEEE Photon. Technol. Lett.*, vol. 4, pp. 1216–1219, 1992.

[15] R. Frankenberger and R. Schimpe, "Origin of nonlinear gain saturation in index-guided InGaAsP laser diodes," *Appl. Phys. Lett.*, vol. 60, pp. 2720–2722, 1992.

[16] A. Uskov, J. Mork, and J. Mark, "Wave mixing in semiconductor laser amplifiers due to carrier heating and spectral hole burning," *IEEE J. Quantum Electron.*, vol. 30, pp. 1769–1781, 1994.

Chapter 4

Nearly Degenerate Four-Wave Mixing in Laser Diodes

4.1 Introduction

The phenomenon of four-wave mixing (FWM) in semiconductor lasers [1, 2] and optical laser amplifiers [3, 4] has been extensively studied recently not only with a view to gaining a better understanding of nonlinear processes in semiconductor devices but also because of its many potential applications. Wave mixing represents one of the fundamental nonlinear optical processes and has an important effect on the dynamical and spectral behaviour of laser diodes. In chapter two and three, intrinsic multiwave mixing occurring in the presence of nonlinear gain has been shown to give rise to self-locking FM oscillation in laser diodes [5, 6]. On the other hand, FWM by external optical signal injection constitutes a powerful tool for high-resolution spectroscopy [7] and has been extensively used to extract basic information on gain saturation [8]–[12] and to characterize many fundamental parameters of semiconductor lasers [13, 14].

In nonlinear optics, optical phase conjugation by FWM has found applications in real-time holography and in adaptive optics [15, 16], as well as being proposed

for utilization in frequency-dispersion compensators in dispersive optical fibre transmission systems [17]. Recently, all-optical frequency conversion via FWM in laser diodes and laser amplifiers was proposed and demonstrated [18]–[20] for use in optical coherent multicarrier communication systems. Studies in FWM also help in the understanding of the generation of undesirable cross-talk and intermodulation distortion between amplified channels in semiconductor laser amplifiers [21, 22].

In a seminal paper [23], Agrawal presented a theory of nondegenerate FWM in semiconductor lasers and amplifiers with particular emphasis on the physical processes that lead to population pulsations (modulation of the carrier density). It was shown that two mechanisms with different characteristic time constants may contribute to the FWM process. The first mechanism is the dynamic modulation of the carrier density at the beat frequency of the intracavity propagating pump and probe waves, which creates gain and refractive-index gratings. Diffraction of the counterpropagating pump waves from these dynamic gratings generates a phase conjugate wave. The effectiveness of the gratings is governed by the spontaneous carrier lifetime (about 1 ns). Since the carrier density cannot be modulated at frequencies much higher than the inverse of the spontaneous lifetime, this mechanism is effective only for frequency detunings of up to a few GHz, and gives rise to the so-called *nearly degenerate four-wave mixing* (ND-FWM). The second mechanism is nonlinear gain arising from the modulation of the occupation probability of carriers within an energy band. This mechanism, which effects the *highly nondegenerate* FWM, is effective for frequency detunings of over 100 GHz because of its short characteristic time (about 0.1–1 ps). This ultrafast mechanism is governed by intraband relaxation processes. There is still a considerable debate on the origin of the nonlinear gain which gives rise to highly nondegenerate FWM. It has been suggested that spectral hole burning [24], car-

rier heating [7, 12] or spatial hole burning [25] may contribute to this nonlinear gain.

Semiconductor lasers biased above threshold are of particular interest for use in optical phase conjugation via NDFWM. In this scheme, an external optical probe wave is incident into a laser diode and the oscillating laser field acts as the pump wave. Very high conjugate amplifications of the order of 30–40 dB can be achieved because of the cavity feedback enhancement of the mixing process and the amplifying effect of the semiconductor gain medium [26]. In addition, the NDFWM bandwidth in a laser diode is determined mainly by the laser's relaxation oscillation frequency [27] and is not entirely limited by the inverse of the effective carrier lifetime. Highly efficient NDFWM with bandwidth of up to 30 GHz can be achieved by biasing the laser diode well above threshold. On the contrary, both external pump and probe sources with high optical powers are required for NDFWM in semiconductor laser amplifiers (SLA) [3, 4]. In this latter scheme, a conjugate amplification of up to 8.3 dB and a maximum NDFWM bandwidth of 12 GHz have been reported [4].

Several theoretical treatments of NDFWM in Fabry-Perot (FP) laser diodes biased above threshold have emphasized the temporal field–matter interactions in the FWM process [28]–[30]. Although the FWM theory presented by Agrawal [23] is based on a travelling-wave formulation, most of the attention is devoted to the discussion of FWM in semiconductor laser amplifiers, and FP cavity effects were not included. Recently, Mecozzi *et al.* [27] presented a detail theoretical analysis of NDFWM in a distributed feedback (DFB) laser using the travelling-wave formulation. By using the mean field approximation, they derived analytical expressions for the probe and the conjugate wave outputs, and demonstrated good agreement between theory and experimental results.

Although the time-domain rate-equation approach is adequate for the analysis of NDFWM in FP laser diodes with symmetric and high facet reflectivities, the coupled-mode travelling-wave formulation in the spatial domain has to be used in the description of NDFWM in laser diodes with low and/or unequal (asymmetric) facet reflectivities and in laser diodes with longitudinal structural variations. In these latter cases, the longitudinal carrier and photon density distributions, and hence the gain, are significantly nonuniform. As a result, the mean field approximation is no longer valid. Another important feature of the spatially dependent coupled-mode analysis of FWM is that it allows the comparison of optical probe injection into either facet of a asymmetric FP laser diode, whereas in a model which assumed uniform gain (or mean field approximation), this would not be possible.

In this chapter, a model for cavity-enhanced NDFWM in above-threshold FP laser diodes with low and/or asymmetric facet reflectivities is described [31]. The model represents a generalisation of the work of Agrawal [23] so as to incorporate

(i) Fabry-Perot cavity effects and notably the generation of both a phase conjugate reflectivity and a phase conjugate transmittivity, and

(ii) longitudinal variations of both the nonlinear interaction and the gain distribution.

In this way it has been possible to obtain a model of wide applicability and which is, in particular, capable of describing FWM properties in laser diodes with nonuniform longitudinal field and gain distribution.

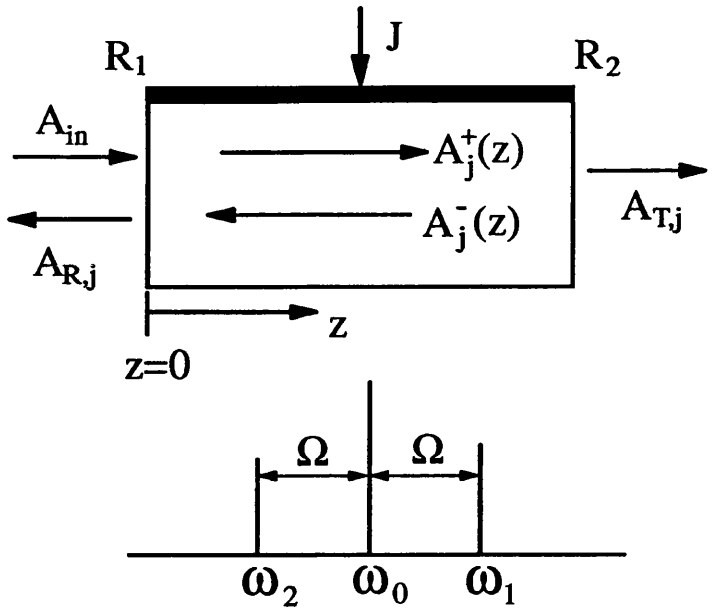

Figure 4.1: Conceptual model of NDFWM in a laser diode. $A_j^{\pm}(z)$ are the normalized slowly varying $+z$ and $-z$ propagating fields, where $j = 0, 1, 2$ correspond to the pump, the probe and the conjugate waves, respectively. A_{in} is the external probe injection at frequency ω_1, and $A_{R,j}$ and $A_{T,j}$ are the reflected and the transmitted output fields, respectively, at the corresponding frequency.

4.2 Travelling-Wave Analysis of Nearly Degenerate FWM

In this section, a theoretical model of cavity-enhanced NDFWM in above-threshold laser diodes is presented. The model is based on a theory proposed by Agrawal [23], generalized to take into account resonant-cavity effects and longitudinal variations of the nonlinear interaction and the internal gain distribution. Fig. 4.1 shows the conceptual model of FWM in a laser diode biased above threshold. The laser is assumed to oscillate in a single transverse- and longitudinal-mode providing the pump wave at frequency ω_0. A collinear probe wave at frequency ω_1 is injected into the pumped laser through the front facet with power reflectivity R_1 at $z = 0$, where z is the distance along the longitudinal direction of the laser. The nonlinear coupling of the intracavity waves modulates the carrier density at

the beat frequency $\Omega = \omega_1 - \omega_0$, and generates a conjugate wave at frequency $\omega_2 = \omega_0 - \Omega$ through NDFWM.

The nonlinear interaction of the intracavity field E in the semiconductor laser, assuming that the laser structure supports only the fundamental waveguide TE mode, is described in the scalar approximation by the wave equation

$$\nabla^2 E - \frac{n^2}{c^2}\frac{\partial^2 E}{\partial t^2} = \frac{1}{\epsilon_0 c^2}\frac{\partial^2 P}{\partial t^2} , \tag{4.1}$$

where n is the refractive index, c is the velocity of light in vacuum, ϵ_0 is the vacuum permittivity and P is the induced polarization given explicitly in Eq. (4.13). The field is normalized to include the factor $\sqrt{n\epsilon_0 c}$, so that the optical intensity I (in units of Watts per square meter) is given by $I = |E|^2$. The total intracavity field and the induced polarization can be written as the sum of the Fourier components:

$$E(x,y,z,t) = U(x,y) \sum_j E_j(z) \exp(-i\omega_j t) , \tag{4.2}$$

$$P(x,y,z,t) = U(x,y) \sum_j P_j(z) \exp(-i\omega_j t) , \tag{4.3}$$

where $U(x,y)$ is the transverse distribution of the fundamental waveguide TE mode and $j = 0,1,2$ correspond to the pump, the probe and the conjugate waves, respectively. The frequencies of the various waves obey the relationship

$$\omega_1 - \omega_0 = \omega_0 - \omega_2 = \Omega , \tag{4.4}$$

where Ω is the angular frequency detuning (or beat frequency) between the pump and the probe waves.

Eqs. (4.2) and (4.3) are substituted into Eq. (4.1), and, following multiplication by $U^*(x,y)$ (where * represents complex conjugate), an integration over the transverse dimensions x and y is performed to obtain the one-dimensional wave equation

$$\frac{d^2 E_j}{dz^2} + k_j^2 E_j = -\frac{\Gamma \omega_j^2}{\epsilon_0 c^2} P_j , \tag{4.5}$$

where $k_j = n_g\omega_j/c = \omega_j/v_g$ are the wavenumbers, n_g is the group refractive index, v_g is the group velocity and Γ is the confinement factor given by

$$\Gamma = \frac{\int_0^w \int_0^d |U(x,y)|^2\, dx\, dy}{\int\int_\infty^\infty |U(x,y)|^2\, dx\, dy}\,, \tag{4.6}$$

which represents the fraction of the mode energy confined within the active region of width w and thickness d.

The carrier density N at an injection current density J can be obtained by solving the carrier rate equation

$$\frac{\partial N}{\partial t} = \frac{J}{ed} - \frac{N}{\tau_s} - \frac{g(N)}{\hbar\omega_0}|E|^2 + D\,\nabla^2 N\,, \tag{4.7}$$

where e is the electronic charge, τ_s is the spontaneous carrier lifetime, $\hbar$ is the Planck's constant divided by 2π, $g(N)$ is the carrier-dependent gain, and D is the diffusion coefficient.

Because the pump–probe frequency detuning (a few GHz) in the nearly degenerate FWM case is much smaller than the gain spectrum bandwidth, it is assumed for simplicity that all waves experience the same gain which is given by

$$g(N) = a\,(N - N_0)(1 - \epsilon\,|E|^2)\,, \tag{4.8}$$

where a is the differential gain, N_0 is the carrier density at transparency, and ϵ is the nonlinear gain coefficient (in units of m^2/W). ϵ is related to the more conventional notation ϵ_{NL} (in units of m^3) by $\epsilon = \epsilon_{NL}/(\hbar\omega_0 v_g)$. The actual dependence of the gain on the field intensity is still a matter of debate [32]. Here a linearized expression which is valid for the case $\epsilon|E|^2 << 1$ is used. Theoretical analysis of NDFWM using Eq. (4.8) has been shown to agree well with experiments [13, 27].

The effect of nonlinear gain saturation has been reported [27] to damp the resonant enhancement of the FWM efficiency near the relaxation oscillation fre-

quency of the pumped laser. The cavity standing waves generated by counter-propagating wave coupling give rise to additional damping of the resonance peak of the FWM response through the mechanism of spatial hole burning. However, experimental results showed that the effect on FWM spectra of spatial hole burning is negligibly small compared to that arising from nonlinear gain saturation [27]. Consequently, longitudinal cavity standing wave effects are neglected in the present analysis. Furthermore, carrier diffusion tends to average the carrier density over the transverse dimensions because the transverse waveguide dimensions are smaller than the diffusion length ($\sqrt{D\tau_s} \approx 2 - 3\,\mu$m). Thus, to a good degree of approximation, the diffusion term in Eq. (4.7) can be neglected, ie. $\nabla^2 N \rightarrow 0$.

To solve the carrier density rate equation, E and $g(N)$ from Eqs. (4.2) and (4.8) are substituted into Eq. (4.7), and an approximate solution of the form

$$N(z,t) = N_s(z) + [\Delta N(z) \exp(-i\Omega t) + \Delta N^*(z) \exp(i\Omega t)] \tag{4.9}$$

is assumed, where N_s is the static carrier density and ΔN is the carrier density deviation (population pulsation). The analysis is carried out for the case where the optical probe injection is very small so that the effect of probe-induced carrier depletion is negligible. The probe and the conjugate waves then act only as small perturbations of the free-running intracavity pump wave. This assumption is consistent with reported experimental investigation of NDFWM in laser diodes in which a very small probe injection power of approximately 0.02 μW was used [27, 28]. The solution of Eq. (4.7) then yields

$$N_s = \frac{(J\tau_s/ed) + N_0\,|E_0|^2/P_s}{1 + |E_0|^2/P_s}\,, \tag{4.10}$$

$$\Delta N = \frac{-C(N_s - N_0)(E_0^* E_1 + E_0 E_2^*)/P_s}{1 + |E_0|^2/P_s - i\,\Omega\tau_s}\,, \tag{4.11}$$

where

$$P_s = \hbar\omega_0/(\,\Gamma a \tau_s\,) \tag{4.12}$$

is the saturation intensity. The overlap factor C is phenomenologically introduced to account for the non-plane-wave nature of the waveguide mode in semiconductor lasers [23] and $C = 1$ is assumed.

The field–carrier interaction is governed by the relation

$$P = \epsilon_0 \chi E \,, \tag{4.13}$$

where the susceptibility is defined as

$$\chi(N) = \frac{-nc}{\omega_0} (\beta + i)\, g(N) \,, \tag{4.14}$$

and β is the linewidth enhancement factor which accounts for the carrier induced index change in semiconductor lasers [33]. The induced polarization components P_j are calculated by substituting Eqs. (4.2), (4.8), (4.10) and (4.11) into Eq. (4.13) to obtain

$$P_0(z) = \epsilon_0 \, A \, g(N_s) \, E_0 \,, \tag{4.15}$$

$$P_1(z) = \epsilon_0 \, A \, g(N_s) \, [E_1 - \Delta n_\Omega \, E_0 - \delta_{NL} \, E_0] \,, \tag{4.16}$$

$$P_2(z) = \epsilon_0 \, A \, g(N_s) \, [E_2 - \Delta n_\Omega^* \, E_0 - \delta_{NL}^* \, E_0] \,, \tag{4.17}$$

where

$$A = -(nc/\omega_0)\,(\beta + i) \,, \tag{4.18}$$

$$\Delta n_\Omega = \frac{-\Delta N_\Omega}{(N_s - N_0)} = \frac{(E_0^* E_1 + E_0 E_2^*)/P_s}{(1 + |E_0|^2/P_s - i\Omega\tau_s)} \,, \tag{4.19}$$

$$\delta_{NL} = \frac{\epsilon \, (E_0^* E_1 + E_0 E_2^*)}{1 - \epsilon \, |E_0|^2} \,, \tag{4.20}$$

and

$$\begin{aligned} g(N_s) &= a(N_s - N_0)(1 - \epsilon \, |E_0|^2) \\ &= \frac{(a\tau_s/ed)J - aN_0}{1 + |E_0|^2/P_s} (1 - \epsilon \, |E_0|^2) \,. \end{aligned} \tag{4.21}$$

The term δ_{NL} has been included to account for the nonlinear gain saturation effects.

4.2.1 Fabry-Perot Cavity Effects

To incorporate the effect of resonant cavity into the analysis, it is necessary to treat both the forward ($+z$) and the reverse ($-z$) propagating waves. In this case, therefore, the z-dependence of the fields is assumed to be

$$E_j(z) = \sqrt{P_s}\left[A_j^+(z)\exp(ik_0z) + A_j^-(z)\exp(-ik_0z)\right] , \tag{4.22}$$

where $A_j^+(z)$ and $A_j^-(z)$ are the normalized complex envelope functions of the forward and the reverse propagating waves respectively. Similarly, the induced polarization at the corresponding frequency is expressed as the sum of the forward and the reverse propagating components,

$$P_j(z) = P_j^+(z)\exp(ik_0z) + P_j^-(z)\exp(-ik_0z) . \tag{4.23}$$

Substituting Eqs. (4.22) and (4.23) into Eq. (4.5), and applying the slowly varying envelope and the rotating wave approximations, the following equations are obtained:

$$\frac{dA_0^\pm}{dz} \pm \frac{\alpha_{int}}{2}A_0^\pm = \pm\frac{i\omega_0\Gamma}{2nc\epsilon_0\sqrt{P_s}}P_0^\pm , \tag{4.24}$$

$$\frac{dA_1^\pm}{dz} \mp \frac{in_g\Omega}{c}A_1^\pm \pm \frac{\alpha_{int}}{2}A_1^\pm = \pm\frac{i\omega_1\Gamma}{2nc\epsilon_0\sqrt{P_s}}P_1^\pm , \tag{4.25}$$

$$\frac{dA_2^\pm}{dz} \pm \frac{in_g\Omega}{c}A_2^\pm \pm \frac{\alpha_{int}}{2}A_2^\pm = \pm\frac{i\omega_2\Gamma}{2nc\epsilon_0\sqrt{P_s}}P_2^\pm , \tag{4.26}$$

where α_{int} is the internal loss coefficient introduced to take into account all losses (diffusion, free-carrier absorption, scattering, etc.) other than mirror loss.

Substituting the induced polarization components from Eqs. (4.15)–(4.17) as the source terms into Eqs. (4.24)–(4.26) gives the coupled-wave equations which describe the evolution of three sets of copropagating and counterpropagating fields along the z direction:

$$\frac{dA_0^\pm}{dz} = \pm\alpha_0 A_0^\pm \mp \frac{\alpha_{int}}{2}A_0^\pm , \tag{4.27}$$

$$\frac{dA_1^{\pm}}{dz} = \pm\alpha_0 \left[A_1^{\pm} - (X+Y)QA_0^{\pm}\right] \mp \frac{\alpha_{int}}{2}A_1^{\pm} \pm \frac{i\Omega}{v_g}A_1^{\pm} , \tag{4.28}$$

$$\frac{dA_2^{\pm}}{dz} = \pm\alpha_0 \left[A_2^{\pm} - (X^*+Y)Q^*A_0^{\pm}\right] \mp \frac{\alpha_{int}}{2}A_2^{\pm} \mp \frac{i\Omega}{v_g}A_2^{\pm} , \tag{4.29}$$

where

$$\alpha_0(z) = \frac{1}{2}\frac{g_0}{1+P_T}(1-\epsilon P_s P_T)(1-i\beta) , \tag{4.30}$$

$$P_T(z) = |A_0^+(z)|^2 + |A_0^-(z)|^2 , \tag{4.31}$$

$$Q(z) = A_0^+(A_2^+)^* + A_0^-(A_2^-)^* + (A_0^+)^*A_1^+ + (A_0^-)^*A_1^- , \tag{4.32}$$

$$X(z) = 1/(1+P_T - i\Omega\tau_s) , \tag{4.33}$$

$$Y(z) = \epsilon P_s/(1-\epsilon P_s P_T) , \tag{4.34}$$

$$g_0 = \Gamma a N_0 (J/J_0 - 1) , \tag{4.35}$$

$$N_s(z) = \frac{N_0[J/J_0 + P_T(z)]}{1+P_T(z)} , \tag{4.36}$$

$$\Delta n_\Omega(z) = XQ , \tag{4.37}$$

and $J_0 = edN_0/\tau_s$ is the transparency current density. Note that the z dependence of the FWM nonlinear interations and the gain distribution is retained in the present model. This is of importance when consideration is given to lasers with low or asymmetric facet reflectivities where significant non-uniformity in the field distribution is anticipated.

The coupled-wave equations must satisfy the boundary conditions at the two laser facets with power reflectivities R_1 and R_2, respectively:

$$A_j^+(z=0) = \sqrt{1-R_1}\ A_{in} + \sqrt{R_1}\ A_j^-(z=0) , \tag{4.38}$$

$$A_{R,j} = \sqrt{1-R_1}\ A_j^-(z=0) + \sqrt{R_1}\ A_{in} , \tag{4.39}$$

$$A_j^-(z=L)\exp(-ik_0L) = \sqrt{R_2}\ A_j^+(z=L)\exp(ik_0L) , \tag{4.40}$$

$$A_{T,j} = \sqrt{1-R_2}\ A_j^+(z=L)\exp(ik_0L) , \tag{4.41}$$

where A_{in} is the normalized incident probe signal amplitude which is zero for $j = 0, 2$, L is the laser cavity length, $A_{R,j}$ and $A_{T,j}$ are the output fields from

the front ($z = 0$) and the rear ($z = L$) facets, respectively, at the corresponding frequency.

The probe (or conjugate) reflectivity, R_p (or R_c) is defined as the ratio of the reflected probe (or conjugate) output power from the front facet ($z = 0$) to the incident probe power at the same facet. Similarly, the probe (conjugate) transmittivity, T_p (T_c) is defined as the ratio of the transmitted probe (conjugate) output from the rear facet ($z = L$) to the incident probe power at the front facet (see Fig. 4.1), ie.,

$$R_p = \left|\frac{A_{R,1}}{A_{in}}\right|^2 , \quad T_p = \left|\frac{A_{T,1}}{A_{in}}\right|^2 , \tag{4.42}$$

$$R_c = \left|\frac{A_{R,2}}{A_{in}}\right|^2 , \quad T_c = \left|\frac{A_{T,2}}{A_{in}}\right|^2 . \tag{4.43}$$

4.3 Numerical Solution

The numerical solution of the system of ordinary differential equations (4.27)–(4.29) that are subject to the boundary conditions at the laser facets allows the evolution of the various fields and their nonlinear interaction to be computed along the propagation direction z. This z dependence of the fields and hence the gain is of particular importance when the laser has low and/or asymmetric facet reflectivities, in which case the mean field approximation is no longer valid. In addition, the effects of a Fabry-Perot cavity with different facet reflectivities on the conjugate output can only be investigated by numerical solution of the differential equations.

Because $A_j^{\pm}(z)$ in the coupled-wave equations are complex quantities, each equation can be separated into its real and imaginary parts and a total of 12 equations are to be solved. Although the free-running pump signal wave equations (4.27) are independent of Eqs. (4.28) and (4.29), numerical solution is required

because of the z dependence of the coefficient α_0.

4.3.1 Piece-Wise Constant Inversion Population Model

An iterative method using the piece-wise constant inversion population (PCIP) model similar to that of Middlemast *et al.* [34] is used to solve Eqs. (4.27). The model is based on solving the field and the carrier density equations self-consistently with the boundary conditions imposed by the two facets. In the model, the longitudinal length of the laser cavity is divided into M equal-length segments, in each of which a constant, but as yet unknown, value of the carrier density (inversion population) and thus the gain is assumed. This approach allows an analytical expression for the forward and the reverse propagating pump fields to be obtained in each segment. The average intensity distribution in each segment is then calculated and used in the charge conservation equation to find the self-consistent, constant value of the carrier density in each corresponding segment. The procedure is repeated until the boundary conditions at the two facets are satisfied to a required degree of accuracy. The PCIP model allows the pump wave equations to be solved with considerable reduction in computation time. The probe and the conjugate wave equations are then solved using a standard library routine for a system of boundary-value ordinary differential equations in conjunction with the obtained pump waves at each mesh point.

In the PCIP model, the static carrier density $N_{s,m}$, and hence the gain G_m, in the m-th segment within $z = Z_m$ and $z = Z_{m+1}$ are assumed constant. Therefore, the pump wave equations (4.27) have analytical solutions of the form

$$A_0^+(z) = A_0^+(Z_m) \exp\left\{\frac{1}{2}\left[(G_m - \alpha_{int}) - iG_m\beta\right](z - Z_m)\right\}, \quad (4.44)$$

$$A_0^-(z) = A_0^-(Z_m) \exp\left\{-\frac{1}{2}\left[(G_m - \alpha_{int}) - iG_m\beta\right](z - Z_m)\right\}, \quad (4.45)$$

where

$$G_m = \Gamma a \left(N_{s,m} - N_0\right)\left[1 - \epsilon P_s(\overline{P}_m + \overline{Q}_m)\right] , \tag{4.46}$$

and $\overline{P}_m$ and $\overline{Q}_m$ are the average values of the forward and the reverse propagating normalized pump intensities in the m-th segment, respectively, which are defined as

$$\begin{aligned}\overline{P}_m &= \frac{1}{\Delta L}\int_{Z_m}^{Z_{m+1}} |A_0^+(z)|^2\, dz \\ &= \frac{|A_0^+(Z_m)|^2}{(G_m - \alpha_{int})\Delta L}\left\{\exp[(G_m - \alpha_{int})\Delta L] - 1\right\} ,\end{aligned} \tag{4.47}$$

and

$$\begin{aligned}\overline{Q}_m &= \frac{1}{\Delta L}\int_{Z_m}^{Z_{m+1}} |A_0^-(z)|^2\, dz \\ &= \frac{|A_0^-(Z_m)|^2}{(G_m - \alpha_{int})\Delta L}\left\{1 - \exp[-(G_m - \alpha_{int})\Delta L]\right\} ,\end{aligned} \tag{4.48}$$

where $\Delta L = L/M$ is the segment width. The continuity of $A_0^+(z)$ and $A_0^-(z)$ in each segment boundary is enforced, whereas their derivitives may be discontinuous.

Eqs. (4.45)–(4.48) are then solved in conjunction with the boundary conditions by following the computational algorithm as follows: while traversing along increasing z, a new iterated distribution of $A_0^+(z)$ is found in each segment. The average value $\overline{P}$ is calculated in each segment and used with the average value $\overline{Q}$ obtained for the corresponding segment in the immediately previous iteration, to obtain self-consistent value of the carrier density in each segment. On reaching the rear facet, the boundary condition is imposed and then similar sequence as above is run traversing along decreasing z. The boundary condition in the front facet allows a new iterated value of $A_0^+(z = 0)$ to be found. The iterations are continued until a specified degree of accuracy in the computed values of the pump field is satisfied at a chosen point. Using initial tests with a variable M, it was

found that a reasonably high degree of accuracy in the solutions of the pump fields could be obtained with $M = 50$ in the PCIP model.

Solving the pump wave equations, the oscillation condition for the free-running laser can be obtained:

$$\sqrt{R_1 R_2}\, \exp\left[\left(\frac{1}{M}\sum_{i=1}^{M} G_i - \alpha_{int}\right) L\right] \exp(i\varphi) = 1\,, \tag{4.49}$$

where φ is the total phase shift of the pump wave in propagating through the laser cavity in one complete round trip and is given by

$$\varphi = 2k_0 L - \frac{\beta L}{M}\sum_{i=1}^{M} G_i\,. \tag{4.50}$$

The last term in Eq. (4.50) is the detuning introduced by phase-amplitude coupling as characterized by the linewidth enhancement factor β. The oscillation condition (4.49) requires that the total phase shift be some integral multiple of 2π. Eq. (4.50) then becomes

$$2k_0 L = 2m\pi + \frac{\beta L}{M}\sum_{i=1}^{M} G_i\,, \tag{4.51}$$

where m is an integer. This defines k_0 in the boundary conditions.

The lasing frequency of the pump wave can be found using $k_0 = n_g\omega_0/c$ and Eq. (4.51) as

$$\omega_0 = \omega_m' + \frac{\beta c}{2n_g}\frac{1}{M}\sum_{i}^{M} G_i\,, \tag{4.52}$$

where ω_m' is the m-th Fabry-Perot mode of the 'cold' (or passive) cavity. Eq. (4.52) shows that the lasing frequency of the pump wave varies as the current injection rate is changed.

4.4 Results and Discussion

In this section, the travelling-wave formulation developed in the previous section is applied to analyse NDFWM in laser diodes biased above threshold. A small probe injection power of $P_{in} = 0.02$ μW [27, 28] is assumed to be incident at the laser front facet at $z = 0$. The following parameter values appropriate to GaAs/AlGaAs laser diodes are used in the analysis (unless stated otherwise): laser volume $V = (300\ \mu\text{m} \times 2.0\ \mu\text{m} \times 0.2\ \mu\text{m})$, reference wavelength $\lambda_0 = 0.83$ μm, $\Gamma = 0.4$, $a = 3 \times 10^{-16}$ cm^2, $N_0 = 1.1 \times 10^{18}$ cm^{-3}, $\beta = 3$, $\tau_s = 1$ ns, $n_g = 4$, $\alpha_{int} = 20$ cm^{-1}, and $\epsilon = 2.8 \times 10^{-13}$ m^2/W (which corresponds to $\epsilon_{NL} = 5.0 \times 10^{-18}$ cm^3).

4.4.1 Longitudinal Variation of NDFWM Interaction

The longitudinal variations of electron density and normalized pump intensity in the laser cavity are illustrated in Fig. 4.2 and Fig. 4.3, respectively. Laser diodes with a constant product of $R_1R_2 = 0.09$, and hence with the same threshold gain (assuming the same internal loss and cavity length), are considered. It should be noted that the electron density in each segment is defined only within the segment and is left unspecified at the segment boundaries in the PCIP model. As a result, the electron density curves in Fig. 4.2 are obtained by plotting and connecting the electron density value at the centre point of each segment. By comparing Fig. 4.2 and Fig. 4.3, it is observed that the spatial distribution of electron density is inversely related to that of the normalized pump intensity. This is due to the fact that in regions of high pump intensity (or photon density), higher stimulated emission is induced. Consequently, the electron density is reduced through interband stimulated recombination. The highly inhomogeneous longitudinal distributions of electron density and normalized pump intensity as shown

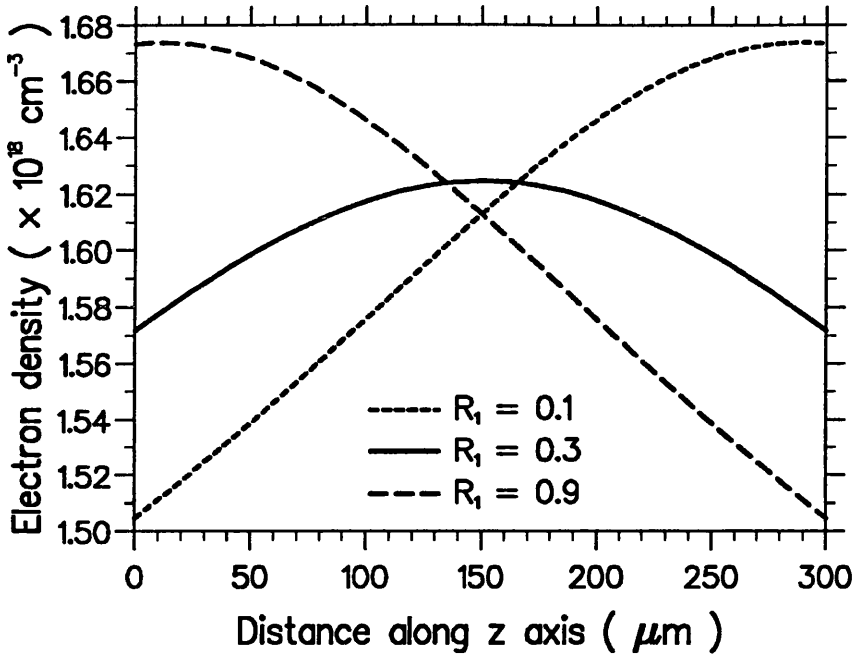

Figure 4.2: Longitudinal variations of electron density in the laser cavity for three laser devices with different facet reflectivities. $R_1R_2 = 0.09$ in all cases.

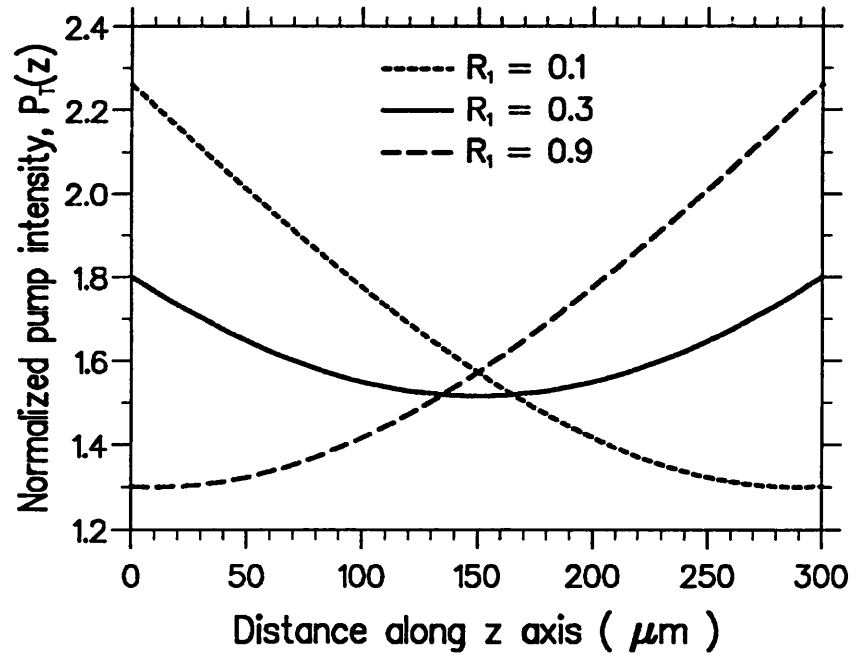

Figure 4.3: Longitudinal variations of normalized pump intensity in the laser cavity for three laser devices with different facet reflectivities. $R_1R_2 = 0.09$ in all cases.

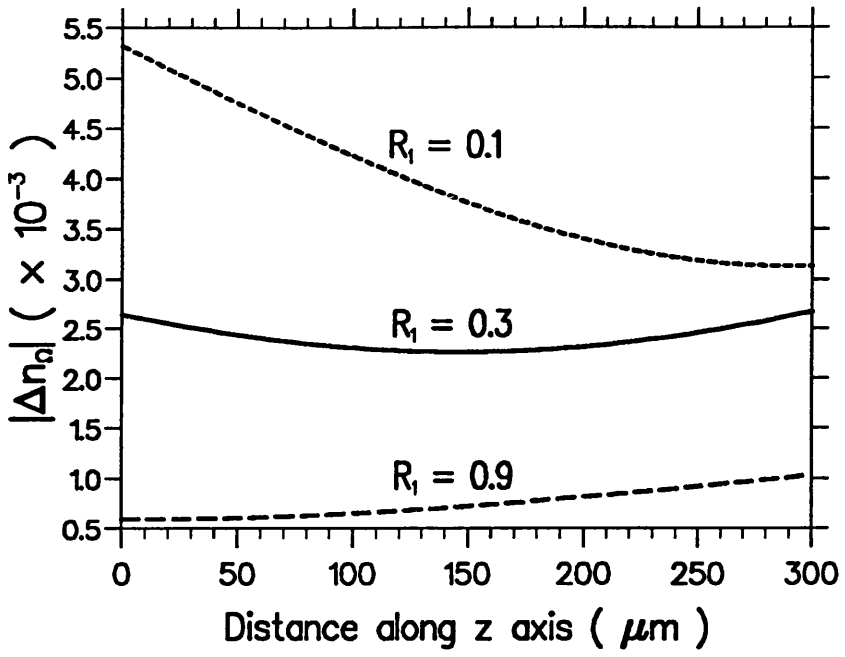

Figure 4.4: Amplitudes of normalized carrier density deviation along the longitudinal axis of the laser cavity for three laser devices with different facet reflectivities. $R_1 \times R_2 = 0.09$ in all three cases.

in Fig. 4.2 and Fig. 4.3 demonstrate that the mean-field approximation cannot be assumed, especially for laser diodes with asymmetric facet reflectivities.

To illustrate the degree of longitudinal non-uniformity in the NDFWM interactions, the amplitudes of the normalized carrier density deviation Δn_Ω along the z axis for three laser devices with different facet reflectivities are plotted in Fig. 4.4. Significant longitudinal non-uniformity is observed in the carrier density deviation distribution, especially for laser diodes with highly asymmetric facet reflectivities. In as much as it is the carrier density fluctuations which drive the NDFWM process it is to be expected that such longitudinal carrier variations will influence achievable phase conjugate reflectivities in these devices. Furthermore, it is observed that the carrier density deviation is the largest in the device with low-reflective front facet and high-reflective rear facet. It is therefore to be

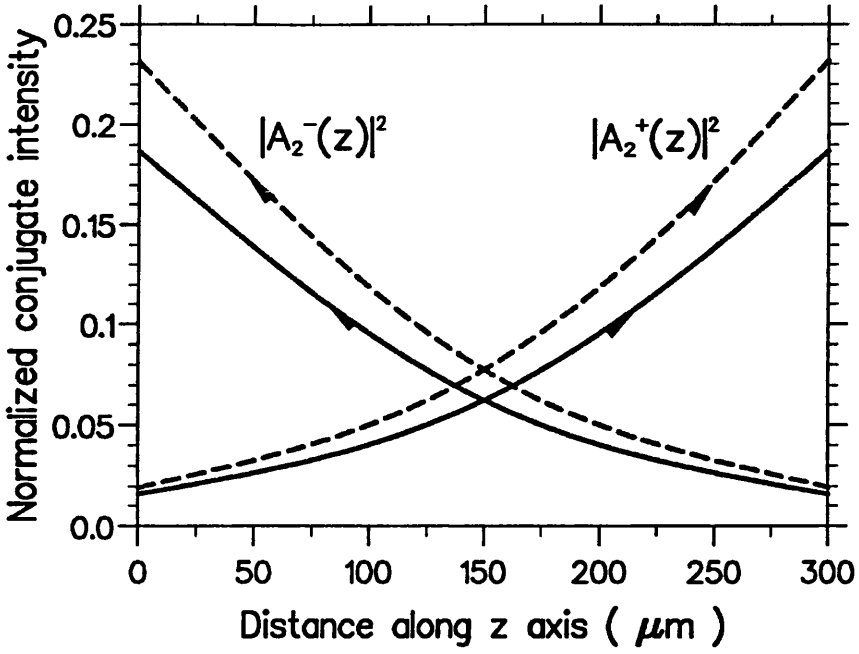

Figure 4.5: Evolution of normalized conjugate intensity along the longitudinal axis of the laser cavity. Solid curves are obtained with the PCIP model whereas dashed curves are obtained with the uniform-gain model.

expected that the efficiency of optical phase conjugation is enhanced in devices with $R_1 < R_2$, and with the probe injection incident at the low reflectivity facet.

The evolution of the counter-travelling conjugate signal intensities along the z direction is shown in Fig. 4.5, where the laser facet reflectivities are $R_1 = R_2 = 0.1$. The solid curves are obtained with the PCIP model. The dashed curves are obtained with a spatially uniform gain model, in which case a z independent normalized *average* intracavity pump intensity $\overline{P}_T$ is assumed, which is given by

$$\overline{P}_T = \frac{1}{L}\int_0^L |A_0^+(z)|^2 + |A_0^-(z)|^2\, dz = \frac{g_0}{g_{th}} - 1 \ , \tag{4.53}$$

and

$$g_{th} = \alpha_{int} + \frac{1}{2L}\ln\left(\frac{1}{R_1 R_2}\right) \tag{4.54}$$

is the threshold gain of the laser diode. Significant differences are observed between the propagation curves of the conjugate intensity computed with the

two models when the laser facet reflectivity is small. This is generally true for $R_1 = R_2 \leq 0.3$ and for lasers with highly asymmetric facet reflectivities. Similar differences are also observed in the values of the probe intensity, although the differences between the pump intensities from the two models are less pronounced. Figure 4.5 also shows that the conjugate intensity along the z axis is highly nonuniform and thus the mean field approximation cannot be assumed in lasers with low facet reflectivities. The above results demonstrate that longitudinal variations of the internal gain should be taken into account in discussions of NDFWM when consideration is given to laser diodes with low and/or asymmetric facet reflectivities.

4.4.2 Probe and Conjugate Output Characteristics

The probe and the conjugate output power at $z = L$ as a function of pump–probe frequency detuning are shown in Figs. 4.6(a) and 4.6(b), respectively. The facet reflectivities are $R_1 = R_2 = 0.3$. The solid and the dashed curves correspond to $\beta = 3$ and $\beta = 4$, respectively. Probe and conjugate output power peaks are observed at frequency detuning approximately equal to

$$\Omega_R = \left(\frac{g_{th} v_g \overline{P}_T}{\tau_s} \right)^{1/2} , \tag{4.55}$$

which corresponds to the relaxation oscillation frequency of the pumped laser.

It is also observed that the conjugate output power curve is symmetric with respect to zero pump–probe frequency detuning, whereas the probe output power curve exhibits strong asymmetry with higher probe output for negative frequency detuning. This agrees well with experimental results of Simpson and Liu [28] and also observations in semiconductor optical amplifiers [3, 4]. Such probe gain asymmetry was theoretically predicted by Bogatov *et al.* [35]. The physical origin of the asymmetric nature of the probe gain is related to the fact that a change in

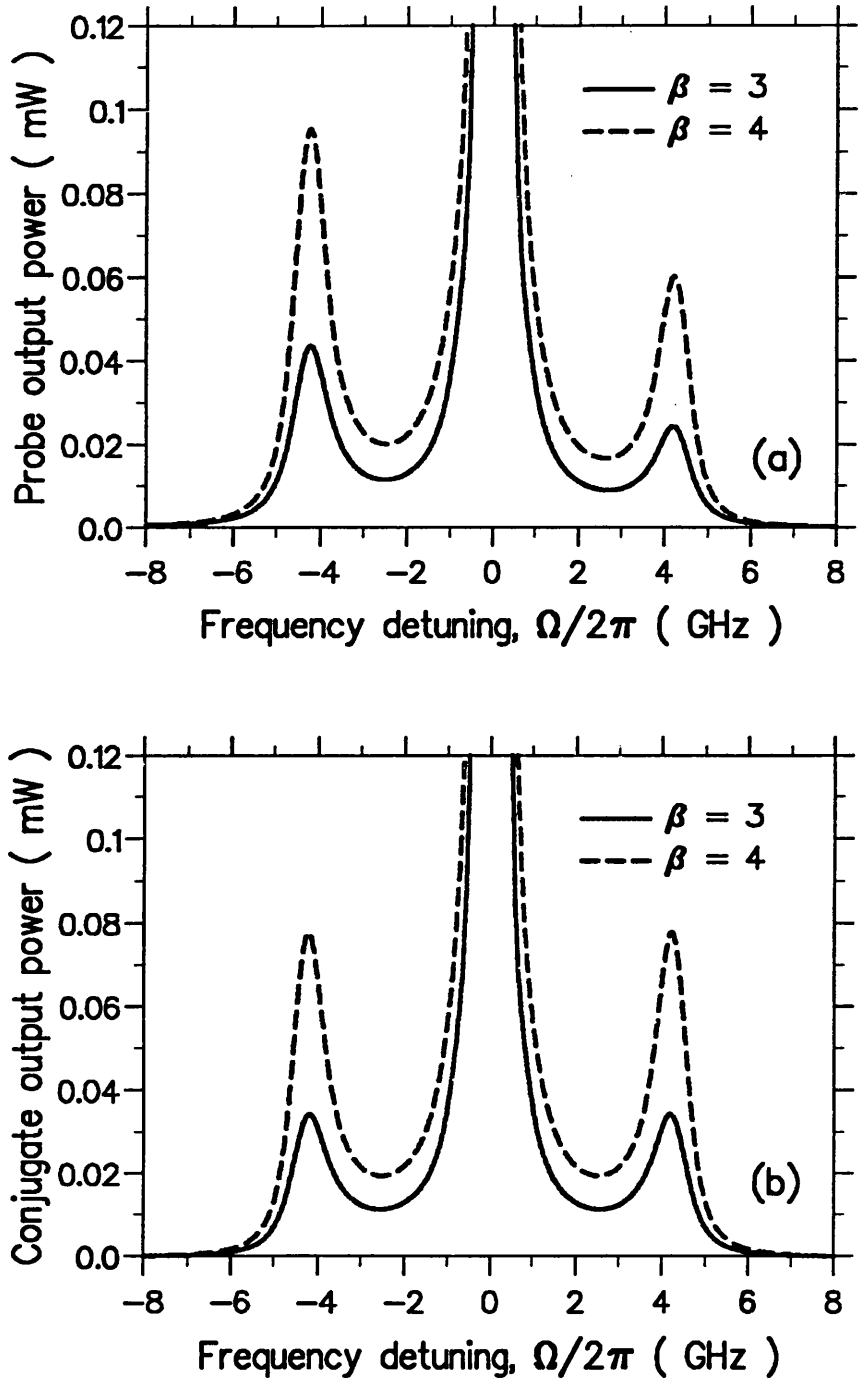

Figure 4.6: (a) Probe and (b) conjugate output power versus frequency detuning for symmetric laser diodes. $P_{out} = 7.73$ mW and $R_1 = R_2 = 0.3$.

carrier density affects both the gain and the refractive index of the active region in semiconductor lasers [23, 36]. Hence, population pulsations create both gain and index gratings simultaneously; the relative contributions of the two gratings are governed by the linewidth enhancement factor β. Figs. 4.6(a) and 4.6(b) also show that probe and conjugate output power increase for larger values of the linewidth enhancement factor, and confirm the significant contribution of the refractive-index grating in the NDFWM process arising from the large β value in semiconductor lasers.

Probe and Conjugate Transmittivities Dependence on Spontaneous Carrier Lifetime

In a symmetric laser diode (where $R_1 = R_2$), the probe (or conjugate) reflectivity is the same as the probe (or conjugate) transmittivity. The transmittivity of the probe T_p and the conjugate T_c waves as a function of frequency detuning are plotted in Figs. 4.7(a) and 4.7(b), respectively, for different values of the spontaneous carrier lifetime, τ_s. T_p and T_c in the range of 30–40 dB can be obtained at frequency detunings near the relaxation oscillation frequency, which agree well with experimental observations [13].

Because the relaxation oscillation frequency Ω_R is inversely related to τ_s as indicated in Eq. (4.55), it is noticed that the FWM bandwidth (frequency range in which the conjugate transmittivity is positive) increases for smaller τ_s. For frequency detunings well above Ω_R, T_p and T_c decrease rapidly with roll-off rates of approximately -20 and -60 dB per-frequency decade, respectively, in accordance with experimental results reported in Ref. [13]. In this reference, Fabry-Perot cavity effects are indicated as being responsible for the observed roll-off rates. The cavity effect is indeed apparent in Fig. 4.7, in which, for large frequency detun-

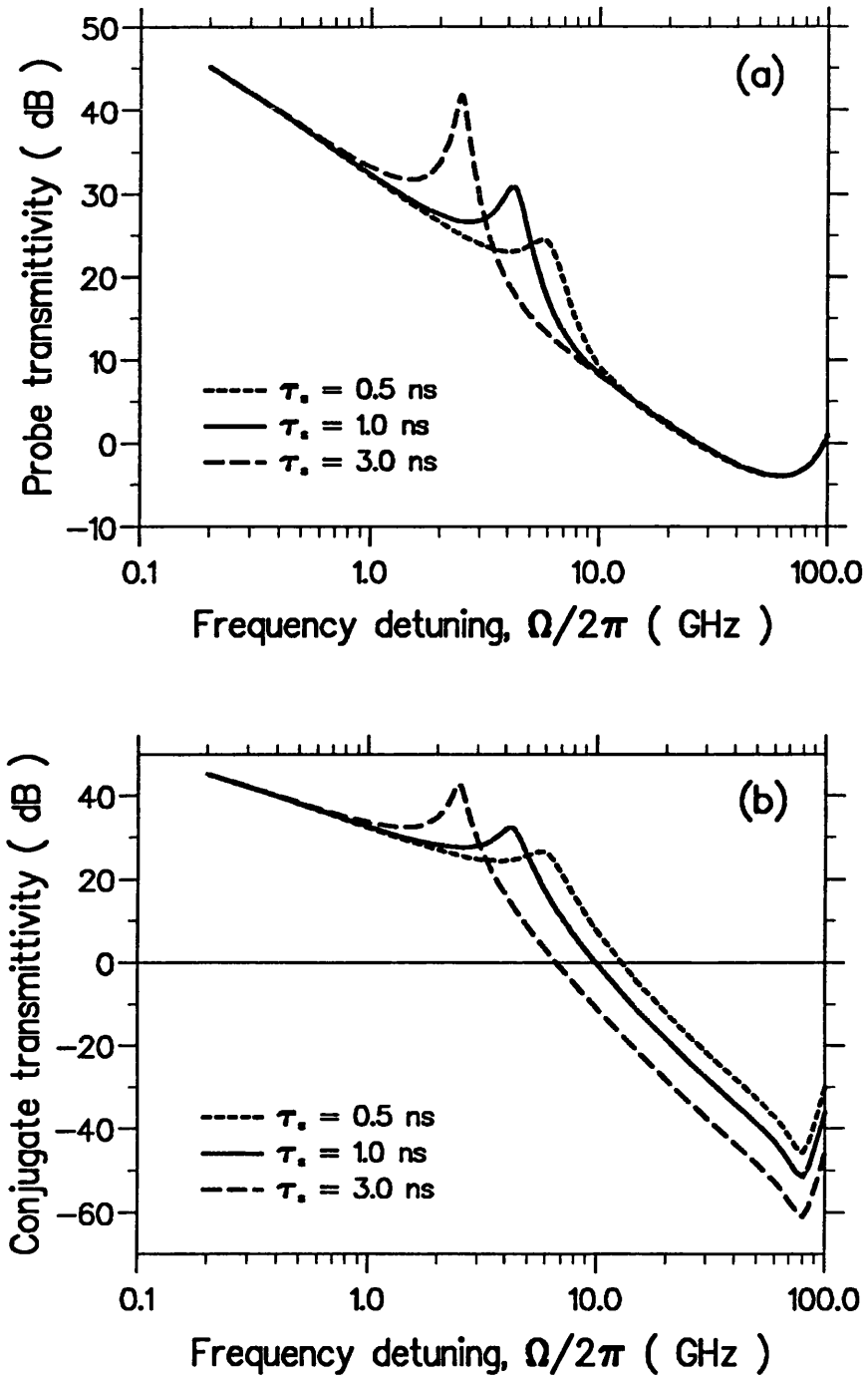

Figure 4.7: (a) Probe and (b) conjugate transmittivity as a function of frequency detuning for different values of spontaneous carrier lifetime. $R_1 = R_2 = 0.3$.

ings, the transmittivities are seen to increase again because of the effect of the adjacent Fabry-Perot resonance.

Probe and Conjugate Transmittivities Dependence on Nonlinear Gain Saturation

The dependence of probe and conjugate transmittivities on nonlinear gain saturation are shown in Figs. 4.8(a) and 4.8(b), respectively. It is observed that the main effect of nonlinear gain saturation is to damp the resonant enhancement of the FWM efficiency near the relaxation oscillation frequency of the pumped laser. Furthermore, the probe transmittivity asymmetry is more pronounced for larger values of the gain compression coefficient, whereas the conjugate transmittivity is always symmetrical with respect to zero pump–probe frequency detuning. The above results suggest that gain saturation plays an important role in the nonlinear spectral dynamics of laser diodes. In particular, FWM interactions in laser diodes are attributed not only to the carrier beating, but also to the nonlinear gain saturation. By fitting theoretical curves to experimental data, the value of ϵ can be deduced from NDFWM experiments [13, 28].

Probe and Conjugate Transmittivities Dependence on Optical Output Power

The probe and the conjugate transmittivity characteristics at different output power levels are shown in Fig. 4.9(a) and 4.9(b), respectively, for a symmetric laser diode with $R_1 = R_2 = 0.3$. It is noted that the side transmittivity peaks occur at larger frequency detunings as the output power is increased. This is a direct consequence of the dependence of the relaxation oscillation frequency on the optical intensity of the laser. In addition, the probe and the conjugate trans-

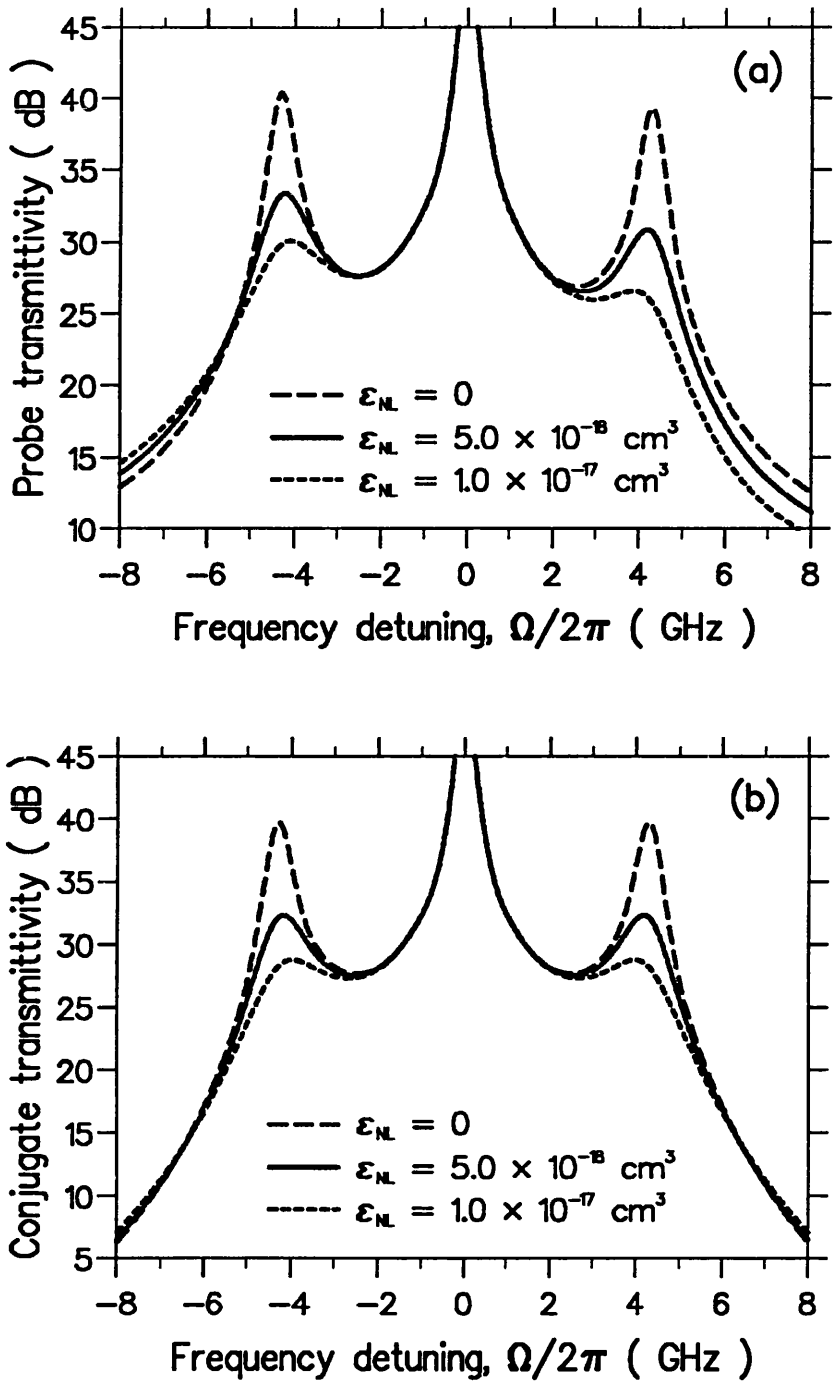

Figure 4.8: (a) Probe and (b) conjugate transmittivity versus frequency detuning for different values of gain compression coefficient. $R_1 = R_2 = 0.3$.

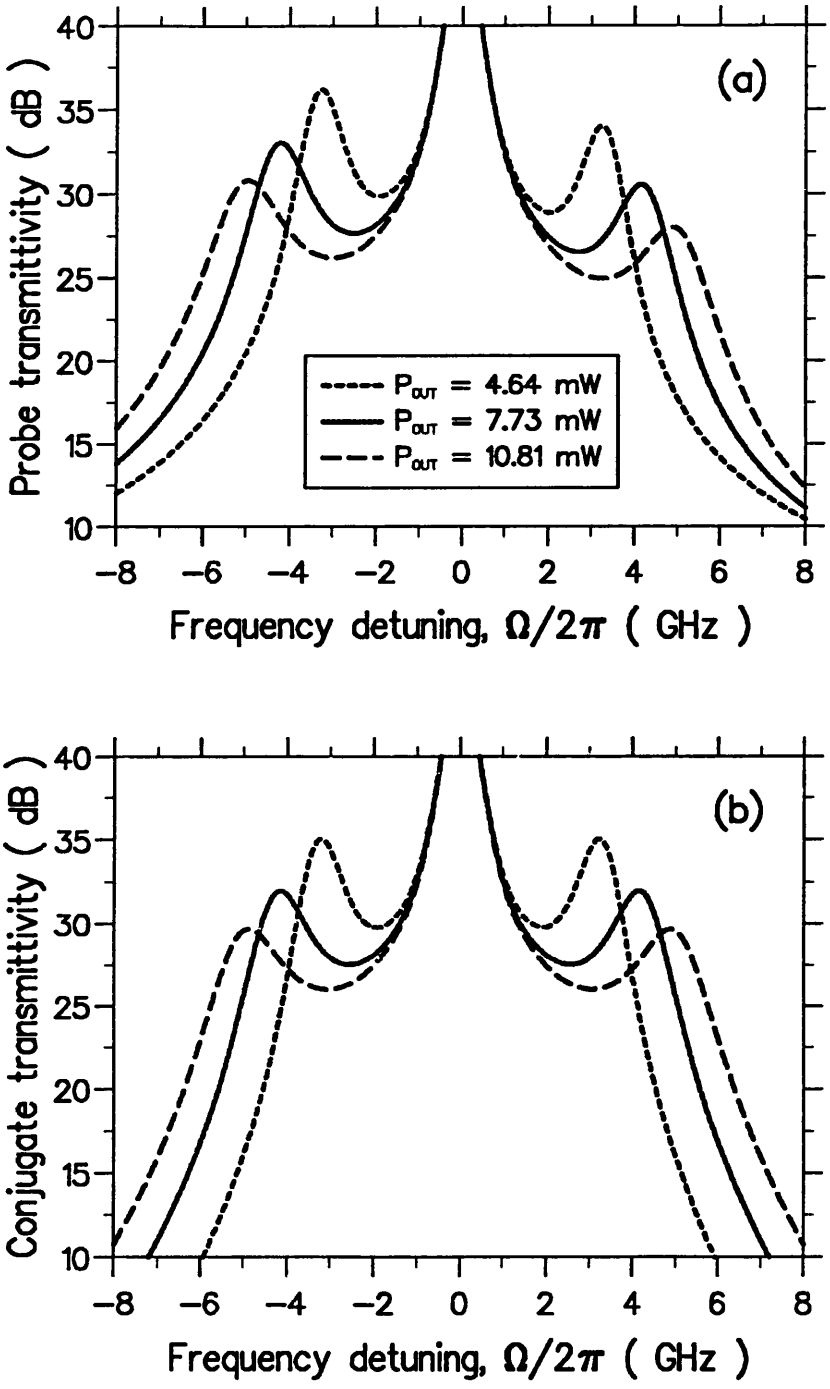

Figure 4.9: (a) Probe and (b) conjugate transmittivity versus frequency detuning for different output power levels. $R_1 = R_2 = 0.3$.

mittivity resonance peaks near Ω_R become less pronounced as the output power (or bias current) is increased. This is in agreement with experimental observations reported in Ref. [27]. The reduction of probe and conjugate transmittivities near Ω_R is due to the dynamic damping effect arising from the gain saturation nonlinearity in semiconductor lasers. As the bias current level is increased, the intracavity pump intensity increases, thereby enhances the effect of gain saturation and the damping of the FWM resonance peaks. Notice also that the probe transmittivity is asymmetrical, whereas the conjugate transmittivity is symmetrical with respect to zero frequency detuning, as has been discussed in preceding paragraphs.

It is also observed from Fig. 4.9(b) that the FWM bandwidth increases, whereas the maximum conjugate transmittivity obtainable decreases, as the output power (or bias current) is increased. Therefore, a trade-off has to be considered when using NDFWM in applications such as all-optical frequency conversion. Larger conversion bandwidth is achievable by biasing the FWM laser diode at higher injection current above threshold, whereas higher coversion efficiency is obtainable at low injection current above threshold.

No change in the above qualitative behaviours is expected, provided that the probe injection power is not too large. Depletion of the gain by the probe and the conjugate signals becomes significant when their powers are comparable to the pump optical power, and in such an operating regime, changes in the behaviour may occur. The present calculations, however, describe the main features relevant to existing experimental work [13, 27, 28]. The good agreement between results from the present formalism and available experimental results is a confirmation of the validity of the theoretical model developed in this work.

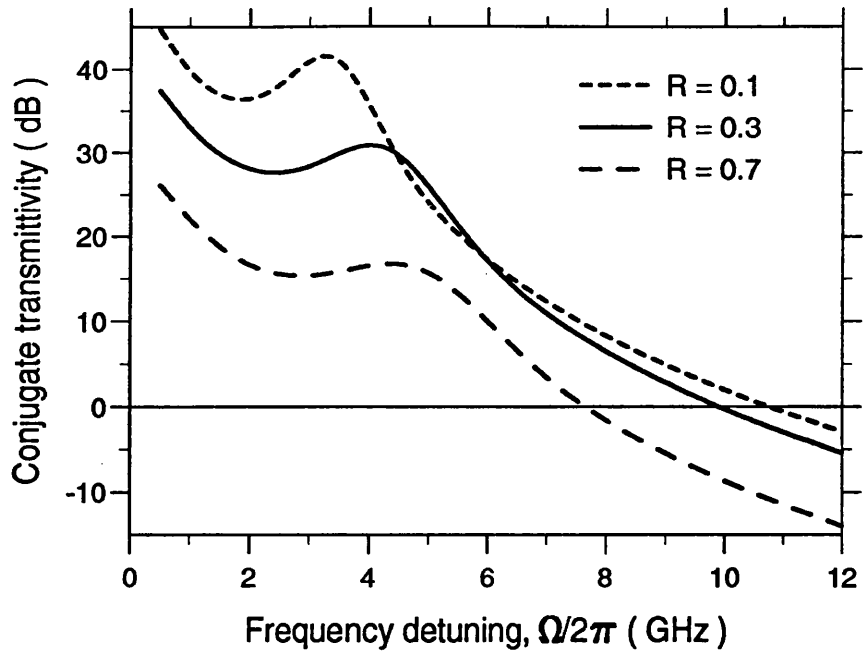

Figure 4.10: Effects of varying the facet reflectivities on conjugate transmittivity in symmetric laser diodes. $R_1 = R_2 = R$. Similar curves are obtained for probe transmittivity.

4.4.3 Conjugate Output Enhancement in Symmetric and Low Facet Reflectivity Laser Diodes

The effects of varying the facet reflectivity $R = R_1 = R_2$ on conjugate transmittivity at a constant injection current density, chosen here to be $J/J_0 = 2.2$, are illustrated in Fig. 4.10. For low facet reflectivity, the average intracavity pump intensity is reduced because of high mirror losses. The relaxation oscillation frequency of the laser is correspondingly reduced, resulting in the shift of the side transmittivity peaks to smaller frequency detuning. Lower pump intensity also means that carrier depletion by the pump wave is decreased, thus enhancing the effective gain experienced by the conjugate and the probe waves. Furthermore, at low facet reflectivity, the coupling efficiency of the constant probe injection power into the laser cavity is increased. Both of these effects contribute to higher

probe and conjugate transmittivities in laser diodes with low reflectivity facets. This nontrivial result can only be found using the present technique in which the coupled-wave equations incorporating the resonant-cavity effects and the z dependence of the nonlinear interaction are numerically integrated subject to the boundary conditions imposed at the laser facets.

It is also observed from Fig. 4.10 that the bandwidth for positive conjugate transmittivity increases as the laser facet reflectivity is reduced. This is purely a cavity effect, resulting from the broadening of the Fabry-Perot resonant transmission bandwidth at low facet reflectivities. This explicit dependence of the conjugate transmission bandwidth on laser facet reflectivity can be computed, again, only by use of the present formalism.

In addition, it is noticed from Fig. 4.10 that the conjugate transmittivity peaks near the relaxation oscillation frequency become less pronounced as the facet reflectivity R is increased. This is because increasing the facet reflectivity increases the average intracavity pump intensity. This induces larger nonlinear gain saturation and hence leads to enhanced dampings of the conjugate transmittivity peaks.

The above results show that enhancement of both the conjugate transmittivity and the conjugate transmission bandwidth can be obtained in low reflectivity laser diodes biased above threshold. Note, however, that higher injection current is required for obtaining a given level of output power when the laser facet reflectivity is reduced. As a matter of practicality, there is a limit to the injection current that one can apply to the laser and hence a limit to how low the reflectivity of the facet can be with anti-reflection coating.

The present analysis has thus shown that the bandwidth of FWM in laser diodes biased above threshold is dependent not only on the spontaneous carrier

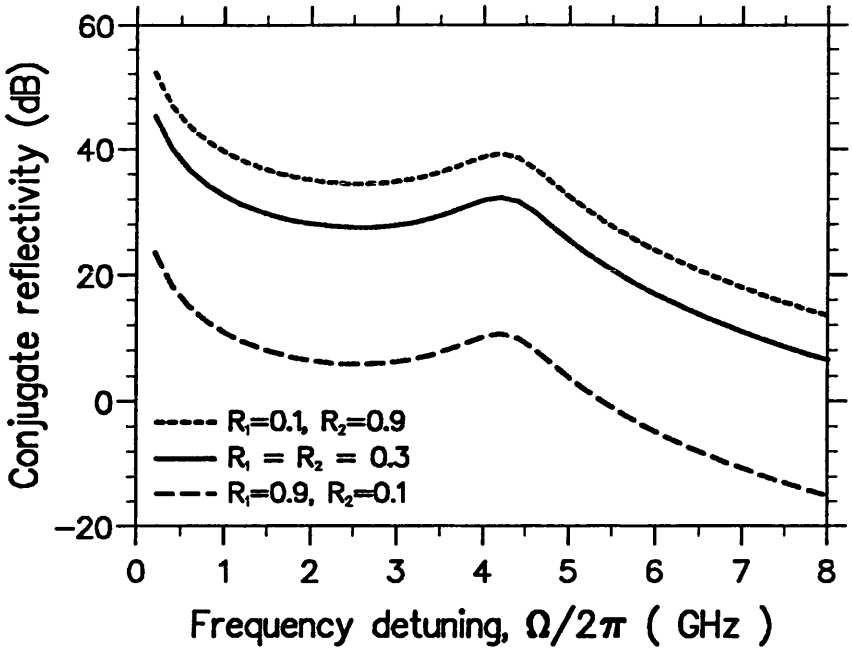

Figure 4.11: Enhanced conjugate reflectivity in asymmetric facet laser diodes.

lifetime as in travelling-wave amplifiers [4], but also on the relaxation oscillation frequency and the facet reflectivities of the pumped laser. It is therefore suggested that experimental investigation could be profitably undertaken on FWM effects in low-facet-reflectivity laser diodes with a view to taking advantage of the enhancements of both the conjugate transmittivity and the FWM bandwidth revealed by the present analysis.

4.4.4 Enhanced Conjugate Reflectivity in Asymmetric Facet Laser Diodes

Fig. 4.11 shows the conjugate reflectivity versus frequency detuning for three laser devices with different facet reflectivities. The devices considered here have the same constant product of $R_1R_2 = 0.09$, and thus have the same threshold gain g_{th}, assuming the same cavity length and internal loss coefficient. As shown

in Fig. 4.11, a 7–8 dB enhancement of the phase conjugate reflectivity can be obtained in the asymmetric laser with $R_1 = 0.1$ and $R_2 = 0.9$, compared to the symmetric laser ($R_1 = R_2 = 0.3$). On the other hand, a reduction of the conjugate reflectivity is obtained if the external probe signal is incident at the high-reflectivity facet of the asymmetric laser diode. This observation is consistent with the results depicted in Fig. 4.4, in which it was found that the normalized carrier density deviation is the largest in the device with low-reflectivity front facet and high-reflectivity rear facet, with the external probe injection incident at the front facet. The role of carrier density fluctuations in driving the NDFWM process is thus clearly demonstrated.

The conjugate reflectivity and the conjugate transmittivity as functions of R_1 are shown in Figs. 4.12(a) and 4.12(b), respectively. The probe signal injection is assumed to be tuned to a frequency near the relaxation oscillation frequency of the laser. The curves are only defined in the range of R_1 such that $R_2 \lesssim 1$ sets the limit on the left hand side of each curve and $R_1 \lesssim 1$ defines the boundary on the right. The cross in each curve represents the point at which $R_1 = R_2$, where $R_c \approx T_c$. For $R_1 < R_2$, it is observed that $R_c > T_c$ and vice-versa. As the front facet reflectivity is increased, R_c decreases. This is because higher R_1 means less external injection power is coupled into the laser cavity and less power is emitted from the front facet because of lower front-facet transmittivity. On the other hand, T_c increases up to a maximum, where $R_1 = R_2$, and then decreases as R_1 is increased. It is also found that T_c is the same if R_1 and R_2 are interchanged for a constant product of R_1R_2. This result means that the transmitted conjugate output power is the same at whichever facet the probe signal is incident. However, the reflected conjugate output power does depend on the facet upon which the probe is incident. Fig. 4.12 shows that the highest conjugate output power can be obtained in a laser diode with asymmetric facet

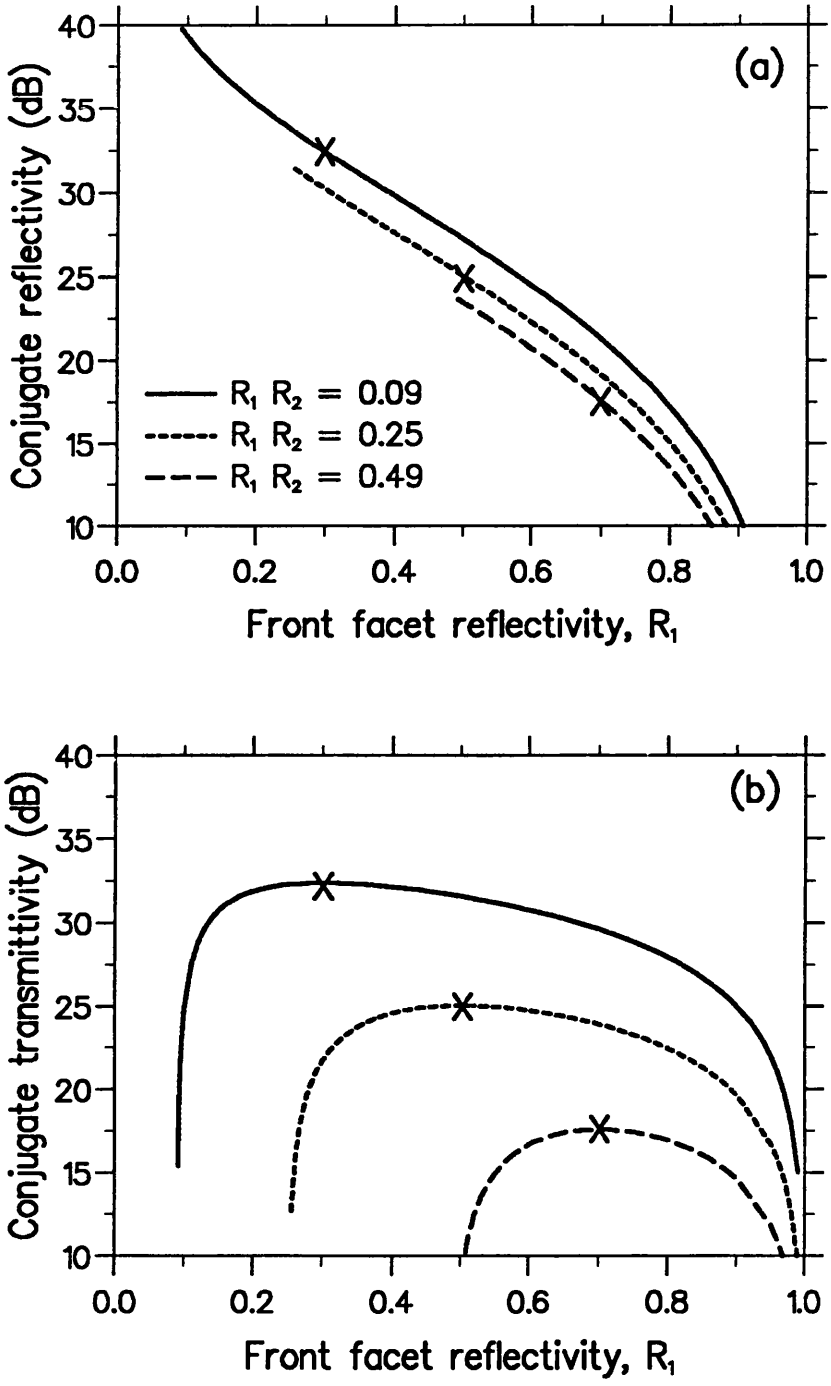

Figure 4.12: (a) Conjugate reflectivity and (b) conjugate transmittivity versus R_1 for asymmetric laser diodes with different threshold gain values.

reflectivities by injecting the probe signal at the facet with low reflectivity and by deriving the conjugate output from the same facet.

The analysis in this section shows that there exist opportunities for enhanced phase-conjugate wave generation using highly asymmetric laser diodes. Experimental investigations of such devices would therefore be of some considerable interest.

4.5 Conclusion

A theoretical model for cavity-enhanced NDFWM in above-threshold Fabry-Perot laser diodes has been described, which takes into account resonant-cavity effects and longitudinal variations of both the nonlinear interaction and the gain distribution. The model has, in particular, been applied to investigate optical phase conjugation via NDFWM in laser diodes with low and/or asymmetric facet reflectivities. The results can be summarised as follows.

- Enhancements of both the conjugate reflectivity and the FWM bandwidth can be obtained in symmetric laser diodes with low-reflectivity facets.
- The FWM bandwidth in laser diodes biased above threshold is dependent not only on the spontaneous carrier lifetime and the relaxation oscillation frequency as have previously been reported [27], but also on the facet reflectivities of the Fabry-Perot laser diodes. The explicit dependence of the FWM bandwidth on facet reflectivities can only be computed using the formalism presented in the present report.
- A 7–8 dB enhancement of the phase conjugate reflectivity can be obtained, compared to a symmetric laser, by reducing the reflectivity of the optical

input facet R_1 from 0.3 to 0.1, while maintaining a constant product of R_1R_2.

The importance of incorporating the longitudinal variations of the nonlinear interaction and the internal gain distribution in the NDFWM model has been established. The model developed here has a wide applicability, and can be used to study FWM processes in optical devices with longitudinal structural variations, such as multisection laser diodes. Specifically, the model can be utilized to analyse FWM in laser diodes used for all-optical frequency conversion. This latter aspect is considered in the next chapter.

FWM has recently been identified for effecting a number of functions in high-speed optical transmission and signal processing systems (see [37] and references therein), such as optical demultiplexing, clock recovery, fiber chromatic dispersion compensation via spectral inversion, optical sampling [38], and cancellation of channel crosstalk [39]. The successful development of optimized laser diodes as optical phase conjugators will provide a key component for these applications. The asymmetric FP laser diode FWM configuration as proposed in this chapter provides a highly efficient means of conjugate signal generation and hence is believed to be having advantages for performing the multitude of functions as indicated above.

References

[1] H. Nakajima and R. Frey, "Collinear nearly degenerate four-wave mixing in intracavity amplifying media," *IEEE J. Quantum Electron.*, vol. QE-22, pp. 1349–1354, 1986.

[2] R. Nietzke, P. Panknin, W. Elsässer, and E. O. Göbel, "Four-wave mixing in GaAs/AlGaAs semiconductor lasers," *IEEE J. Quantum Electron.*, vol. 25, pp. 1399–1406, 1989.

[3] F. Favre and D. L. Guen, "Four-wave mixing in traveling wave semiconductor laser amplifiers," *IEEE J. Quantum Electron.*, vol. 26, pp. 858–864, 1990.

[4] T. Mukai and T. Saitoh, "Detuning characteristics and conversion efficiency of nearly degenerate four-wave mixing in a 1.5 μm traveling-wave semiconductor laser amplifier," *IEEE J. Quantum Electron.*, vol. 26, pp. 865–874, 1990.

[5] K. A. Shore and W. M. Yee, "Theory of self-locking FM operation in semiconductor lasers," *Proc. IEE Part J*, vol. 138, pp. 91–96, 1991.

[6] W. M. Yee and K. A. Shore, "Multimode analysis of self-locked FM operation in laser diodes," *Proc. IEE Part J*, vol. 140, pp. 21–25, 1993.

[7] J. Zhou, N. Park, J. W. Dawson, K. J. Vahala, M. A. Newkirk, and B. I. Miller, "Terahertz four-wave mixing spectroscopy for study of ultrafast dynamics in a semiconductor optical amplifier," *Appl. Phys. Lett.*, vol. 63, pp. 1179–1181, 1993.

[8] L. F. Tiemeijer, "Effects of nonlinear gain on four-wave mixing and asymmetric gain saturation in a semiconductor laser amplifier," *Appl. Phys. Lett.*, vol. 59, pp. 499–501, 1991.

[9] S. R. Chinn, "Measurement of nonlinear gain suppression and four-wave mixing in quantum well lasers," *Appl. Phys. Lett.*, vol. 59, pp. 1673–1675, 1991.

[10] K. Kikuchi, M. Kakui, C. E. Zah, and T. P. Lee, "Observation of highly nondegenerate four-wave mixing in 1.5 μm traveling-wave semiconductor optical amplifiers and estimation of nonlinear gain coefficient," *IEEE J. Quantum Electron.*, vol. 28, pp. 151–156, 1992.

[11] K. Kikuchi and M. Amano, "Analysis of the origin of the nonlinear gain in 1.5 μm semiconductor active layers by highly nondegenerate four-wave mixing," *Appl. phys. Lett.*, vol. 64, pp. 548–550, 1994.

[12] A. D'Ottavi, E. Iannone, A. Mecozzi, S. Scotti, and P. Spano, "Investigation of carrier heating and spectral hole burning in semiconductor amplifiers by highly nondegenerate four-wave mixing," *Appl. Phys. Lett.*, vol. 64, pp. 2492–2494, 1994.

[13] S. Jiang and M. Dagenais, "Nearly degenerate four-wave mixing in Fabry-Perot semiconductor lasers," *Opt. Lett.*, vol. 18, pp. 1337–1339, 1993.

[14] J. M. Liu and T. B. Simpson, "Characterization of fundamental parameters of a semiconductor laser with an injected optical probe," *IEEE Photon. Technol. Lett.*, vol. 4, pp. 380–382, 1993.

[15] R. A. Fisher, *Optical Phase Conjugation*, New York: Academic Press, 1983.

[16] Y. R. Shen, *The Principle of Nonlinear Optics*, New York: Wiley, 1984.

[17] G. Grosskopf, L. Kuller, R. Ludwig, R. Schnabel, and H. G. Weber, "Semiconductor laser optical amplifiers in switching and distribution networks," *Opt. Quantum Electron.*, vol. 21, pp. S59–S74, 1989.

[18] G. Grosskopf, R. Ludwig, and H. G. Weber, "140 Mbit/s DPSK transmission using an all-optical frequency convertor with a 4000 GHz conversion range," *Electron Lett.*, vol. 24, pp. 1106–1107, 1988.

[19] N. Schunk, G. Grosskopf, R. Ludwig, R. Schnabel, and H. G. Weber, "Frequency conversion by nearly-degenerate four-wave mixing in travelling-wave semiconductor laser amplifiers," *IEE Proc. Part J*, vol. 137, pp. 209–214, 1990.

[20] S. Murata, A. Tomita, J. Shimizu, and A. Suzuki, "THz optical-frequency conversion of 1 Gb/s signals using highly nondegenerate four-wave mixing in an InGaAsP semiconductor laser," *IEEE Photon. Technol. Lett.*, vol. 3, pp. 1021–1023, 1991.

[21] T. E. Darcie, R. M. Jopson, and R. W. Tkach, "Intermodulation distortion in optical amplifiers from carrier density modulation," *Electron. Lett.*, vol. 23, pp. 1392–1394, 1987.

[22] G. P. Agrawal, I. M. I. Habbab, "Effects of four-wave mixing on multichannel amplification in semiconductor laser amplifiers," *IEEE J. Quantum Electron.*, vol. 26, pp. 501–505, 1990.

[23] G. P Agrawal, "Population pulsations and nondegenerate four-wave mixing in semiconductor lasers and amplifiers," *J. Opt. Soc. America B*, vol. 5, pp. 147–159, 1988.

[24] G. P. Agrawal, "Gain nonlinearity in semiconductor lasers: theory and application to distributed feedback lasers," *IEEE J. Quantum Electron.*, vol. QW-23, pp. 860–868, 1987.

[25] C. B. Su, "Dielectric grating induced by cavity standing wave as a new explanation of the origin of nonlinear gain in semiconductor diode lasers," *Electron. Lett.*, vol. 24, pp. 370–371, 1988.

[26] S. Jiang and M. Dagenais, "Observation of nearly degenerate and cavity-enhanced highly nondegenerate four-wave mixing in semiconductor lasers," *Appl. Phys. Lett.*, vol. 62, pp. 2757–2759, 1993.

[27] A. Mecozzi, A. D'Ottavi, and R. Hui, "Nearly degenerate four-wave mixing in distributed feedback semiconductor lasers operating above threshold," *IEEE J. Quantum Electron.*, vol. 29, pp. 1477–1487, 1993.

[28] T. B. Simpson and J. M. Liu, "Phase and amplitude characteristics of nearly degenerate four-wave mixing in Fabry-Perot semiconductor lasers," *J. Appl. Phys.*, vol. 73, pp. 2587–2589, 1993.

[29] L. Li and K. Petermann, "Characteristics of the optical-frequency conversion in a semiconductor laser," *IEEE J. Quantum Electron.*, vol. 29, pp. 2793–2798, 1993.

[30] R. Hui, S. Benedetto, and I. Montrosset, "Optical frequency conversion using nearly degenerate four-wave mixing in a distributed-feedback semiconductor laser: theory and experiment," *J. Lightwave Technol.*, vol. 11, pp. 2026–2032, 1993.

[31] W. M. Yee and K. A. Shore, "Nearly degenerate four-wave mixing in laser diodes with nonuniform longitudinal gain distribution," *J. Opt. Soc. America B*, vol. 11, pp. 1221-1228, 1994.

[32] K. A. Shore and M. W. McCall, "Nonlinear and quantum optics in semiconductor lasers," *Progress in Quantum Electronics*, vol. 14, pp. 63–129, 1990.

[33] M. Osinski and J. Buus, "Linewidth broadening factor in semiconductor lasers – an overview," *IEEE J. Quantum Electron.*, vol. QE-23, pp. 9–29, 1987.

[34] I. Middlemast, J. Sarma, K. A. Shore, A. I. Kucharska, E. D. Fletcher, and P. Blood, "Absorptive bistability in inhomogeneously pumped quantum well laser diodes," *IEE Proc. Part J*, vol. 138, pp. 301–308, 1991.

[35] A. P. Bogatov, P. G. Eliseev, and B. N. Sverdlov, "Anomalous interaction of spectral modes in semiconductor laser," *IEEE J. Quantum Electron.*, vol. QE-11, pp. 510–515, 1975.

[36] M. Yamada, "Theoretical analysis of nonlinear optical phenomena taking into account the beating vibration of the electron density in semiconductor lasers," *J. Appl. Phys.*, vol. 66, pp. 81–89, 1989.

[37] S. Kawanishi, T. Morioka, O. Kamatani, H. Takara, J. M. Jacob and M. Saruwatari, "100 Gbit/s all-optical demultiplexing using four-wave mixing in a travelling wave laser diode amplifier," *Electron. Lett.*, vol. 30, pp. 981–982, 1994.

[38] M. Jinno, J. B. Schlager, and D. L. Franzen, "Optical sampling using non-degenerate four-wave mixing in a semiconductor laser amplifier," *Electron. Lett.*, vol. 30, pp. 1489–1491, 1994,

[39] S. Watanabe and T. Chikama, "Cancellation of four-wave mixing in multi-channel fibre transmission by midway optical phase conjugation," *Electron. Lett.*, vol. 30, pp. 1156–1157, 1994.

Chapter 5

Optical Frequency Conversion and Tuning in Two-Section Laser Diodes

5.1 Introduction

All-optical frequency converters and electronically frequency tunable laser sources are expected to be key components for future optical coherent multicarrier transmission systems, as well as for optical computing and optical signal processing applications. In dense wavelength-division-multiplexed (WDM) switching networks (for example, interconnection of local area networks), network and system oriented functions such as routing, switching, and service segregation are performed on the basis of the wavelength (or frequency) of the optical carrier [1, 2]. In such a system, the role of the frequency converter is to transform the incoming data signal at a given optical carrier frequency into an image signal at a different carrier frequency. At the transmitter and the receiver ends of the system, monolithically integrated, electronically wavelength tunable laser diodes are needed for a variety of applications, such as frequency modulation (FM) of lasers and local oscillator tuning for coherent detection schemes.

The most straight forward way for effecting optical frequency conversion is *optoelectronic* conversion using a heterodyne receiver and an optical transmitter. Several techniques have been proposed and demonstrated to perform *all-optical* frequency conversion, for example,

- nearly degenerate four-wave mixing (NDFWM) in laser diodes [3]–[5] and laser amplifiers [6]–[9],
- cavity-enhanced highly nondegenerate FWM in laser diodes [10]–[13], and highly nondegenerate FWM in laser amplifiers [14]–[18],
- saturable absorption in bistable multisection distributed feedback (DFB) lasers [19]–[21] and distributed Bragg-reflector (DBR) lasers [22]–[24],
- nonlinear gain saturation effect in laser amplifiers [25]–[27] and DBR lasers [28], and
- optically-controlled refractive index change in laser diodes [29] and laser amplifiers [30] utilizing Mach-Zehnder interferometer.

In particular, all-optical frequency conversion based on NDFWM in laser diodes and laser amplifiers has been widely studied and shown to be very promising [3]–[9] for use in optical coherent multicarrier communication systems.

On the other hand, wavelength tuning in semiconductor lasers can be achieved by varying the injected carrier density in the active region through variation of the bias current. Variation of carrier density induces a change in both the refractive index and the gain of the active region; the change in refractive index is attributed to the carrier-induced shift of the absorption edge and the plasma resonance frequency, whereas changes of the carrier inversion populations affect

the gain. A change in the refractive index of the laser gain medium shifts the cavity resonance wavelengths.

In a conventional single-electrode laser diode biased above threshold, the modal gain is approximately clamped, save for the spontaneous emission, at a value determined by the cavity losses. Consequently, the electron density is clamped at its lasing threshold value, resulting in a limited wavelength tuning range in a single-electrode laser diode. Multi-electrode laser diodes have been extensively studied recently as wavelength tunable optical transmitters because of the ability to vary the electron density distribution in the laser cavity, and hence the lasing wavelength, over a relatively large range by inhomogeneous pumping. Several reports have concentrated on the use of multi-electrode DFB [31] or DBR [32] laser diodes as wavelength tunable laser sources. On the other hand, there has also been some effort in developing a much simpler device, the two-section single-cavity (TSSC) Fabry-Perot (FP) laser diode, as a wavelength tunable optical transmitter [33, 34]. The potential of the TSSC FP laser diode as a single longitudinal mode, wavelength tunable laser source suitable for high density WDM transmission systems has been experimentally demonstrated in recent studies by Chawki *et al.* [35, 36]. Furthermore, it was proposed that the 'gain-lever' effect [37], based on the highly sublinear optical gain versus carrier density characteristics of quantum wells (QW's) and gain clamping above lasing threshold, can substantially enhance the wavelength tunability of two-section laser diodes [38].

In the previous chapter, a model for cavity-enhanced NDFWM in above-threshold laser diodes has been described. The model takes into account the longitudinal variations of the nonlinear wave-mixing interaction and the gain distribution, and thus has a wide applicability. The model can, in particular, be used to study the all-optical frequency conversion characteristics by NDFWM of

laser diodes with asymmetric facet reflectivities and other longitudinal structural variations. In this chapter, the NDFWM model is extended and used to investigate the frequency conversion characteristics of asymmetric laser diodes with two active sections. In addition, a travelling-wave formulation is developed to investigate the wavelength tuning characteristics of a two-section, gain-levered Fabry-Perot QW laser diode, taking into account the longitudinal variations of the carrier and the photon densities in the laser cavity. The piece-wise constant inversion population (PCIP) model introduced in the previous chapter is used in the numerical solution of the photon and the carrier density conservation equations to obtain the wavelength tuning characteristics of a TSSC gain-levered QW laser diode.

5.2 All-Optical Frequency Conversion using NDFWM

5.2.1 Introduction

A conceptual model of all-optical frequency conversion using FWM in laser diodes and semiconductor laser amplifiers is depicted in Fig. 5.1. In the case of a laser diode biased above threshold, the intracavity pump signal P0 at angular frequency ω_0 is provided by the laser field, whereas for a laser amplifier, a high power external pump source is used. An optical data signal S1 at a probe carrier frequency ω_1 is injected into the laser diode or laser amplifier. A frequency-converted replica of the injected data signal is generated by FWM at the conjugate carrier frequency $\omega_2 = 2\omega_0 - \omega_1$ [8]. The data signal is thus converted from a carrier frequency ω_1 to a different carrier frequency ω_2, with a conversion bandwidth of 2Ω, where $\Omega = \omega_1 - \omega_0$ is the frequency detuning between the pump and the probe waves.

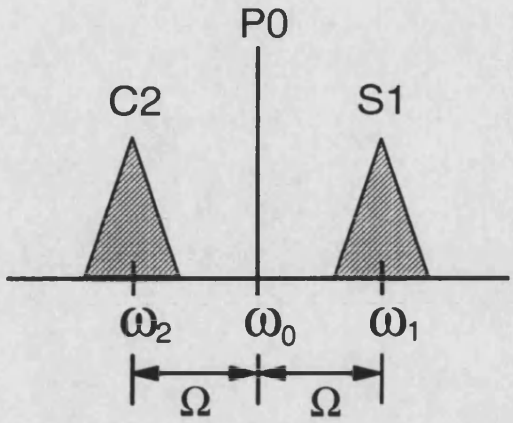

Figure 5.1: Conceptual model of all-optical frequency conversion using FWM in laser diodes and laser amplifiers. C2 is the spectrum of the frequency-converted replica of the input data S1, generated via NDFWM interaction.

Broadband optical frequency conversion can be realized using cavity-enhanced highly nondegenerate FWM in laser diodes [10]–[13] or highly nondegenerate FWM in laser amplifiers [14]–[18]. Cavity-enhanced highly nondegenerate FWM refers to wave-mixing interaction in Fabry-Perot cavities in which each of the pump, probe and conjugate waves coincides with a cavity mode. The physical mechanism giving rise to highly nondegenerate FWM is nonlinear gain saturation [39] with an effective characteristic time of 0.1–1.0 ps. Based on this ultrafast optical nonlinearity, optical frequency conversion with bandwidth of a few terahertz (10^{12} Hz) can be achieved using highly nondegenerate FWM.

On the other hand, optical frequency conversion using nearly degenerate four-wave mixing (NDFWM) is suitable for the application of dense frequency-domain multiple access systems. In this respect, NDFWM in laser diodes biased above threshold [3]–[5] is of particular interest because very high frequency conversion efficiencies (or conjugate reflectivities) of order 30–40 dB [40] can be achieved owing to the combined effects of optical gain and resonant cavity feedback. Fur-

thermore, the effective frequency conversion bandwidth using NDFWM in a laser diode is determined mainly by the laser's relaxation oscillation frequency, and highly efficient frequency conversion with bandwidth of up to 30 GHz can be achieved by biasing the laser diode well above threshold [3]. In contrast, a conversion efficiency of up to 8.3 dB and a maximum conversion bandwidth of 12 GHz were reported in the case of NDFWM in a travelling-wave amplifier [7].

Because the NDFWM process is effected by the dynamic modulation of carrier density in the laser cavity, it is of interest to investigate the influence of longitudinal nonuniformity of carrier density resulting from inhomogeneous pumping on the NDFWM efficiency. In this section, all-optical frequency conversion using NDFWM in two-section single-cavity laser diodes with asymmetric facet reflectivities is studied theoretically. It is demonstrated that, under appropriate biasing conditions, a two-section laser device exhibits a uniform frequency conversion efficiency response over a frequency detuning range of more than 10 GHz. Enhancement of frequency conversion bandwidth and efficiency can simultaneously be achieved by injecting the probe signal at and deriving the conjugate output from the low-reflectivity facet of an asymmetric two-section laser diode.

5.2.2 Frequency Conversion in a Two-Section Laser Diode

A schematic diagram of a two-section laser diode is shown in Fig. 5.2. h is the fraction of the total laser cavity length occupied by section a, and is chosen here to be $h = 0.2$. The two active sections are pumped differently with injection current densities J_a and J_b, respectively, which are normalized to the current density at transparency, J_0. The laser is assumed to oscillate in a single transverse and longitudinal mode providing the intracavity pump wave at frequency ω_0. A collinear probe wave at frequency ω_1 is injected into the pumped laser through

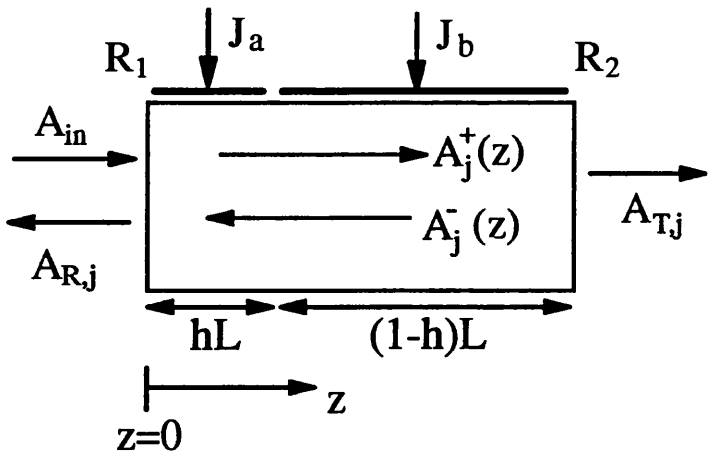

Figure 5.2: Schematic diagram of a two-section single-cavity laser diode for optical frequency conversion using NDFWM. The subscript $j = 0, 1, 2$ corresponds to the pump, the probe and the conjugate waves, respectively.

the front facet with power facet reflectivity R_1 at $z = 0$. The mixing of the intracavity waves modulates the carrier density at the beat frequency Ω and generates a conjugate wave at frequency ω_2 through NDFWM.

The nonlinear interaction of the intracavity normalized complex slowly-varying fields, $A_j^+(z)$ and $A_j^-(z)$, along the cavity axis z is described by the coupled-wave equations as given in Sec. 4.2 of the previous chapter. The subscript $j = 0, 1, 2$ corresponds to the pump, the probe and the conjugate waves, respectively. The coupled-wave equations are solved numerically subject to the boundary conditions at the two laser facets. The numerical solution technique and laser parameter values are as given in the previous chapter.

The frequency conversion efficiency (or conjugate reflectivity) is defined as the ratio of the conjugate wave output power from the front facet (at $z = 0$) to the probe injection power at the same facet, ie.,

$$R_c = \left| \frac{A_{R,2}}{A_{in}} \right|^2 . \tag{5.1}$$

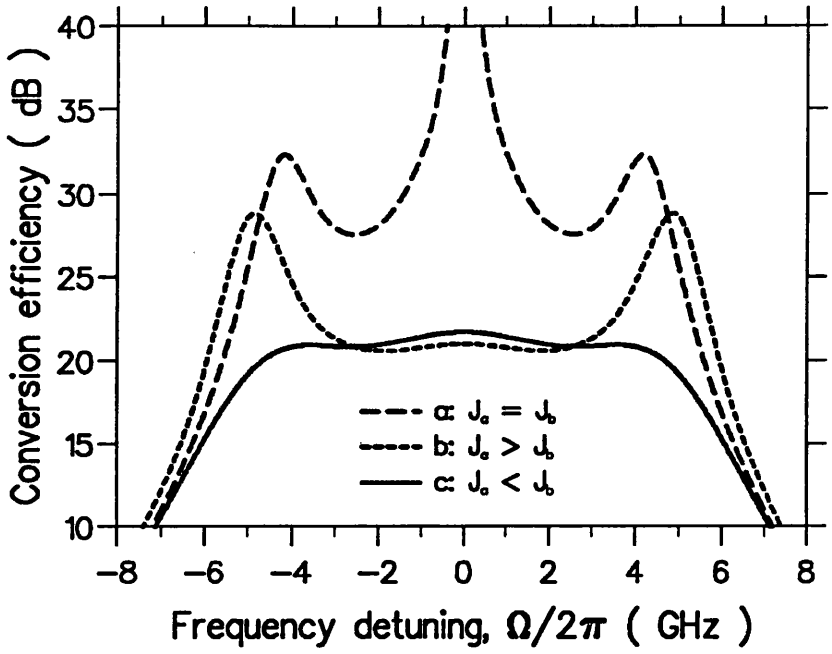

Figure 5.3: Frequency conversion efficiency versus frequency detuning for three different biasing conditions of a symmetric laser diode with $R_1 = R_2 = 0.3$.

The effective frequency conversion bandwidth is defined as the frequency range in which the frequency conversion efficiency is positive (ie., with positive gain over the input probe power).

5.2.3 Frequency Conversion Characteristics of Symmetric Two-Section Laser Diodes

Fig. 5.3 shows the frequency conversion efficiency versus frequency detuning curves for three different current pumping conditions of a symmetric laser diode with $R_1 = R_2 = 0.3$. Curve (a) corresponds to homogeneous pumping with $J_a = J_b = 2.20$. Curves (b) and (c) correspond to $J_a = 2.25$, $J_b = 2.19$ and $J_a = 2.15$, $J_b = 2.21$, respectively. In all the cases the pump output power per-facet is the same at $P_{out} = 7.73$ mW.

It is observed from Fig. 5.3 that the frequency conversion efficiency versus frequency detuning curve is symmetrical with respect to zero frequency detuning. When the two sections are biased at different injection current levels (curves (b) and (c)), the conversion efficiency decreases. Because of the carrier-induced refractive index change, the nonuniform distribution of carrier density between the two sections resulting from inhomogeneous pumping induces different phase shifts when the intracavity fields propagate through the device. The phase mismatch inhibits injection-locking around zero frequency detuning for small probe injection power (which, in accordance with Ref. [41], is assumed to be 0.02 μW in the present analysis) when the two sections are pumped differently.

It is also observed that the resonant peaks of the conversion efficiency near the relaxation oscillation frequency is enhanced when the probe injection is incident at the higher gain section (curve (b)) whereas the resonant peaks are highly damped when the probe injection is incident at the lower gain section (curve (c)). A uniform frequency conversion efficiency response can thus be obtained using a two-section laser diode with the probe injection incident at the low-gain section. The uniform conversion efficiency over a frequency detuning range of more than 10 GHz as revealed by the present analysis is important for distortionless frequency conversion of wide-band signals. It should however be pointed out that only slightly inhomogeneous current pumping is considered in our analysis. When the two sections are pumped with highly different currents, the wavelength dependence of the gain in the two sections may need to be taken into account.

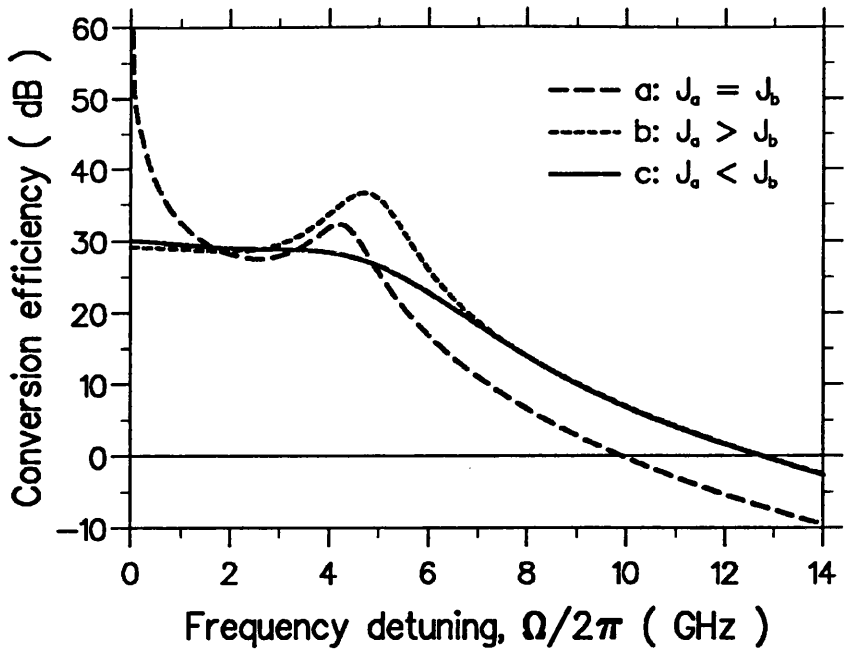

Figure 5.4: Frequency conversion efficiency versus frequency detuning curves. Curve (a) is for a symmetric laser diode, whereas curves (b) and (c) are obtained for a asymmetric laser diode with $R_1 = 0.1$ and $R_2 = 0.9$. Current injection condition for each curve is the same as the corresponding curve in Fig. 5.3.

5.2.4 Frequency Conversion Characteristics of Asymmetric Two-Section Laser Diodes

Fig. 5.4 shows the frequency conversion efficiency versus frequency detuning curves with the same corresponding biasing conditions for curves (a), (b) and (c) as in Fig. 5.3. However, curve (a) is obtained for a symmetric laser with $R_1 = R_2 = 0.3$, as in Fig. 5.3, but curves (b) and (c) are obtained for a asymmetric laser diode with $R_1 = 0.1$ and $R_2 = 0.9$. Note that the product R_1R_2, and hence the threshold gain are the same in all three cases.

By comparing curves (b) and (c) from Fig. 5.3 and Fig. 5.4, it is found that frequency conversion efficiency enhancements of 7–8 dB can be obtained using asymmetric-facet laser diodes rather than symmetric laser diodes. In addition, frequency conversion bandwidth is also enhanced from 20 GHz in a symmetric

laser to 26 GHz in a asymmetric laser diode. Higher conversion bandwidth is possible by biasing the laser diodes with higher injection currents above threshold.

It is therefore established that the frequency conversion bandwidth in laser diodes is dependent not only on spontaneous carrier lifetime and relaxation oscillation frequency as has previously been reported [41], but also on the facet reflectivities of the laser diodes. The present analysis demonstrated that a uniform conversion efficiency response could be obtained in a two-section laser diode by injecting the data (probe) signal at the low-gain section. Enhancement of frequency conversion bandwidth and efficiency can simultaneously be achieved by applying anti-reflection (AR) coating to the input facet at the low-gain section, and deriving the conjugate output from the same facet of a asymmetric two-section laser diode. Utilizing the flat frequency conversion efficiency response in an inhomogeneously-pumped and asymmetric-facet laser diode, highly efficient optical frequency conversion (with approximately 30 dB amplification over the probe input power) of wide-band (few Gbit/s) signals could be achieved without pattern distortion which may otherwise arise because of the peak and trough in the conversion efficiency response typical of single-electrode laser diodes. The experimental verification of these predictions would appear to be a worthwhile tests.

5.3 Wavelength Tuning in Two-Section Laser Diodes

5.3.1 Introduction

Monolithically integrated, electronically tunable laser diodes are essential components for future coherent and high density multiple access WDM communication

systems. In particular, two-section single-cavity (TSSC) Fabry-Perot (FP) laser diodes are very attractive as wavelength tunable optical transmitters [33, 34] because of their much simpler device structures as compared to multielectrode DFB or DBR lasers [31, 32]. Recently, single-longitudinal-mode TSSC FP laser diodes (with 20 dB side-mode suppression ratios) have been developed [35] and their potential as wavelength tunable optical transmitters has been demonstrated in a 1.5 Gbit/s FSK transmission experiment by Chawki *et al.* [36].

Previous studies of TSSC FP laser diodes as wavelength tunable optical sources [33, 34] have used average values of carrier and photon densities in each of the two separately-pumped sections of the laser devices. In this section, a formulation is developed to investigate the wavelength tuning characteristics of a TSSC FP gain-levered QW laser diode, taking into account longitudinal variations of the carrier and the photon densities in the laser cavity. The model can, in particular, be used to study the wavelength tunability of laser diodes with low and/or asymmetric facet reflectivities, in which case the carrier and the photon density distributions are highly nonuniform along the laser longitudinal axis. It will be shown using the present formulation that the carrier and the photon densities are highly nonuniform even within each of the two separately-pumped active sections, especially for a asymmetric laser diode. As a result of these longitudinal inhomogeneities, it is demonstrated that, depending on the biasing conditions of the two active sections, asymmetric laser diodes exhibit an enhancement or reduction of wavelength tunability compared to that of symmetric lasers.

Fig. 5.5 shows a schematic two-section laser structure together with a optical gain versus carrier density curve typical of QW material. The fractional length of the sections is devised to optimize the tuning range of gain-levered QW laser diodes in accordance with Ref. [38] such that $h = 0.7$. When, as shown in Fig. 5.5,

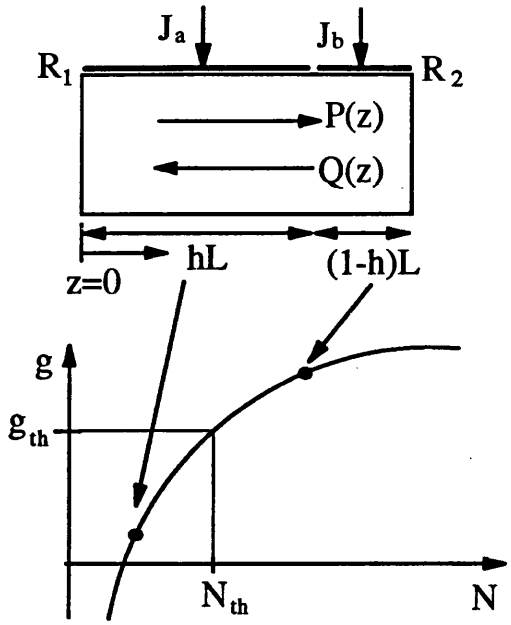

Figure 5.5: Schematic diagram of a two-section laser diode together with a gain versus carrier density curve typical of QW material. g_{th} and N_{th} are the threshold gain and threshold carrier density, respectively. R_1 and R_2 are the front and the rear facet power reflectivities of the laser, respectively.

the two sections are biased above transparency the overall modal gain is approximately clamped at a value determined by the cavity losses. This means that changes in the gain associated with one section of the device must be compensated by an equal and opposite change in the gain of the other section. Because of the highly sublinear nature of the gain versus carrier density characteristic of the quantum wells, a small change in carrier density in the low-gain section will lead to a much larger swing in carrier density in the high-gain section, so as to satisfy the gain clamping condition. The large change in average carrier density produced by this 'gain-lever' effect [37] causes a large change in the refractive index of the FP cavity, thereby shifting the lasing wavelength of the laser device.

5.3.2 Formulation

A Fabry-Perot approach incorporating the counter-travelling photon fluxes in the laser cavity is used to determine the lasing wavelength and the output power. Since the phase-coupling interaction of the intracavity travelling waves is not required here (in contrary to the case of FWM as discussed in the previous chapter), it is numerically simpler to deal with photon fluxes (per unit area per unit time) rather than optical fields. Note, however, that the phase information needed to calculate the FP resonance wavelengths is retained in the present model, as will be explained in the following paragraphs. To solve for the photon and the carrier densities, an iterative method based on the piecewise constant inversion population (PCIP) model as described in the previous chapter is used.

The photon conservation equations for the counter-travelling fluxes can be written as

$$\frac{dP}{dz} = G(N)P + \frac{1}{2}\beta R_{sp}(N) , \tag{5.2}$$

$$\frac{dQ}{dz} = -G(N)Q - \frac{1}{2}\beta R_{sp}(N) , \tag{5.3}$$

where $P(z)$ and $Q(z)$ are the forward $(+z)$ and backward $(-z)$ travelling photon fluxes, respectively, and $G(N) = \Gamma g(N) - \alpha_{int}$. A sublinear peak gain of the form [42]

$$g(N) = g_{N1} \ln\left(\frac{N}{N_0}\right) , \tag{5.4}$$

and a bimolecular recombination $R_{sp} = B_r N^2$, which are appropriate for QW structures [38] are assumed in the analysis. The photon density $S(z)$ (per unit volume) is obtained by the superposition of the two travelling fluxes:

$$S(z) = [P(z) + Q(z)]/v_g . \tag{5.5}$$

The description of symbols and parameter values are listed in table 5.1.

Parameter	Symbol	Value	Unit
Spontaneous emission factor	β	10^{-4}	
Effective mode confinement factor	Γ	0.06	
Effective internal loss	α_{int}	500	m^{-1}
Gain coefficient	g_{N1}	1.5×10^5	m^{-1}
Transparency carrier density	N_0	1.5×10^{24}	m^{-3}
Bimolecular recombination coefficient	B_r	10^{-16}	m^3s^{-1}
Group velocity	v_g	8.1×10^7	ms^{-1}
Laser cavity length	L	300	μm
Differential refractive index	$\delta n/\delta N$	8.0×10^{-27}	m^3
Effective refractive index	$\overline{n}$	3.21	

Table 5.1: List of symbol definitions and parameter values

In the PCIP model, the carrier density, N_m, in the m-th segment within $z = Z_m$ and $z = Z_{m+1}$ is assumed constant. Therefore, Eqs. (5.2) and (5.3) have analytical solutions of the form

$$P(z) = P(Z_m)\ \exp[G_m(z - Z_m)] + \frac{\beta R_{sp,m}}{2G_m}\ \{\exp[G_m(z - Z_m)] - 1\ \}, \quad (5.6)$$

$$Q(z) = Q(Z_m)\ \exp[-G_m(z - Z_m)] + \frac{\beta R_{sp,m}}{2G_m}\ \{\exp[-G_m(z - Z_m)] - 1\ \} \quad (5.7)$$

The continuity of $P(z)$ and $Q(z)$ in each segment boundary is enforced, whereas their derivitives may be discontinuous.

The carrier conservation equation is written in the form

$$\frac{J}{ed} = g_m(\overline{P}_m + \overline{Q}_m) + R_{sp,m}\ , \quad (5.8)$$

where e is the electronic charge, d is the total well thickness, $\overline{P}_m$ and $\overline{Q}_m$ are the average values for the $+z$ and $-z$ travelling photon fluxes in the m-th segment, respectively. The average value $\overline{P}_m$ is defined as

$$\begin{aligned}\overline{P}_m &= \frac{1}{\Delta L}\int_{Z_m}^{Z_{m+1}} P(z)\ dz \\ &= \frac{P(Z_m) + \zeta_m}{G_m\,\Delta L}[\exp(G_m\,\Delta L) - 1] - \zeta_m\ , \end{aligned} \quad (5.9)$$

where $\Delta L = L/M$ is the segment width, $\zeta_m = \beta R_{sp,m}/(2G_m)$, and $\overline{Q}_m$ is similarly defined. $M = 60$ is the total number of segments in the PCIP model.

Eqs. (5.6)–(5.9) are then solved self-consistently subject to the boundary conditions at the two laser facets:

$$P(z = 0) = R_1\, Q(z = 0)\,, \tag{5.10}$$

$$Q(z = L) = R_2\, P(z = L)\,. \tag{5.11}$$

Using the PCIP model, the computational algorithm proceeds as described in the previous chapter.

Because we are interested mainly in the effects of longitudinal variations of carrier density on wavelength tuning characteristics of one lasing mode, only single longitudinal mode operation is considered in the present study. Multi-longitudinal mode operation can be extended in the PCIP model in a straight forward way as in Ref. [43], but at the expense of significant increase in computation time.

The lasing wavelength, λ, of the laser device is obtained from the Fabry-Perot phase-closure condition as given by

$$k\frac{\lambda}{2} = \frac{L}{M}\sum_{i=1}^{M} n_i\ , \tag{5.12}$$

where k is an integer and n is the refractive index, which is dependent on the carrier density, N in the form

$$n = \overline{n} - \frac{\delta n}{\delta N}N\,. \tag{5.13}$$

The above two expressions account for wavelength tuning resulting from the carrier-dependent refractive index change, $\delta n/\delta N$, which is unique for semiconductor lasers.

The above analysis recognizes the laser device as a FP resonator containing an active amplifying medium. The effects of the resonant cavity, and thus the phase information required for the calculation of the lasing wavelength, are accommodated in the analysis through the boundary conditions at the laser facets and the phase-closure condition.

In the following, analysis is carried out for InGaAs–InGaAsP separate- confinement heterostructure multi-quantum well (SCH-MQW) laser diodes with four QW's and well width of 80 Å for operation at 1.55 μm wavelength. Other parameter values are given in table 5.1.

5.3.3 Nonuniform Carrier and Photon Density Distributions in Two-Section Laser Diodes

To illustrate the degree of longitudinal non-uniformity, the carrier and the photon density distributions along the z axis are plotted in Figs. 5.6(a) and 5.6(b), respectively, for three laser devices with different front facet reflectivities. The product $R_1R_2 = 0.09$, is the same for all three devices. The two active sections are biased such that $J_a = 2$ kA/cm^2 and $J_b = 5$ kA/cm^2, respectively. It is noted that the constant carrier density in each segment is defined only within the segment and is left unspecified at the segment boundaries in the PCIP model. Consequently, the carrier density curves in Fig. 5.6(a) are obtained by plotting and connecting the carrier density at the centre point of each segment.

It is observed in Figs. 5.6(a) and 5.6(b) that the carrier and the photon densities are significantly nonuniform along the laser cavity, especially for laser diodes with asymmetric facet reflectivities. It is also noted that the carrier density distribution within the high-gain section is particularly nonuniform, thus showing the importance of incorporating longitudinal variations of carrier density even within

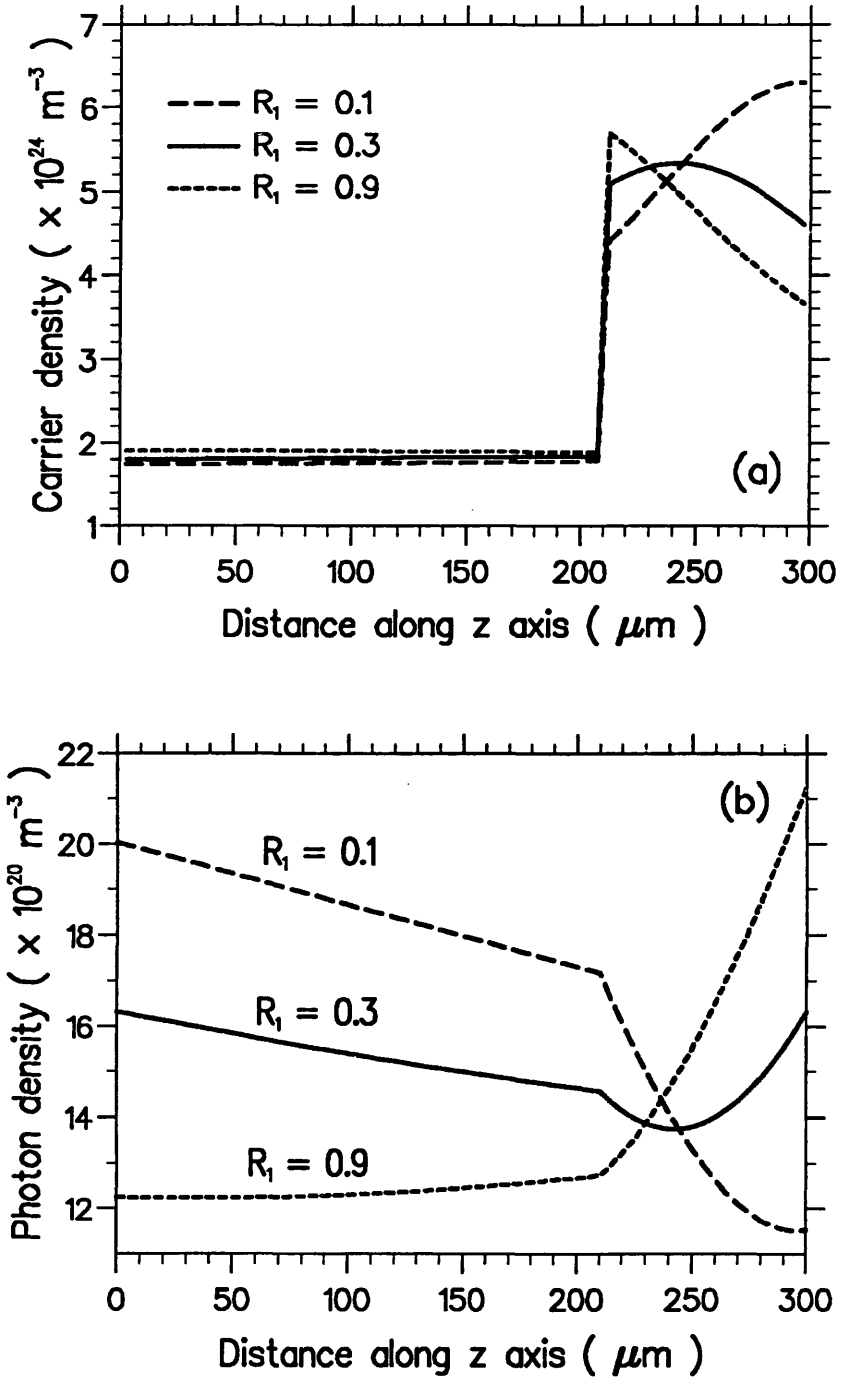

Figure 5.6: (a) Carrier density and (b) photon density distributions along the z axis in two-section laser diodes with different front facet reflectivities. $R_1 R_2 = 0.09$.

the two separately-pumped active sections. More importantly, the carrier density distribution is significantly different among the three laser devices, especially in the high-gain section. In as much as it is the average change in electron density along the length of the cavity that gives rise to the lasing wavelength shift, it is to be expected that such differences in the electron density profiles will affect the wavelength tunability characteristics of the three laser devices considered here.

Carrier diffusion effects would be expected to modify the longitudinal variation of the carriers, particularly near the interface between the two active sections. However, with typical diffusion lengths of the order of a few microns, the modification of the carrier profile would not be expected to be substantial. In consequence, it is expected that the present model will give quite accurate predictions of both qualitative and quantitative response of the laser devices.

5.3.4 Wavelength Tuning Characteristics of Two-Section Laser Diodes

To determine the relation between device configuration and wavelength tunability, the average electron density, $\overline{N}$, versus injection current, J_a, is shown in Fig. 5.7 for three laser devices with different front facet reflectivities. In each case, as J_a is varied, the injection current into the second section, J_b, is changed simultaneously so that the total output power remains constant – chosen here to be 1.2 mW. When J_a is set at a level just above transparency, represented by the left hand limit of the curves, $\overline{N}$ is at the maximum. $\overline{N}$ decreases as J_a is increased above transparency. The minimum $\overline{N}$ occurs when $J_a \approx J_b$. $\overline{N}$ starts to increase again when $J_a > J_b$. It is thus concluded that a larger change in average electron density (slope of the curves in Fig. 5.7) can be obtained with a inhomogeneously-pumped (two-section) laser diode compared to a uniformly-pumped laser (where

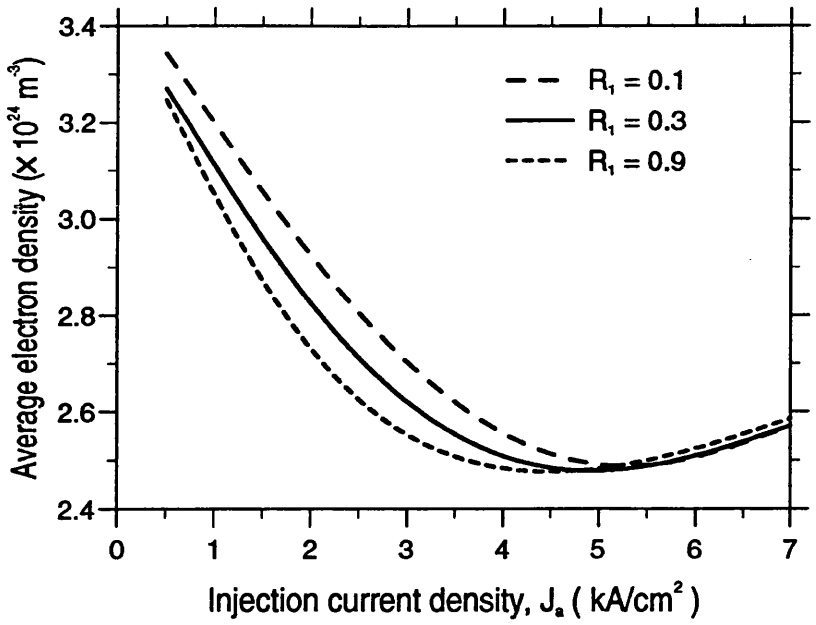

Figure 5.7: Average electron density in the laser cavity as a function of injection current density, J_a. $R_1R_2 = 0.09$ in all cases.

the gradient of the curves is zero at $J_a \approx J_b$).

Furthermore, it is observed that an increase in the average electron density can be obtained in a asymmetric laser, compared to a symmetric laser ($R_1 = R_2$), if the facet at the low-gain section is anti-reflection (AR) coated; whereas a reduction in $\overline{N}$ results if the facet at the low-gain section is high-reflection (HR) coated. This observation can be explained in a physically intuitive way as follows. It is recalled that the gain-lever effect relies on the different gains associated with differing carrier densities in the two sections of the device. The use of asymmetric-facet structures can result in an enhanced gain-lever effect when the difference between the carrier densities in the two sections is increased. Conversely, a reduced gain-lever effect will be obtained if the carrier density difference is decreased. An increase in carrier density difference is obtained when the facet at the low-gain section is AR coated and the facet at the high-gain

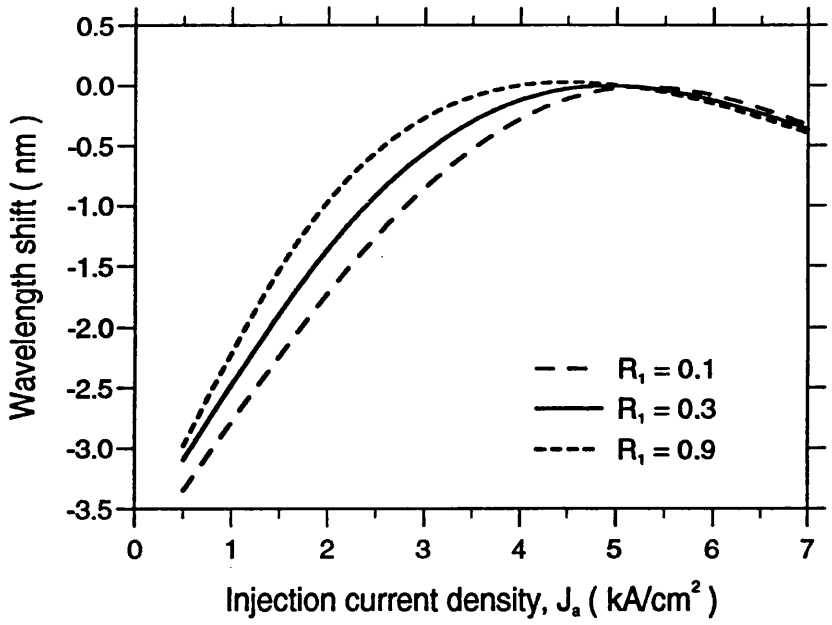

Figure 5.8: Wavelength shift relative to the wavelength at $J_a = J_b$, as a function of injection current density, J_a.

section is HR coated. Then because of the nonuniform photon distribution in the asymmetric cavity, the low-gain carrier density is decreased whilst the high-gain carrier density is increased. An enhanced gain-lever effect is thus obtained. Similarly, a reduced gain-lever effect is found when the low-gain facet is HR coated and the high-gain facet is AR coated.

As a result of the change in average electron density arising from inhomogeneous pumping of a two-section gain-levered laser diode, the lasing wavelength is shifted from that of the case when the laser is uniformly pumped. Fig. 5.8 shows the wavelength shift relative to the wavelength at $J_a = J_b = 5$ kA/cm^2, obtained with identical parameters as in Fig. 5.7. The negative wavelength shift in Fig. 5.8 is due to the fact that an increase in $\overline{N}$ because of inhomogeneous pumping of the laser device causes a decrease in the refractive index, thereby blue-shifted (to shorter wavelength) the lasing wavelength from that of the uniformly-pumped

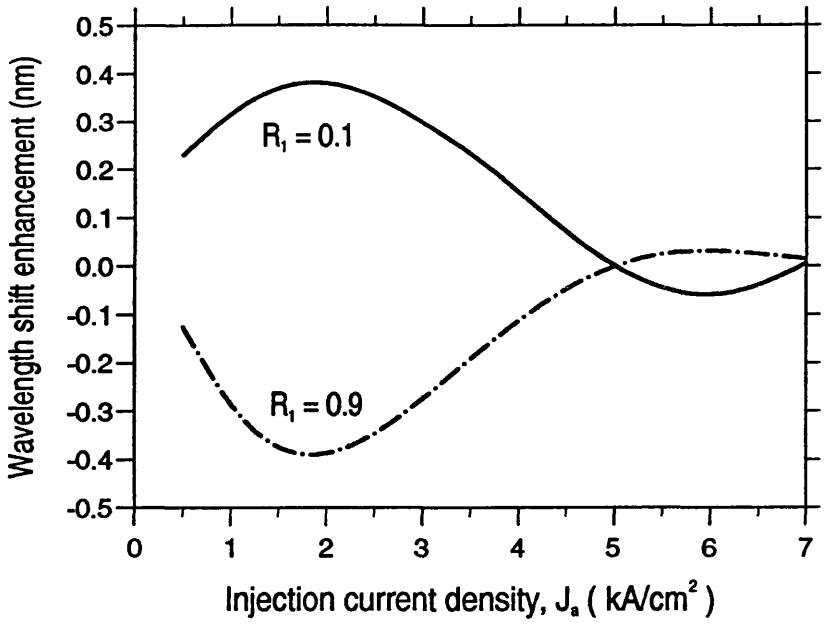

Figure 5.9: Wavelength shift enhancement of asymmetric two-section laser diodes over the symmetric laser.

case. Since the average electron density change is different in the three laser devices considered here, it is as expected to note that significant differences exist in the wavelength shift among the three laser devices.

5.3.5 Enhanced Wavelength Tunability in Asymmetric Two-Section Laser Diodes

To see how the facet coating influences the wavelength tunability, the difference in wavelength shift of the asymmetric lasers over that of the symmetric case ($R_1 = R_2 = 0.3$) is shown in Fig. 5.9. For $J_a < J_b$, enhancement of wavelength shift relative to the symmetric laser can be obtained in the laser diode with $R_1 = 0.1$ and $R_2 = 0.9$, whereas reduction of wavelength shift (negative enhancement) is obtained in the laser with $R_1 = 0.9$ and $R_2 = 0.1$. The reverse is true for $J_a > J_b$, with a cross-over between the curves at $J_a = J_b = 5$ kA/cm^2, at which point the relative wavelength shift is zero for all three laser devices (as in Fig. 5.8).

It has thus been demonstrated that enhancement of wavelength shift can be achieved in a asymmetric two-section gain-levered QW laser diode by AR coating the facet at the low-gain section and HR coating the facet at the high-gain section. A maximum wavelength shift enhancement of about 4 Å can be obtained in asymmetric gain-levered QW laser diodes. Experimental investigations of such devices will therefore be of some considerable interest with a view to taking advantage of the enhanced wavelength tunability for utilization in wavelength tunable laser sources. The ability to vary the average electron density over a large range in a asymmetric gain-levered QW laser may also result in an enhanced frequency modulation (FM) response, making it suitable for use as a FM optical transmitter.

5.4 Conclusion

All-optical frequency conversion using NDFWM in two-section single-mode laser diodes with asymmetric facet reflectivities has been studied theoretically based on a travelling-wave coupled-mode formalism. An important feature of the coupled-mode analysis of NDFWM in the spatial domain is that it allows comparisons to be made of optical probe injection into either section of a two-section laser, and/or into either facet of a asymmetric laser. This would not be possible in models which used the mean field approximation [3]–[5], [41]. In particular, the present analysis demonstrated that

- a uniform frequency conversion efficiency can be obtained over a frequency detuning range of more than 10 GHz by injecting the probe signal into the low-gain section of a two-section laser diode, and

- enhancement of frequency conversion bandwidth and efficiency can simultaneously be achieved by applying anti-reflection (AR) coating to the input facet at the low-gain section, and deriving the converted conjugate output from the same facet of a asymmetric two-section laser diode.

It is also pointed out that the uniform conversion efficiency response can be utilized in distortionless optical frequency conversion of wide-band signals.

A theoretical model has also been developed to study the wavelength tuning characteristics of asymmetric gain-levered FP QW laser diodes, which takes into account longitudinal variations of the photon and the carrier density distributions in the laser cavity. The carrier density has been shown to be highly nonuniform even within the two separately-pumped active sections, thus justifying the need to incorporate longitudinal variations of carrier density in the model. The present analysis demonstrated that enhancement of wavelength tunability could be achieved in a asymmetric laser diode over that of a symmetric laser by applying AR coating to the facet at the low-gain section and applying high-reflection (HR) coating to the facet at the high-gain section.

References

[1] G. Grosskopf, L. Kuller, R. Ludwig, R. Schnabel, and H. G. Weber, "Semiconductor laser optical amplifiers in switching and distribution networks," *Opt. Quantum Electron.*, vol. 21, pp. S59–S74, 1989.

[2] C. A. Brackett, "Dense wavelength division multiplexing networks: principles and applications," *IEEE J. Selected Areas in Communications*, vol. 8, pp. 948–964, 1990.

[3] R. Hui, S. Benedetto, and I. Montrosset, "Optical frequency conversion using nearly degenerate four-wave mixing in a distributed feedback semiconductor laser: theory and experiment," *J. Lightwave Technol.*, vol. 11, pp. 2026–2032, 1993.

[4] L. Li and K. Petermann, "Characteristics of optical frequency conversion in a semiconductor laser," *IEEE J. Quantum Electron.*, vol. 29, pp. 2793–2798, 1993.

[5] L. Li and K. Petermann, "Small-signal analysis of optical frequency conversion in an injection-locked semiconductor laser," *IEEE J. Quantum Electron.*, pp. 43–48, 1994.

[6] G. Grosskopf, R. Ludwig, and H. G. Weber, "140 Mbit/s DPSK transmission using an all-optical frequency convertor with a 4000 GHz conversion range," *Electron. Lett.*, vol. 24, pp. 1106–1107, 1988.

[7] T. Mukai and T. Saitoh, "Detuning characteristics and conversion efficiency of nearly degenerate four-wave mixing in a 1.5 μm traveling-wave semiconductor laser amplifier," *IEEE J. Quantum Electron.*, vol. 26, pp. 865–874, 1990.

[8] N. Schunk, G. Grosskopf, R. Ludwig, R. Schnabel, and H. G. Weber, "Frequency conversion by nearly-degenerate four-wave mixing in travelling-wave semiconductor laser amplifiers," *IEE Proc. Part J*, vol. 137, pp. 209–214, 1990.

[9] N. Schunk, "All-optical frequency conversion in a traveling-wave semiconductor laser amplifiers," *IEEE J. Quantum Electron.*, vol. 27, pp. 1271–1279, 1991.

[10] S. Murata, A. Tomita, J. Shimizu, and A. Suzuki, "THz optical-frequency conversion of 1 Gb/s signals using highly nondegenerate four-wave mixing in an InGaAsP semiconductor laser," *IEEE Photon. Technol. Lett.*, vol. 3, pp. 1021–1023, 1991.

[11] P. P. Iannone, P. R. Prucnal, G. Raybon, U. Koren, and C. A. Burrus, "Broadband wavelength shifter for picosecond optical pulses at 1.5 μm," *Electron. Lett.*, vol. 29, pp. 1518–1520, 1993.

[12] L. Li and K. Petermann, "Conversion efficiency and bandwidth of THz optical frequency conversion in a semiconductor laser," *IEE proc. Part J*, vol. 140, pp. 260–266, 1993.

[13] L. Li and K. Petermann, "Small-signal analysis of THz optical-frequency conversion in an injection-locked semiconductor laser," *IEEE J. Quantum Electron.*, vol. 29, pp. 2988–2994, 1993.

[14] R. Schnabel, W. Pieper, R. Ludwig, and H. G. Weber, "Multiterahertz frequency conversion of a picosecond pulse train using nonlinear gain dynamics in a 1.5 μm MQW semiconductor laser amplifier," *Electron. Lett.*, vol. 29, pp. 821–822, 1993.

[15] M. C. Tatham, G. Sherlock, and L. D. Westbrook, "20-nm optical wavelength conversion using nondegenerate four-wave mixing," *IEEE Photon. Technol. Lett.*, vol. 5, pp. 1303–1306, 1993.

[16] R. Schnabel, et al., "Polarization insensitive frequency conversion of a 10-channel OFDM signal using four-wave mixing in a semiconductor laser amplifier," *IEEE Photon. Technol. Lett.*, vol. 6, pp. 56–58, 1994.

[17] J. Zhou, N. Park, J. W. Dawson, K. J. Vahala, M. A. Newkirk, and B. I. Miller, "Efficiency of broadband four-wave mixing wavelength conversion using semiconductor traveling-wave amplifiers," *IEEE Photon. Technol. Lett.*, vol. 6, pp. 50–52, 1994.

[18] J. Zhou, N. Park, K. J. Vahala, M. A. Newkirk, and B. I. Miller, "Broadband wavelength conversion with amplification by four-wave mixing in semiconductor travelling-wave amplifiers," *Electron. Lett.*, vol. 30, pp. 859–860, 1994.

[19] H. Kawaguchi, K. Oe, H. Yasaka, K. Magari, M. Fukuda, and Y. Itaya, "Tunable optical-wavelength conversion using a multielectrode distributed-feedback laser diode with a saturable absorber," *Electron. Lett.*, vol. 23, pp. 1088–1090, 1987.

[20] H. Kawaguchi, K. Magari, H. Yasaka, M. Fukuda, and K. Oe, "Tunable optical-wavelength conversion using an optically triggerable multielectrode distributed feedback laser diode," *J. Quantum Electron.*, vol. 24, pp. 2153–2159, 1988.

[21] H. Tsuda, K. Nonaka, K. Hirabayashi, H. Uenohara, H. Iwamura, and T. Kurokawa, "Wide range wavelength conversion experiment using a side-injection light-controlled bistable laser diode," *Appl. Phys. Lett.*, vol. 63, pp. 3116–3118, 1993.

[22] K. Kondo, M. Kuno, S. Yamakoshi, and K. Wakao, "A tunable wavelength-conversion laser," *IEEE J. Quantum Electron.*, vol. 28, pp. 1343–1348, 1992.

[23] A. Paradisi and I. Montrosset, "Analysis of wavelength conversion using a multielectrode DBR laser with a saturable absorber," *IEEE J. Quantum Electron.*, vol. 29, pp. 1285–1294, 1993.

[24] K. Kasaya, K. Takahata, and H. Yasaka, "Optical frequency conversion device with asymmetric κ-DBR structure," *IEEE Photon. Technol. Lett.*, vol. 5, pp. 321–324, 1993.

[25] I. Valiente, J. C. Simon, and M. L. Ligne, "Theoretical analysis of semiconductor optical amplifier wavelength shifter," *Electron. Lett.*, vol. 29, pp. 502–503, 1993.

[26] C. Joergensen, T. Durhuus, C. Braagaard, B. Mikkelsen, and K. E. Stubkjaer, "4 Gb/s optical wavelength conversion using semiconductor optical amplifiers," *IEEE Photon. Technol. Lett.*, vol. 5, pp. 657–659, 1993.

[27] J. M. Wiesenfeld, B. Glance, J. S. Perino, and A. H. Gnauck, "Wavelength conversion at 10 Gb/s using a semiconductor optical amplifier," *IEEE Photon Technol. Lett.*, vol. 5, pp. 1300–1303, 1993.

[28] T. Durhuus, R. J. S. Pedersen, B. Mikkelsen, K. E. Stubkjaer, M. Oberg, and S. Nilsson, "Optical wavelength conversion over 18 nm at 2.5 Gb/s by DBR-laser," *IEEE Photon. Technol. Lett.*, vol. 5, pp. 86–88, 1993.

[29] K. Inoue and N. Takato, "Wavelength conversion for FM light using light injection induced frequency shift in DFB-LD," *Electron. Lett.*, vol. 25, pp. 1360–1361, 1989.

[30] T. Durhuus, C. Joergensen, B. Mikkelsen, R. J. S. Pedersen, and K. E. Stubkjaer, "All optical wavelength conversion by SOA's in a Mach-Zehnder configuration," *IEEE Photon. Technol. Lett.*, vol. 6, pp. 53–55, 1994.

[31] M. Kuznetsov, "Theory of wavelength tuning in two-segment distributed feedback lasers," *IEEE J. Quantum Electron.*, vol. 24, pp. 1837–1844, 1988.

[32] X. Pan, H. Olesen, and B. Tromborg, "A theoretical model of multielectrode DBR lasers," *IEEE J. Quantum Electron.*, vol. 24, pp. 2423–2432, 1988.

[33] R. F. O'Dowd and M. G. Davis, "Theoretical study of a two-section single-cavity semiconductor laser for use as a wavelength-tunable source," *Opt. Quantum Electron.*, vol. 20, pp. 383–393, 1988.

[34] J. Le Bihan, J. M. Goujon, R. Auffret, and M. J. Chawki, "Theoretical characteristics of a tunable two-electrode Fabry-Perot (TEFP) laser diode," *J. Lightwave Technol.*, vol. 10, pp. 1931–1934, 1992.

[35] M. J. Chawki, R. Auffret, D. Dumay, and L. Berthou, "Single frequency tunable two-section single-cavity buried heterostructure (TSSC-BH) laser diode," *J. Opt. Commun.*, vol. 11, pp. 63–64, 1990.

[36] M. J. Chawki, R. Auffret, L. Berthou, and L. Demeure, "1.5 Gbit/s FSK transmission system using two-electrode Fabry-Perot buried heterostructure laser," *Electron. Lett.*, vol. 27, pp. 417–418, 1991.

[37] K. J. Vahala, M. A. Newkirk, and T. R. Chen, "The optical gain lever: a novel gain mechanism in the direct modulation of quantum well semiconductor lasers," *Appl. Phys. Lett.*, vol. 54, pp. 2506–2508, 1989.

[38] K. Y. Lau, "Broad wavelength tunability in gain-levered quantum well semiconductor lasers," *Appl. Phys. Lett.*, vol. 57, pp. 2632–2634, 1990.

[39] G. P. Agrawal, "Population pulsations and nondegenerate four-wave mixing in semiconductor lasers and amplifiers," *J. Opt. Soc. America B*, vol. 5, pp. 147–158, 1988.

[40] S. Jiang and M. Dagenais, "Observation of nearly degenerate and cavity-enhanced highly nondegenerate four-wave mixing in semiconductor lasers," *Appl. Phys. Lett.*, vol. 62, pp. 2757–2759, 1993.

[41] A. Mecozzi, A. D'Ottavi, and R. Hui, "Nearly degenerate four-wave mixing in distributed feedback semiconductor lasers operating above threshold," *IEEE J. Quantum Electron.*, vol. 29, pp. 1477–1487, 1993.

[42] H. Olesen, J. I. Shim, M. Yamaguchi, and M. Kitamura, "Proposal of novel gain-levered MQW DFB lasers with high and red-shifted FM response," *IEEE Photon. Technol. Lett.*, vol. 5, pp. 599–602, 1993.

[43] I. Middlemast, J. Sarma, K. A. Shore, A. I. Kucharska, E. D. Fletcher, and P. Blood, "Absorptive bistability in inhomogeneously pumped quantum well laser diodes," *IEE Proc. Part J*, vol. 138, pp. 301–308, 1991.

Chapter 6

Intersubband Population Inversion in Coupled Quantum Well Structures

6.1 Introduction

The advent of advanced semiconductor growth techniques such as molecular beam epitaxy (MBE) and metalorganic chemical vapour deposition (MOCVD) has made possible the fabrication of novel material structures with tailored electronics and optical properties. Most notable among these are ultrathin semiconductor heterostructures such as multiple quantum wells (MQW) and superlattices. The physics and applications of these reduced-dimensionality structures [1] have been extensively studied recently in light of the possibility of developing a new generation of quantum electronic and optical devices.

The electromagnetic energy that covers the wavelength region of $\approx$ 1–1000 μm is often called *infrared radiation.* Infrared radiation is usually divided into a mid-infrared region (1–30 μm) and a far-infrared region ($>$ 30 μm). Despite great potential applications in medicine, spectroscopy, radio astronomy, space-based communications, remote sensing, and pollution monitoring, infrared wavelengths

remain among the most underdeveloped electromagnetic spectra. The lack of instrumentation in this spectral regime is mainly due to the fact that the terahertz frequency (or infrared wavelength) range falls between two other frequency ranges in which conventional semiconductor devices have been successfully employed. On the lower frequency spectra end of the infrared is the microwave and millimeter-wave frequency range, and on the higher frequency spectra end is the near-infrared and optical frequency range. Semiconductor devices which utilize the classical diffusive and drift transport of electrons, such as diodes and transistors, have a high frequency limit of a few hundred gigahertz. On the other hand, semiconductor devices based on *interband transitions*, such as laser diodes, are limited to frequencies corresponding to the semiconductor bandgap energy, which is higher than 10 THz for most bulk semiconductors. Therefore, there exists a large frequency range from 100 GHz to 10 THz in which very few solid-state devices are available.

In this and the next chapter, the feasibility of extending the stimulated emission spectra of semiconductor lasers (fabricated using III–V materials) to the infrared wavelength range is explored. The possibility of infrared laser emission utilizing *intersubband transitions* and *tunnelling* in semiconductor superlattices was first proposed more than twenty years ago by Kazarinov and Suris [2]. The report by West *et al.* of the first observation of an extremely large dipole infrared transition between quantum well (QW) subbands [3] has spurred extensive research efforts on the optical properties of semiconductor coupled QW structures and superlattices in the infrared wavelength range. *Spontaneous intersubband radiative emission* in GaAs–AlGaAs superlattices was first observed and reported by Helm *et al.* [4, 5]. Extremely large dipole infrared intersubband transitions in GaAs–AlGaAs step QW's have also been observed in an absorption spectroscopy experiment [6]. Recently, infrared photodetectors based on intersubband absorp-

tions in QW structures have been extensively studied and successfully implemented for wavelengths in the range of 4–12 μm [7, 8]. In view of the many potential applications in the infrared wavelength regime, it is of considerable interest to achieve the reverse process of coherent *stimulated intersubband radiative emission* for possible realization of infrared semiconductor lasers, fabricated using the III–V material systems such as GaAs and InGaAs because of their well developed technologies and the possibility of optoelectronic integration.

In order to obtain coherent infrared lasing from intersubband transitions, it is necessary to achieve a sufficiently high degree of *intersubband population inversion* at a reasonably low pumping. This represents a major challenge because of the overwhelming contribution of *nonradiative phonon emission*, which depopulates the upper subband of the lasing transition at a very fast rate. Many schemes have been proposed to achieve intersubband population inversion, most of which concentrate on current injection pumping [9]–[25], while a few approaches focus on optical pumping using a CO_2 laser source [26]–[28].

In this chapter, the possibility of achieving intersubband population inversion in coupled triple-QW structures using injection current pumping is theoretically studied. A carrier transport model incorporating the relevant physical mechanisms of resonant tunnelling and intersubband absorption–emission processes is described [23]. Based on this carrier transport model, the intersubband population inversion is explicitly calculated as a function of the injection current density at different operating temperatures. Previous theoretical studies [12, 18] on the feasibility of intersubband infrared lasers in resonant tunnelling QW structures have assumed a simple relation between the intersubband population inversion and the injection current density, without taking into account resonant tunnelling and intersubband emission–absorption processes in the electron transport dynam-

ics.

Very recently, room temperature intersubband electroluminescence at wavelength $\lambda = 5$ μm was reported by Faist and co-workers [29]. More significantly, an intersubband semiconductor laser operating at $\lambda = 4.3$ μm and at temperatures of up to about 125 K [30] was also demonstrated. This new MQW intersubband laser is referred to as the 'quantum cascade' laser, which utilizes tunnelling to achieve intersubband population inversion. The demonstration of the quantum cascade laser should, it is argued, be seen as providing an invaluable proof-of-concept demonstration of intersubband lasing. This observation of intersubband lasing has also clearly demonstrated the feasibility of tunnelling current injection pumping for use in an intersubband infrared laser structure. It is apparent, however, that much device development work is required to both raise the operating temperature of the intersubband lasers and to achieve lasing at longer wavelengths.

6.2 Intersubband Transitions in Coupled QW Structures

In this section, fundamental concepts of semiconductor coupled QW structures and intersubband transitions related to the achievement of intersubband population inversion are discussed.

6.2.1 Coupled QW Structures and Superlattices

Fig. 6.1 shows a semiconductor single quantum well (SQW), which is formed when a very thin layer of a small bandgap semiconductor material (the well layer) is sandwiched between two thick layers of a wide bandgap material (the

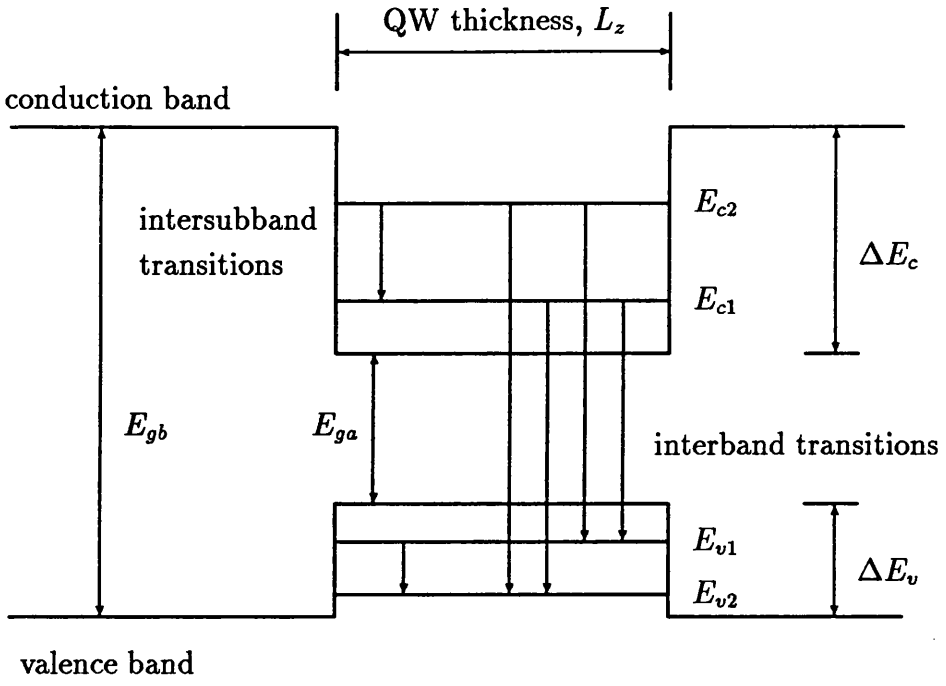

Figure 6.1: Schematic diagram of a single quantum well. Both interband and intersubband transitions are possible in a quantum well structure.

barrier layers). The thickness of the QW is comparable to the electron de Broglie wavelength, which is typically $\lesssim$ 10 nm. Because of the quantum size effect, the allowed electron (or hole) energies are quantized. The actual values of the discrete energy levels in the QW are determined by the thickness and the depth of the well. The depth of the well is the band discontinuity of the two materials; conduction band discontinuity ΔE_c for electrons and valence band discontinuity ΔE_v for holes.

If several quantum wells are grown on top of one another and the barrier layers are made thick enough that interactions between electrons in adjacent QW's are negligibly small, then the structure is called a *multiple quantum well* (MQW). The electronic properties of MQW heterostructures are obtained simply as a superposition of those obtained for a single QW. If the barrier layer thickness is made thin enough that a significant probability exists for electrons to tunnel

through barriers to adjacent QW's, a *coupled quantum well* structure is formed. If a large number of QW's are grown successively and the barrier layers are so thin (thickness < 50 Å) that electron tunnelling between wells is significant, the result is a *superlattice* [1]. Because of the overlapping of electronic wave functions among the wells, the discrete electron energy levels of an isolated well become minibands in a superlattice material.

6.2.2 Intersubband Transitions

As well as the usual interband transitions between the valence and the conduction bands allowed in bulk semiconductors, intraband transitions called *intersubband transitions* are possible in QW structures, as shown in Fig. 6.1. Intersubband transitions can occur within the potential wells of either the valence or the conduction bands. Three different intersubband transition processes can be identified, namely stimulated radiative emission, intersubband relaxations (which include both spontaneous radiative and nonradiative emission), and intersubband absorption. Because of the discrete energy levels in a QW, only certain wavelengths will be in resonance with the intersubband transitions. For QW structures fabricated using the III–V semiconductor material systems, conduction band intersubband transitions can be induced using electromagnetic radiation in the infrared wavelength range.

The resonant wavelength (or the energy separation) associated with conduction band intersubband transitions can be changed in several ways, for example,

- changing the layer structures such as the thickness of the QW and the barriers,
- changing the material systems of the QW structures, and

- applying an electric field perpendicular to the QW layer structure, which change the resonant wavelength via the quantum-confined Stark effect [31].

For GaAs–AlGaAs material system, intersubband absorption wavelengths varying from $\lambda = 8$ μm to $\lambda = 14$ μm have been reported [32, 33], which are ideal for device application in communication systems operating near the 10 μm atmospheric spectral window. Much longer wavelengths are possible from intersubband transitions by increasing the well width and by lowering the barrier height (using lower Al composition) so as to decrease the energy separations of the discrete energy levels. However, wavelengths much shorter than $\lambda = 6$ μm would be difficult to obtain using GaAs–AlGaAs because of the maximum barrier height (conduction band discontinuity) achievable using this material system. For applications at shorter wavelengths (eg., free-space communications corresponding to the $\lambda = 3$–5 μm atmospheric window), the InGaAs–InAlAs material system can be used. Resonant intersubband absorption peaks at $\lambda = 4.4$ μm with lattice-matched superlattices [34] and at $\lambda = 3.1$ μm with highly-strained MQW's [35] grown on InP substrates have been reported. The quantum-confined Stark shift of the intersubband resonant wavelength by the application of an electric field is useful for device applications such as electro-optic modulators, optical switching and tunable optical sources and detectors.

6.3 QW Structures for Intersubband Infrared Sources

Recent advances in semiconductor epitaxial growth technology have revived significant interest in the original proposal by Kazarinov and Suris [2] for the achievement of intersubband infrared emission in QW structures and superlattices. There are a number of advantages in using intersubband transitions in QW

structures for the realization of semiconductor infrared lasers, for example,

- the emission wavelength can be tailored over a wide spectral range from the mid-infrared to the far-infrared wave region by varying the QW layer structures such as the thickness of the well and the barrier, or by choosing a different semiconductor material system for the QW structures,
- intersubband emission with small linewidth is expected because of the discrete and narrow subbands involved in the transition,
- QW structures fabricated using indirect band-gap materials such as Si and Ge may be used for intersubband lasing because the intersubband transition is direct regardless of the host materials,
- wavelength tunable intersubband infrared sources may be feasible via the quantum-confined Stark effect which shifts the emission wavelength by the application of an electric field perpendicular to the QW heterostructures.

From the fundamental viewpoint, intersubband lasers represent a new class of semiconductor laser devices which utilize only one kind of charge carrier. Such devices may be termed *unipolar semiconductor lasers* [30]. In the present analysis, electron intersubband transitions are considered, but semiconductor lasers utilizing intersubband transitions between hole states in the valence band are also conceivable.

In this section, several QW structures that have been proposed for the achievement of intersubband infrared emission are discussed, so as to gain an insight into the requirements for obtaining intersubband population inversion. There are basically two different theoretical concepts for achieving intersubband lasing. In the first one, which was originally proposed by Kazarinov and Suris [2], electrons

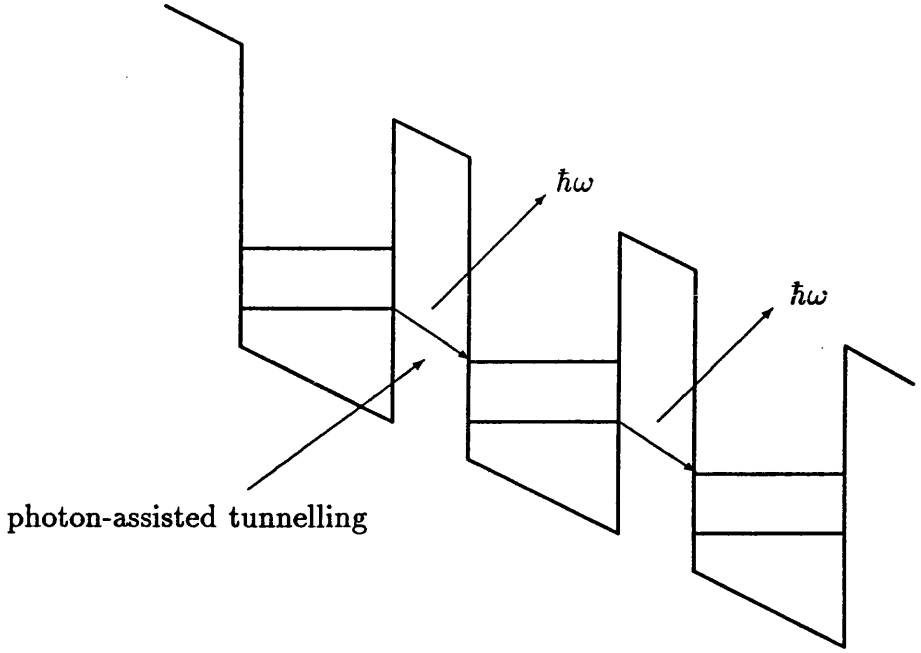

Figure 6.2: Coupled QW structure utilizing photon-assisted tunnelling to provide intersubband emission.

undergo transitions between quantum subbands in neighbouring QW's, a process known as *photon-assisted tunnelling.* In the second, electrons make *photon-mediated transitions* between subbands in the same QW. Examples of both of these intersubband transitions are discussed in the following.

6.3.1 Photon-Assisted Tunnelling Coupled QW Structures

Fig. 6.2 shows a schematic conduction band profile of a coupled QW structure utilizing photon-assisted tunnelling to achieve intersubband emission [2]. The coupled QW structure is biased with an electric field such that the ground state of one QW lies above an excited state of its 'down-field' neighbour. Electron tunnelling occurs with the aid of a photon to make up the energy difference between the ground and the excited states of adjacent QW's. Because the intersubband transition that provides optical gain spans across a barrier, the corresponding overlapping of electronic wave functions between the upper and the lower transi-

tion subbands is substantially reduced, resulting in a low radiative emission rate. However, the nonradiative intersubband relaxation rate across the barrier is also reduced, which is desirable for intersubband population inversion. The ratio of the radiative over the nonradiative emission rates gives the *radiative emission efficiency* of the QW structure. Neither intersubband absorption nor emission has been experimentally observed in the photon-assisted tunnelling coupled QW structure as shown in Fig. 6.2. The difficulty in obtaining intersubband emission/absorption from this structure may be due to space-charge effects which distort the potential along the coupled QW's and result in nonuniform transition energies across the whole structure.

6.3.2 Sequential Resonant Tunnelling QW Structures

The second infrared-emission scheme that has attracted much research effort is injection current pumped *photon-mediated intersubband transitions* that occur between subbands in the same QW. One of the many proposals was to use *sequential resonant tunnelling* to achieve intersubband population inversion [4]. Fig. 6.3 shows a sequential resonant tunnelling QW structure which is biased such that the ground state in the n-th well is degenerate (or aligned) with the first or the second excited state in the $(n+1)$-th well. Under such conditions, electrons tunnel resonantly between adjacent QW's and subsequently undergo intersubband relaxation within a QW, with the emission of phonons or photons. Although weak spontaneous radiative emission has been observed using this structure [4], intersubband population inversion has not been demonstrated. This is due to the fact that sequential resonant tunnelling from the ground state of one QW to the first excited state of an adjacent QW represents carrier transport in an essentially two-level system, and that population inversion cannot be achieved using just two states. On the other hand, while population inversion may be possible

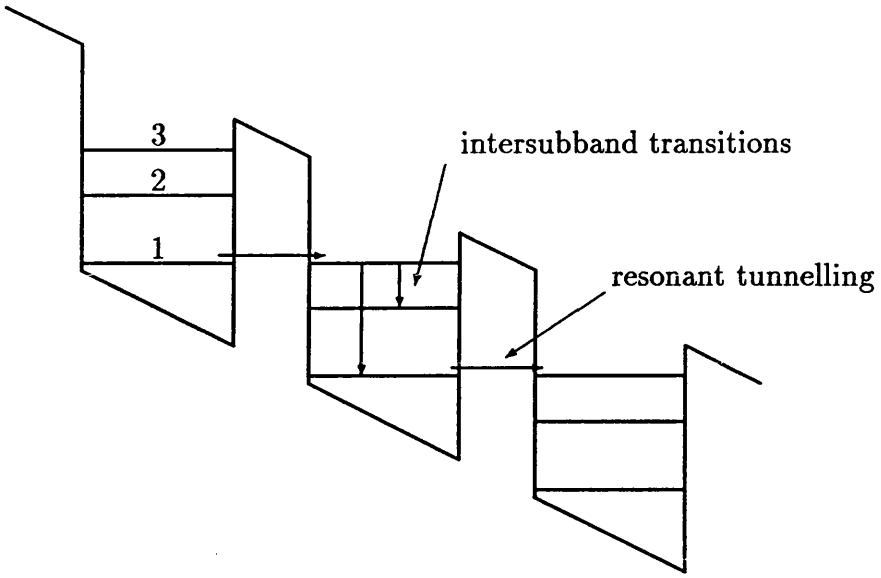

Figure 6.3: Sequential resonant tunnelling QW structure. Resonant tunnelling of electrons from the ground state of one QW selectively populates an excited state of the adjacent QW. Electrons undergo intersubband transitions within a QW.

using sequential resonant tunnelling from the ground state of one QW to the second excited state of an adjacent QW, the subsequent 'rain down' of electrons to the first excited state and the ground state within a QW makes population inversion between these two states very difficult.

6.3.3 Quantum Cascade Laser Structure

Very recently, quantum well intersubband electroluminescence and intersubband lasing were demonstrated by Faist *et al.* [29, 30] using the 'quantum cascade' MQW structure as shown in Fig. 6.4. The laser structure was grown with the $Al_{0.48}In_{0.52}As$–$Ga_{0.47}In_{0.53}As$ heterojunction material system latticed-matched to InP. The structure consists of 25 periodically repeated units, each of which comprises three elementary blocks: a coupled-well active region, an energy filter well, and a graded-gap injector. Intersubband emission occurs in the double-coupled-well active region via *photon-assisted tunnelling* process. The spatial separation between the upper and the lower states of the lasing transition in the active re-

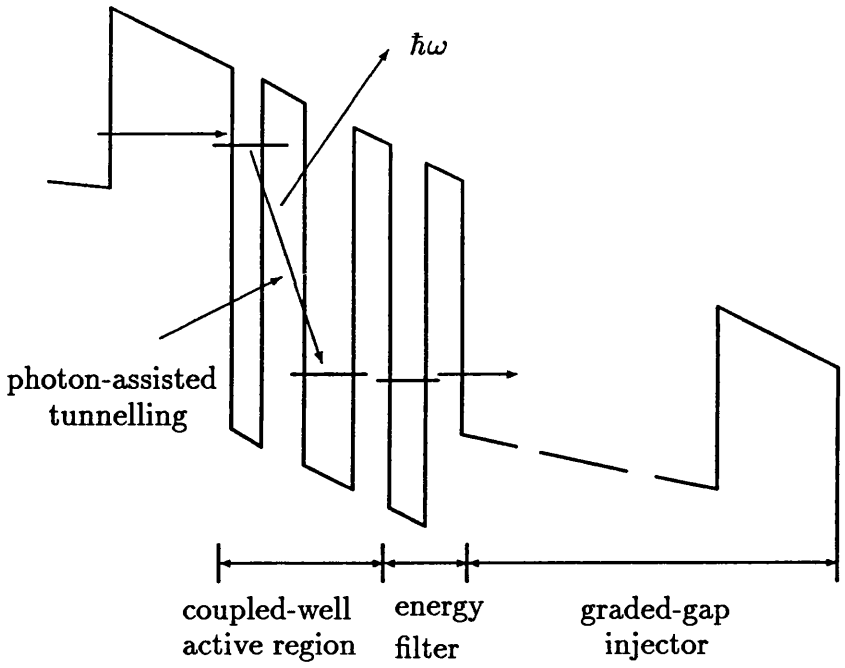

Figure 6.4: Quantum cascade laser structure utilizing photon-assisted tunnelling to effect the intersubband emission.

gion greatly reduces both the nonradiative relaxation rate and the electron escape rate to the continuum. Under operating bias, efficient depopulation of the lower lasing state in the active region is effected by resonant tunnelling through the filter well. The graded-gap injector consists of a superlattice with constant period and varying duty-cycle to obtain a graded gap pseudoquaternary alloy. The functions of this n-doped graded-gap injector are to provide electron injection by tunnelling into the upper lasing state of the following active region, and also to efficiently screen electrons leaving the filter well so as to minimize space-charge effects. It is clear from the complexity of the coupled QW structure (Fig. 6.4) that the successful demonstration of the quantum cascade laser is a result of careful design of the structure, complemented by extremely intricate and challenging semiconductor growth.

Although mid-infrared lasing at $\lambda = 4.3$ μm operating at temperatures of up to 125 K has been demonstrated using the quantum cascade laser structure

as shown in Fig. 6.4, it may be difficult to achieve far-infrared lasing at wavelengths exceeding 30 μm using this structure. At mid-infrared wavelengths, it is of most importance to reduce the rate of nonradiative intersubband relaxation (being dominated by optical phonon emission) in a laser structure. Because the quantum cascade laser structure utilizes the photon-assisted tunnelling process to effect the intersubband emission, the nonradiative intersubband relaxation time between the two spatially separated laser states is greatly increased (from $\approx$ 1 ps to $\approx$ 6 ps [30]). This means that the nonradiative intersubband relaxation rate is greatly reduced in the quantum cascade laser structure. Although radiative photon emission rate is also reduced in the quantum cascade structure, the *radiative emission efficiency* is improved over other structures which utilize photon-mediated intersubband transitions for the laser emission. However, at far-infrared wavelengths, the nonradiation intersubband relaxation time is much longer (a few hundred picoseconds), being limited by acoustic phonon scattering. As a result, it may not be necessary to induce a spatial separation between the laser transition states. In this case, QW structures which utilize the photon-mediated intersubband transitions may be favourable in terms of higher radiative emission efficiency.

6.4 Resonant Tunnelling Coupled QW Structures

In this section, two prototype coupled QW structures are considered [23] for the achievement of intersubband population inversion via *photon-mediated transitions*. The two structures have intersubband energy separations of 124 meV (corresponding to an intersubband resonant wavelength $\lambda = 10$ μm) and 21 meV ($\lambda = 60$ μm), respectively. The schematic conduction band profiles of the two

structures are shown in Fig. 6.5 and Fig. 6.6, respectively. In order to facilitate the selective injection of electrons into the upper subband and the removal of electrons from the lower subband of the emission QW, resonant tunnelling QW energy filters are used [12, 18].

In the figures, QW2 is the emission well where intersubband transitions take place between the first excited state with energy $E_2^{(2)}$, and the ground state with energy $E_2^{(1)}$. The emission wavelength corresponding to the intersubband energy separation $E_2^{(2)} - E_2^{(1)}$ is determined mainly by the choice of the emission well thickness L_2. QW1 and QW3 act as resonant tunnelling energy filters, which are designed to have only one quasibound state each (with energy E_1 and E_3, respectively). Under zero bias, the well widths of the resonant tunnelling energy filters are engineered such that E_1 and E_3 are in the middle of $E_2^{(1)}$ and $E_2^{(2)}$ in the emission well, as shown in Fig. 6.5(a). When the structures are biased to the operating voltage given by $V_b \approx (E_2^{(2)} - E_2^{(1)})/2$, the energy states are aligned as shown in Fig. 6.5(b) and Fig. 6.6. Electrons are efficiently injected into the first excited state of QW2 through filter well QW1, and are removed from the ground state of QW2 through QW3, via resonant tunnelling. The confined electrons in the emission well (QW2) undergo intersubband transitions such as intersubband relaxation, stimulated radiative emission and absorption. Because QW3 has only one subband, it serves not only to efficiently depopulate the ground state of QW2 via resonant tunnelling, but also to enhance the confinement of electrons in the first excited state of QW2 by minimizing electron escape to the collector. As the whole device structure relies on energy filtering to selectively populate the respective subbands, the influence of any non-resonant energy bands would be small. In particular, the contribution of any other subbands which may exist in QW2 can be neglected since those states would not be resonant with the aligned states in QW1 and QW3.

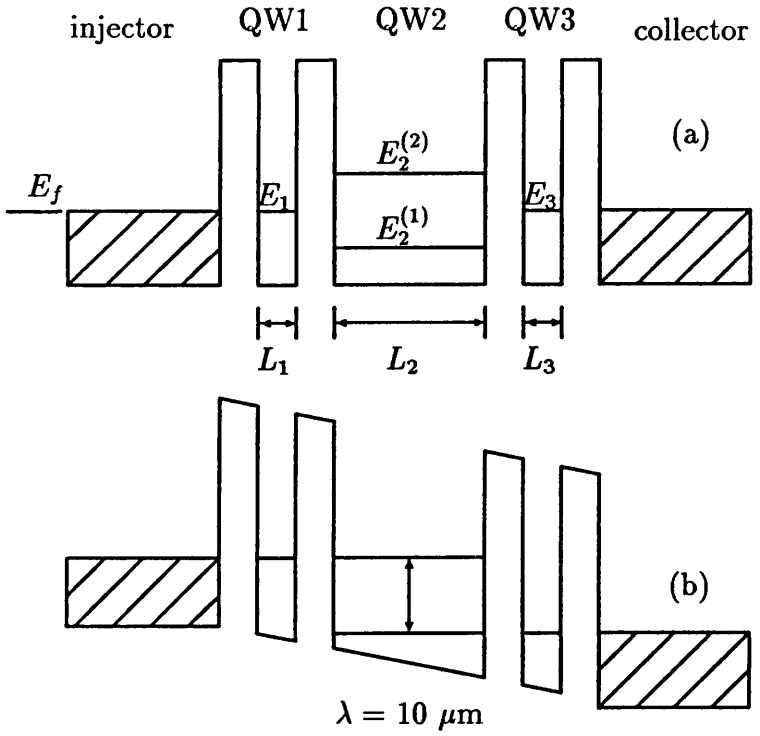

Figure 6.5: Coupled QW structure I with intersubband energy separation of 124 meV in QW2. The structure is under (a) zero bias, and (b) operating bias (not drawn in proportion). Hatched regions represent n-doped cladding layers with Fermi energy level E_f.

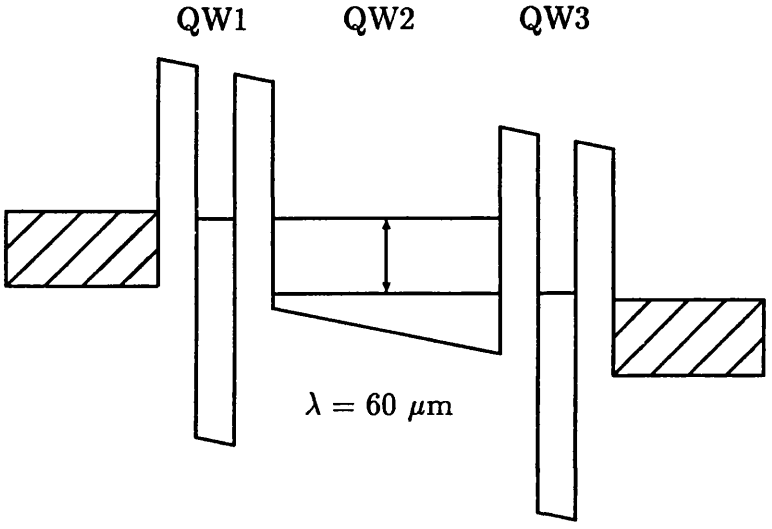

Figure 6.6: Coupled QW structure II biased to the operating voltage, with intersubband energy separation of 21 meV in QW2 (not drawn in proportion).

The resonant tunnelling QW structures are sandwiched between n-doped regions of the cladding layers, which are called the injector and the collector. The functions of the injector and the collector are to reduce space-charge effects and to provide optical confinement to the active QW region. Because of the higher electron density in the n-doped injector and collector, the refractive index in the cladding layers is lower than that in the coupled QW region, thus effecting a waveguide structure for the confinement of photons in the active region.

The GaAs–$Al_xGa_{1-x}As$ ($x = 0.45$) material system is employed in structure I (Fig. 6.5). On the other hand, because the intersubband energy separation of 21 meV corresponding to the far-infrared frequency of 5 THz in structure II is very small, rather wide emission well is required. As a result, the upper and the lower laser transition states in the emission well are situated very near to the bottom of the well. In order to ensure that the energy filter wells of structure II have only one quasi-bound state each and that the various energy states align properly under operating bias, very deep filter wells are required. These requirements are satisfied by using the $In_yGa_{1-y}As$–$Al_xGa_{1-x}As$ ($x = 0.45$, $y = 0.15$) material system in the filter wells and GaAs in the emission well for structure II (Fig. 6.6).

6.5 Electron Transport Dynamics

6.5.1 Four-Level Electron Rate Equations

Since the intersubband transition and resonant tunnelling processes occur at a much faster rate than the interband transitions, it is assumed that there is no carrier source or sink in the coupled quantum wells. Thus the external injection current density J leaving the structure is the same as that which enters. The temporal variations of electron density in the respective subbands are described

by carrier rate equations of an essentially four-level system [23]:

$$\frac{dn_1}{dt} = \frac{J}{eL_1} + \frac{L_2}{L_1}\frac{n_2^{(2)}}{\tau_{12}} - \frac{n_1}{\tau_{12}} , \tag{6.1}$$

$$\frac{dn_2^{(2)}}{dt} = \frac{L_1}{L_2}\frac{n_1}{\tau_{12}} - \frac{n_2^{(2)}}{\tau_{12}} - \left(n_2^{(2)} - n_2^{(1)}\right) X(P) - A_{sp} , \tag{6.2}$$

$$\frac{dn_2^{(1)}}{dt} = \left(n_2^{(2)} - n_2^{(1)}\right) X(P) + A_{sp} + \frac{L_3}{L_2}\frac{n_3}{\tau_{23}} - \frac{n_2^{(1)}}{\tau_{23}} , \tag{6.3}$$

$$\frac{dn_3}{dt} = \frac{L_2}{L_3}\frac{n_2^{(1)}}{\tau_{23}} - \frac{n_3}{\tau_{23}} - \frac{J}{eL_3} , \tag{6.4}$$

where $n_a^{(b)}$ denotes the electron density in quantum well a ($a = 1, 2, 3$) and subband b (since there is only one subband in QW1 and QW3, the superscript b is omitted), e is the electronic charge, and X is the *stimulated radiative emission coefficient* (inverse time) which is a function of the photon density P.

The tunnelling times τ_{12} and τ_{23} between QW1 and QW2, and QW2 and QW3, respectively, are given by

$$\tau_{12} = \frac{\pi\hbar}{\Delta E} , \quad \tau_{23} = \frac{\pi\hbar}{\Delta E'} , \tag{6.5}$$

where $\hbar$ is the Planck's constant divided by 2π, ΔE and $\Delta E'$ are the energy level broadening resulting from the coupling of QW1 and QW2, and QW2 and QW3, respectively. The total intersubband relaxation rate A_{sp} in QW2 (per-unit volume per-unit time), appropriate for a two-dimensional system, is given by [36]

$$A_{sp} = S\left(n_2^{(2)} - n_2^{(1)}\right) \frac{\exp(n_2^{(2)}/n_{c_2}) - 1}{\exp(n_2^{(2)}/n_{c_2}) - \exp(n_2^{(1)}/n_{c_2})} , \tag{6.6}$$

where S is the intersubband relaxation coefficient (inverse time), and

$$n_{c_2} = \frac{m_2^* k_B T}{\pi\hbar^2 L_2} \tag{6.7}$$

is the quasi-two-dimensional degeneracy concentration, $m_2^* = 0.067\, m_0$ is the electron effective mass in GaAs, m_0 is the free electron mass, k_B is the Boltzmann

constant and T is the electron temperature. The above expression incorporates energy dependence of the carriers using Fermi-Dirac statistics as appropriate to semiconductor laser operation [36].

Since the current injection is equal to the rate of total charge passing through the resonant tunnelling quantum well structure, J can be written as

$$J = \frac{e}{\tau_T}\left[n_1 L_1 + (n_2^{(1)} + n_2^{(2)})L_2 + n_3 L_3\right] , \tag{6.8}$$

where τ_T is the effective transit time of electrons through the whole structure which includes not only the transmission times through the barriers and the intersubband transition times, but also time delays caused by intrasubband scattering and electron diffusion. The electron densities in the various subbands can be obtained as a function of the external injection current density by solving the electron rate equations in steady-state subject to the constraint imposed by Eq. (6.8).

The coupled QW structures utilizing resonant tunnelling energy filters provide an efficient means of electron injection into the upper subband and electron removal from the lower subband of the emission well. It should be noted that without the energy filter QW's the structure becomes essentially a two-level system, and in that case intersubband population inversion cannot be obtained. To assess the possibility of intersubband population inversion in the proposed quantum well structures, the relevant physical mechanisms of intersubband emission-absorption processes have to be taken into account.

The principal intersubband transition processes include stimulated emission of radiation, absorption and intersubband relaxation. For current injection pumping and below lasing threshold operation of the coupled quantum well infrared laser structures, the stimulated emission and absorption rates are negligibly small compared to the intersubband relaxation rate. As a result, the term proportional

to $X(P)$ in the carrier rate equations can be neglected. The intersubband relaxation coefficient S is given by

$$S = \frac{1}{\tau_R} + \frac{1}{\tau_{sp}}, \tag{6.9}$$

where τ_R is the nonradiative intersubband relaxation time and τ_{sp} is the spontaneous intersubband radiative emission time. Because τ_{sp} is in the order of a few microseconds and τ_R is in the order of 0.1–300 ps (depending on the nonradiative intersubband relaxation mechanisms, which will be discussed in the following subsection), it can be assumed that $S \approx \tau_R^{-1}$.

6.5.2 Intersubband Relaxation Mechanisms

The study of carrier dynamics in semiconductor structures of reduced dimensionality is of fundamental importance not only for the understanding of the basic physics of the various scattering and energy relaxation processes involved, but also for the development of high speed electronics and optical devices. In particular, the injection current level needed for the achievement of intersubband population inversion in an infrared optical source is critically dependent on the intersubband relaxation time.

The carrier transport dynamics in quasi-two-dimensional semiconductor QW structures has been extensively studied both theoretically [37]–[39] and experimentally [40]–[45]. These studies have shown that nonthermal carrier occupation of excited states in QW structures can be achieved using electrical or optical pumping, and that excited carriers subsequently relax to the ground state and cool down to the lattice temperature through *intersubband* and *intrasubband* relaxation processes, respectively. Conceptually, the intersubband relaxation process is different from intrasubband thermalization and cooling simply by the fact that momentum (and hence the wavevector k) is quantized and discrete in the

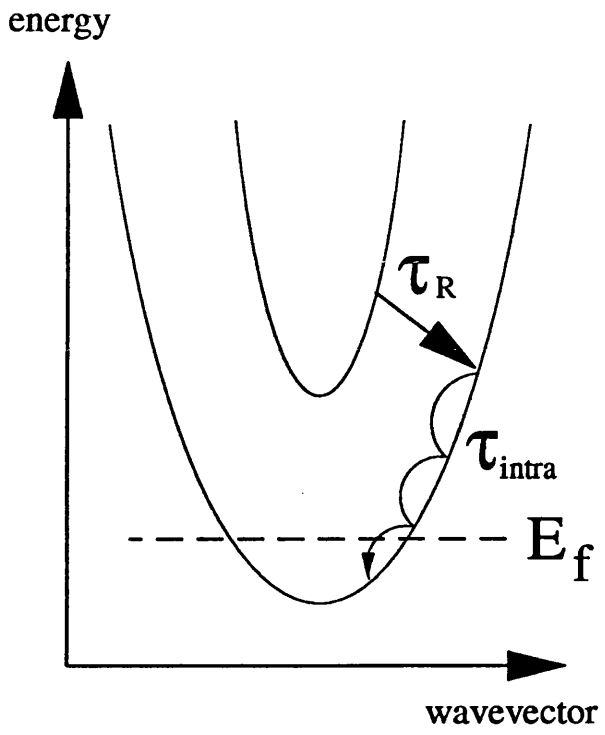

Figure 6.7: Schematic diagram of intersubband and intrasubband relaxation processes. The Fermi energy is indicated by the broken line.

former case, while it is continuous in the latter. The quantization of energy and momentum in a QW implies that intersubband transitions can occur only through the emission of specific phonon combinations that obey energy and momentum conservation.

The schematic intersubband and intrasubband relaxation processes in the energy–momentum space is shown in Fig 6.7. Neglecting radiative transition, the excited carriers are scattered first with finite k to the ground state via intersubband relaxation with characteristic time τ_R. Cooling of the carriers then occurs within the ground state by intrasubband relaxation with characteristic time τ_{intra}. There exist several mechanisms for the relaxation of excited carriers in QW structures, namely polar optical phonon interaction, acoustic phonon interaction and electron-electron scattering.

For intersubband energy separation greater than the optical phonon energy ($\approx$ 36 meV in GaAs), optical phonon scattering is the main intersubband relaxation process. The reported intersubband relaxation times by optical phonon scattering vary over more than one order of magnitude. Relaxation times of the order of 10 ps at 300 K for an intersubband energy separation of 120 meV in GaAs QW were reported by Seilmeier and co-workers [42]. However, recent experimental measurements [44, 45] and theoretical calculations [39] reported subpicosecond to 1 ps relaxation times arising from optical phonon scattering. In general, the optical phonon scattering time of InGaAs–InAlAs QW's is slightly longer than that of GaAs–AlGaAs QW's. This is attributed to the lower effective mass of InGaAs as compared to GaAs.

Acoustic phonon scattering is expected to be the dominant mechanism for intersubband relaxation if the intersubband energy separation is less than the optical phonon energy. Oberli *et al.* [40] reported intersubband relaxation times of the order of several hundred picoseconds arising from acoustic phonon scattering in wide GaAs–AlGaAs MQW at low temperatures. Recent measurement [41] reported intersubband relaxation times of (300 $\pm$ 100) ps, correponding to the emission of acoustic phonons. Electron-electron scattering is believed to be important only for thermalization of carriers within each subband, and hence is a dominant mechanism for intrasubband scattering. Electron-electron scattering occurs essentially in a femtosecond time scale.

From the above discussion, it is noted that intersubband relaxation time decreases by more than two orders of magnitude if the QW width is reduced such that the intersubband energy separation exceeds $\approx$ 36 meV, an energy above which optical phonon scattering dominates the intersubband relaxation process. It has been observed, however, that intersubband relaxation time increases with

	Structure I	Structure II	
λ	10	60	μm
L_1	40	70	Å
L_2	82	285	Å
L_3	40	70	Å
ΔE	7	0.2	meV
$\Delta E'$	5	0.1	meV
S	10^{12}	$(3 \times 10^{-10})^{-1}$	s^{-1}

Table 6.1: Parameter values used in the calculation

intersubband energy separation for subband energy difference larger than the optical phonon energy [42]. This is due to the fact that a larger intersubband energy separation (corresponding to a smaller well width) requires a larger wavevector for the intersubband transition, whist the density of final states decreases with increasing wavevector owing to longitudinal optical phonon dispersion [39].

Furthermore, it is important to point out that in a QW in which the upper subband is very close to the top of the potential well, the electron wave-function penetrates deeper into the barrier layers. As a result, a reduction in the overlap integral between the wide-spread wave-function of the upper subband and that of the lower subband is obtained. This leads to an increase in the intersubband relaxation time in a QW with small well thickness or with a shallow well. The above factors which affect the intersubband relaxation time in QW structures have to be considered when designing an infrared intersubband laser device.

In the following, intersubband population inversion is calculated using parameter values as tabulated in table 6.1.

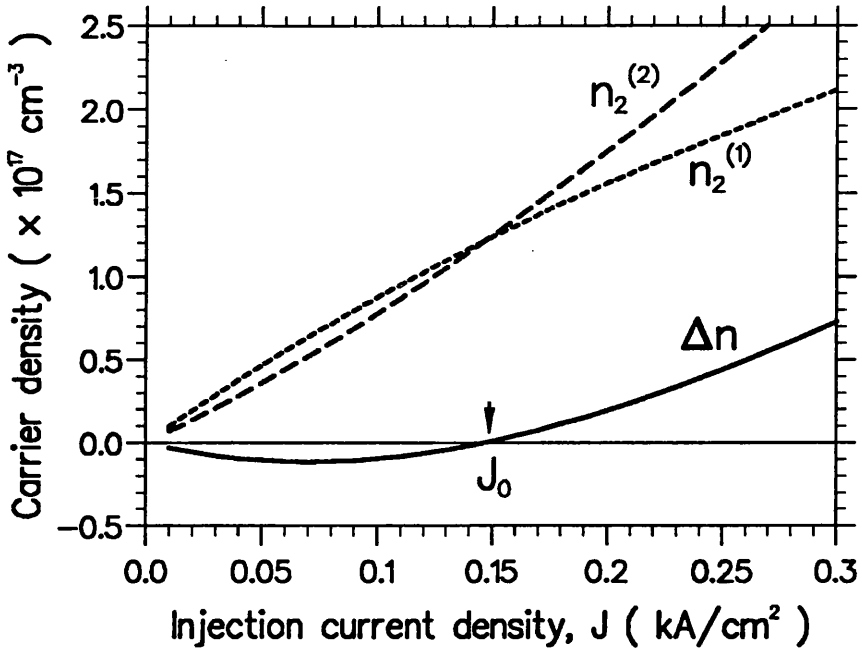

Figure 6.8: Dependence of carrier density and intersubband population inversion on injection current density for QW structure II. Intersubband population inversion becomes positive when J exceeds the transparency value, J_0.

6.6 Intersubband Population Inversion

The carrier densities in all subbands increase as the external injection current density is increased. The injection current density dependence of carrier density in the upper and the lower subbands of QW2 for structure II is illustrated in Fig. 6.8. It is observed that the intersubband population inversion, $\Delta n = n_2^{(2)} - n_2^{(1)}$, becomes positive when the external injection current density exceeds the level J_0, which is termed the *transparency current density.*

Figs. 6.9(a) and 6.9(b) show the calculated intersubband population inversion as a function of J at different temperatures for structures I and II, respectively. It is noted that significantly higher injection current density is needed to achieve intersubband population inversion in structure I as compared to structure II. This

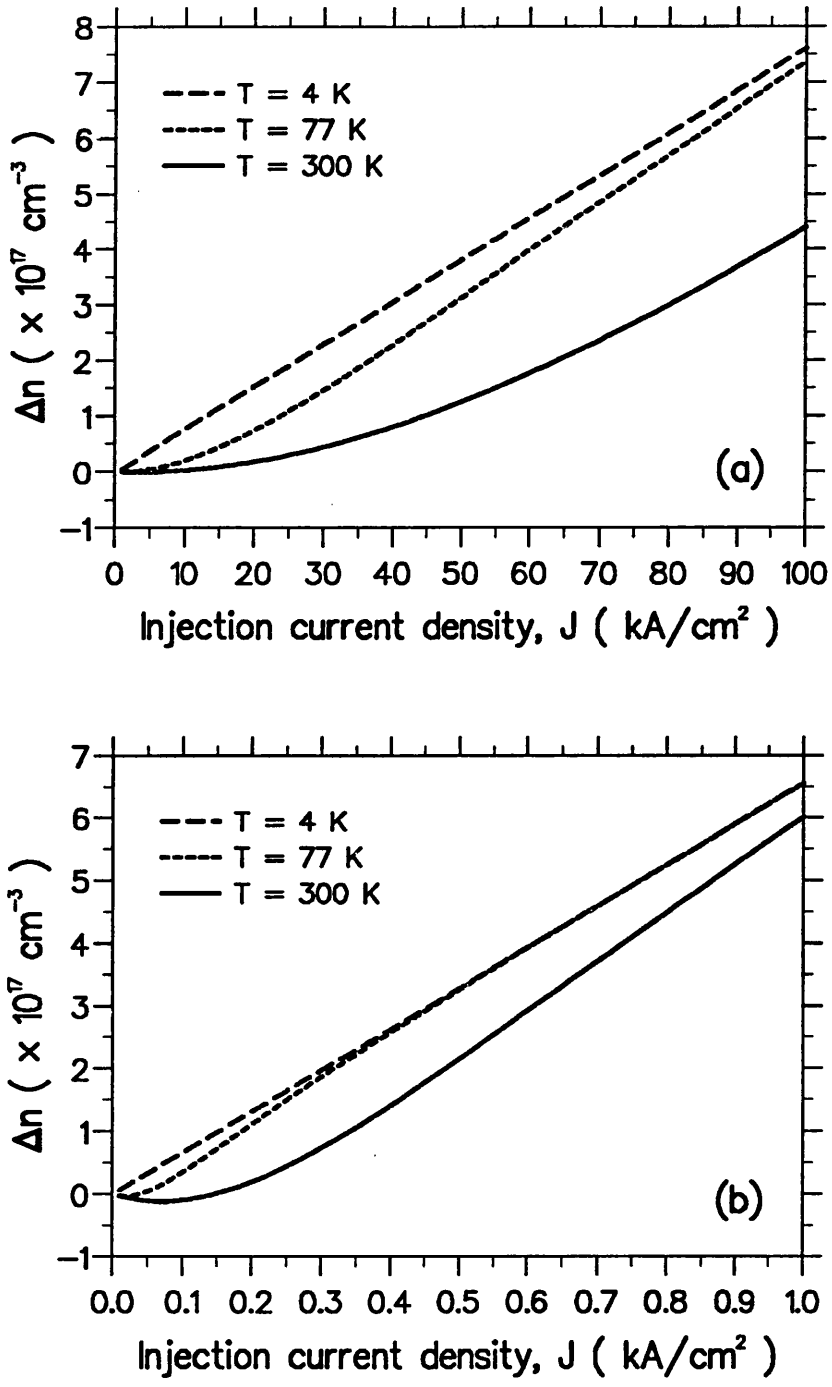

Figure 6.9: Intersubband population inversion versus injection current density at different temperatures for (a) structure I, $\tau_T = 4.0$ ps, and (b) structure II, $\tau_T = 1.5$ ns.

is because the upper lasing state of structure I is depopulated at a very fast rate by intersubband relaxation with the emission of optical phonons, whereas a much slower acoustic phonon scattering limits the downward transition in structure II. It therefore appears that lasing action based on intersubband transition may, at a reasonable level of injection current, be feasible only in the far-infrared wavelength range. However, the optical absorptive loss is greater for longer wavelengths, and thus there is a trade-off to be considered when designing such a laser. This aspect will be dealt with in the next chapter.

It is also observed from Fig. 6.9 that higher injection current densities are needed to obtain a given level of population inversion as the temperature is increased. In the calculations, it has been assumed that non-resonant tunnelling and thermionic induced carrier leakage from the upper subband of QW2 to the collector are negligibly small. In view of the uncertainties in the reported experimental values of the intersubband relaxation times, it is difficult to incorporate the temperature dependence of the intersubband relaxation time τ_R in the analysis. The temperature dependence of Δn arises mainly because of the quasi-two-dimensional degeneracy density, n_{c_2}, being a function of temperature. In practice, the intersubband relaxation rates increase with temperature and this may affect the temperature dependence of Δn.

It should be noted that since the upper subband is closer to the barrier edge and hence the electronic wave function spreads more widely than that of the lower subband in QW2, the energy broadening is larger in the upper subband, that is $\Delta E > \Delta E'$. This implies that $\tau_{12} < \tau_{23}$ according to Eq. (6.5). In this case, intersubband population inversion is still possible. It is clear therefore that inversion of the tunnelling rates is not a necessary condition for intersubband population inversion. It is, however, found that lower transparency current den-

sity can be achieved by decreasing τ_{23} and increasing τ_{12} so that $\tau_{12} \approx \tau_{23}$. This can be achieved by designing different barrier widths between the quantum wells such that the coupling between QW1 and QW2 is reduced whereas the coupling between QW2 and QW3 is increased. Nevertheless, decreasing the coupling between QW1 and QW2 by increasing the barrier width will increase the effective transit time, and increasing the coupling between QW2 and QW3 by reducing the barrier width will in practice increase the leakage current. All these will eventually increase the transparency current density.

6.7 Conclusion

A theoretical model of electron transport in resonant tunnelling QW structures, incorporating the relevant physical mechanisms of resonant tunnelling and intersubband emission-absorption processes, has been presented. In particular, the intersubband population inversion for two coupled QW structures with emission wavelengths at $\lambda = 10$ μm and $\lambda = 60$ μm, respectively, has been explicitly calculated as a function of injection current density at different operating temperatures. The results show that intersubband population inversion is achievable at acceptable injection current densities (of the order of 1.0 kA/cm^2) even for room-temperature operation in the case of $\lambda = 60$ μm. However, achievement of intersubband population inversion is significantly more difficult at the shorter wavelength. This chapter has concentrated on the transport processes related to the achievement of intersubband population inversion. Analysis of lasing threshold conditions of the two prototype resonant tunnelling QW structures will be described in the next chapter.

References

[1] L. Esaki, "A bird's-eye view on the evolution of semiconductor superlattices and quantum wells," *IEEE J. Quantum Electron.*, vol. QE-22, pp. 1611–1624, 1986.

[2] R. F. Kazarinov and R. A. Suris, "Possibility of the amplification of electromagnetic waves in a semiconductor with a superlattice," *Sov. Phys. Semicond.*, vol. 5, pp. 707–709, 1971.

[3] L. C. West and S. J. Eglash, "First observation of an extremely large-dipole infrared transition within the conduction band of a GaAs quantum well," *Appl. Phys. Lett.*, vol. 46, pp. 1156–1158, 1985.

[4] M. Helm, E. Colas, P. England, F. DeRosa, and S. J. Allen, Jr., "Observation of grating-induced intersubband emission from GaAs/AlGaAs superlattices," *Appl. Phys. Lett.*, vol. 53, pp. 1714–1716, 1988.

[5] M. Helm, P. England, E. Colas, F. DeRosa, and S. J. Allen, Jr., "Intersubband emission from semiconductor superlattices excited by sequential resonant tunneling," *Phys. Rev. Lett.*, vol. 63, pp. 74–77, 1989.

[6] Y. J. Mii, K. L. Wang, R. P. G. Karunasiri, and P. F. Yuh, "Observation of large oscillator strengths for both $1 \rightarrow 2$ and $1 \rightarrow 3$ intersubband transitions of step quantum wells," *Appl. Phys. Lett.*, vol. 56, pp. 1046–1048, 1990.

[7] B. F. Levine, "Device physics of quantum well infrared photodetectors," *Semicond. Sci. Technol.*, vol. 8, pp. S400–S405, 1993.

[8] M. O. Manasreh (editor), *Semiconductor quantum wells and superlattices for long-wavelength infrared detectors*, Boston: Artech House, 1993.

[9] P. F. Yuh and K. L. Wang, "Novel infrared band-aligned superlattice laser," *Appl. Phys. Lett.*, vol. 51, pp. 1404–1406, 1987.

[10] K. L. Wang and P. F. Yuh, "Theory and applications of band-aligned superlattices," *IEEE J. Quantum Electron.*, vol. 25, pp. 12–19, 1989.

[11] H. C. Liu, "A novel superlattice infrared source," *J. Appl. Phys.*, vol. 63, pp. 2856–2858, 1988.

[12] S. Borenstain and J. Katz, "Intersubband Auger recombination and population inversion in quantum-well subbands," *Phys. Rev. B*, vol. 39, pp. 10852–10857, 1989.

[13] S. I. Borenstain and J. Katz, "Evaluation of the feasibility of a far-infrared laser based on intersubband transitions in GaAs quantum wells," *Appl. Phys. Lett.*, vol. 55, pp. 654–656, 1989.

[14] M. Helm and S. J. Allen, Jr, "Can barriers with inverted tunneling rates lead to subband population inversion ?" *Appl. Phys. Lett.*, vol. 56, pp. 1368–1370, 1990.

[15] J. W. Choe, A. G. U. Perera, M. H. Francombe, and D. D. Coon, "Estimates of infrared intersubband emission and its angular dependence in GaAs/AlGaAs multiquantum well structures," *Appl. Phys. Lett.*, vol. 59, pp. 54–56, 1991.

[16] J. P. Loehr, J. Singh, R. K. Mains, and G. I. Haddad, "Theoretical studies of the applications of resonant tunneling diodes as intersubband laser and interband excitonic modulators," *Appl. Phys. Lett.*, vol. 59, pp. 2070–2072, 1991.

[17] A. Kastalsky, V. J. Goldman, and J. H. Abeles, "Possibility of infrared laser in a resonant tunneling structure," *Appl. Phys. Lett.*, vol. 59, pp. 2636–2638, 1991.

[18] Q. Hu and S. Feng, "Feasibility of far-infrared lasers using multiple semiconductor quantum wells," *Appl. Phys. Lett.*, vol. 59, pp. 2923–2925, 1991.

[19] S. J. Allen, G. Brozak, E. Colas, F. DeRosa, P. England, J. Harbison, M. Helm, L. Florez, and M. Leadbeater, "Far-infrared emission and absorption by hot carriers in superlattices," *Semicond. Sci. Technol.*, vol. 7, pp. B1–B5, 1992.

[20] A. A. Andronov, "Proposed optical-phonon-mediated population inversion and stimulated FIR emission in superlattices," *Semicond. Sci. Technol.*, vol. 7, pp. B629–B632, 1992.

[21] G. N. Henderson, L. C. West, T. K. Gaylord, C. W. Roberts, E. N. Glytsis, and M. T. Asom, "Optical transitions to above-barrier quasibound states in asymmetric semiconductor heterostructures," *Appl. Phys. Lett.*, vol. 62, pp. 1432–1434, 1993.

[22] A. Kastalsky, "Infrared intraband laser induced in a multiple-quantum-well interband laser," *IEEE J. Quantum Electron.*, vol. 29, pp. 1112–1115, 1993.

[23] W. M. Yee, K. A. Shore, and E. Schöll, "Carrier transport and intersubband population inversion in coupled quantum wells," *Appl. Phys. Lett.*, vol. 63, pp. 1089–1091, 1993.

[24] W. M. Yee and K. A. Shore, "Threshold current density calculations for far-infrared semiconductor lasers," *Semicond. Sci. Technol.*, vol. 9, pp. 1190–1197, 1994.

[25] J. W. Cockburn, M. S. Skolnick, D. M. Whittaker, P. D. Buckle, A. R. K. Willcox, and G. W. Smith, "Evidence for population inversion in excited electron states of a double barrier resonant tunneling structure," *Appl. Phys. Lett.*, vol. 64, pp. 2400–2402, 1994.

[26] K. M. Lau and W. Xu, "Optically pumped submillimeter wave semiconductor lasers," *IEEE J. Quantum Electron.*, vol. 28, pp. 1773–1777, 1992.

[27] G. Sun and J. B. Khurgin, "Optically pumped four-level infrared laser based on intersubband transitions in multiple quatum wells: feasibility study," *IEEE J. Quantum Electron.*, vol. 29, pp. 1104–1111, 1993.

[28] V. Berger, "Three-level laser based on intersubband transitions in asymmetric quantum wells: a theoretical study," *Semicond. Sci. Technol.*, vol. 9, pp. 1493–1499, 1994.

[29] J. Faist, F. Capasso, C. Sirtori, D. L. Sivco, A. L. Hutchinson, S. N. G. Chu, and A. Y. Cho, "Quantum-well intersub-band electroluminescent diode at $\lambda = 5$ μm," *Electron. Lett.*, vol. 29, pp. 2230–2231, 1993;
J. Faist, *et al.*, "Mid-infrared field-tunable intersubband electroluminescence at room temperature by photon-assisted tunneling in coupled-quantum wells," *Appl. Phys. Lett.*, vol. 64, pp. 1144–1146, 1994;
J. Faist, *et al.*, "Narrowing of the intersubband electroluminescent spectrum in coupled-quantum-well heterostructures," *Appl. Phys. Lett.*, pp. 94–96, 1994.

[30] J. Faist, F. Capasso, D. L. Sivco, C. Sirtori, A. L. Hutchinson, and A. Y. Cho, "Quantum cascade laser," *Science*, vol. 264, pp. 553–556, 1994;
J. Faist, *et al.*, "Quantum cascade laser: an intersubband semiconductor laser operating above liquid nitrogen temperature," *Electron. Lett.*, vol. 30, pp. 865–866, 1994.

[31] A. Harwit and J. S. Harris, Jr., "Observation of Stark shifts in quantum well intersubband transitions," *Appl. Phys. Lett.*, vol. 50, pp. 685–687, 1987.

[32] B. F. Levine, R. J. Malik, J. Walker, K. K. Choi, C. G. Bethea, D. A. Kleinman, and J. M. Vandenberg, "Strong 8.2 μm infrared intersubband absorption in doped GaAs/AlAs quantum well waveguides," *Appl. Phys. Lett.*, vol. 50, pp. 273–275, 1987.

[33] M. O. Manasreh, B. Jogai, C. E. Stutz, and D. C. Reynolds, "Optical absorption of the intersubband transitions in GaAs/$Al_{0.4}Ga_{0.6}As$ multiple quantum

wells with superlattice barriers," *Appl. Phys. Lett.*, vol. 73, pp. 3105–3107, 1993.

[34] B. F. Levine, A. Y. Cho, J. Walker, R. J. Malik. D. A. Kleinman, and D. L. Sivco, "InGaAs/InAlAs multiquantum well intersubband absorption at a wavelength of $\lambda = 4.4$ μm," *Appl. Phys. Lett.*, vol. 52, pp. 1481–1483, 1988.

[35] H. Asai and Y. Kawamura, "Intersubband absorption in highly strained InGaAs/InAlAs multiquantum wells," *Appl. Phys. Lett.*, vol. 56, pp. 746–748, 1990.

[36] R. E. Kunz and E. Schöll, "Bistability and negative photoconductivity in optically induced real-space transfer," *Phys. Rev. B*, vol. 47, pp. 4337–4347, 1993.

[37] B. K. Ridley, "The electron-phonon interaction in quasi-two-dimensional semiconductor quantum-well structures," *J. Phys. C: Solid State Phys.*, vol. 15, pp. 5899–5917, 1982.

[38] J. Shah, "Hot carriers in quasi-2-D polar semiconductors," *IEEE J. Quantum Electron.*, vol. QE-22, pp. 1728–1743, 1986.

[39] R. Ferreira and G. Bastard, "Evaluation of some scattering times for electrons in unbiased and biased single and multiple quantum well structures," *Phys. Rev. B*, vol. 40, pp. 1074–1086, 1989.

[40] D. Y. Oberli, D. R. Wake, M. V. Klein, J. Klem, T. Henderson, and H. Morkoc, "Time-resolved Raman scattering in GaAs quantum wells," *Phys. Rev. Lett.*, vol. 59, pp. 696–699, 1987;
D. Y. Oberli, *et al.*, "Intersubband relaxation of photoexcited hot carriers in quantum wells," *Solid-State Electron.*, vol. 31, pp. 413–418, 1988.

[41] J. Faist, C. Sirtori, F. Capasso, L. Pfeiffer, and K. W. West, "Phonon limited intersubband lifetimes and linewidths in a two-dimensional electron gas," *Appl. Phys. Lett.*, vol. 64, pp. 872–874, 1994.

[42] A. Seilmeier, H. J. Hübner, G. Abstreiter, G. Weimann, and W. Schlapp, "Intersubband relaxation in GaAs–$Al_xGa_{1-x}As$ quantum well structures observed directly by an infrared bleaching technique," *Phys. Rev. Lett.*, vol. 59, pp. 1345–1348, 1987;
A. Seilmeier, *et al.*, "Direct observation of intersubband relaxation in narrow multiple quantum well structures," *Solid-State Electron.*, vol. 31, pp. 767–770, 1988.

[43] J. A. Levenson, G. Dolique, J. L. Oudar, and I. Abram, "Time resolved intersubband relaxation in GaAs/GaAlAs multiple quantum wells," *Solid-State Electron.*, vol. 32, pp. 1869–1873, 1989.

[44] H. T. Grahn, H. Schneider, W. W. Rühle, K. von Klitzing, and K. Ploog, "Nonthermal occupation of higher subbands in semiconductor superlattices via sequantial resonant tunneling," *Phys. Rev. Lett.*, vol. 64, pp. 2426–2429, 1990.

[45] J. Faist, F. Capasso, C. Sirtori, D. L. Sivco, A. L. Hutchinson, S. N. G. Chu, and A. Y. Cho, "Measurement of the intersubband scattering rate in semiconductor quantum wells by excited state differential absorption spectroscopy," *Appl. Phys. Lett.*, vol. 63, pp. 1354–1356, 1993.

Chapter 7

Transparency and Threshold Current Calculations for Infrared Intersubband Lasers

7.1 Introduction

The development of room-temperature semiconductor lasers operating in the mid to far-infrared wavelength range has been pursued by various workers for over twenty years. Significant progress has been made towards this goal. Room-temperature operation of electroluminescent diodes at an emission wavelength of $\lambda = 5$ μm was recently reported [1]. More spectacularly, the 'quantum cascade laser' operating at $\lambda = 4.3$ μm and at temperatures of up to about 125 K was demonstrated [2]. Although these results are encouraging, there remain two major challenges to building a room-temperature intersubband infrared semiconductor laser. One is to achieve a sufficiently high level of intersubband population inversion at a reasonably low current density; and the other is to overcome optical losses so as to obtain laser oscillation at an acceptable threshold current density. The aim of this chapter is to quantify the challenges which need to be met to reach the goal of operating room-temperature mid and far-infrared semiconductor lasers.

In the previous chapter, a description was given of a electron transport model [3] which demonstrated the opportunity for the achievement of intersubband population inversion in two prototype resonant tunnelling QW structures having intersubband resonant wavelengths of 10 μm and 60 μm, respectively. In this chapter, the electron transport model is used to calculate the transparency current density as a function of both the effective electron transit time through the coupled QW structures and the intersubband relaxation time. The prescription of lasing conditions in the two resonant tunnelling QW structures is also presented. In this respect, optical loss analysis is carried out which takes into account the configuration of the infrared semiconductor laser devices. The incorporation of optical loss analysis into the electron transport model provides a complete formulation [4], which enables the lasing threshold current density to be calculated for room-temperature operation of the mid- and the far-infrared intersubband laser structures.

7.2 Calculation of Transparency Current Density

In this section, the dependence of transparency current density J_0 on effective electron transit time τ_T, and intersubband relaxation time τ_R is calculated for the two prototype resonant tunnelling QW structures as shown in Figs. 6.5 and 6.6 in the previous chapter.

7.2.1 Dependence of Transparency Current Density on Electron Transit Time

The transparency current density J_0 is defined as the current density level above which the intersubband population inversion becomes positive. Figs. 7.1(a) and

7.1(b) show the transparency current density as a function of the effective electron transit time τ_T for QW structure I ($\lambda = 10$ μm) and structure II ($\lambda = 60$ μm), respectively. The effective transit time includes not only the tunnelling times τ_{12} and τ_{23}, and the intersubband relaxation time τ_R, but also tunnelling times through the outer barriers, electron dephasing times in the various subbands, and electron diffusion time. The electron dephasing time is governed by intrasubband scattering processes which are believed to be dominated by electron-electron scatterings. Any extra time delays caused by these intrasubband processes will lead to higher electron accumulation in the various quantum subbands and further increase J_0.

It is noted from Figs. 7.1(a) and 7.1(b) that transparency current densities of a few tens of kA/cm^2 are required to obtain room-temperature intersubband population inversion at resonant wavelength of 10 μm (structure I). On the other hand, significantly lower transparency current densities in the range of 0.1–0.3 kA/cm^2 are achievable at $\lambda = 60$ μm (structure II) for room-temperature operation. In both cases, the achievement of intersubband population inversion is more readily facilitated at lower temperatures. Furthermore, the minimum transit times for the two coupled QW structures can be obtained from Figs. 7.1(a) and 7.1(b). The minimum transit time for structure I is approximately 3.8 ps. The transit time dependence of J_0 for structure II is less sensitive; a large change in τ_T (of the order of nanoseconds) produces only a relatively small change in J_0. This is possibly because the intersubband relaxation time in structure II is much longer than both the electron dephasing time (of the order of subpicosecond) and the tunnelling time. As a result, a small change in τ_T would not have a significant effect on J_0. From Fig. 7.1(b), the minimum τ_T is approximately 1.2 ns for structure II.

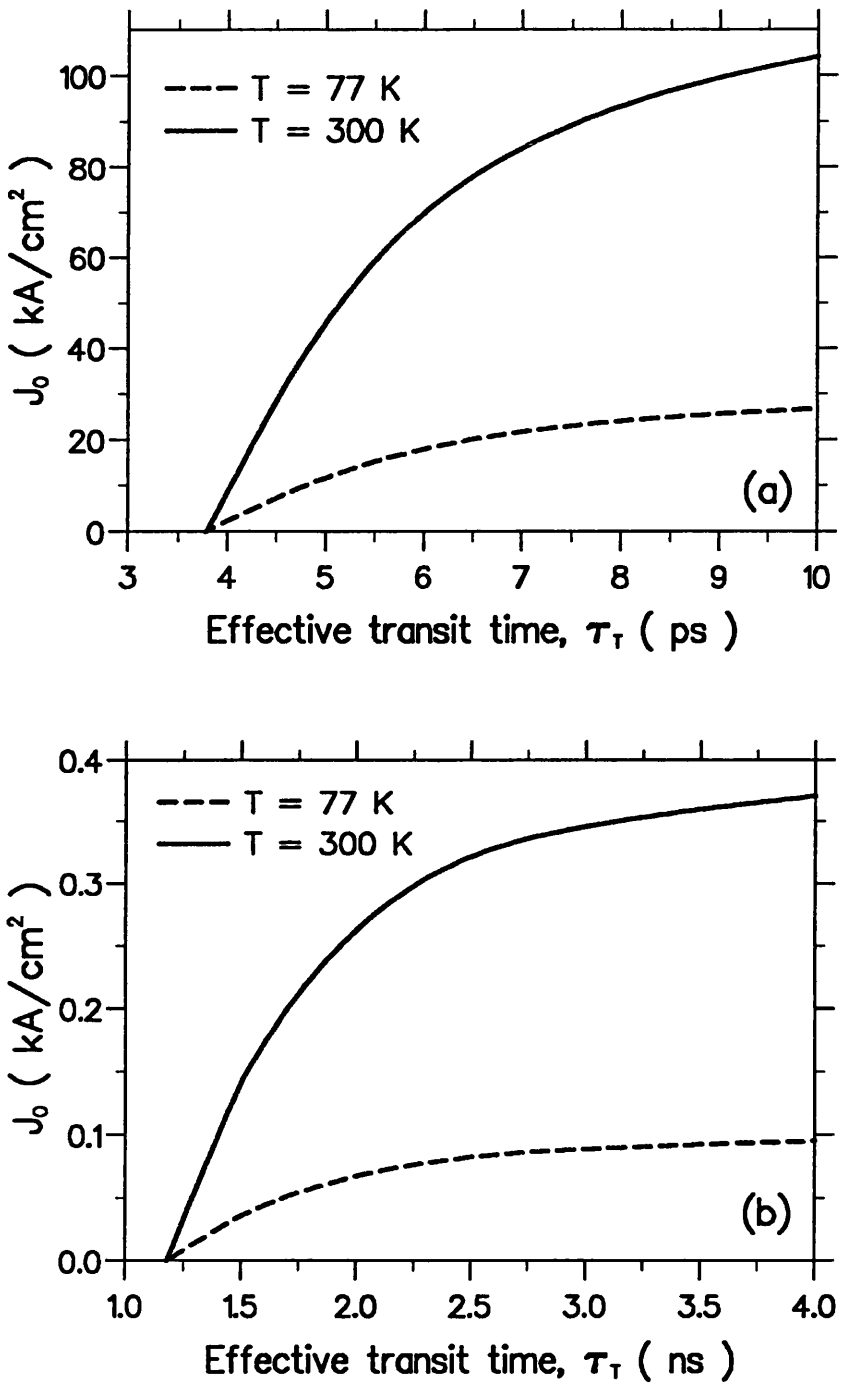

Figure 7.1: Dependence of transparency current density on effective electron transit time for (a) QW structure I ($\lambda = 10$ μm), and (b) QW structure II ($\lambda = 60$ μm).

7.2.2 Dependence of Transparency Current Density on Intersubband Relaxation Time

As has been noted in the previous chapter, the reported experimental values of intersubband relaxation time τ_R arising from optical phonon scattering for GaAs–AlGaAs quantum wells differ by more than one order of magnitude. However, recent experiments tend to give values of τ_R in the subpicosecond to 1.0 ps range [5]. For intersubband energy separation less than the optical phonon energy, the intersubband relaxation rate is reduced by about two orders of magnitude [6], being limited by the slower acoustic phonon emission. In view of such uncertainties in the values of the intersubband relaxation time, it is instructive to investigate the sensitivity of the dependence of transparency current density on intersubband relaxation time.

Figs. 7.2(a) and 7.2(b) show the transparency current density as a function of the intersubband relaxation time τ_R for structure I and structure II, respectively. J_0 increases by more than two orders of magnitude if τ_R is reduced from 1.0 ps to 0.1 ps for structure I. Similarly, J_0 increases by approximately one hundred times when τ_R is reduced from 0.35 ns to 0.035 ns for structure II. The results suggest that intersubband population inversion is highly dependent on τ_R, and that in order to reduce the transparency current density, it is crucial to reduce the intersubband relaxation rate. Several ways may be used to reduce the intersubband relaxation rate:

- Phonon emission rate can be reduced considerably by lowering the temperature of operation of the device, thus enhancing the electron lifetime in the upper subband of the emission well.

- It is found that material with a lower effective mass has a longer inter-

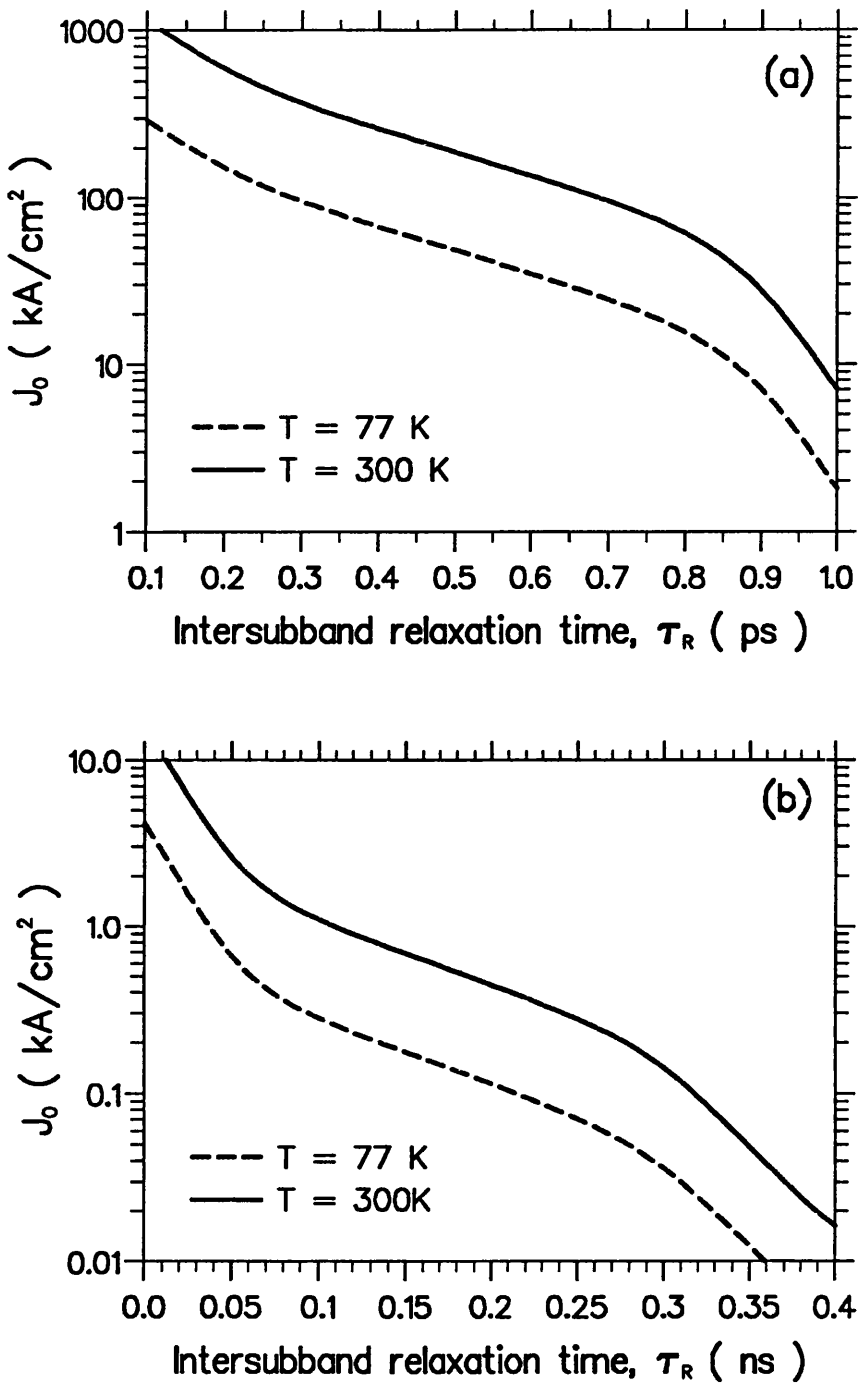

Figure 7.2: Dependence of transparency current density on intersubband relaxation time for (a) QW structure I, τ_T = 4.0 ps, and (b) QW structure II, τ_T = 1.5 ns.

subband relaxation time. Hence material such as InGaAs, with a lower effective mass and a longer intersubband relaxation time than GaAs [5], may be used to fabricate the emission quantum well.

- For intersubband energy separation larger than the optical phonon energy, the intersubband relaxation rate can be reduced by reducing the quantum well width [7, 8]. This is because a larger intersubband energy separation (corresponding to a smaller well width) requires a larger wavevector for the intersubband transition, whilst the density of final states decreases with increasing wavevector. Therefore, intersubband population inversion may be achieved at lower injection current densities for emission wavelength $\lambda < 10$ μm. This, together with the fact that optical absorptive loss decreases for shorter wavelengths, indicates that lasing action based on intersubband transitions may be easier to achieve for $\lambda < 10$ μm compared to $\lambda = 10$ μm. Experimental investigation into intersubband population inversion and lasing for wavelengths shorter than 10 μm could, therefore, be of considerable interest with a view to designing mid-infrared lasers operating at the $\lambda = 3$–5 μm atmospheric window [2].

- A double-coupled QW active region can be engineered such that intersubband emission occurs via the photon-assisted tunnelling process [2]. In such a structure, the spatial separation between the upper and the lower lasing states greatly reduces the intersubband relaxation rate. However, intersubband radiative emission rate is also reduced. The photon-assisted tunnelling QW structure may, in terms of improved radiative emission efficiency, be favourable only for operation in the mid-infrared wavelengths (say, between 3 to 10 μm), where it is of paramount importance to reduce the intersubband relaxation rate arising from optical phonon scattering.

7.3 Calculation of Threshold Current Density

Having shown that intersubband population inversion can indeed be achieved at reasonable injection current densities in the proposed resonant-tunnelling QW structures, this section is devoted to quantifying the lasing threshold conditions which need to be satisfied for the achievement of room-temperature mid- and far-infrared lasing. In this respect, optical loss analysis is carried out [4] taking into account the infrared QW laser geometry in a way similar to Borenstain [9]. The four-level electron rate equations from the previous chapter are solved in conjunction with the balance of gain and optical loss, thus determining the threshold current density as a function of free electron density in the n-doped regions of the cladding layers of the two proposed QW laser structures (as shown in Figs. 6.5 and 6.6).

7.3.1 Optical Absorption Calculation

The optical properties of III–V semiconductor materials at energies smaller than the fundamental bandgap energy are determined by two major physical processes, namely lattice vibrations (photon–phonon interactions) and collective oscillation of free carriers (photon–plasmon interactions). The refractive index $\overline{n}$ and the extinction coefficient k can be calculated through the complex dielectric constant [9, 10] as given by

$$\begin{aligned}\epsilon(\omega) &= (\overline{n} - ik)^2 \\ &= \epsilon_\infty \left[1 + \frac{\omega_L^2 - \omega_T^2}{\omega_T^2 - \omega^2 + i\omega\gamma_{ph}} - \frac{\omega_p^2}{\omega(\omega - i\gamma_{pl})} \right] ,\end{aligned} \tag{7.1}$$

where ϵ_∞ is the high frequency dielectric constant, ω_L, ω_T and ω_p are the angular frequencies of the longitudinal optical (LO) phonons, the transverse optical (TO) phonons and the plasmons, respectively, γ_{ph} and γ_{pl} are the damping constants of

Symbol	Value	Unit
ϵ_∞	11.1	
ω_L	291.5	cm^{-1}
ω_T	268.2	cm^{-1}
γ_{ph}	2.3	cm^{-1}
μ_e	5000	$cm^2\ V^{-1}\ s^{-1}$
ϵ_r	12.25	
T_2	0.21	ps
R	0.3	
L_c	1.0	mm

Table 7.1: List of parameter values

the phonons and the plasmons, respectively, $\gamma_{pl} = e/2\pi\mu_e m^*$, e is the electronic charge, m^* is the electron effective mass in GaAs, μ_e is the electron mobility, $\omega_p^2 = N_c e^2/m^*\epsilon_\infty\epsilon_0$, ϵ_0 is the permittivity of free space, and N_c is the free electron density in the n-doped conducting layers. The absorption coefficient in the n-doped conducting layers (the injector and the collector) is calculated from the extinction coefficient in Eq. (7.1) using

$$\alpha_c = \frac{4\pi k}{\lambda}\,. \tag{7.2}$$

The calculated refractive index and optical absorption coefficient as a function of wavelength for different values of free electron density are depicted in Figs. 7.3 and 7.4, respectively. The parameter values used in the calculation are listed in table 7.1.

As shown in Fig. 7.3, the variation of the refractive index shows a pronounced dispersive characteristic at $\lambda \approx 30$–40 μm, which arises because of induced ionic polarization in the semiconductor medium at infrared wavelengths. The refractive index curve for $N_c = 0$ represents a theoretical fitting curve of experimental data [10] using Eq. (7.1) and parameter values tabulated in table 7.1. The rapidly varying refractive index near the LO and TO phonon frequencies is the typical

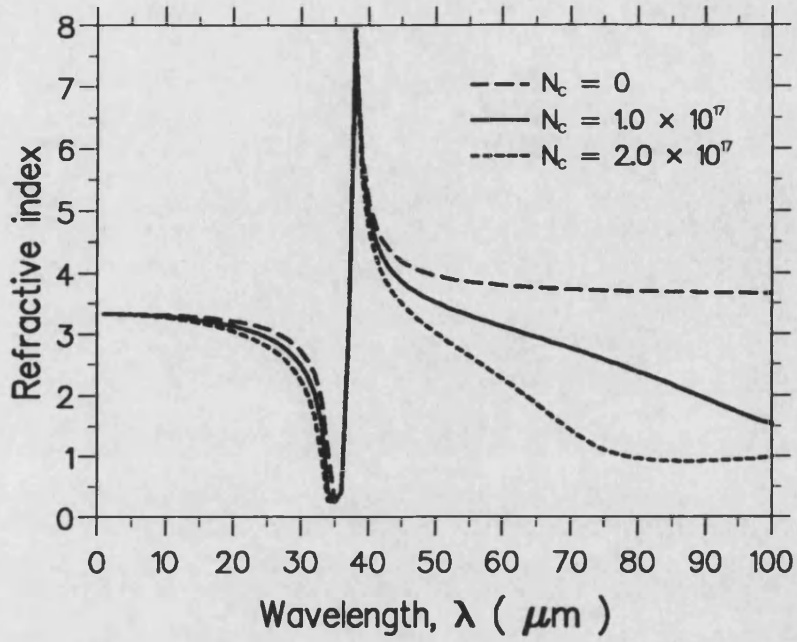

Figure 7.3: Refractive index versus wavelength for different values of free electron density. N_c is in units of cm^{-3}.

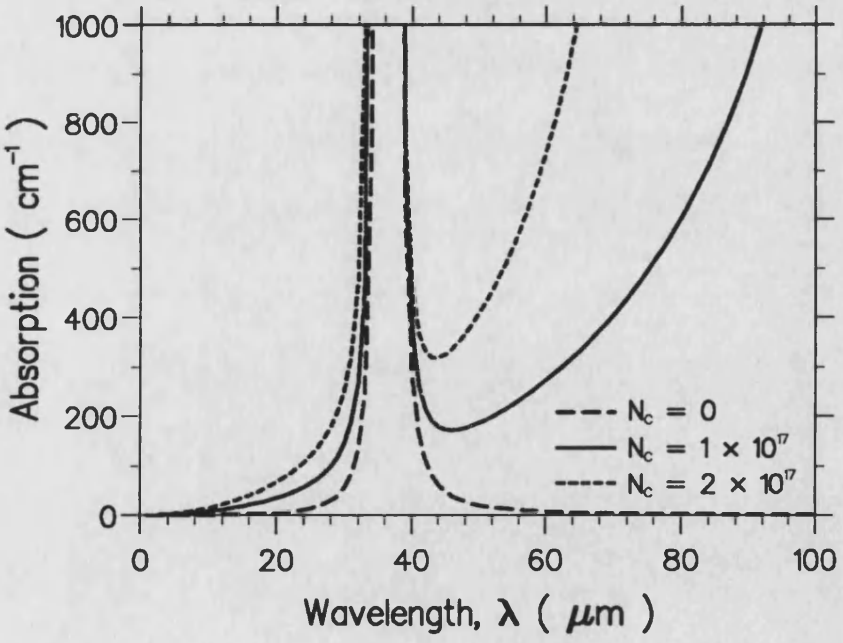

Figure 7.4: Optical absorption versus wavelength for different values of free electron density. N_c is in units of cm^{-3}.

anomalous dispersion characteristic associated with resonance absorption, which is as shown in Fig. 7.4. In this region, no wave can propagate through the medium. Instead there is an evanescent wave that decays exponentially as it penetrates the medium and there is *total external reflection* of radiation incident on the medium from outside. As $\overline{n} \rightarrow \infty$ near the TO phonon frequency, almost all incident radiation is reflected, save for some absorbed energy. This effect can be amplified by repeated reflections of radiation from the medium interface. After many rounds of reflection, only the component of radiation with frequencies close to ω_T will survive. This surviving radiation is known as the *reststrahl* (residual ray). Hence, it is seen in Fig. 7.4 that the optical absorptive loss in the *reststrahlen* region is extremely large, and that infrared lasing from intersubband transitions in GaAs is feasible only at wavelengths above or below the reststrahlen region.

From Figs. 7.3 and 7.4, it is noted that the effects of increasing the free electron density (doping density) in the conducting region of the cladding layers are to decrease the refractive index and to increase the optical absorptive loss. These effects are particularly pronounced at wavelengths above the reststrahlen region.

Figs. 7.5(a) and 7.5(b) show the effects of varying the free electron density on optical absorption and refractive index for wavelengths of 10 μm and 60 μm, respectively. It is noted that, for N_c in the range of 1–5 $\times$ 10^{17} cm^{-3}, optical absorption of 10–40 cm^{-1} is obtained at λ = 10 μm (Fig. 7.5(a)). However, at λ = 60 μm (Fig. 7.5(b)), much higher absorption of 500–6000 cm^{-1} results over the same range of N_c. Therefore, despite the lower transparency current densities achievable at an operating wavelength of 60 μm (as revealed in the previous section), high optical losses may lead to high threshold current densities for laser operation in this emission wavelength. However, at λ = 10 μm, optical losses become less daunting but it is relatively more difficult to achieve population

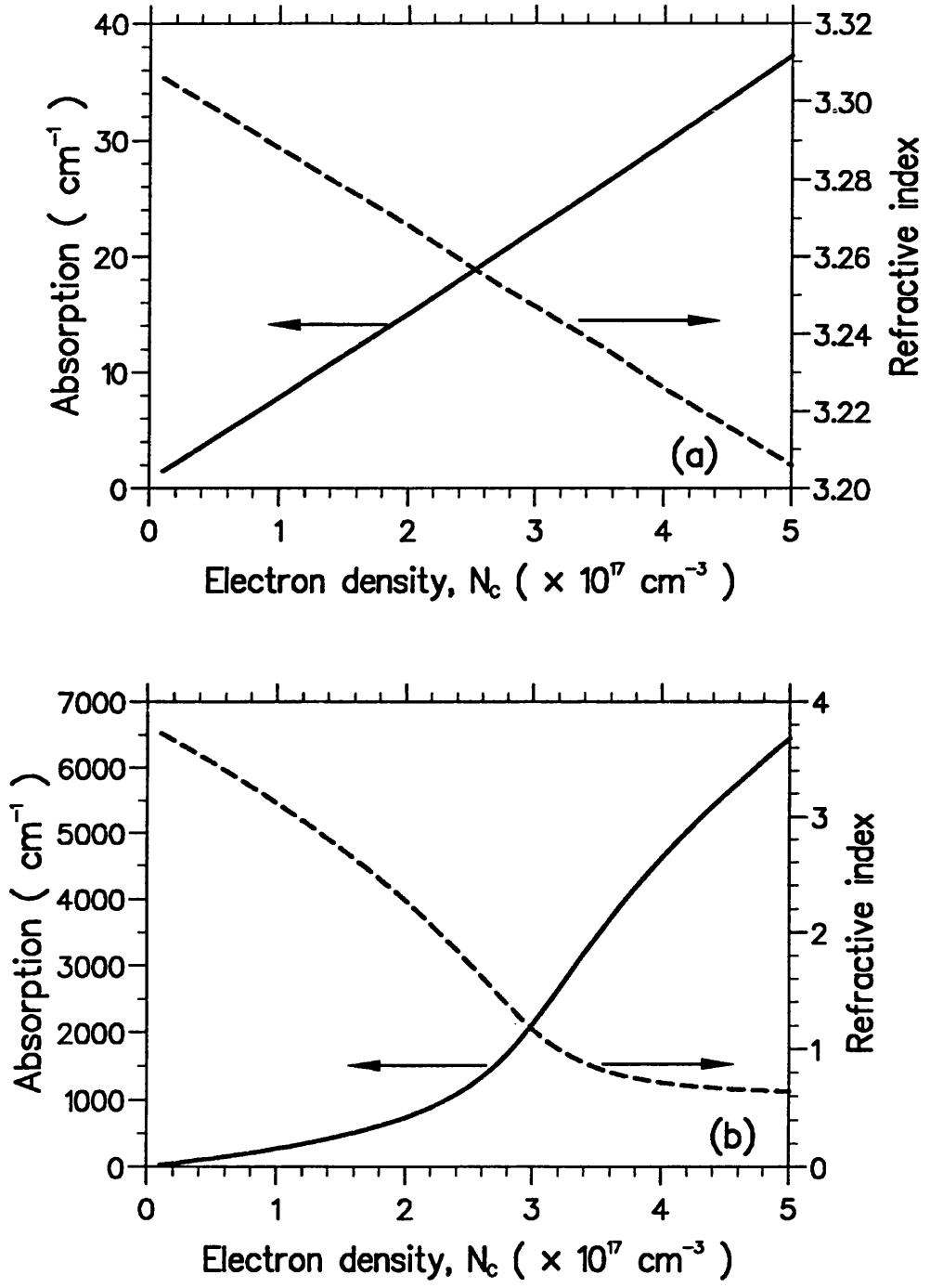

Figure 7.5: Effects of variation of free electron density on optical absorption and refractive index at (a) $\lambda = 10$ μm and (b) $\lambda = 60$ μm.

inversion. Hence, it is concluded that the critical issue in designing mid-infrared (1–30 μm) semiconductor lasers is to reduce the intersubband relaxation rates so as to lower the transparency current density. On the other hand, the challenge to designing far-infrared (> 30 μm) semiconductor lasers is to overcome optical absorptive losses so as to lower the lasing threshold current density.

From Figs. 7.5(a) and 7.5(b), it appears that lower threshold current density may be achieved by reducing the free electron density in the n-doped region of the cladding layers. However, it is also noted that reducing the electron density leads to an increase in the refractive index of the cladding layers. This gives rise to an anti-guiding effect on the generated photons and thus reduces the optical confinement. As a result, higher threshold current density may be required to achieve laser action if the doping density in the cladding region is low. There is, therefore, another trade-off to be considered when designing an infrared semiconductor laser. The effect of varying N_c on refractive index is particularly pronounced at $\lambda = 60$ μm as shown in Fig. 7.5(b); a significant drop of refractive index from 3 to 0.6 is obtained when N_c is increased from 1.0 $\times 10^{17}$ cm^{-3} to 5.0 $\times 10^{17}$ cm^{-3}. This optical property of the material is useful when consideration is given to designing a waveguiding structure to improve the optical confinement in a far-infrared semiconductor laser.

7.3.2 Lasing Threshold Condition

In contrast to semiconductor lasers based on interband transitions, the energy difference associated with transitions between any given pair of intersubband states is exactly the same and gives rise to a narrow resonance. It is therefore reasonable to model the intersubband transitions in the emission QW (QW2 in Figs. 6.5 and 6.6) by a two-level system. The optical gain, g (per unit length) in

the emission quantum well can be written as [9]

$$g(\lambda) = \frac{\lambda^2}{4\pi\epsilon_r\tau_e}\frac{T_2}{1+(\omega-\omega_0)^2T_2^2}\Delta n\ , \tag{7.3}$$

where $\Delta n = n_2^{(2)} - n_2^{(1)}$, ϵ_r is the relative permittivity of GaAs, T_2 is the electron dephasing time in the quantum subbands, ω_0 is the angular frequency at resonance and τ_e is the spontaneous radiative time given by

$$\tau_e^{-1} = \frac{2\pi\epsilon_r^{1/2}e^2}{m^*\epsilon_0\lambda^2 c}f_{ij}\ , \tag{7.4}$$

where c is the velocity of light in vacuum and f_{ij} is the oscillator strength of the transition from the i level to the j level, which can be approximated by $f_{ij} = 64(ij)^2/\pi^2(i^2-j^2)^3$.

To establish the lasing threshold condition, the device structures as shown in Figs. 6.5 and 6.6 are considered. It is assumed that free electrons are confined to just two n-doped conducting layers (the injector and the collector) with total thickness t_c. The generated photons are confined to an effective mode thickness of $t_m = \lambda/2\overline{n}$. Lasing action in the structures occurs when the optical gain equals the total losses, ie.,

$$\frac{L_2}{t_m}g_{th} = \frac{L_2}{t_m}\alpha_a + \eta_c\alpha_c + \eta_i\alpha_i + \frac{1}{L_c}\ln\left(\frac{1}{R}\right)\ , \tag{7.5}$$

where α_a, α_c and α_i are the loss coefficients (per unit length) in the active QW layer, the conducting layers and the intrinsic region of the cladding layers, respectively, η_c and η_i are the mode filling factors in the conducting and the intrinsic cladding layers, respectively. The last term accounts for mirror loss of the laser structures with cavity length L_c and facet reflectivity R.

The loss coefficient in the conducting layers α_c is calculated using Eqs. (7.1) and (7.2). The loss coefficient in the intrinsic regions α_i is similarly calculated by putting $N_c = 0$. Absorption by plasmon interaction in the emission quantum well

(active region) is negligible because radiation emitted from intersubband transitions is polarized perpendicular to the QW layers, whereas plasmon oscillations can interact only with radiation polarized parallel to the QW layers. Furthermore, because of the small active layer thickness, absorption from photon–phonon interaction in the emission well is negligibly small for wavelengths well above or below the reststrahlen region. Hence it can be assumed that $\alpha_a \approx 0$.

It is assumed that $t_c = 2$ μm in both structures. Since $t_c > t_m \approx 1.43$ μm in structure I, the mode filling factors are given by $\eta_c = (t_m - L_2)/t_m$ and $\eta_i = 0$. In structure II, however, $t_c < t_m$ and in this case $\eta_c = t_c/t_m$ and $\eta_i = (t_m - t_c)/t_m$. The intersubband population inversion at lasing threshold $(\Delta n)_{th}$ is obtained by equating Eqs. (7.3) and (7.5) for $\omega = \omega_0$. The electron rate equations from the previous chapter are then solved in steady-state for J_{th} consistent with the obtained threshold population inversion. The parameter values used in the calculation are given in table 7.1.

7.3.3 Dependence of Threshold Current Density on Electron Density in Cladding Layers

Figs 7.6(a) and 7.6(b) shows the calculated threshold current density as a function of the free electron density in the conducting layers for the two infrared laser structures respectively. As N_c is increased through doping, the absorption arising from plasmon interaction increases, thus increasing the threshold gain and J_{th}. It is observed from Fig. 7.6(b) that J_{th} remains relatively low at low N_c but increases sharply when N_c exceeds $\approx 2.3 \times 10^{17}$ cm^{-3} for structure II. This is because for electron density above this value, the plasma frequency ω_p in the conducting layers becomes higher than the emission frequency ($\approx$ 5 THz) of structure II. Since the generated laser wave can not propagate through the free-

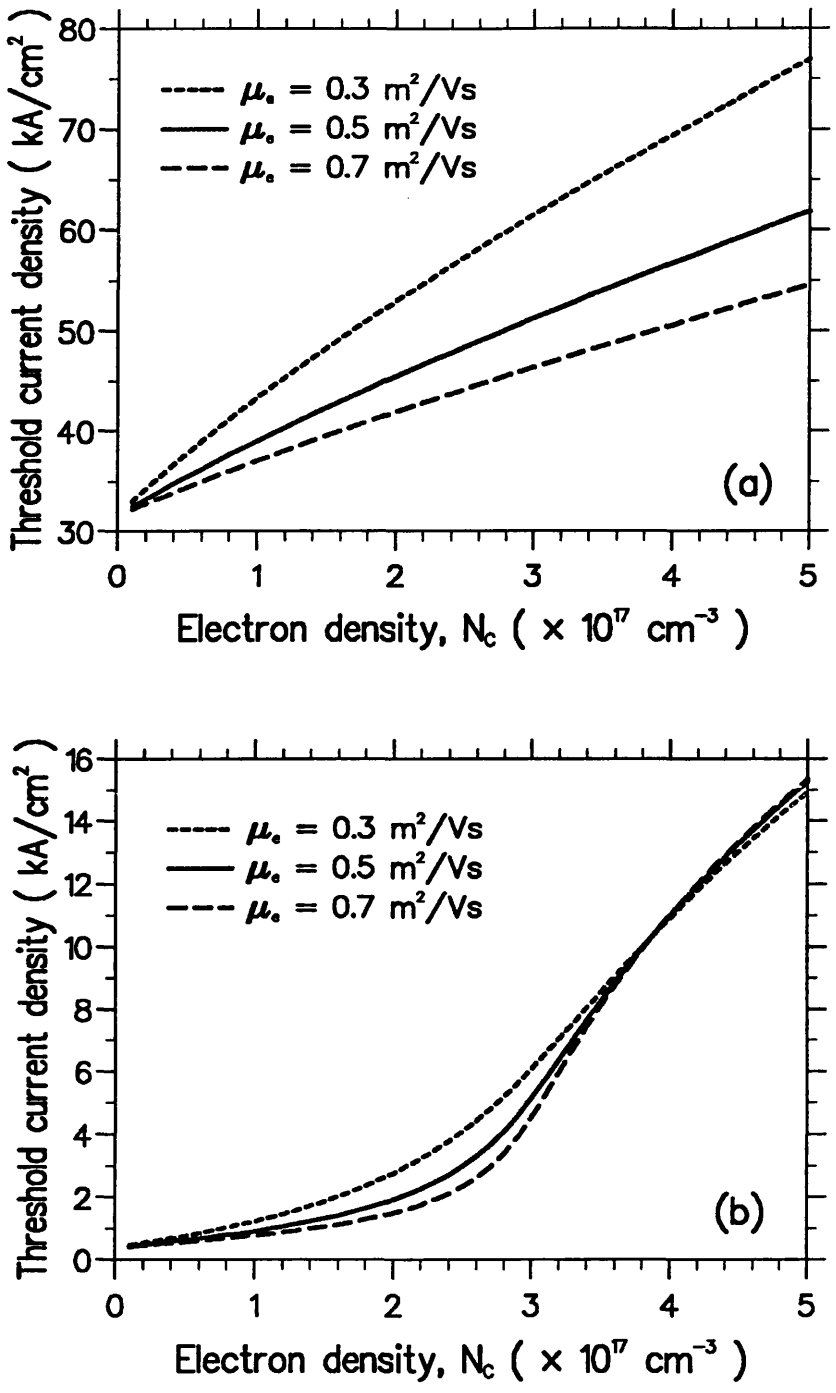

Figure 7.6: Dependence of threshold current density on electron density in the conducting layers for (a) structure I ($\lambda = 10$ μm), and (b) structure II ($\lambda = 60$ μm).

carrier plasmas at frequencies below the plasma frequency, optical absorption through photon–plasmon interaction increases rapidly. No such rapid increase in J_{th} is observed in Fig. 7.6(a) because the plasma frequency is lower than the emission frequency ($\approx$ 30 THz) of structure I over the range of N_c considered here.

It is also observed that increasing the electron mobility reduces the threshold current density at a given N_c. This is because higher electron mobility means longer scattering time (or lower scattering rate) of free electrons in the n-doped cladding layers, which leads to lower plasmon damping and thus lower optical absorption. The dependence of threshold current density on electron mobility is less sensitive in the case of structure II. This is possibly due to the very high absorption at the far-infrared wavelength of 60 μm, and hence a change in electron mobility will not affect the optical absorption significantly. It is also noted that electron mobility is inversely related to temperature. Thus, at high temperature electron mobility decreases and higher threshold current density is required for lasing. This is consistent with results shown in Figs. 7.6(a) and 7.6(b). Assuming $\mu_e = 0.5$ m^{2}V^{-1}s^{-1} at $T = 300$ K, it is found that reasonable threshold current densities of order 1–5 kA/cm^2 is achievable in structure II for room-temperature far-infrared ($\lambda = 60$ μm) lasing with N_c in the range of 1–3 $\times$ 10^{17} cm^{-3}. To achieve room-temperature mid-infrared ($\lambda = 10$ μm) lasing using structure I, J_{th} around 40–50 kA/cm^2 is required over the same range of N_c.

The analysis of carrier transport and lasing threshold operation presented in this thesis is based on the triple-coupled resonant tunnelling QW structures as shown in Figs. 6.5 and 6.6 of the previous chapter. Further optimization of these device structures needs to be carried out to lower the threshold current density for practical device operation. In this respect, the triple-coupled resonant tunnelling

QW structures as advocated in this thesis may be periodically repeated to form a superstructure. Such a superstructure, with graded-gap spacer [2] between each unit block of triple-coupled QW's to ensure efficient electron injection and charge screening, will effect a much higher multiplicative optical gain as well as provide better optical confinement. In addition, waveguide design based on the use of Bragg reflector waveguide structures [11] may be considered for enhancing the waveguiding properties of the infrared laser devices. Optimization of the triple-coupled resonant tunnelling QW structures based on the above design proposals would be expected to yield lower threshold current density for room-temperature operation of mid and far-infrared semiconductor lasers.

7.4 Conclusion

The transparency current density for achieving intersubband population inversion at $\lambda = 10$ μm and $\lambda = 60$ μm using triple-coupled resonant tunnelling QW structures has been calculated based on the electron transport model developed in the previous chapter. The transparency current density has been shown to be extremely sensitive to variation of the intersubband relaxation time. Optical loss analysis has also been carried out taking into account the device structures. Solution of the four-level electron rate equations from the transport model, consistent with the balance of optical gain and loss in the laser devices, enables the threshold current density to be calculated explicitly as a function of electron doping density in the cladding layers. The results show that a reasonably low threshold current density in the range of 1–5 kA/cm^2 is achievable for room-temperature lasing at $\lambda = 60$ μm. A significantly higher threshold current density of 40–50 kA/cm^2 is required for lasing at $\lambda = 10$ μm. The present analysis of carrier transport and lasing threshold operation in the mid and far-infrared wavelengths demonstrates

the feasibility of using current injection resonant tunnelling QW structures to realize semiconductor lasers based on intersubband transitions.

References

[1] J. Faist, F. Capasso, C. Sirtori, D. L. Sivco, A. L. Hutchinson, S. N. G. Chu, and A. Y. Cho, "Quantum-well intersub-band electroluminescent diode at $\lambda = 5$ μm," *Electron. Lett.*, vol. 29, pp. 2230–2231, 1993.

[2] J. Faist, F. Capasso, D. L. Sivco, C. Sirtori, A. L. Hutchinson, and A. Y. Cho, "Quantum cascade laser: a intersub-band semiconductor laser operating above liquid nitrogen temperature," *Electron. Lett.*, vol. 30, pp. 865–866, 1994.

[3] W. M. Yee, K. A. Shore, and E. Schöll, "Carrier transport and intersubband population inversion in coupled quantum wells," *Appl. Phys. Lett.*, vol. 63, pp. 1089–1091, 1993.

[4] W. M. Yee and K. A. Shore, "Threshold current density calculations for far-infrared semiconductor lasers," *Semicond. Sci. Technol.*, vol. 9, pp. 1190–1197, 1994.

[5] J. Faist, F. Capasso, C. Sirtori, D. L. Sivco, A. L. Hutchinson, S. N. G. Chu, and A. Y. Cho, "Measurement of the intersubband scattering rate in semiconductor quantum wells by excited state differential absorption spectroscopy." *Appl. Phys. Lett.*, vol. 63, pp. 1354–1356, 1993.

[6] J. Faist, C. Sirtori, F. Capasso, L. Pfeiffer, and K. W. West, "Phonon limited intersubband lifetimes and linewidths in a two-dimensional electron gas," *Appl. Phys. Lett.*, vol. 64, pp. 872–874, 1994.

[7] A. Seilmeier, H. J. Hübner, M. Wörner, G. Abstreiter, G. Weimann, and W. Schlapp, "Direct observation of intersubband relaxation in narrow multiple quantum well structures," *Solid-State Electron.*, vol. 31, pp. 767–770, 1988.

[8] R. Ferreira and G. Bastard, "Evaluation of some scattering times for electrons in unbiased and biased single- and multiple-quantum-well structures," *Phys. Rev. B*, vol. 40, pp. 1074–1086, 1989.

[9] S. I. Borenstain and J. Katz, "Evaluation of the feasibility of a far-infrared laser based on intersubband transitions in GaAs quantum wells," *Appl. Phys. Lett.*, vol. 55, pp. 654–656, 1989.

[10] E. D. Palik (editor), *Handbook of Optical Constants of Solid*, Orlando: Academic Press, 1985.

[11] P. M. Lambkin and K. A. Shore, "Nonlinear semiconductor Bragg reflection wave-guide structures," *IEEE J. Quantum Electron.*, vol. 27, pp. 824–829, 1991.

Chapter 8

Conclusions

This thesis has been concerned with the spectral properties of semiconductor lasers, with particular attention being paid to nonlinearity-induced spectral characteristics which may be utilized for device applications, and to the feasibility of extending the emission spectra of semiconductor lasers to the infrared wavelength region. Specifically, four main aspects of the spectral properties of semiconductor lasers have been studied, including self-locking FM laser operation, nearly degenerate four-wave mixing (NDFWM), all-optical frequency conversion and tuning, and infrared intersubband lasing. In the following, the significance of the results obtained from an investigation of these various aspects of the spectral properties of semiconductor lasers is summarized. Proposals for future work which may be undertaken to further enhance the understanding of these spectral properties are also presented.

8.1 Self-Locking FM Laser Operation

A multimode semiconductor laser model has been developed, based on the Lamb semiclassical laser theory, to study the multi-longitudinal-mode spectral behaviours of semiconductor lasers (chapter 2 and 3). Numerical integration of the multi-

mode semiconductor laser rate equations has been carried out. It has been shown that, for nonlinear gain parameters appropriate to long-wavelength (1.3–1.55 μm) semiconductor lasers, a self-induced phase-locked state may be obtained. The self-phase-locking has been shown to correspond to FM laser oscillation (as opposed to AM optical-pulse operation). Specifically, it has been demonstrated that *intrinsic multiwave mixing nonlinearities* occurring in the presence of nonlinear gain are responsible for the self-locking FM laser operation. The calculated optical output power and FM index in the self-locked state are in good agreement with experimental results. A small AM component is always present in the self-locked state, and pure self-locking FM oscillation is inhibited.

Nonlinear gain diagnostics have also been carried out to map out regions in the nonlinear coefficient parameter space where self-locking FM operation is expected to occur. Comparison between the presently calculated and the experimentally determined values of output power under which self-locking FM operation occurs provides a quantitative test for the possible range of values of the various nonlinearities present in semiconductor lasers.

A study of self-locking FM operation is important both for the understanding of nonlinear physical mechanisms in semiconductor lasers, and for possible device applications. The suppression of self-locking FM oscillation is critical for single-mode operation of laser diodes utilized in communication systems. On the other hand, FM operation of laser diodes is of current interest because of the possibility of using FM laser diodes in future coherent communication systems. Another important application of self-locking FM operation is short-pulse generation through the use of a dispersive optical fiber to convert the self-locking FM oscillation to an AM pulse train.

The present multimode laser model has been adapted from semiclassical gas

laser model to account for the properties of semiconductor lasers. As such, only the mode-amplitude and the phase rate equations are considered in the model. Nevertheless, significant insight has been gained into the nature of self-locking FM operation in semiconductor lasers using the present model. To provide a complete description of the self-locking dynamics in semiconductor lasers, there may be a need for the incorporation of the carrier density rate equation in the model. This latter aspect may be of interest for future consideration.

8.2 Nearly Degenerate Four-Wave Mixing

The effects of an external optical injection on the spectral properties of semiconductor lasers have been considered. Specifically, external probe signal induced nearly degenerate four-wave mixing (NDFWM) in laser diodes with nonuniform longitudinal gain distribution has been studied in chapter 4. A model for cavity-enhanced NDFWM in above-threshold Fabry-Perot (FP) laser diodes has been developed, which takes into account the FP cavity effects and the longitudinal variations of both the nonlinear wave-mixing interaction and the gain distribution. The importance of incorporating these longitudinal effects in the model has been established, particularly for laser diodes with low and/or asymmetric facet reflectivities.

The NDFWM model has been utilized to study the characteristics of phase conjugate signal generation in FP laser diodes. It has been shown that enhancements of conjugate output and NDFWM bandwidth can be obtained using laser diodes with low facet reflectivities. In particular, a 7–8 dB enhancement of conjugate reflectivity can be achieved in an asymmetric laser diode compared to a symmetric laser by reducing the input facet reflectivity from 0.3 to 0.1.

The successful development of optimized laser diodes for phase conjugate signal generation will provide a key component for implementing a wide range of high-speed optical information processing functions including cross-talk cancellation, optical-demultiplexing, optical sampling, optical fiber dispersion compensation via spectral inversion, and clock extraction. The high efficiency and the flexibility of the asymmetric FP laser diodes to act in both reflection and transmission modes serve to underline the wide applicability of the proposed structures. Further work may be undertaken to implement the semiconductor laser structures identified in the present work as phase conjugators for the multitude of applications indicated above.

8.3 All-Optical Frequency Conversion and Tuning

The NDFWM model has also been used to study the frequency conversion characteristics of asymmetric two-section laser diodes in chapter 5. It has been shown that a uniform frequency conversion efficiency can be obtained over a frequency detuning range of more than 10 GHz by injecting the input optical probe signal into the low-gain section of a two-section laser diode. Enhancement of frequency conversion bandwidth and efficiency can simultaneously be achieved by applying anti-reflection (AR) coating to the input facet at the low-gain section, and deriving the converted conjugate output from the same facet of the asymmetric two-section laser diode. The uniform conversion efficiency response is important for distortionless optical frequency conversion of wide-band signals.

In addition, a travelling-wave model has been developed in chapter 5 to investigate the wavelength tuning characteristics of asymmetric gain-levered (two-section) FP QW laser diodes. The carrier density has been shown to be highly

nonuniform along the longitudinal axis of the two-section laser, thus justifying the need for incorporating longitudinal variations of carrier density in the model. The present analysis has demonstrated that enhancement of wavelength tunability could be achieved in a asymmetric laser diode, compared to a symmetric laser, by applying AR coating to the facet at the low-gain section and applying HR coating to the facet at the high-gain section.

8.4 Infrared Intersubband Lasing

The possibility of extending the emission spectra of semiconductor lasers to the infrared wavelength regime has been explored in chapter 6 and 7. A carrier transport model has been developed which takes into account resonant tunnelling and intersubband emission–absorption processes. Opportunity for the achievement of intersubband population inversion in two prototype resonant tunnelling QW structures has been revealed.

Optical loss analysis taking into account the resonant tunnelling laser device geometry has also been carried out. The incorporation of optical loss analysis into the carrier transport model provides a complete formulation for the calculation of lasing threshold current density. It has been shown that reasonably low threshold current densities of 1–5 kA/cm^2 are achievable for room-temperature lasing at an operating wavelength of 60 μm. Significantly higher threshold current densities of 40–50 kA/cm^2 are required for lasing at 10 μm wavelength. The present analysis of carrier transport and optical loss in the infrared wavelengths has demonstrated the feasibility of using current injection resonant tunnelling QW structures to realize intersubband semiconductor lasers.

It is considered that the carrier transport model developed in this thesis gives

a useful prescription of the microscopic processes which determine the conditions for population inversion in intersubband semiconductor lasers. Incorporation of optical losses into the transport model underlines the challenge which remains to be faced in order to attain low-threshold devices. Attention now needs to be given to device design aspects which may serve to mitigate optical losses and hence assist in the implementation of practical room-temperature mid- and far-infrared semiconductor lasers.

Appendix A

List of Publications

A.1 Journal Publications

1. K. A. Shore and W. M. Yee, "Theory of self-locking FM operation in semiconductor lasers," *IEE Proc. Part J*, vol. 138, pp. 91–96, 1991.

2. W. M. Yee and K. A. Shore, "Multimode analysis of self locked FM operation in laser diodes," *IEE Proc. Part J*, vol. 140, pp. 21–25, 1993.

3. W. M. Yee, K. A. Shore, E. Schöll, "Carrier transport and intersubband population inversion in coupled quantum wells," *Appl. Phys. Lett.*, vol. 63, pp. 1089–1091, 1993.

4. W. M. Yee and K. A. Shore, "Threshold current density calculations for far-infrared semiconductor lasers," *Semicond. Sci. Technol.*, vol. 9, pp. 1190–1197, 1994.

5. W. M. Yee and K. A. Shore, "Nearly degenerate four-wave mixing in laser diodes with nonuniform longitudinal gain distribution," *J. Opt. Soc. America B*, vol. 11, pp. 1221–1228, 1994.

6. W. M. Yee and K. A. Shore, "Enhanced uniform phase conjugation in two-section asymmetric laser diodes," *Opt. Lett.*, accepted for publication.

A.2 Conference Papers

1. W. M. Yee and K. A. Shore, "Multimode analysis of FM locking in laser diodes," SIOE'92 (Semiconductor Integrated Optoelectronics '92), Cardiff, Wales, 1992.

2. W. M. Yee, K. A. Shore, and E. Schöll, "Intersubband population inversion by resonant tunnelling in semiconductor coupled quantum wells," SIOE'93, Cardiff, Wales, 1993.

3. W. M. Yee, K. A. Shore, and E. Schöll, "Intersubband population inversion in coupled quantum well structures," IEE Colloquium, Digest No. 1993/057, London, UK, 1993.

4. W. M. Yee, K. A. Shore, and E. Schöll, "Quantum-well structures for intersubband population inversion," Opt. Soc. America, Annual Meeting, Paper FB3, Toronto, Canada, 1993.

5. W. M. Yee and K. A. Shore, "Threshold characteristics of far-infrared laser diodes," SIOE'94, Cardiff, Wales, 1994.

6. W. M. Yee and K. A. Shore, "Enhanced multiwave mixing and phase conjugation in asymmetric laser diodes," SIOE'94, Cardiff, Wales, 1994.

7. W. M. Yee and K. A. Shore, "Gain and threshold current calculations for far-infrared semiconductor lasers," CLEO/Europe–EQEC, Paper CTuK24, Amsterdam, The Netherlands, 1994.

8. W. M. Yee and K. A. Shore, "Enhancement of multiwave mixing in laser diodes with longitudinal gain variations," CLEO/Europe–EQEC, Paper QThG17, Amsterdam, The Netherlands, 1994.

Theory of self-locking FM operation in semiconductor lasers

K.A. Shore
W.M. Yee

Indexing terms: Semiconductor lasers, Modulation

Abstract: Gain saturation and multiwave mixing are shown to give rise to self-locking effects in semiconductor lasers resulting in FM operation. The analysis is shown to be in agreement with recently reported experimental observations of this phenomenon.

1 Introduction

The use of amplitude modulation (AM) and phase or frequency modulation (FM) to achieve mode-locking is very well known in several laser systems [1]. Particular emphasis has been given to developing various AM-locking techniques with a view to the production of ultrashort (picosecond and subpicosecond) optical pulses. In contrast, rather less effort has been given over to the study and application of FM locking properties of lasers. For semiconductor lasers, in particular, the possibilities of achieving FM-locking have received relatively little attention. Although Saito *et al.* [2] reported FM laser operation in an external cavity semiconductor laser some time ago, there has not been a sustained attempt to explore this topic using semiconductor lasers. Lately, however, a number of workers have begun to address important issues related to the FM locking phenomenon in semiconductor lasers. Bosl and coworkers have shown how an intracavity phase modulator may be used to demonstrate *active* FM-locking in AlGaAs laser diodes [3]. Schremer and Tang [4] (and references therein) also have studied FM locking effects in external cavity AlGaAs lasers and have shown a phase reversal effect in this configuration. In this paper it is shown that nonlinear optical properties may, in contrast, give rise to self-locked FM behaviour in semiconductor lasers. The basic physical effect which arises in these circumstances is that, due to gain nonlinearities, longitudinal modes of the laser become equally spaced in frequency. The cavity modes then form a single frequency-modulated optical wave called an 'FM supermode'. As a result, in pure FM operation, the field of the FM supermode has a constant amplitude E_0 and is of the form

$$E(t) = E_0 \cos(\omega_0 t + m \cos \omega t) \quad (1)$$

Then the relative amplitude of the cavity modes is defined by Bessel functions:

$$E(t) = E_0 \sum_n J_n(m) \cos[(\omega_0 + n\omega)t - n\pi/2] \quad (2)$$

The FM supermode is then characterised by a modulation index, m, a central frequency ω_0, and a mode spacing frequency ω.

Clearly, the above forms are appropriate also to (deliberately) frequency-modulated lasers. It is emphasised, however, that here the form of the output arises due to the intrinsic properties of nonlinear multimode interactions in the semiconductor lasers and does not result from modulation (of either the amplitude or the frequency) of the semiconductor laser.

2 Experimental basis

The motivation for the present theoretical treatment is the experimental work of Tiemeijer *et al.* who recently demonstrated self-induced (passive) FM locking in multimode Fabry-Perot InGaAsP laser diodes [5]. The Tiemeijer approach was to measure the fundamental and second harmonic spectrum of the lasers. Then, using the measured fundamental multimode spectrum, a comparison was made between the measured second harmonic spectrum and the second harmonic spectrum expected in the cases

(i) free-running
(ii) mode-partitioned behaviour
(iii) FM-locked behaviour.

On this basis it was concluded that FM-locking was occuring in the devices. Tiemeijer then proceeded with some analysis of the behaviour but predicated that analysis on the assumption that an FM-locked state had been attained. The objective of this paper is to show, via an integration of multimode laser rate equations, that the occurrence of self-locking FM operation in semiconductor lasers may indeed be attributed to nonlinear mechanisms arising in these devices. In particular, it is demonstrated that the strength of nonlinearity required to obtain FM-locking is in accordance with values of gain saturation and multiwave mixing coefficients typically encountered in long-wavelength semiconductor lasers.

3 Formalism

Passive FM locking was examined in gas lasers many years ago [6, 7] and has been analysed in that context using the model developed by Lamb [8]. An important conclusion from that earlier work is that the inclusion of three cavity modes is adequate to establish the criteria for mode-locking [9]. In the present analysis, the three-mode Lamb model is adapted to account for the properties of semiconductor lasers. We consider three modes of frequencies ν_1, ν_2, ν_3 where mode 2 is taken to be nearest to

Paper 7872J (E3, E13), first received 27th July and in revised form 7th December 1990

The authors are with the University of Bath, School of Electronic and Electrical Engineering, Bath, BA2 7AY, United Kingdom

the peak gain. The modes are defined by field phasors of amplitude E_1, E_2, E_3 and phase ϕ_1, ϕ_2, ϕ_3.

The amplitude and frequency determining equations given by Lamb in the case of three modes are

$$\dot{E}_1 = E_1\left(\alpha_1 - \sum_{m=1}^{3} \Theta_{1m} E_m^2\right) - E_2^2 E_3(\eta_{23} \cos \Psi + \xi_{23} \sin \Psi) \quad (3a)$$

$$\dot{E}_2 = E_2\left(\alpha_2 - \sum_{m=1}^{3} \Theta_{2m} E_m^2\right) - E_1 E_2 E_3(\eta_{13} \cos \Psi - \xi_{13} \sin \Psi) \quad (3b)$$

$$\dot{E}_3 = E_3\left(\alpha_3 - \sum_{m=1}^{3} \Theta_{3m} E_m^2\right) - E_2^2 E_1(\eta_{21} \cos \Psi + \xi_{21} \sin \Psi) \quad (3c)$$

$$\nu_1 + \dot{\phi}_1 = \Omega_1 + \sigma_1 + \sum_{m=1}^{3} \tau_{1m} E_m^2 - (E_2^2 E_3/E_1)(\eta_{23} \sin \Psi - \xi_{23} \cos \Psi) \quad (4a)$$

$$\nu_2 + \dot{\phi}_1 = \Omega_2 + \sigma_2 + \sum_{m=1}^{3} \tau_{2m} E_m^2 + (E_1 E_3)(\eta_{13} \sin \Psi + \xi_{13} \cos \Psi) \quad (4b)$$

$$\nu_3 + \dot{\phi}_3 = \Omega_3 + \sigma_3 + \sum_{m=1}^{3} \tau_{3m} E_m^2 - (E_2^2 E_1/E_3)(\eta_{21} \sin \Psi - \xi_{21} \cos \Psi) \quad (4c)$$

where Ω_1, Ω_2 and Ω_3 are the resonance frequencies of the passive cavity.

α_m is the linear net (amplitude) gain; Θ_{nm} is the self/cross saturation coefficient describing the effect of gain suppression on mode n due to the presence of oscillating mode m; it consists of nonlinear components due to hole-burning and population pulsation gain suppression; η and ξ are the the general saturation coefficients describing the phase dependent coupling between modes, produced by combination tones in the active medium (multiwave mixing effect); σ is the power independent pulling coefficient arising from the dispersive nature of the medium; τ_{nm} is the cross/self pushing coefficient which takes into account power dependent 'mode repulsion' effects between the various modes, and Ψ is the relative phase angle defined as

$$\Psi = (2\nu_2 - \nu_1 - \nu_3)t + 2\phi_2 - \phi_1 - \phi_3 \quad (5)$$

Using eqn. 5, we obtain the equation of motion for Ψ,

$$\dot{\Psi} = 2(\nu_2 + \dot{\phi}_2) - (\nu_1 + \dot{\phi}_1) - (\nu_3 + \dot{\phi}_3) \quad (6)$$

Substituting the frequency-determining eqns. 4 into 6, we obtain

$$\dot{\Psi} = S + A \sin \Psi + B \cos \Psi \quad (7)$$

where

$$S = 2\sigma_2 - \sigma_1 - \sigma_3 + E_1^2(2\tau_{21} - \tau_{11} - \tau_{31}) + E_2^2(2\tau_{22} - \tau_{12} - \tau_{32}) + E_3^2(2\tau_{23} - \tau_{13} - \tau_{33}) \quad (8)$$

$$A = 2E_1E_3\eta_{13} + (E_2^2E_3/E_1)\eta_{23} + (E_2^2E_1/E_3)\eta_{21} \quad (9)$$

$$B = 2E_1E_3\xi_{13} - (E_2^2E_3/E_1)\xi_{23} - (E_2^2E_1/E_3)\xi_{21} \quad (10)$$

Hence it is seen that the frequency and amplitude determining equations do not depend on the phases individually, but only in combination as the relative phase angle Ψ.

Eqns. 3*a–c* and 7 are the four basic working equations in this analysis. These simultaneous differential equations were solved numerically (using the Kutta-Merson method of integration within a standard library routine) to obtain the mode amplitudes and the relative phase angle Ψ.

3.1 Estimation of parameter values

The amplitude and frequency determining equations introduced above were originally developed for gas lasers. As such it is necessary to identify the semiconductor laser analogues of the various terms contributing to the nonlinear dynamics. It is apparent that the coupled mode equations used to analyse multimode semiconductor laser operation are very similar to the equations given above. It is straight forward then to obtain the correspondence between the self and cross saturation coefficients.

Consider the amplitude determing eqn. 3*a*

$$\dot{E}_1 = E_1\alpha_1\left[1 - \frac{\Theta_{11}}{\alpha_1} E_1^2 - \frac{\Theta_{12}}{\alpha_1} E_2^2 - \frac{\Theta_{13}}{\alpha_1} E_3^2\right] + \cdots \quad (11)$$

If we let

$$I = E^2 \quad (12)$$

and differentiate with respect to t, we obtain

$$\dot{I} = 2E\dot{E} \quad (13)$$

It follows from eqn. 11 that

$$\dot{I}_1 = 2\alpha_1 I_1\left[1 - \frac{\Theta_{11}}{\alpha_1} I_1 - \frac{\Theta_{12}}{\alpha_1} I_2 - \frac{\Theta_{13}}{\alpha_1} I_3\right] + \cdots \quad (14)$$

This equation is compared with the coupled mode equations for multimode lasers [10] given by equation

$$\dot{p}_1 = v_g g_0 p_1[1 - \beta_{11}p_1 - \beta_{12}p_2] + \text{other terms} \quad (15)$$

where $v_g = c/n_g$ is the group velocity and g_0 is the linear gain.

We note that $I = p$ is the photon density (with units cm^{-3}) and

$$\alpha_1 = (v_g g_0/2) \quad (16)$$

$$\Theta_{11} = \alpha_1\beta_{11} \quad (17)$$

Using values given by Agrawal [10] where $n_g \approx 4$ and $\beta \approx 6.7 \times 10^{-17}$ cm^3 and assuming $g_0 = 60$ cm^{-1}, we find

$$v_g = 7.49 \times 10^9 \text{ cm s}^{-1}$$

$$\alpha_1 = 2.25 \times 10^{11} \text{ s}^{-1}$$

$$\Theta_{11} = 1.51 \times 10^{-5} \text{ cm}^3 \text{ s}^{-1}$$

The values of other parameters such as σ, τ, η and ξ are assumed to have the same order of magnitudes as Θ. With these values, the amplitude and frequency determining equations are adapted to model semiconductor laser multimode operation and then may be solved numerically.

4 Self-locking FM operation

As explained by Sayers and Allen [7], to determine the conditions under which locking occurs it is necessary to integrate the field amplitude and phase rate equations allowing the phase angle to become either constant (self-

locked state) or monotonically increasing with time (unlocked state). For the present work it is shown that for nonlinear gain parameters appropriate to semiconductor lasers, a self-locked state may be obtained in this way.

From the preceding Section we estimate that all the nonlinear parameters required for the present analysis are of the order 10^{-5} cm^3/s. Then, for example, using the value 1.5×10^{-5} cm^3/s for all the nonlinear coefficients, it was found that the three-mode semiconductor laser evolved to a self locking state. The dynamical behaviours of the field amplitudes and phase angle are shown in Fig. 1.

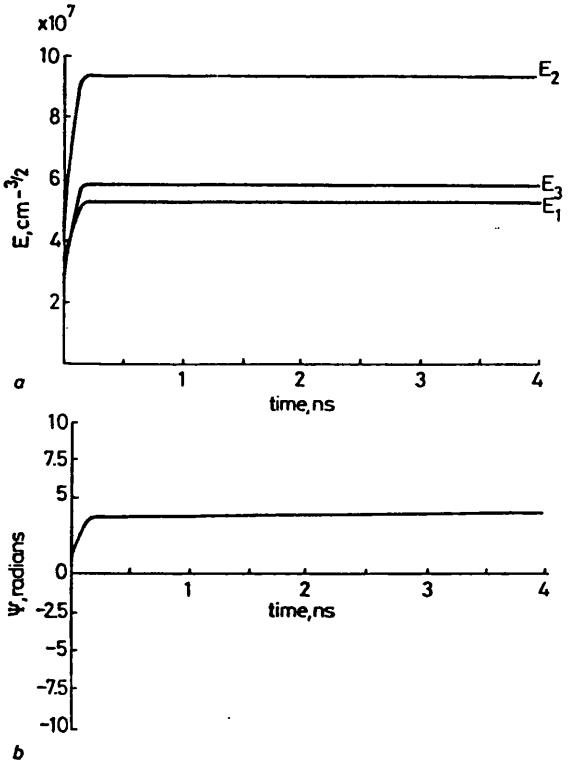

Fig. 1 *Mode amplitudes and phase angle against time for gain nonlinearities of 1.5 × 10^{-5} cm^3/s when a self-locked state is not achieved*
a Mode amplitudes
b Phase angle

It must be stressed that this is a highly nontrivial result. It has been demonstrated here that gain nonlinearities typical of semiconductor lasers are indeed sufficient to cause self-locking to occur in multimode devices. In the following Section, attention will be given to the parameter dependence of self-locking. Here though we give an immediate illustration of the time dependence of the field amplitudes when self-locking does not occur. In Fig. 2 it is shown that in an unlocked state the phase angle increases linearly with time. In this case, side mode suppression to a large nonlinear gain causes the laser to run single mode.

4.1 Output power in self-locked state

To make a comparison with experimental observations of FM locking it is necessary to calculate the output power of the laser in the self-locked state. It is possible to relate the output power per facet P to the photon density in the laser cavity p by way of the relationship

$$P = 0.5 h\nu n_g g_0 p V \tag{18}$$

considering the InGaAsP laser diodes and taking typical values [5] of V, the device active volume (28 μm^3); n_g, the group refractive index [4]; g_0, the linear gain (60 cm^{-1}) and taking the photon energy $h\nu$ corresponding to an operating wavelength of 1.3 μm, it is found that eqn. 18 may be written as

$$P = 9.6 \times 10^{-16} p \text{ mW} \tag{19}$$

where p is the photon density.

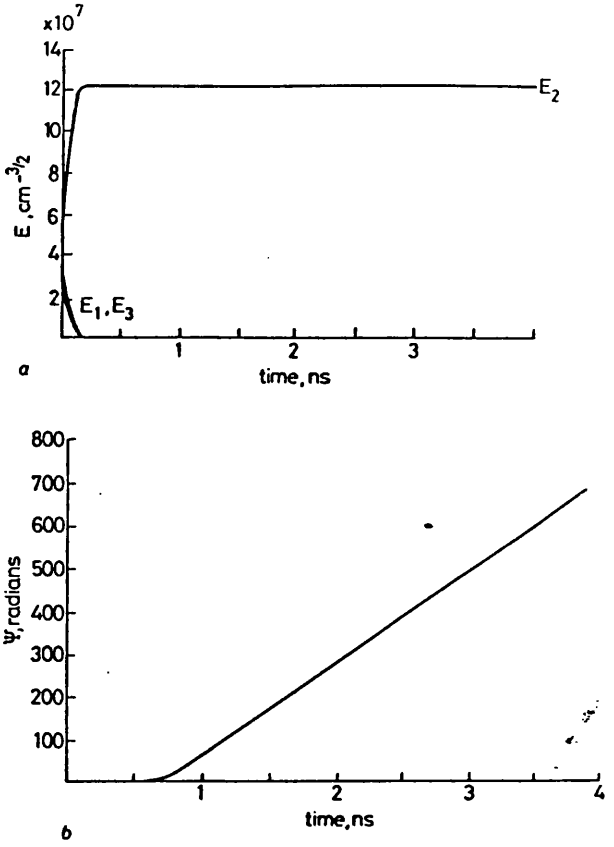

Fig. 2 *Mode amplitudes and phase angle against time for gain nonlinearities of 10 × 19^{-5} cm^3/s when a self-locked state is not achieved*
a Mode amplitudes
b Phase angle

For the self-locked state shown in Fig. 1 the field amplitudes are

$$E^1 = 5.273 \times 10^7 \text{ cm}^{-3/2}$$

$$E_2 = 9.364 \times 10^7 \text{ cm}^{-3/2}$$

$$E_3 = 5.825 \times 10^7 \text{ cm}^{-3/2}$$

The corresponding total photon density is then estimated to be 1.494×10^{16} cm^{-3}. With this value it is found that the laser output in the self-locked state is about 14.3 mW. That estimate is in excellent agreement with the experimental results reported by Tiemeijer *et al.* [5], where FM operation was observed powers in the range 7 mW to 15 mW.

In contrast, using parameters appropriate to GaAs lasers, where the nonlinear parameters are typically of order 10^{-6} cm^3/s [10], it was found that self-locking was predicted at output powers of the order of 200 mW to 300 mW. Hence these effects would not be anticipated in GaAs lasers under normal operating conditions.

4.2 FM operation

The above consideration of the output power in the self-locked state provides strong support for the assertion that gain nonlinearities account for the observations of Tiemeijer *et al.* [5]. It is also important to consider the

phase information obtained from the simulations described in this paper. In particular, the purity or otherwise of the FM operation may be assessed from the calculated value of the phase angle Ψ. Where Ψ is an integer multiple of 2π, AM locking behaviour would be expected. On the other hand, FM locking would be obtained when Ψ has a value of π. In the calculations described here, Ψ is found to lie in the range 3 to 4 radians. For example, in the case shown in Fig. 1 the value of Ψ is 3.788. It is clear then that AM locking does not occur here but also it is apparent that pure FM locking is not predicted within the present formalism. However, since the simulations described here consider only three oscillating modes it is clear the the full set of Bessel-function side bands contained in eqn. 2 are not included in the present treatment. For this aspect, in particular, there is a need to generalise the present analysis to a multimode formalism. As indicated below, that extension is reserved for future work. At the moment it is simply noted that the predicted temporal evolution of the self-locked state in the three-mode analysis does not correspond to pure FM operation.

5 Nonlinear gain diagnostics

In this Section we summarise results obtained from an investigation of the parameter dependence of self-locked operation using a three-mode model. Within the acknowledged limitation of this model it is sought to map out regions in the nonlinear coefficient parameter space where FM-locking is expected to occur. It is suggested that this procedure may be useful as a means of calibrating nonlinear gain mechanisms in semiconductor lasers. A considerable effort has been directed at elucidating the mechanism(s) for gain nonlinearities in semiconductor lasers (see Reference 11 for a recent review). In particular, the role of multiwave mixing processes has been emphasised recently [12]. It is argued, therefore, that the results given below may be used to give quantitative tests for theories of nonlinear gain in semiconductor lasers.

5.1 Self and cross saturation effects

The dependence of the mode amplitudes and relative phase angle on the self and cross saturation coefficient, Θ_{nm}, is illustrated in Figs. 3 and 4. It is found that

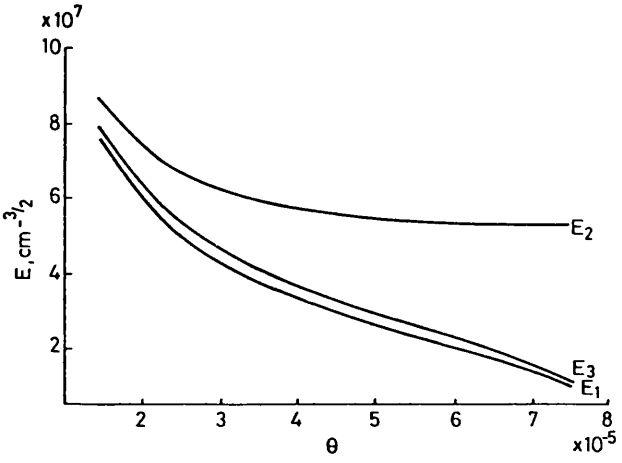

Fig. 3 *Mode amplitudes in the self-locked state as functions of the self-cross saturation coefficient*

increasing the value of Θ (other things being held constant) will decrease the amplitudes of the various modes but will increase the steady-state value of the relative phase angle, in mode-locked operation.

The reduction in mode amplitudes for increased values of Θ_{nm} can be explained as follows.

Consider the amplitude determining equation for mode 1:

$$\dot{E}_1 = E_1[\alpha_1 - \Theta_{12}E_2^2 - \Theta_{13}E_3^2] - \Theta_{11}E_1^3 + \text{other terms} \quad (20)$$

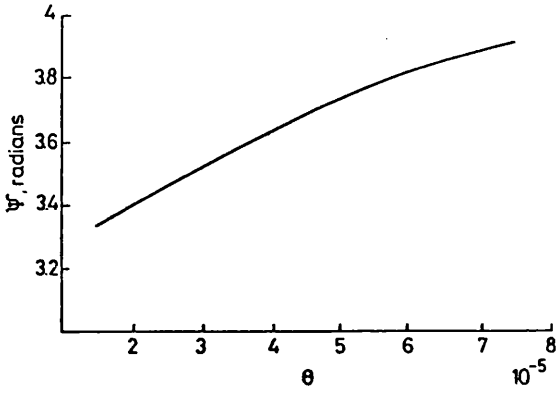

Fig. 4 *Phase angle in the self-locked state as functions of the self-cross saturation coefficient*

In the absence of any interaction between the modes, the single mode equation would be

$$\dot{E}_1 = \alpha E_1 - \beta_1 E_1^3 \quad (21)$$

where $\beta_1 = \Theta_{11}$ is the self saturation coefficient for mode 1. Comparing these two equations, we see that the effect of the interaction terms Θ_{12} and Θ_{13} is to reduce the effective gain of mode 1. α in eqn. 21 is effectively replaced by terms in brackets in eqn. 20. Hence, increasing Θ_{nm} will decrease the effective gain of that mode resulting in reduced steady-state amplitudes.

It is also found that the rate of decrease of amplitude with respect to Θ is smallest in the central mode compared with the side-modes. For $\Theta > 8 \times 10^{-5}$, the amplitudes of the two sidemodes reduce to zero rapidly leaving only mode 2 in oscillation and mode-locking ceases to occur. We thus see that there is an upper limit to the value of Θ above which no-locking is observed. Since Θ is inversely related to mode amplitudes and thus optical power, this implies that mode-locking occurs only when the laser optical power exceeds a minimum value. Furthermore, increasing Θ will increase the steady-state values of the relative phase angle, thus increasing the deviation of Ψ from the value π radians. The resulting FM intensity curve will be highly distorted due to the increase in the AM component in the FM optical wave.

5.2 Multiwave mixing effects

The parameter η and ξ represents the general saturation terms which take into account multiwave mixing effects on the mode coupling between the lasing modes. Figs. 5 and 6 illustrate the dependence of the mode amplitudes and relative phase angle upon these general saturation terms. It is observed that the amplitudes of the side modes increase monotonically with increasing η, whereas the amplitude of the central mode decreases at first and then increases after passing through a minimum point. For values of $\eta \geq 2 \times 10^{-5}$, the output power of the laser is found to be greater than 30 mW and this output power increases exponentially as η is further increased. Since for typical semiconductor lasers, the output power at mode-locking is of the order of 12 to 15 mW, we deduce that

under normal circumstances, the value of η is likely to be smaller than 2×10^{-5}.

From the amplitude variations curve, we also observe that the amplitudes of the side-modes decay to zero rapidly for values of $\eta < 0.3 \times 10^{-5}$, and that the laser

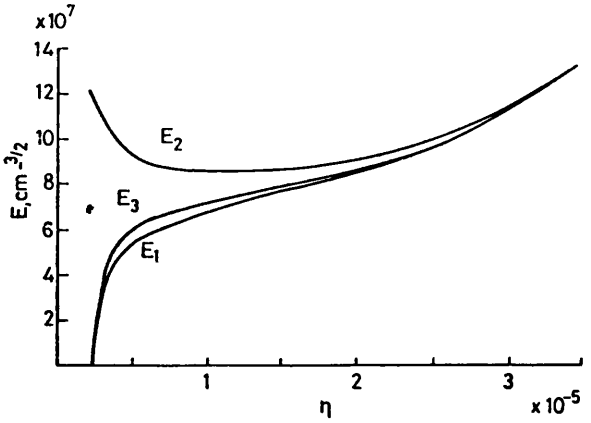

Fig. 5 *Mode amplitudes in the self-locked state as functions of the multiwave mixing nonlinearity coefficient*

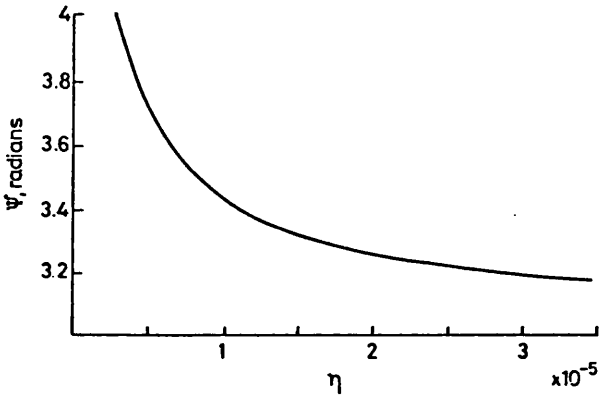

Fig. 6 *Phase angle in the self-locked state as functions of the multiwave mixing nonlinearity coefficient*

operation goes to no-locking below this value. Furthermore, only one single longitudinal mode is oscillating under the no-locking situation. Thus, mode-locked operation only occurs when η exceeds a minimum threshold value.

The parameters τ and σ describe the mode pushing and pulling effects of the laser modes. It is found that mode-locking is critically dependent upon the relative magnitudes of η, ξ, τ and σ, as will be discussed in the following paragraphs.

Since mode amplitudes always settle to constant values in steady-state (regardless of whether or not there is mode-locking), the parameters S, A and B in the frequency determining equation can be treated as constants,

$$\Psi = S + A \sin \Psi + B \cos \Psi \tag{22}$$

where S, A and B are given in eqns. 8–10. Hence, we can treat the frequency determining equation independently from the amplitude-determining equations in steady-state analysis. Eqn. 20 can be expressed as

$$\Psi = S + C \sin (\Psi - \Psi') \tag{23}$$

where

$$C = \sqrt{(A^2 + B^2)} \tag{24}$$

and

$$\Psi' = -\arctan (B/A) \tag{25}$$

From eqn. 23, two situations exist. If $A^2 + B^2 < S^2$, $\dot{\Psi}$ is always positive and hence Ψ is monotonically changing with time and thus the modes are not locked. If $A^2 + B^2 > S^2$, $\dot{\Psi} = 0$ in some instances. This implies that Ψ is independent of time and thus, by definition, $\nu_2 - \nu_1 = \nu_3 - \nu_2$ and the relative phase angle rapidly approaches a constant value, the actual value being dependent on S and other parameters in the amplitude-determining equations. The modes are therefore locked. Thus the necessary criterion for self locking is given by

$$A^2 + B^2 \geq S^2 \tag{26}$$

Since A and B are dependent upon η and ξ, whereas S is a function of σ and τ, from eqn. 26 we see that the mode locking may be achieved if the value of η and ξ is large compared to σ and τ. On the other hand, eqn. 26 is a necessary, but not sufficient, condition for mode-locking: to achieve locking it is also essential that the optical power of the laser exceeds a threshold value at which the nonlinear gain is significant [5]. Since the optical power, and hence the mode amplitudes are dependent upon Θ_{nm}, α, η and ξ, there is no explicit relationship to determine when, and at what values of the various parameters, mode-locking takes place. It is found that generally mode-locking is critically dependent on the relative magnitudes of η and ξ with respect to α and Θ. It is also established that locking is more sensitive to the multiwave mixing parameters, η and ξ than the mode pulling/pushing effects, σ and τ.

In summary, it has been shown that

(i) For gain saturation parameters greater than about 8×10^{-5} cm^3/s, side mode suppression is such that the laser operates in a single longitudinal mode (at the central mode frequency) and hence FM operation cannot occur.

(ii) For four-wave mixing nonlinearities less than about 2.5×10^{-5} cm^3/s the central frequency again dominates due to insufficient cross-mode coupling.

(iii) For four-wave mixing nonlinearities greater than about 2×10^{-5} cm^3/s self-locking requires laser output powers in excess of 30 mW. The self-locked output power increases with increased nonlinearity.

Also it was found that

(iv) The value of the linear gain parameter does not significantly affect the behaviours described above. The value of the linear gain does, of course, help determine the powers in the locked state.

The results summarised in (i) and (ii) delimit regions in the nonlinear parameter space for which self-locking is sustained. Similarly, the determination of optical output powers in the self-locked state, indicated in (iii) and (iv), provide further indications of the gain nonlinearities present in the laser.

6 Conclusion

A three-mode model has been used to demonstrate the role of gain nonlinearities in effecting self-locked FM oscillation in semiconductor lasers. The requisite gain nonlinearities and lasing field intensities have been shown to be consistent with experimental observations. To demonstrate intensity-invariant FM operation and to establish the depth of FM modulation in the self-locked state, it is necessary to take more than three modes into account. An extension of the above formalism to include

a larger number of oscillating modes may easily be made. However, since considerable numerical work is required in that case, the application of the multimode model is reserved for future work.

7 Acknowledgments

Dr. L.F. Tiemeijer, Philips Research Labs., Eindhoven is thanked for discussions and correspondence on this topic. The work described here was supported by SERC grant no. GR/D/74437.

8 References

1 SIEGMAN, A.E.: 'Lasers' (University Science Books, 1986), pp. 1041–1049
2 SAITO, S., NILSSON, O., and YAMAMOTO, Y.: 'Oscillation center frequency tuning, quantum FM noise and direct frequency modulation characteristics in external grating loaded semiconductor lasers', *IEEE J. Quant. Electron.*, 1982, QE-18, pp. 961–970
3 BOSL, J., BAUER, R., RAUCH, H., PENNING, U., WEIMANN, G., and SCHLAPP, W.: 'Modelocking of AlGaAs laser diode by intracavity AlGaAs phase modulator', *Electron. Lett.*, 1989, 25, pp. 864–866
4 SCHREMER, A., and TAN, C.L.: 'Abrupt phase reversal in frequency-modulated external cavity semiconductor lasers', *Appl. Phys. Lett.*, 1989, 55, pp. 1832–1834
5 TIEMEIJER, L.F., KUINDERSMA, P.I., THIJS, P.J., and RIKKEN, G.L.J.: 'Passive FM locking in InGaAsP semiconductor lasers', *IEEE J. Quant. Electron.*, 1989, QE-25, pp. 1385–1392
6 HARRIS, S.E., and McDUFF, O.P.: 'Theory of FM laser oscillation', *IEEE J. Quant. Electron.*, 1965, QE-1, pp. 245–262
7 SAYERS, M.D., and ALLEN, L.: 'Amplitude, competition, self-locking, beat frequency and time development in a three-mode gas laser', *Phys. Rev. A*, 1970, 1, pp. 1730–1746
8 LAMB, W.E.: 'Theory of an optical maser', *Phys. Rev.*, 1964, 134, pp. A1429–A1450
9 SARGENT, M., SCULLY, M.P., and LAMB, W.E.: 'Laser physics' (Addison Wesley, Reading, Mass., USA, 1974)
10 AGRAWAL, G.P.: 'Gain nonlinearities in semiconductor lasers', *IEEE J. Quantum Electron.*, 1987, QE-23, pp. 860–868
11 SHORE, K.A., and McCALL, M.W.: 'Nonlinear and quantum optics of semiconductor laser devices', *Prog. Quantum Electron.*, 1990, 14, pp. 63–129
12 DE FONZO, A.P., and GOMATAM, B.: 'Gain nonlinearities in semiconductor lasers and amplifiers', *Appl. Phys. Lett.*, 1990, 56, pp. 611–613

Multimode analysis of self locked FM operation in laser diodes

W.M. Yee
K.A. Shore

Indexing terms: FM laser operation, Optical fibre communication

Abstract: A multimode formalism has been used to estimate the intrinsic modulation index of semiconductor lasers. The calculated value of 1.3 is in agreement with the available experimental evidence. Pure FM operation is inhibited and a small AM component is present in the self locked FM supermode.

1 Introduction

Active and passive mode locking of lasers, effected either by applying amplitude modulation (AM) or phase/frequency modulation (FM) inside the laser cavity to cause the longitudinal modes to interact with one another, thereby locking them in phase, have been widely used to generate ultrashort (picosecond and subpicosecond), repetitive optical pulses. FM mode locking, apart from providing a technique to produce periodic optical pulses, can also generate an FM supermode signal in which the amplitude envelope is constant but a periodic frequency sweep occurs in the time signal [1, 2]. Some effort has been given to the study of FM locking phenomenon in semiconductor lasers in view of the possibility of using frequency modulation in optical fibre communications. The relationship of FM laser operation and short pulse generation was investigated by Schremer and coworkers [3]. Nietzke *et al.* have studied the generation of near-FM-operation sidebands by four-wave mixing nonlinearities [4]. Recently, Tiemeijer *et al.* experimentally demonstrated self induced FM supermode operation in multimode Fabry–Perot InGaAsP laser diodes [5]. In earlier work [6], we established the role of gain nonlinearities in causing self locked FM oscillation in semiconductor lasers, using a three-mode model. The requisite gain saturation and multiwave mixing nonlinearities have been shown to be consistent with experimental observations of Tiemeijer *et al.* Although a three-mode model is sufficient to demonstrate the occurrence of intrinsic FM locking, it is necessary to extend the model of Reference 6 to take more than three modes into account to calculate the depth of frequency modulation.

In the present work, a multimode analysis of self locked FM operation using five, seven and nine modes in semiconductor lasers is reported. A modulation index of 1.3 has been found for the case of a five-mode FM supermode. This calculated modulation index is in agreement with available experimental evidence. Comparison between the calculated amplitude spectrum and the theoretical ideal Bessel function sideband spectrum shows that the self locked oscillation approaches pure FM operation. The inhibition of pure FM operation is evident from the time-domain representations of the self locked supermode.

Paper 9294J (E3, E13), first received 12th June and in revised form 12th October 1992

The authors are with the University of Bath, School of Electronic and Electrical Engineering, Bath BA2 7AY, United Kingdom

2 Formalism

Passive FM locking was examined in gas lasers many years ago [2, 7] and theoretical analysis performed in that context based on Lamb's model of self consistent multimode equations [8]. It was concluded from the work that the inclusion of three cavity modes is adequate to establish the criteria for mode locking. In a previous work [6], the Lamb equations for three cavity modes were adapted to account for semiconductor laser properties and used to analyse self locked FM operation in semiconductor lasers. It was established that nonlinearities in semiconductor lasers may indeed give rise to self locked FM operation at output power level consistent with experiment of Tiemeijer [5]. In the present work, more than three modes are incorporated into the Lamb self consistent equations to obtain pure FM operation and calculate the modulation index of the FM supermode.

We consider an odd number of modes N with frequencies ν_n where $n = 1, 2, \ldots, N$, and $\nu_{(1+N)/2}$ is the central mode nearest to the gain peak. The modes are defined by field phasors of amplitudes E_n and phases ϕ_n. The amplitude and frequency determining equations given by Lamb for a multimode laser are

$$\dot{E}_n = \alpha_n E_n - \sum_\mu \sum_\rho \sum_\sigma E_\mu E_\rho E_\sigma \times \mathrm{Im}\,\{\vartheta_{n\mu\rho\sigma} \exp(i\Psi_{n\mu\rho\sigma})\} \quad (1)$$

$$\nu_n + \dot{\phi}_n = \Omega_n + \sigma_n - \sum_\mu \sum_\rho \sum_\sigma E_\mu E_\rho E_\sigma E_n^{-1} \times \mathrm{Re}\,\{\vartheta_{n\mu\rho\sigma} \exp(i\Psi_{n\mu\rho\sigma})\} \quad (2)$$

where $\Psi_{n\mu\rho\sigma}$ is the relative phase angle defined as

$$\Psi_{n\mu\rho\sigma} = (\nu_n - \nu_\mu + \nu_\rho - \nu_\sigma)t + \phi_n - \phi_\mu + \phi_\rho - \phi_\sigma \quad (3)$$

and $i = \sqrt{(-1)}$, Im and Re denote the imaginary and real parts of the complex quantity in the curly braces, respectively, and α_n prescribes the linear gain of the laser. Gain

This work is supported by SERC grant GR/G 13525

saturation and multiwave mixing nonlinearities are contained in the coefficients $\vartheta_{n\mu\rho\sigma}$. σ_n is the power independent pulling coefficient arising from the dispersive nature of the medium and Ω_n is the passive cavity resonance frequency of the nth mode.

In deriving the Lamb eqns. 1 and 2, the field E_n cannot respond to frequency variations much larger than the cavity bandwidth v/Q, so that only terms that satisfy the following equation are retained:

$$\nu_n - \nu_\mu + \nu_\rho - \nu_\sigma \simeq 0 \tag{4}$$

or equivalently

$$n = \mu - \rho + \sigma \tag{5}$$

In the three-mode case, it was found that there are four nonzero relative phase angles satisfying eqn. 5, all of which could be written in terms of a single relative phase angle, Ψ_{2123}, that is $\Psi_{2321} = \Psi_{2123}$ and $\Psi_{1232} = \Psi_{3212} = -\Psi_{2123}$. Hence only one independent $\Psi_{n\mu\rho\sigma}$ could be determined in a three-mode laser. This is because one phase angle is arbitrary and another is determined by the choice of time origin [8]. In the N-mode problem, therefore, there are in fact $N-2$ linearly independent relative phase angles, which could be taken to have the form

$$\Psi_{j+1,j,j+1,j+2} = (2\nu_{j+1} - \nu_j - \nu_{j+2})t + 2\phi_{j+1} - \phi_j - \phi_{j+2} \tag{6}$$

where $j = 1, \ldots, N-2$. To determine the initial conditions of the phases, consider time $t = 0$. From eqn. 6,

$$2\phi_{j+1} - \phi_j - \phi_{j+2} = \Psi_{j+1,j,j+1,j+2} \tag{7}$$

If we choose the time origin so that $\phi_1 = \phi_2 = \phi$, where ϕ is an arbitrary constant, then $\phi_3 = \phi - \Psi_{2123}$, and, in general,

$$\phi_m = 2\phi_{m-1} - \phi_{m-2} - \Psi_{m-1,m-2,m-1,m} \quad (m = 3, \ldots, N) \tag{8}$$

Hence by specifying the initial values of $N-2$ number of independent $\Psi_{n\mu\rho\sigma}$s and $\phi_1 = \phi_2 = \phi$, ϕ being an arbitrary constant, all the phases are defined. Furthermore, other dependent $\Psi_{n\mu\rho\sigma}$s in the amplitude and frequency determining equations which satisfy eqn. 5 are properly and completely defined in the initial conditions ($t = 0$) by

$$\Psi_{n\mu\rho\sigma} = \phi_n - \phi_\mu + \phi_\rho - \phi_\sigma \tag{9}$$

since all ϕ_n are defined.

To identify the semiconductor laser analogues of the various terms contributing to the nonlinear dynamics, we introduce the cross/self saturation coefficient θ_{nm} and cross/self pushing coefficient τ_{nm} as

$$\theta_{nm} = \text{Im}\,\{\vartheta_{nnmm} + \vartheta_{nmmn}\} \tag{10}$$

$$\tau_{nm} = \text{Re}\,\{\vartheta_{nnmm} + \vartheta_{nmmn}\} \tag{11}$$

The amplitude determining eqn. 1 then becomes

$$\dot{E}_n = \alpha_n E_n - \sum_m \theta_{nm} E_m^2 E_n + \cdots \tag{12}$$

Letting $I = E^2$ and differentiating with respect to t, the rate equation of I becomes

$$\dot{I}_n = 2\alpha_n I_n \left\{1 - \frac{1}{\alpha_n}\sum_m \theta_{nm} I_m\right\} + \cdots \tag{13}$$

The semiconductor coupled-mode equation which is widely used to analyse multimode semiconductor laser operation is [9]

$$\dot{P}_n = v_g g_0^L P_n \left\{1 - \sum_m \beta_{nm} P_m\right\} - v_g P_n \gamma + R_{sp} \tag{14}$$

where $v_g = c/n_g$ is the group velocity, c is the velocity of light in vacuum, n_g is the group index, g_0^L is the linear gain coefficient per unit length, γ is the loss coefficient per unit length and R_{sp} is the rate of spontaneous emission. It is apparent that the semiconductor coupled-mode equation is very similar to eqn. 13. Comparing the two, $\alpha = v_g g_0^L/2$ and $\theta_{nm} = \alpha_n \beta_{nm}$. Using values from Reference 9, gives

group index	$n_g = 4$
saturation coefficient	$\beta = 6.7 \times 10^{-17}$ cm^3
linear gain	$g_0^L = 60$ cm^{-1}
group velocity	$v_g = 7.49 \times 10^9$ cm s^{-1}
linear net gain	$\alpha = 2.25 \times 10^{11}$ s^{-1}
saturation coefficient	$\theta = 1.51 \times 10^{-5}$ cm^3 s^{-1}

The values of other nonlinear parameters such as ϑ, τ and σ are assumed to have the same order of magnitude as θ. With all these parameter values and initial conditions for the amplitudes and relative phase angles, the N-mode amplitude and frequency determining eqns. 1 and 2 can be solved numerically to obtain the time evolutions of the mode amplitudes and phases.

3 Self locked FM operation

For nonlinear gain parameters appropriately adapted to take into account of semiconductor laser properties, it was found that a self locked state may indeed occur. Here it is shown that, with a multimode treatment, almost pure FM operation can be obtained.

3.1 Modulation index

In pure FM operation, the field of the FM supermode has a constant amplitude, E_0 and is of the form

$$E(t) = E_0 \cos(\omega_0 t + \beta \cos \omega t) \tag{15}$$

where β is the modulation index, ω is the beat frequency between adjacent modes and ω_0 is the frequency of the dominant mode, taken as the central mode. The relative amplitudes of the cavity modes are defined by the Bessel functions

$$E(t) = E_0 \sum_n J_n(\beta) \cos\left\{(\omega_0 + n\omega)t - |n|\frac{\pi}{2}\right\} \tag{16}$$

The modulation index β for the self locked FM oscillation may then be deduced from the calculated mode amplitudes by making use of the standard Bessel function identity

$$\frac{2n}{\beta} J_n(\beta) = J_{n+1}(\beta) + J_{n-1}(\beta) \tag{17}$$

Using a five-mode model, the steady-state mode amplitudes were computed and plotted against frequency as shown in Fig. 1*a*. This calculated amplitude spectrum is compared with the theoretical ideal FM sidebands in Fig. 1*b*. The general agreement between the calculated and the theoretical FM sideband spectra suggests that the self locked oscillation approaches pure FM operation.

For a typical FM supermode with five frequency components, the calculated field amplitudes were normalised with respect to the central mode amplitude and the modulation index β was found using eqn. 17. A modula-

tion index of 1.3 is obtained for the parameters given in Section 2 and which are appropriate to long wavelength laser diodes. This calculated modulation index is in good agreement with values observed experimentally [5].

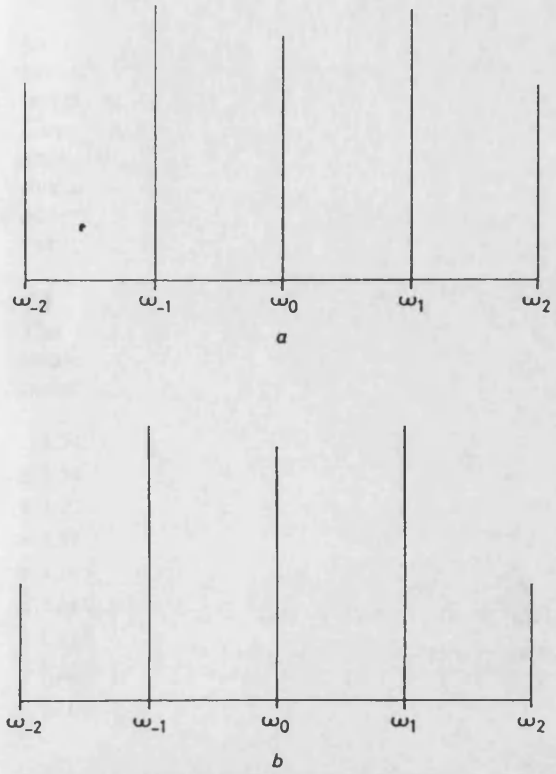

Fig. 1 *General agreement between two spectra*
a Calculated five-mode self locked amplitude spectrum
b Ideal Bessel function sideband spectrum

3.2 Limitations to pure FM operation

The time-domain representations of the self locked supermodes with five, seven and nine frequency components, together with the respective computed output power and modulation index, are shown in Fig. 2. It is evident from the observation of the waveforms that a small periodic variation in the signal amplitude envelope is present and pure FM operation is inhibited. This indicates an admixture of AM component in the self locked FM supermode. The periodic nature of the amplitude envelope variation is due to the locking of the longitudinal modes at the same beat frequency. Thus, instead of a pure FM oscillation as given in eqn. 15, the field of the self locked oscillation can be written in the form

$$E(t) = E_0\{1 + f(t)\} \cos \{\omega_0 t + \beta \cos (\omega t + \theta)\} \qquad (18)$$

where $f(t)$ denotes a time function describing the variation of the signal amplitude envelope, which is not explicitly specified in the present multimode context, and is a result of the residue amplitude modulation, and θ is the relative phase between the frequency and amplitude modulation.

It was found that self locked FM operation, caused by medium nonlinearities, is always accompanied by a small AM component for nonlinear parameters associated with semiconductor lasers. A qualitative explanation for the admixiture of AM and FM components in the self locked FM supermode is given below which involves the contributions of various nonlinearities.

As explained by Agrawal [9], the physical origins of nonlinearities in semiconductor lasers are static hole burning, population pulsations due to the modulation of carrier population by intermodel beating, and multiwave mixing occurring in the presence of population pulsations. It was established in our earlier work [6] that FM

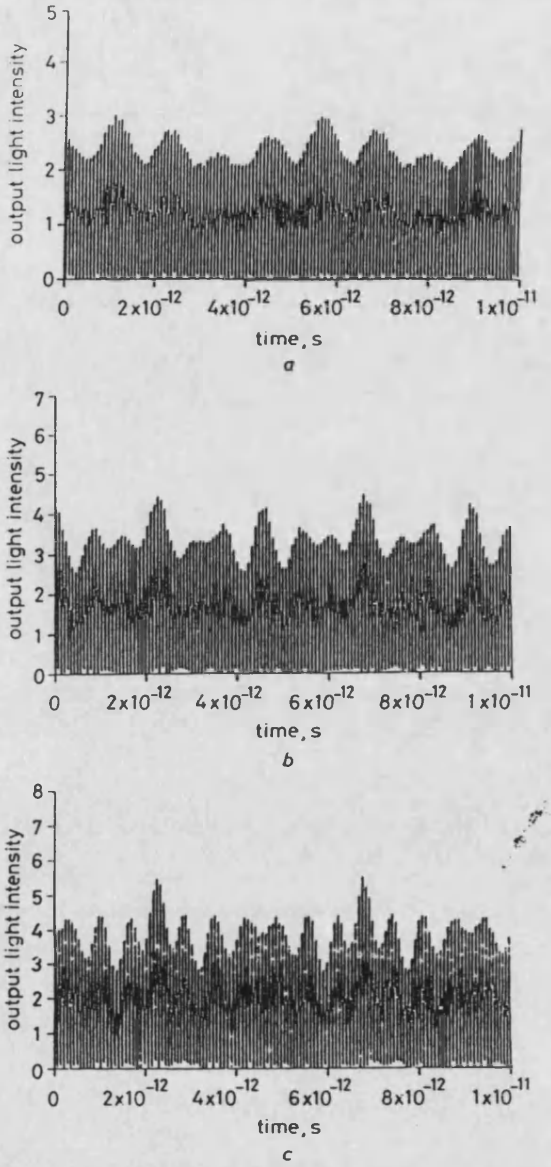

Fig. 2 *Time waveforms of self-locked FM operation; output power and modulation index increase as number of modes in analysis is increased*
a Five lasing modes; mean output power: 11.7 mW; FM index: 1.25
b Seven lasing modes; mean output power: 16.4 mW; FM index: 1.35
c Nine lasing modes: mean output power: 18.9 mW; FM index: 1.90

self locking is critically sensitive to multiwave mixing parameters, $\vartheta_{n\mu\rho\sigma} \exp(i\Psi_{n\mu\rho\sigma})$. The term $\Psi_{n\mu\rho\sigma}$ represents the phase dependent coupling between modes and arises due to the beating of beat frequencies between lasing modes, which in semiclassical laser theory are often referred to as combination tones [8]. Owing to multiwave mixing in the presence of population pulsations, the carrier population of the active medium is modulated at the beat frequency between lasing modes. This carrier density modulation translates to a modulation of refractive index because of the free-carrier contribution to the refractive index. The modulation of the refractive index in turn causes the optical length of the laser cavity to be modulated and thereby modulates the eigenfrequency of the Fabry–Perot resonator. Thus self locked FM operation is affected. On the other hand, owing to the carrier dependence of medium gain, the carrier modulation also leads to gain/loss modulation of the active

medium. This gain/loss modulation results in the mode amplitudes variation and thus produces an AM component in the self locked FM supermode.

4 Modulation index dependence on nonlinearities

In this Section, we present results obtained from an investigation of the dependence of frequency modulation index on medium nonlinearities using a five-mode model. Comparison of the calculated output optical power with experimentally determined output power of semiconductor lasers under which self locked FM operation was observed renders an estimation of the range of valid values for the various nonlinear parameters.

4.1 Self and cross saturation nonlinear effects

The presence of self/cross gain saturation in multimode semiconductor laser operation causes the mode amplitudes to be suppressed. Figs. 3 and 4 illustrate the effects

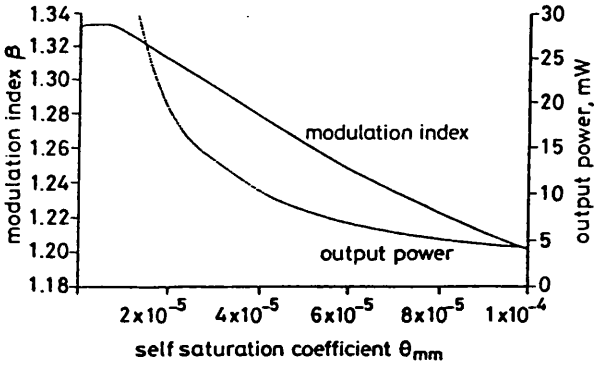

Fig. 3 *Effects of self saturation nonlinearities, θ_{mm} on frequency modulation index and output power*

——— modulation index
- - - - output power

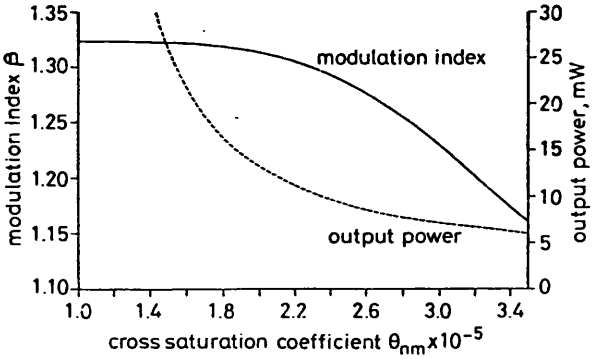

Fig. 4 *Effects of cross saturation nonlinearities, θ_{nm} on frequency modulation index and output power*

——— modulation index
- - - - output power

of self and cross saturation nonlinearities on frequency modulation index and output optical power, respectively. Both the modulation index and output power decrease as the self/cross saturation coefficients get larger. Since self locked FM operation was observed in laser diodes for output powers below 20 mW [5], we deduce from the Figures that the values of self/cross saturation coefficients are likely to be equal or greater than approximately 1.5×10^{-5} cm^3 s^{-1}. It is also observed that the modulation index drops off sharply and FM locking ceases to occur for $\theta_{nm} > 3.5 \times 10^{-5}$ cm^3 s^{-1}. It is therefore seen that for appropriate values of θ_{nm}, other things being held constant, the modulation index lies approximately between 1.15 and 1.30 for a five-mode laser model.

4.2 Multiwave mixing nonlinear effects

The general saturation term $\vartheta_{n\mu p\sigma}$ is a complex quantity arising from the polarisation of the active medium due to the interaction of the medium with an electromagnetic field. The complex polarisation P can be related to the electric field component E by a complex susceptibility χ, that is

$$P = \varepsilon_0 \chi E$$
$$= \varepsilon_0(\chi' + i\chi'')E \quad (19)$$

where ε_0 is the permittivity of free space. Re $\{\vartheta\}$ is proportional to χ' which is associated with the refractive index of the medium whereas Im $\{\vartheta\}$ varies directly with χ'' which gives the medium gain of semiconductor lasers [10].

The variations of modulation index with the real and imaginary parts of ϑ are depicted in Fig. 5 and Fig. 6, respectively. The modulation index increases as Re $\{\vartheta\}$ is

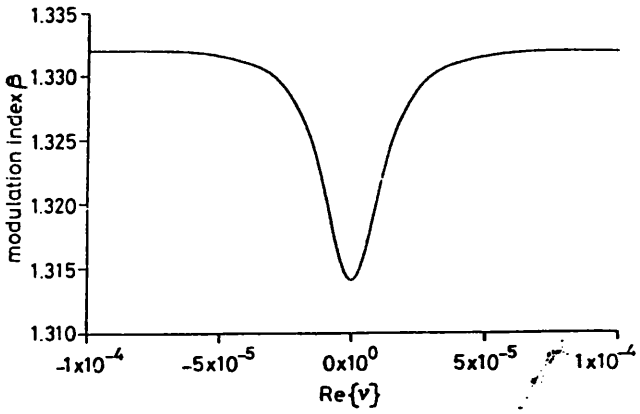

Fig. 5 *Frequency modulation index dependence on Re $\{\vartheta\}$*

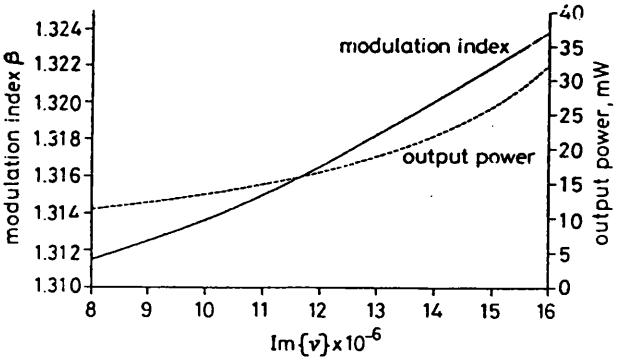

Fig. 6 *Frequency modulation index dependence on Im $\{\vartheta\}$*

——— modulation index
- - - - output power

increased and saturates at the value of 1.332. The output power does not seem to have a significant correlation with Re $\{\vartheta\}$. On the other hand, both modulation index and output power increase with increasing Im $\{\vartheta\}$. This is because higher values of Im $\{\vartheta\}$ mean higher medium gain and therefore increasing the output light power. Consideration of experimentally determined output power for which self locked FM operation occurs suggests that the value of Im $\{\vartheta\}$ is likely to be below 1.5×10^{-5} cm^3 s^{-1}. However, there is a threshold value of Im $\{\vartheta\}$, and therefore a minimum output power, below which the oscillation ceases to be mode locked [6].

In summary, we have obtained the values of the self and cross saturation coefficients θ_{nm} for realistic semiconductor laser parameters, by suitably adapting the Lamb amplitude-determining equation and comparing it with

the semiconductor coupled-mode equation frequently used to analyse multimode semiconductor laser operations. The values of other nonlinear parameters such as ϑ, τ and σ were assumed to be equal to $\theta_{nm} \simeq 1.5 \times 10^{-5}\,cm^3\,s^{-1}$. These nonlinear parameters were then varied independently in the vicinity of $1.5 \times 10^{-5}\,cm^3\,s^{-1}$ to analyse the self locked FM operation and investigate the nonlinear gain dependence of the modulation index and optical output power.

It was shown that the modulation index increases with the optical output power, which in turn is determined by the various nonlinear parameters. Self and cross saturation coefficients cause gain suppression and hence reduce output power and modulation index, whereas Im $\{\vartheta\}$ is proportional to medium gain and thus enhances optical output power and modulation index. For a five-mode laser, a modulation index in the range of 1.15 to 1.3 at an output power less than 20 mW is typical for nonlinear parameters appropriate to semiconductor lasers. These values are in good agreement with experimental evidence. When seven and nine modes were taken into account in the analysis, the output power increases at a given linear gain value compared to the five-mode case and the modulation index increases correspondingly with the optical output power.

5 Conclusion

A multimode analysis of self-locked FM operation of laser diodes has been reported. Calculation of the modulation index using this multimode semiconductor laser model yields a value of 1.3 which is in good agreement with experimental value. A small AM component which gives rise to slight amplitude envelope variations is shown to be present in the FM supermode and inhibits pure FM operation. The contributions of various nonlinearities on the self locked FM operation dynamics are also pointed out. Further work is in progress to incorporate the carrier density in the self locking dynamics of FM operation and to determine the injection current level necessary to obtain FM locking. There may also be scope for revealing novel external cavity effects related to recently reported phase-reversal behaviour in semiconductor lasers [11].

6 References

1 SIEGMAN, A.E.: 'Lasers' (University Science Books, 1986)
2 HARRIS, S.E., and McDUFF, O.P.: 'Theory of FM laser oscillation', *IEEE J. Quantum Electron.*, 1965, QE-1, pp. 245–262
3 SCHREMER, A., FUJITA, T., LIN, C.F., and TANG, C.L.: 'Instability threshold resonances in directly modulated external-cavity semiconductor lasers', *Appl. Phys. Lett.*, 1988, 52, (4) pp. 263–265
4 NIETZKE, R., PANKNIN, P., ELSÄSSER, W., and GÖBEL, E.O.: 'Four-wave mixing in GaAs/AlGaAs semiconductor lasers', *IEEE J. Quantum Electron.*, 1989, QE-25, (6), pp. 1399–1406
5 TIEMEIJER, L.F., KUINDERSMA, P.I., THIJS, P.J.A., and RIKKEN, G.L.J.: 'Passive FM locking in InGaAsP semiconductor lasers', *IEEE J. Quantum Electron.*, 1989, QE-25, pp. 1385–1392
6 SHORE, K.A., and YEE, W.M.: 'Theory of self-locking FM operation in semiconductor lasers', *IEE Proc.-J.*, 1991, 138, (2)
7 SAYERS, M.D., and ALLEN, L.: 'Amplitude, competition, self-locking, beat frequency and time development in a three-mode gas laser', *Phys. Rev. A*, 1970, 1, pp. 1730–1746
8 SARGENT, M., SCULLY, M.P., and LAMB, W.E.: 'Laser physics' (Addison–Wesley, Reading, MA, USA, 1974)
9 AGRAWAL, G.P.: 'Gain nonlinearities in semiconductor lasers', *IEEE J. Quantum Electron.* 1987, QE-23, pp. 860–868
10 YARIV, A.: 'Quantum electronics' (Wiley, 3rd edn.)
11 SCHREMER, A., and TAN, C.L.: 'Abrupt phase reversal in frequency-modulated external cavity semiconductor lasers', *Appl. Phys. Lett.*, 1989, 55, 1832–1834

Carrier transport and intersubband population inversion in coupled quantum wells

W. M. Yee and K. A. Shore
University of Bath, School of Electronic and Electrical Engineering, Bath BA2 7AY, United Kingdom

E. Schöll
Institute of Theoretical Physics, Technical University of Berlin, Hardenbergstrasse 36, D-1000 Berlin 12, Germany

(Received 25 January 1993; accepted for publication 9 June 1993)

We theoretically study the possibility of achieving intersubband population inversion in coupled GaAs quantum wells, taking into account the relevant physical mechanisms of resonant tunneling and intersubband emission-absorption processes. Two coupled quantum well structures having intersubband resonant wavelengths of 10 and 60 μm are considered. We find that, in the case of an operating wavelength of 60 μm, intersubband population inversion is achievable at acceptable injection current densities even for room-temperature operation. However, achievement of intersubband population inversion is significantly more difficult at the shorter wavelength. The temperature and carrier transit time dependence of intersubband population inversion are also calculated.

Recent advances in semiconductor epitaxial growth technology have made feasible the fabrication of ultrathin novel structures such as coupled quantum wells and superlattices and has motivated an extensive study of the physics and applications of these reduced-dimensionality devices.[1] A large research effort has been devoted to the tunneling effects in semiconductor superlattices and coupled quantum wells.[2–4] Also, studies on intersubband transitions of confined electrons in quantum wells have shown large values of oscillator strength and dipole moment,[5] and suggest that intersubband transitions may be utilized to generate coherent radiation in the infrared and far-infrared frequency ranges.[6–8] Several structures have been proposed for intersubband population inversion,[9–11] and in most of these cases, quantum well energy filters were used to selectively inject carriers into the upper subband and remove carriers from the lower subband by resonant tunneling. Reported studies on the feasibility of lasing action in the infrared wavelength range involving intersubband transitions in resonant tunneling quantum well structures have so far been based on the assumption that intersubband population inversion is achieved at a certain level of injection current.

In this letter, we incorporate resonant tunneling and intersubband absorption-emission processes in a theoretical model of carrier transport in coupled GaAs quantum wells. Specifically, we assess the possibility of achieving intersubband population inversion and explicitly calculate the intersubband population inversion as a function of injection current density. Comparison is made of the level of injection current density needed to obtain intersubband population inversion between two coupled quantum well structures having intersubband resonant wavelengths in the infrared and far-infrared ranges, respectively. The dependence of intersubband population inversion on temperature and carrier transit time through the coupled quantum well structures are considered.

The analysis is performed for two different coupled quantum well structures having intersubband energy separations of 124 meV ($\lambda=10$ μm) and 20.7 meV ($\lambda=60$ μm), respectively. The schematic conduction band profiles of the two structures under operating bias are shown in Fig. 1. Both structures consist of two energy filter wells, QW1 and QW3, having only one quasibound state each (E_1 and E_3, respectively) and an emission quantum well (QW2), where intersubband transitions take place between two states, $E_2^{(2)}$ and $E_2^{(1)}$. The $Al_xGa_{1-x}As$-GaAs ($x=0.45$) material system is used in structure I. Due to the small energy scales corresponding to the far-infrared frequencies associated with structure II, rather wide emission well is required. In order that the energy filter quantum wells of structure II have only one quasi-bound state each and that the various energies align properly under operating bias, $In_yGa_{1-y}As$-$Al_xGa_{1-x}As$ ($y=0.15$) the material

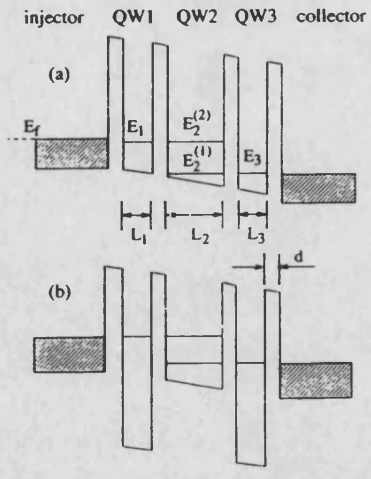

FIG. 1. Coupled quantum wells biased to the operating voltage (not drawn in proportion). Two structures are considered in which the intersubband energy separation in QW2 of (a) structure I is 124 meV and (b) structure II is 20.7 meV. The coupled quantum wells are sandwiched between n-doped injector and collector (shaded regions). E_f is the Fermi energy in the doped injector.

 0003-6951/93/63(8)/1089/3/$6.00

system is employed in the filter wells and GaAs in the emission well. Under zero bias, the well widths of both structures are designed such that E_1 and E_3 in the filter wells are in the middle of $E_2^{(1)}$ and $E_2^{(2)}$ in the emission well. When the structures are biased to the operating voltage, $V_b \simeq (E_2^{(2)}-E_2^{(1)})/2$, the energy subbands are aligned as shown in Fig. 1. Electrons are injected into the upper subband of QW2 through filter well QW1 and are removed from the lower subband of QW2 through QW3, via resonant tunneling. The confined electrons in the emission well undergo intersubband transitions such as stimulated radiative emission, absorption, and intersubband relaxation.

We assume that there is no carrier source or sink in the coupled wells and thus the external injection current density J_{ext} entering and leaving the structures are the same. The carrier rate equations describing the temporal variation of electron densities in the respective subbands of the coupled quantum wells are

$$\dot{n}_1=\frac{1}{eL_1}(j_{1\to 2}-j_{2\to 1}+J_{ext}), \tag{1}$$

$$\dot{n}_2^{(2)}=-A+\frac{1}{eL_2}(j_{2\to 1}-j_{1\to 2}), \tag{2}$$

$$\dot{n}_2^{(1)}=A+\frac{1}{eL_2}(j_{2\to 3}-j_{3\to 2}), \tag{3}$$

$$\dot{n}_3=\frac{1}{eL_3}(j_{3\to 2}-j_{2\to 3}-J_{ext}), \tag{4}$$

where $\dot{n}_a^{(b)}$ denotes the time rate of change of electron density in quantum well a ($a=1,2,3$) and subband b (there is only one subband in QW1 and QW3 and thus the superscript b is omitted). The net downward intersubband transition rate in QW2, A (per unit volume and time) appropriate for a two-dimensional system, is given by[12]

$$A=\frac{n_2^{(2)}-n_2^{(1)}}{e^{n_2^{(2)}/n_{c_2}}-e^{n_2^{(1)}/n_{c_2}}}$$

$$\times[(X+S)(e^{n_2^{(2)}/n_{c_2}}-1)-X^*(e^{n_2^{(1)}/n_{c_2}}-1)] \tag{5}$$

and the transversal electric current densities through the barriers resulting from resonant tunneling are[12]

$$j_{1\to 2}=\frac{eL_2}{\pi\bar{h}}\Delta E n_2^{(2)},\quad j_{2\to 1}=\frac{eL_1}{\pi\bar{h}}\Delta E n_1,$$

$$j_{2\to 3}=\frac{eL_3}{\pi\bar{h}}\Delta E' n_3,\quad j_{3\to 2}=\frac{eL_2}{\pi\bar{h}}\Delta E' n_2^{(1)}, \tag{6}$$

and $n_{c2}=(m_2^* k_B T)/(\pi\bar{h}^2 L_2)$ is the quasi-two-dimensional degeneracy concentration, X is the stimulated radiative emission rate, X^* is the absorption rate, S is the intersubband relaxation rate, ΔE and $\Delta E'$ are the energy level broadening due to the coupling of adjacent quantum wells, k_B is the Boltzmann constant, T is the electron temperature, $\bar{h}=h/(2\pi)$, where h is the Planck's constant, e is the electronic charge, and m^* is the effective mass of electron.

In steady state, Eqs. (1)–(4) reduce to

TABLE I. Numerical parameters used in the simulations.

	Structure I	Structure II
λ (μm)	10	60
L_1 (Å)	40	70
L_2 (Å)	82	285
L_3 (Å)	40	70
d (Å)	20	20
ΔE (meV)	7	3
$\Delta E'$ (meV)	5	1
S (s^{-1})	10^{12}	$(3\times 10^{-10})^{-1}$
X (s^{-1})	10^7	10^7

$$\frac{e\Delta E}{\pi\bar{h}}(L_1 n_1-L_2 n_2^{(2)})=J_{ext}, \tag{7}$$

$$\frac{e\Delta E'}{\pi\bar{h}}(L_2 n_2^{(1)}-L_3 n_3)=J_{ext}, \tag{8}$$

$$AeL_2=J_{ext}. \tag{9}$$

Since the current injection is equal to the rate of total charge passing through the quantum well structure, we can write

$$J_{ext}=\frac{e}{\tau_T}[n_1 L_1+(n_2^{(1)}+n_2^{(2)})L_2+n_3 L_3], \tag{10}$$

where τ_T is the effective transit time of carriers through the whole structure which includes not only the transmission time through the barriers and the intersubband transition time, but also time delays caused by intrasubband scattering and electron diffusion.

The electron densities in the various subbands are highly dependent on the rates of stimulated radiative emission, absorption, and intersubband relaxation as indicated by Eq. (5). For intersubband energy separation greater than ~36 meV, optical phonon scattering is the main intersubband relaxation process. Relaxation times of the order of 10 ps at 300 K for intersubband energy separation of 120 meV in GaAs quantum well were reported by Seilmeier,[13] whereas recent experimental measurement and theoretical calculation reported subpicosecond intersubband relaxation time.[14,15] We use an intersubband relaxation time of 1 ps for structure I. A typical value of acoustic phonon relaxation time[16] of $\simeq 3\times 10^{-10}$ s is used for structure II which has an intersubband energy separation less than the optical phonon energy. In both structures, an intersubband radiative emission time of 0.1 μs is used. The stimulated emission rate X is equal to the absorption rate X^*.

Table I shows the various numerical parameters for the two structures used in the calculation. The result shows that carrier densities in all subbands increase as the external injection current density is increased. The calculated intersubband population inversion, $\Delta n=n_2^{(2)}-n_2^{(1)}$, for the two structures are shown in Figs. 2(a) and 2(b), respectively. Comparison between the two results shows that significantly higher injection current density is needed to achieve intersubband population inversion in structure I. This is because the downward transition of structure I is

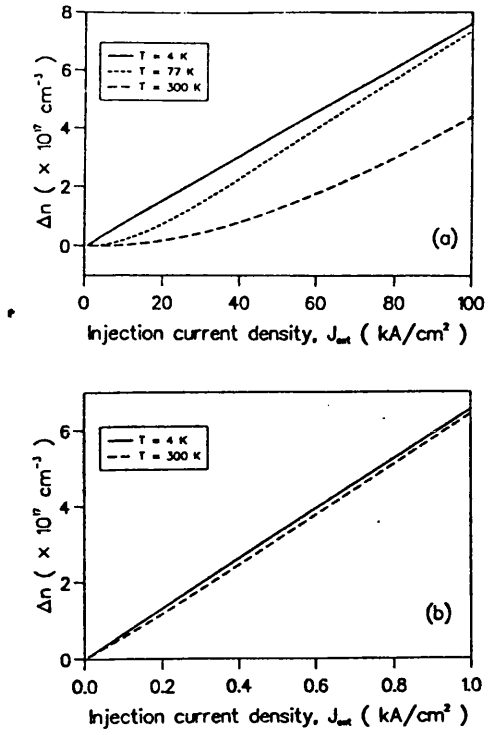

FIG. 2. Intersubband population inversion, Δn dependence on injection current density at different temperatures for (a) structure I, where τ_T =4.0 ps, and (b) structure II where τ_T=0.7 ns.

dominated by the very fast optical phonon relaxation whereas a much slower acoustic phonon relaxation (down by $\approx$2 orders of magnitude) limits the downward transition in structure II. It therefore appears that lasing action based on intersubband transition may be feasible only, at reasonable level of injection current, in the far-infrared wavelength range. However, the absorptive loss is higher for longer wavelengths, and thus there is a trade-off to be considered when designing such a laser. Figure 2 also shows that intersubband population inversion is more difficult to achieve if the temperature is increased, although the temperature dependence of population inversion for structure II is relatively small. We have assumed that nonresonant tunneling and thermionic induced carrier leakage from the upper subband of QW2 to the collector are negligibly small. In practice, thermionic excitation of carriers in high-temperature operation may affect the temperature dependence of the intersubband population inversion.

The minimum level of injection current density required to achieve intersubband population inversion, which we define as the population inversion threshold current density J_{tr}, is dependent on the effective transit time τ_T as shown in Fig. 3 for structure I. Any extra time delays caused by intrasubband scattering such as carrier-carrier scattering or the increase in transmission time due to thick barriers will increase J_{tr}. The minimum transit time for

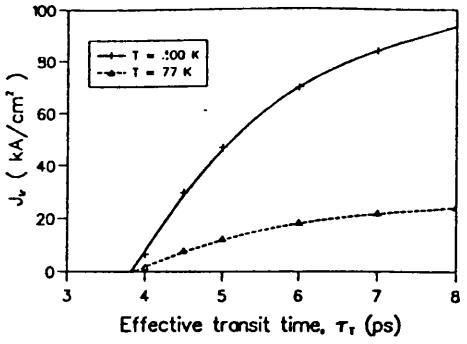

FIG. 3. Calculated inversion threshold current density J_{tr} as a function of transit time at various temperatures for quantum well structure I.

structure I is $\approx$3.8 ps from Fig. 3. The transit time dependence of J_{tr} for structure II is much less pronounced, possibly due to the much larger transit time, $\tau_T \approx 0.65$ ns.

In conclusion, we have theoretically studied the carrier transport in coupled quantum wells, taking into account of resonant tunneling and intersubband transitions. The intersubband population inversion has been explicitly calculated as a function of injection current density for two structures. The results show that intersubband population inversion is achievable at acceptable injection current densities even for room-temperature operation in the case of an emission wavelength of 60 μm. This letter has concentrated on the transport processes related to the achievement of intersubband population inversion. Further work is now in progress to address the issue of designing an optimized structure for far-infrared lasing. In this respect, attention also needs to be given to the requirements for reducing optical losses at the wavelength of interest.

This work has been partly supported by the UK SERC. Travel support under the UK/Germany Academic Research Collaboration scheme of the British Council is also acknowledged.

[1] L. Esaki, IEEE J. Quantum Electron. QE-22, 1611 (1986).
[2] F. Capasso, K. Mohammed, and A. Y. Cho, IEEE J. Quantum Electron. QE-22, 1853 (1986).
[3] K. F. Brennan and C. J. Summers, J. Appl. Phys. 61, 614 (1987).
[4] S. Luryi, Superlatt. Microstruct. 5, 375 (1989).
[5] L. C. West and S. J. Eglash, Appl. Phys. Lett. 46, 1156 (1985).
[6] P. F. Yuh and K. L. Wang, Appl. Phys. Lett. 51, 1404 (1987).
[7] H. C. Liu, J. Appl. Phys. 63, 2856 (1988).
[8] M. Helm, P. England, E. Colas, F. DeRosa, and S. J. Allen, Jr., Phys. Rev. Lett. 63, 74 (1989).
[9] S. I. Borenstain and J. Katz, Appl. Phys. Lett. 55, 654 (1989).
[10] A. Kastalsky and V. J. Goldman, Appl. Phys. Lett. 59, 2636 (1991).
[11] Q. Hu and S. Feng, Appl. Phys. Lett. 59, 2923 (1991).
[12] R. E. Kunz and E. Schöll, Phys. Rev. A 47, 4337 (1993).
[13] A. Seilmeier, H. J. Hübner, G. Abstreiter, G. Weimann, and W. Schlapp, Phys. Rev. Lett. 59, 1345 (1987).
[14] H. T. Grahn, H. Schneider, W. W. Rühle, K. von Klitzing, and K. Ploog, Phys. Rev. Lett. 64, 2426 (1990).
[15] J. K. Jain and S. Das Sarma, Phys. Rev. Lett. 62, 2305 (1989).
[16] D. Y. Oberli, D. R. Wake, M. V. Klein, J. Klem, T. Henderson, and H. Morkoç, Phys. Rev. Lett. 59, 696 (1987).

Semicond. Sci. Technol. 9 (1994) 1190–1197. Printed in the UK

Threshold current density calculations for far-infrared semiconductor lasers

W M Yee and K A Shore

University of Bath, School of Electronic and Electrical Engineering, Bath BA2 7AY, UK

Received 1 February 1994, accepted for publication 14 March 1994

Abstract. We study theoretically the conditions for achieving lasing action at infrared and far-infrared wavelengths based on intersubband transitions in semiconductor quantum well structures, taking into account resonant tunnelling and intersubband absorption–emission processes. Analysis of optical losses in the semiconductor quantum well structures reveals that a reasonably low threshold current density in the range of 1–5 kA cm^{-2} is achievable for room temperature lasing at emission wavelength of $\lambda = 60$ μm. A significantly higher threshold current density of 40–50 kA cm^{-2} is required for lasing at $\lambda = 10$ μm.

1. Introduction

The ability to fabricate ultrathin semiconductor heterostructures such as multiple quantum wells (QW) and superlattices has motivated in recent years an extensive study of the physics and applications of these reduced-dimensionality devices [1]. In particular, the optical properties of semiconductor coupled QW structures and superlattices in the infrared wavelength range have attracted considerable attention since the first observation of large values of oscillator strength and dipole moment between QW subbands by West *et al* [2]. Infrared photodetectors based on intersubband absorptions in QW structures have been extensively studied and successfully implemented for wavelengths in the range 4–12 μm [3]. In view of the great potential applications in medicine, spectroscopy, radio astronomy and free-space communication, it is of considerable interest to achieve the reverse process of intersubband radiative emission for possible realization of infrared semiconductor lasers.

The first observation of spontaneous intersubband radiative emission in GaAs–AlGaAs superlattices was reported by Helm *et al* [4, 5]. However, in order to obtain coherent infrared lasing from intersubband transitions, it is necessary to achieve a sufficiently high degree of intersubband population inversion at reasonably low pumping. This represents a major challenge due to the overwhelming contribution of non-radiative phonon emission, which depopulates the upper subband at a very fast rate. Many schemes have been proposed to achieve intersubband population inversion, most of which concentrate on current injection pumping [6–13], while a few approaches focus on optical pumping using a CO_2 laser source [14, 15].

In early studies on current injection pumped infrared semiconductor lasers based on intersubband transitions, sequential resonant tunnelling has been used to populate the excited state and depopulate the ground state of an electrically biased multiple QW structure [5–7]. Although weak spontaneous emission has been observed [5] using this process, intersubband population inversion has not been achieved. This is due to the fact that sequential resonant tunnelling from the ground state of one QW to the first excited state of the adjacent QW represents carrier transport in an essentially two-level system, and that population inversion cannot be achieved using just two states. On the other hand, while population inversion may be possible using sequential resonant tunnelling from the ground state to the second or higher excited state of an adjacent QW, the subsequent relaxation of electrons to the first excited state and the ground state makes population inversion between these two states very difficult. It was also found that intersubband population inversion is not likely to be achievable in double-barrier single-QW structures [16].

In order to facilitate the selective injection of electrons into the first excited state and removal of electrons from the ground state of an emission QW, resonant tunnelling quantum well energy filters have been proposed and shown to lead to intersubband population inversion [8–10]. These studies, however, assumed a simple relation between the intersubband population inversion and the injection current density, without taking into account the relevant physical mechanisms of resonant tunnelling and intersubband emission–absorption processes in the electron transport dynamics.

By careful engineering of a new multi-quantum well heterostructure utilizing tunnelling processes to populate the first excited state and depopulate the ground state, intersubband electroluminescence at $\lambda = 5$ μm has been observed very recently by Faist *et al* [17] at

0268-1242/94/061190+08$19.50

room temperature. This observation has brought the development effort a step closer to the realization of an infrared semiconductor laser and clearly demonstrates the feasibility of tunnelling current injection pumping for use in a laser structure.

In an earlier letter [18], we outlined a carrier transport model related to the achievement of intersubband population inversion in triple-QW structures. The purpose of this paper is to report a theoretical investigation into the possibility of achieving infrared lasing in resonant tunnelling QW structures based on intersubband transitions. In this respect, optical loss analysis is carried out taking into account the configuration of the semiconductor laser device. The threshold current density is explicitly calculated consistent with the optical losses in the laser device for emission wavelengths of 10 and 60 μm. In section 2 we present a transport model describing the electron population dynamics in resonant tunnelling QW structures, which takes into account intersubband emission–absorption processes. The transparency current density is calculated in section 3 taking into account the dependence on carrier transit time and intersubband relaxation time. In section 4 the issue of optical loss is addressed for different doping densities in the cladding layers. The solution of the four-level carrier rate equations from the transport model in conjuction with the balance of gain and optical loss yields the threshold current density. The feasibility of using current injection resonant tunnelling QW structures for far-infrared lasing is thus demonstrated. Finally, we summarize the results in section 5.

2. Model

2.1. Resonant tunnelling quantum well structures

We study the feasibility of achieving lasing action in triple-coupled QW structures which utilize resonant tunnelling to selectively populate the upper level and depopulate the lower level of the lasing transition. The analysis is performed for two different resonant tunnelling QW structures as shown in figure 1. QW2 is the emission well where intersubband transitions take place between the first excited state with energy $E_2^{(2)}$ and the ground state with energy $E_2^{(1)}$. The emission wavelength corresponding to the intersubband energy separation $E_2^{(2)} - E_2^{(1)}$ is determined mainly by the choice of the emission well thickness L_2. We consider here two different structures: structure I with an intersubband energy separation of 124 meV (corresponding to an intersubband emission wavelength of $\lambda = 10$ μm) and structure II with an intersubband energy separation of 21 meV ($\lambda = 60$ μm).

QW1 and QW3, which are designed to have only one quasibound state each (with energies E_1 and E_3 respectively), act as resonant tunnelling QW energy filters. Under zero bias, the well widths of the resonant tunnelling energy filters are engineered such that E_1 and E_3 are in the middle of $E_2^{(1)}$ and $E_2^{(2)}$ in the emission

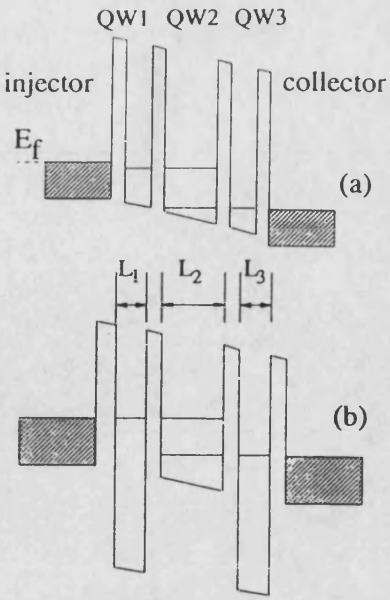

Figure 1. Schematic conduction band profiles of the resonant tunnelling quantum well structures biased to the operating voltage (not drawn in proportion) for (*a*) infrared lasing at $\lambda = 10$ μm and (*b*) far-infrared lasing at $\lambda = 60$ μm. Hatched regions represent n-doped conducting layers. E_f is the Fermi energy level.

well. When the structures are biased to the operating voltage, $V_b \approx (E_2^{(2)} - E_2^{(1)})/2$, the energy states are aligned as shown in figure 1. Electrons are efficiently injected into the first excited state of QW2 through filter well QW1, and are removed from the ground state of QW2 through QW3, via resonant tunnelling. The confined electrons in the emission well QW2 undergo intersubband transitions such as intersubband relaxation, stimulated radiative emission and absorption. As the device acts as an energy filter, the influence of any non-resonant energy bands would be small. In particular, the contribution of any other subbands that may exist in QW2 can be neglected since those states would not be resonant with the aligned levels in QW1 and QW3.

The triple-QW resonant tunnelling structures are sandwiched between n-doped regions of the cladding layers which are called the injectors and collectors. The injectors and collectors, apart from serving as the electron reservoirs for the resonant tunnelling QW structures, also provide optical confinement to the active QW regions since the refractive index drops significantly in the n-doped regions due to the higher electron density. The $Al_xGa_{1-x}As$–GaAs ($x = 0.45$) material system is employed in structure I. Since the intersubband energy separation of 21 meV corresponding to the far-infrared frequency of 5 THz in structure II is very small, a rather wide emission well is required. In order to ensure that the energy filter QW of structure II have only one quasi-bound state each and that the various energies align properly under operating bias, very deep filter wells are required. These requirements are satisfied by using the $In_yGa_{1-y}As$–$Al_xGa_{1-x}As$ ($x = 0.45$, $y = 0.15$) material system in the filter wells and GaAs in the emission well for structure II.

2.2. Carrier population dynamics

Since the intersubband transition and resonant tunnelling processes occur at a much faster rate than the interband transitions, we assume that there is no carrier source or sink in the coupled quantum wells. Thus the external injection current density J leaving the structure is the same as that which enters. The temporal variations of electron density in the respective subbands are described by the carrier rate equations of an essentially four-level system [18]:

$$\frac{dn_1}{dt} = \frac{J}{eL_1} + \frac{L_2}{L_1}\frac{n_2^{(2)}}{\tau_{12}} - \frac{n_1}{\tau_{12}} \tag{1}$$

$$\frac{dn_2^{(2)}}{dt} = \frac{L_1}{L_2}\frac{n_1}{\tau_{12}} - \frac{n_2^{(2)}}{\tau_{12}} - \left(n_2^{(2)} - n_2^{(1)}\right)X(P) - A_{sp} \tag{2}$$

$$\frac{dn_2^{(1)}}{dt} = \left(n_2^{(2)} - n_2^{(1)}\right)X(P) + A_{sp} + \frac{L_3}{L_2}\frac{n_3}{\tau_{23}} - \frac{n_2^{(1)}}{\tau_{23}} \tag{3}$$

$$\frac{dn_3}{dt} = \frac{L_2}{L_3}\frac{n_2^{(1)}}{\tau_{23}} - \frac{n_3}{\tau_{23}} - \frac{J}{eL_3} \tag{4}$$

where $n_a^{(b)}$ denotes the electron density in quantum well a ($a = 1, 2, 3$) and subband b (there is only one subband in QW1 and QW3 and thus the superscript b is omitted), e is the electronic charge and X is the stimulated radiative emission coefficient (inverse time), which is a function of the photon density P. The tunnelling times τ_{12} and τ_{23} between QW1 and QW2, and QW2 and QW3, respectively, are given by

$$\tau_{12} = \frac{\pi\hbar}{\Delta E} \qquad \tau_{23} = \frac{\pi\hbar}{\Delta E'} \tag{5}$$

where $\hbar$ is the Planck's constant divided by 2π; ΔE and $\Delta E'$ are the energy level splittings due to the coupling of QW1 and QW2, and QW2 and QW3, respectively. The total intersubband relaxation rate A_{sp} in QW2 (per unit volume and time), appropriate for a two-dimensional system, is given by [19]

$$A_{sp} = S\left(n_2^{(2)} - n_2^{(1)}\right)\frac{\exp(n_2^{(2)}/n_{c_2}) - 1}{\exp(n_2^{(2)}/n_{c_2}) - \exp(n_2^{(1)}/n_{c_2})}$$

where S is the intersubband relaxation coefficient (inverse time), $n_{c_2} = m_2^* k_B T/\pi\hbar^2 L_2$ is the quasi-two-dimensional degeneracy concentration, $m_2^* = 0.067\,m_0$ is the electron effective mass in GaAs, m_0 is the free electron mass, k_B is the Boltzmann constant and T is the electron temperature. The above expression incorporates the energy dependence of the carriers using Fermi–Dirac statistics as appropriate to semiconductor laser operation [19].

Since the current injection is equal to the rate of total charge passing through the resonant tunnelling quantum well structure, we can write

$$J = \frac{e}{\tau_T}\left[n_1 L_1 + (n_2^{(1)} + n_2^{(2)})L_2 + n_3 L_3\right] \tag{6}$$

where τ_T is the effective transit time of the carriers through the whole structure, which includes not only the transmission times through the barriers and the intersubband transition times, but also time delays caused by intrasubband scattering and electron diffusion. The electron densities in the various subbands can be obtained as a function of the external injection current density by solving the carrier rate equations in a steady state subject to the constraint imposed by equation (7).

The coupled quantum well structures utilizing resonant tunnelling energy filters provide an efficient means of carrier injection into the upper subband and carrier removal from the lower subband of the emission well. It should be noted that without the energy filter quantum wells the structure becomes essentially a two-level system, and in that case intersubband population inversion cannot be obtained. To assess the possibility of intersubband population inversion in the proposed quantum well structures, the relevant physical mechanisms of intersubband emission–absorption processes have to be taken into account.

The principal intersubband transition processes include stimulated emission of radiation, absorption and intersubband relaxation. For current injection pumping and operation below lasing threshold of the coupled quantum well infrared laser structures, the stimulated emission and absorption rates are negligibly small compared with the intersubband relaxation rate. As a result, the term proportional to $X(P)$ in the carrier rate equations can be neglected.

The intersubband relaxation coefficient, S, is given by the inverse of the intersubband relaxation time, τ_s. For intersubband energy separation greater than approximately 36 meV, optical phonon scattering is the main intersubband relaxation process. The reported intersubband relaxation times due to optical phonon scattering vary over more than one order of magnitude. Relaxation times of the order of 10 ps at 300 K for an intersubband energy separation of 120 meV in GaAs quantum wells were reported by Seilmeier and co-workers [20], whereas recent experimental measurements and theoretical calculations reported subpicosecond intersubband relaxation times [21]. We use $\tau_s = 1$ ps for structure I, which has an intersubband energy separation greater than the optical phonon energy. Acoustic phonon scattering is expected to be the dominant mechanism for intersubband relaxation if the intersubband energy separation is less than the optical phonon energy. Oberli *et al* [22] reported intersubband relaxation times of the order of several hundred picoseconds due to acoustic phonon scattering in wide GaAs–AlGaAs multiple quantum

Table 1. Numerical parameters used in the simulations.

	Structure I	Structure II
λ (μm)	10	60
L_1 (Å)	40	70
L_2 (Å)	82	285
L_3 (Å)	40	70
ΔE (meV)	7	0.2
$\Delta E'$ (meV)	5	0.1

wells at low temperature. A typical value of acoustic phonon scattering time of 300 ps is used in structure II. Table 1 shows the various numerical parameters for the two structures used in the calculation.

3. Calculation of the transparency current density

3.1. Intersubband population inversion

The carrier densities in all subbands increase as the external injection current density is increased. The dependence on injection current density, J, of carrier densities in the upper and lower subbands of QW2 and intersubband population inversion for structure I is illustrated in figure 2. It is observed that the intersubband population inversion, $\Delta n = n_2^{(2)} - n_2^{(1)}$, becomes positive when the external injection current density exceeds the level J_0, which is termed the transparency current density.

Figure 3 shows the calculated intersubband population inversion as a function of J at different temperatures for structures I and II. It is noted that the injection current density needed to achieve intersubband population inversion in structure I is significantly higher than that required in structure II. This is because the downward intersubband transition of structure I is effected by the very fast optical phonon scattering, whereas a much slower acoustic phonon scattering limits the downward transition in structure II. It therefore appears that lasing action based on intersubband transition may, at a reasonable level of injection current, be feasible only in the far-infrared wavelength range. However, the absorptive loss is greater for longer wavelengths, and thus there is a trade-off to be considered when designing such a laser.

It is also observed that higher injection current densities are needed to obtain a given level of population inversion as the temperature is increased. We have assumed that non-resonant tunnelling and thermionic

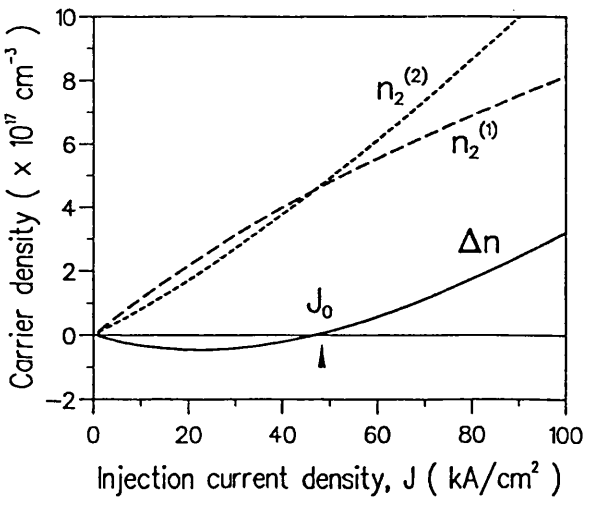

Figure 2. Dependence of carrier density and population inversion on injection current density for structure I. Intersubband population inversion becomes positive when J exceeds the transparency current density, J_0.

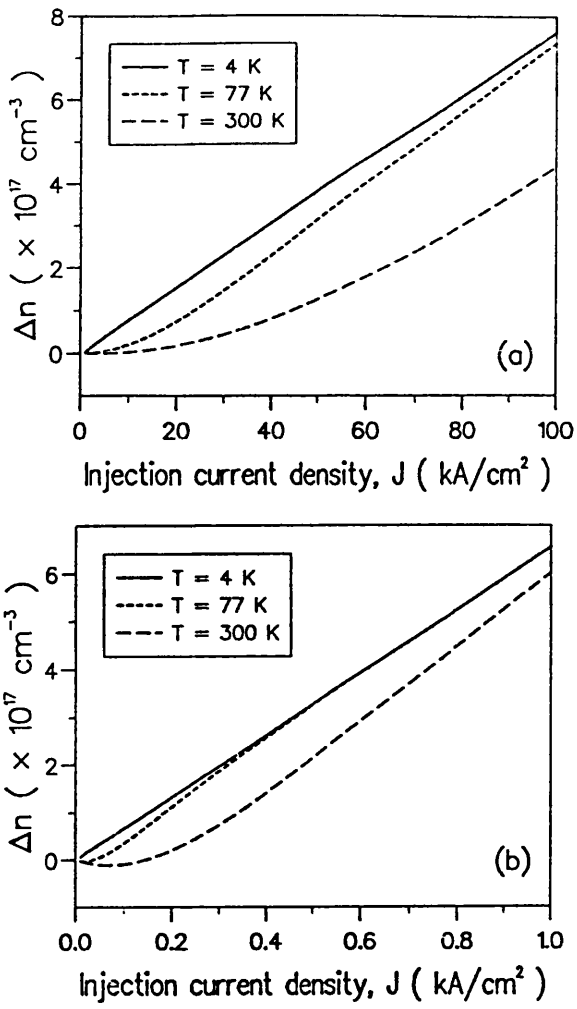

Figure 3. Intersubband population inversion as a function of injection current density at different temperatures for (*a*) structure I, $\tau_T = 4.0$ ps, and (*b*) structure II, $\tau_T = 1.5$ ns.

induced carrier leakage from the upper subband of QW2 to the collector are negligibly small. In view of the uncertainties in the reported experimental values of the intersubband relaxation times, it is difficult to incorporate the temperature dependence of τ_s in the analysis. The temperature dependence of Δn arises mainly because the quasi-two-dimensional degeneracy density, n_{c_2}, is a function of temperature. In practice, the intersubband relaxation rates increase as the temperature is increased, and this may affect the temperature dependence of Δn.

It should be noted that since the upper subband is closer to the barrier edge, and hence is less tightly bound than the lower subband in QW2, the energy broadening is larger in the upper subband, that is $\Delta E > \Delta E'$. This implies that $\tau_{12} < \tau_{23}$ according to equation (5). We see that intersubband population inversion is still possible in this case. It is clear therefore that inversion of the tunnelling rates is not a necessary condition for intersubband population inversion. It is found, however, that a lower transparency current density can be achieved by decreasing τ_{23} and increasing τ_{12} so that $\tau_{12} \approx \tau_{23}$. This can be done by designing different barrier widths between the quantum wells such that the coupling between QW1 and QW2 is reduced whereas the coupling

between QW2 and QW3 is increased. Nevertheless, decreasing the coupling between QW1 and QW2 by increasing the barrier width will increase the effective transit time, and increasing the coupling between QW2 and QW3 by reducing the barrier width will in practice increase the leakage current. All these will eventually increase the transparency current density.

3.2. Transit time dependence of the transparency current density

The dependence of the transparency current density on effective carrier transit time is illustrated in figure 4. The effective transit time includes not only the tunnelling times τ_{12} and τ_{23} and the intersubband transition time τ_s, but also tunnelling times through the outer barriers, electron dephasing times in the various subbands effected by intrasubband scattering events such as electron–electron scattering, and also electron diffusion time. Any extra time delays caused by these intrasubband processes will lead to higher electron accumulation in the various subbands and further increase J_0. The minimum transit time for structure I is approximately 3.8 ps from figure 4(*a*). The transit time dependence of J_0 for structure II is less sensitive; a large change in τ_T (of the order of nanoseconds) produces only a small change in J_0. This is possibly because the transit time of structure II is much larger than the electron dephasing time (of the order of subpicosecond). From figure 4(*b*) the minimum τ_T is approximately 1.2 ns for structure II.

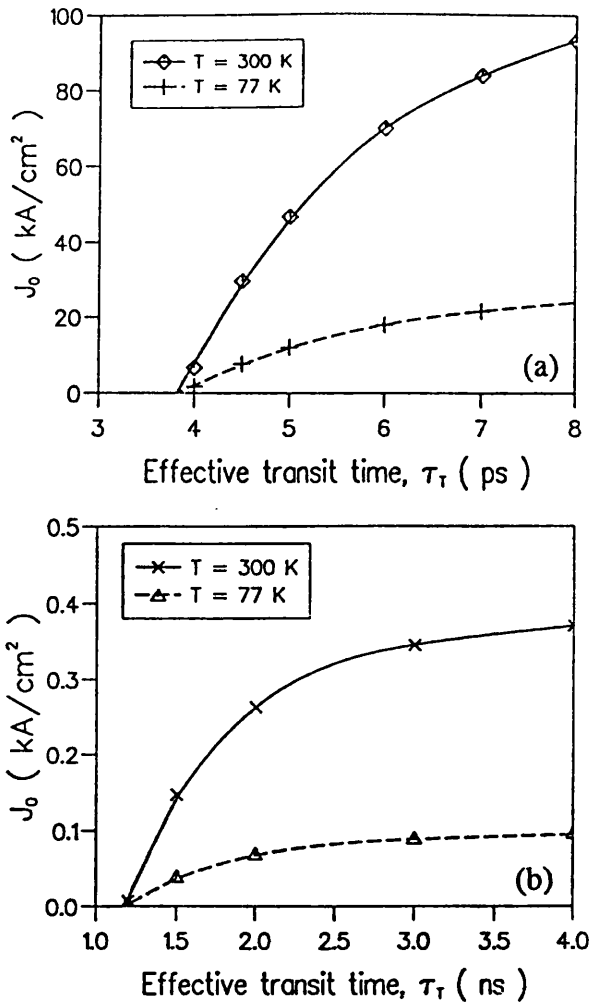

Figure 4. Dependence of transparency current density on effective carrier transit time for (*a*) structure I and (*b*) structure II. Minimum transit times for the two structures can be obtained from the figure.

3.3. Dependence of the transparency current density on intersubband relaxation time

As has been noted earlier, the reported experimental values of intersubband relaxation time due to optical phonon scattering for GaAs–AlGaAs quantum wells differ by more than one order of magnitude. However, recent experiments tend to give values of τ_s in the subpicosecond to 1 ps range. For intersubband energy separation less than the optical phonon energy, the intersubband relaxation rate is reduced by about two orders of magnitude, being limited by the slower acoustic phonon emission. In view of such uncertainties in the values of the intersubband relaxation time, it is instructive to investigate the sensitivity of the dependence of the transparency current density on intersubband relaxation time.

Figure 5 shows the transparency current density as a function of the intersubband relaxation time for the two structures. J_0 increases by more than two orders of magnitude if τ_s is reduced from 1.0 ps to 0.1 ps for structure I. Similarly, J_0 increases by almost one hundred times when τ_s is reduced from 0.35 ns to 0.035 ns for structure II. The results suggest that intersubband population inversion is highly dependent on τ_s and that in order to achieve population inversion it is crucial to reduce the intersubband relaxation rate.

Several ways may be used to reduce the intersubband relaxation rate. Firstly, phonon emission can be reduced considerably by lowering the temperature of operation of the device, thus enhancing the electron lifetime in the upper subband of the emission well. Secondly, it is found that material with a lower effective mass has a longer intersubband relaxation time, and hence material such as InGaAs, with a lower effective mass and longer intersubband relaxation time than GaAs [21], may be used in the emission quantum well. Finally, for intersubband energy separation larger than the optical phonon energy, the intersubband relaxation rate can be reduced by reducing the quantum well width [20, 23]. The latter effect arises because the larger intersubband energy separation (corresponding to smaller well width) requires a larger wavevector for the intersubband transition whilst the density of final states decreases with increasing wavevector. Hence intersubband population inversion may be achieved at lower injection current densities for emission wavelength $\lambda < 10$ μm. This, together with the fact that optical absorptive loss decreases for shorter wavelengths, indicates that lasing action based on intersubband transitions may be easier to achieve for $\lambda < 10$ μm than for $\lambda = 10$ μm. The above analysis suggests that experimental investigation into intersubband population

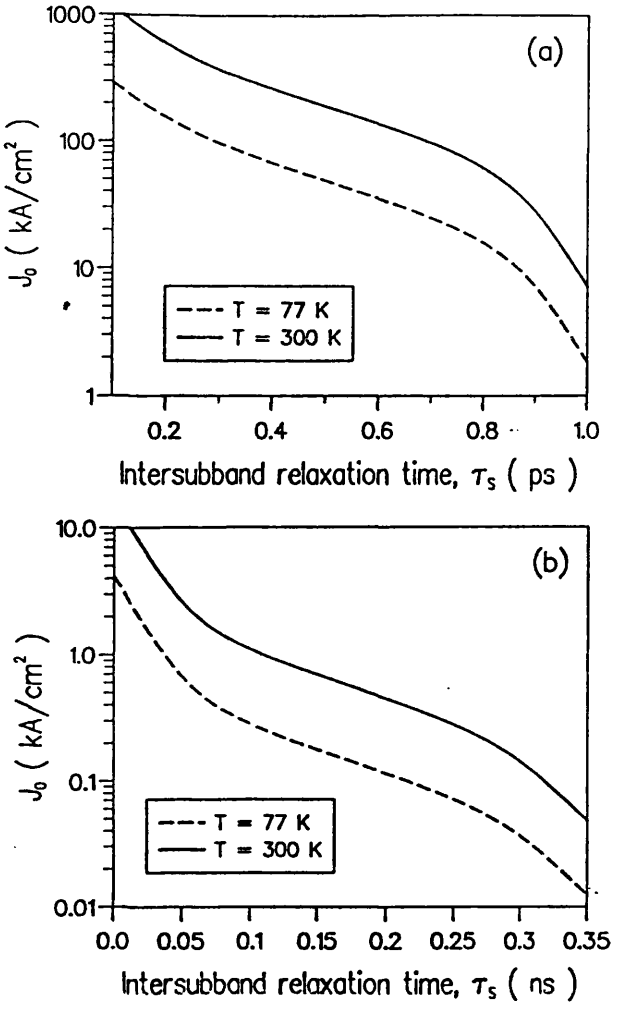

Figure 5. Dependence of transparency current density on intersubband relaxation time for (*a*) structure I and (*b*) structure II.

inversion for wavelengths shorter than 10 μm could be of considerable interest with a view to designing near-infrared lasers operating in the $\lambda = 3$–5 μm atmospheric window [17].

4. Calculation of the threshold current density

Having shown that intersubband population inversion can indeed be achieved at reasonable injection current densities in the resonant tunnelling quantum well structures, this section is devoted to assessing the potential for infrared lasing. In this respect, we analyse optical losses taking into account the device geometry in a way similar to Borenstain [9], and calculate the threshold current density required for lasing action in the two structures.

The optical gain, g (per unit length), in the emission quantum well is given by [9]

$$g(\lambda) = \frac{\Delta n \lambda^2}{4\pi \epsilon_r \tau_e} \frac{T_2}{1 + (\omega - \omega_0)^2 T_2^2} \tag{7}$$

where ϵ_r is the relative permittivity of GaAs, T_2 is the electron dephasing time, ω_0 is the angular frequency at resonance and τ_e is the spontaneous radiative time given by

$$\tau_e^{-1} = (2\pi \epsilon_r^{1/2} e^2 / m^* \epsilon_0 \lambda^2 c) f_{ij} \tag{8}$$

where ϵ_0 is the permittivity of free space, c is the velocity of light in vacuum and f_{ij} is the oscillator strength of the transition from level i to level j, which can be approximated by $f_{ij} = 64(ij)^2/\pi^2(i^2 - j^2)^3$.

To establish the lasing threshold condition, we consider the device configuration in figure 1, in which free carriers are confined to just two conducting layers (injector and collector) with total thickness t_c. The generated photons are confined to an effective mode thickness of $t_m = \lambda/2\bar{n}$, $\bar{n}$ being the refractive index. Lasing action in the structures occurs when the optical gain equals the total losses, i.e.

$$\frac{L_2}{t_m} g_{th} = \frac{L_2}{t_m} \alpha_a + \eta_c \alpha_c + \eta_i \alpha_i + \frac{1}{L_c} \ln\left(\frac{1}{R}\right) \tag{9}$$

where α_a, α_c and α_i are the loss coefficients (per unit length) in the active quantum well layer, the conducting layers and the intrinsic region of the cladding layers respectively, η_c and η_i are the mode filling factors in the conducting and intrinsic cladding layers respectively. The last term accounts for mirror loss of the laser with cavity length L_c and facet reflectivity R.

For photon energies below the fundamental bandgap energy, the two chief sources of optical loss are the absorptions caused by interaction of electromagnetic radiation with lattice vibrations (phonon interaction) and by collective oscillation of free carriers (plasmon interaction). These losses can be calculated through the complex dielectric constant given by

$$\epsilon(\omega) = (\bar{n} - ik)^2 = \epsilon_\infty \left(1 + \frac{\omega_L^2 - \omega_T^2}{\omega_T^2 - \omega^2 + i\omega\gamma_{ph}} - \frac{\omega_p^2}{\omega(\omega - i\gamma_{pl})}\right) \tag{10}$$

where ϵ_∞ is the high-frequency dielectric constant, ω_L, ω_T and ω_p are the angular frequencies of the LO phonons, TO phonons and plasmons respectively, γ_{ph} and γ_{pl} are the damping constants of the phonons and the plasmons respectively, $\gamma_{pl} = e/2\pi\mu_e m^*$, μ_e is the electron mobility, $\omega_p^2 = N_c e^2/m^* \epsilon_\infty \epsilon_0$ and N_c is the electron density in the conducting layers. The loss coefficient in the conducting layers can be calculated from the extinction coefficient k in equation (11) using $\alpha_c = 4\pi k/\lambda$. Similarly, α_i is calculated using k with $N_c = 0$. Absorption by plasmon interaction in the emission quantum well is negligible because radiation emitted from intersubband transitions is polarized perpendicular to the quantum well layers, whereas plasmon oscillations can interact only with radiation polarized parallel to the quantum well layers. Furthermore, due to the small active layer thickness, absorption from photon–phonon interaction in the emission well is negligibly small for wavelengths well above or below the reststrahlen region at wavelengths between 34 and 37 μm. Hence $\alpha_a \approx 0$.

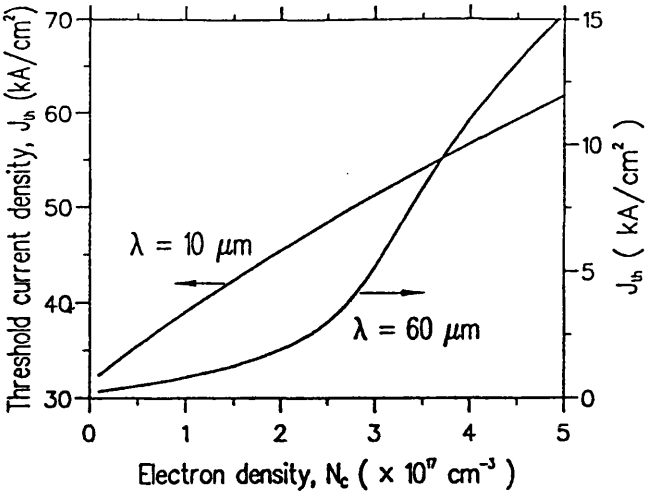

Figure 6. Dependence of the threshold current density on the electron density in the conducting layers for the two structures. Note the different scales on the two y-axes.

The intersubband population inversion at lasing threshold is obtained by equating equations (8) and (10) for $\omega = \omega_0$. The carrier rate equations are then solved for J_{th} consistent with the obtained threshold population inversion. The numerical parameters used are: $\epsilon_r = 12.25$, $T_2 = 0.21$ ps [21], $R = 0.3$, $L_c = 1$ mm, $\epsilon_\infty = 11.1$, $\omega_L = 291.5$ cm^{-1}, $\omega_T = 268.2$ cm^{-1}, $\gamma_{ph} = 2.3$ cm^{-1} and $\mu_e = 5000$ cm^2 V^{-1} s^{-1}.

We assume $t_c = 2$ μm in both structures. Since $t_c > t_m \approx 1.43$ μm in structure I, the mode filling factors are given by $\eta_c = (t_m - L_2)/t_{in}$ and $\eta_i = 0$. In structure II, however, $t_c < t_m$ and in this case $\eta_c = t_c/t_m$ and $\eta_i = (t_m - t_c)/t_m$. Figure 6 shows the calculated threshold current density as a function of the electron density in the conducting layers for the two structures at room temperature. As N_c is increased through doping, the absorption due to plasmon interaction increases, thus increasing the threshold gain and J_{th}. It is observed that J_{th} remains relatively low at low N_c but increases sharply when N_c exceeds 2.3×10^{17} cm^{-3} for structure II. This is because, for electron density above this value, the plasma frequency in the conducting layers becomes higher than the emission frequency ($\approx$ 5 THz) of structure II, and thus enhances the plasmon interaction absorption. It is noted, however, that low electron density in the conducting layers will increase the refractive index of the cladding layers towards the value of that in the active region, and this will have an anti-guiding effect on the generated photon and thus reduces the photon confinement. From figure 6 we find that reasonable threshold current densities of the order of 1–5 kA cm^{-2} are achievable in structure II with $N_c = 1$–3×10^{17} cm^{-3}. For structure II, J_{th} around 40–50 kA cm^{-2} is required over the same range of N_c. The calculated values of threshold current density for the $\lambda = 10$ μm structure in the present analysis agree very well with estimates of Faist [17] for their $\lambda = 5$ μm structure, the small difference being due to the fact that optical absorptive loss decreases for shorter wavelengths. As the operating temperature is lowered, the electron mobility μ_e increases and it is found that the absorption loss in the conducting layers decreases. It is thus expected that lower threshold current density can be achieved in both structures for low temperature operation.

The analysis of carrier transport and optical loss presented here is based on the triple-coupled quantum well structures shown in figure 1. For practical device operation, such a triple-coupled quantum well structure can be periodically repeated to form a superstructure. Such a superstructure would be expected to provide better optical confinement and, as a result, lower threshold current density should be achievable. Resonant optical waveguide structures may also be considered for enhancing the waveguiding properties of the device.

5. Summary

We have presented a theoretical model of electron transport in resonant tunnelling quantum well structures, incorporating the relevant physical mechanisms of resonant tunnelling and intersubband emission–absorption processes. Optical loss analysis has been carried out taking into account the device structure. Solution of the four-level carrier rate equations from the transport model, consistent with the balance of gain and loss in the laser devices, enables the threshold current density to be calculated explicitly as a function of electron doping density in the cladding layers. The results show that a reasonably low threshold current density in the range of 1–5 kA cm^{-2} is achievable for room temperature lasing at $\lambda = 60$ μm. A significantly higher threshold current density of 40–50 kA cm^{-2} is required for emission at $\lambda = 10$ μm. The transparency current density has also been shown to be extremely sensitive to the intersubband relaxation time. Our analysis demonstrates the feasibility of using current injection resonant tunnelling quantum well structures for far-infrared lasing. The carrier transport model presented here is very general and can be used to analyse carrier dynamics in resonant tunnelling QW structures. Specifically, superstructures consisting of periodically repeated triple-coupled QW such as those reported by Faist [17] can be analysed using the carrier transport model presented in this work.

References

[1] Esaki L 1986 *IEEE J. Quantum Electron.* **22** 1611
[2] West L C and Eglash S J 1985 *Appl. Phys. Lett.* **46** 1156
[3] Levine B F 1993 *Semicond. Sci. Technol.* **8** S400
[4] Helm M, Colas E, England P, DeRosa F and Allen S J Jr 1988 *Appl. Phys. Lett.* **53** 1714
[5] Helm M, England P, Colas E, DeRosa F and Allen S J Jr 1989 *Phys. Rev. Lett.* **63** 74
[6] Liu H C 1988 *J. Appl. Phys.* **63** 2856
[7] Allen S J, Brozak G, Colas E, DeRosa F, England P, Harbison J, Helm M, Florez L and Leadbeater M 1992 *Semicond. Sci. Technol.* **7** B1
[8] Wang K L and Yuh P F 1989 *IEEE J. Quantum Electron.* **25** 12
[9] Borenstain S I and Katz J 1989 *Appl. Phys. Lett.* **55** 654
[10] Hu Q and Feng S 1991 *Appl. Phys. Lett.* **59** 2923

[11] Kastalsky A, Goldman V J and Abeles J H 1991 *Appl. Phys. Lett.* **59** 2636
[12] Kastalsky A 1993 *IEEE J. Quantum Electron.* **29** 1112
[13] Henderson G N, West L C, Gaylord T K, Roberts C W, Glytsis E N and Asom M T 1993 *Appl. Phys. Lett.* **62** 1432
[14] Lau K M and Xu W 1992 *IEEE J. Quantum Electron.* **28** 1773
[15] Sun G and Khurgin J B 1993 *IEEE J. Quantum Electron.* **29** 1104
[16] Helm M and Allen S J Jr 1990 *Appl. Phys. Lett.* **56** 1368
[17] Faist J, Capasso F, Sirtori C, Sivco D L, Hutchinson A L, Chu S N G and Cho A Y 1993 *Electron. Lett.* **29** 2230
[18] Yee W M, Shore K A and Schöll E 1993 *Appl. Phys. Lett.* **63** 1089
[19] Kunz R E and Schöll E 1993 *Phys. Rev.* B **47** 4337
[20] Seilmeier A, Hübner H J, Wörner M, Abstreiter G, Weimann G and Schlapp W 1988 *Solid-State Electron.* **31** 767
[21] Faist J, Capasso F, Sirtori C, Sivco D L, Hutchinson A L, Chu S N G and Cho A Y 1993 *Appl. Phys. Lett.* **63** 1354
[22] Oberli D Y, Wake D R, Klein M V, Henderson T and Morkoç H 1988 *Solid-State Electron.* **31** 413
[23] Ferreira R and Bastard G 1989 *Phys. Rev.* B **40** 1074

Nearly degenerate four-wave mixing in laser diodes with nonuniform longitudinal gain distribution

W. M. Yee and K. A. Shore

School of Electronic and Electrical Engineering, University of Bath, Bath BA2 7AY, UK

Received October 4, 1993; revised manuscript received February 15, 1994.

Nearly degenerate four-wave mixing in above-threshold laser diodes with low or asymmetric facet reflectivities is investigated theoretically. It is shown that the conjugate reflectivity and the four-wave mixing bandwidth are enhanced in lasers with low-reflectivity facets. It is shown, in particular, that the maximum conjugate reflectivity can be obtained in lasers with highly asymmetric facet reflectivities. Longitudinal variations of both the nonlinear interaction and the gain distribution in the laser cavity are taken into account in the model. Such variations are shown to be essential in describing four-wave mixing in laser diodes with low or strongly asymmetric facet reflectivities.

INTRODUCTION

Multiwave mixing processes in laser diodes[1,2] and semiconductor optical amplifiers[3,4] have attracted considerable attention in recent years. Optical phase conjugation through nearly degenerate four-wave mixing (FWM) in semiconductor lasers is of particular interest because very high conjugate reflectivities of the order of 30–40 dB can be achieved because of the amplifying effect of the semiconductor gain medium and the cavity enhancement of the mixing process.[5,6] Wave mixing also represents one of the fundamental nonlinear-optical processes and has an important effect on the dynamical and spectral behavior of laser diodes. In multilongitudinal-mode InGaAsP laser diodes, multiwave mixing occurring in the presence of nonlinear gain was shown to effect self-locked FM operation.[7–9] FWM may also be used to extract basic information on gain saturation[10–13] and to characterize many fundamental parameters of semiconductor lasers.[6,14] Furthermore, all-optical frequency conversion with FWM[15] was proposed for use in optical coherent multicarrier systems. Studies in FWM also help in the understanding of the generation of undesirable cross talk and intermodulation distortion between amplified channels in semiconductor laser amplifiers.[16]

In a seminal paper,[17] Agrawal presented a theory of nondegenerate FWM in semiconductor lasers and amplifiers with particular emphasis on the physical processes that lead to population pulsations. However, Fabry–Perot cavity effects were not included in the analysis. By using the homogeneous field approximation, Mecozzi *et al.*[18] and Hui and Mecozzi[19] recently derived analytical expressions for the probe and the conjugate wave output through nearly degenerate FWM in distributed-feedback semiconductor lasers operating above threshold. In recent research, Simpson and Liu[20] successfully incorporated cavity effects into a time-domain description of phase and amplitude characteristics of nearly degenerate FWM and demonstrated excellent agreement with experimental results. As was appropriate to their experiments, the theoretical treatment of Simpson and Liu took no account of spatial variations along the laser cavity.

In the present paper, cavity-enhanced nearly degenerate FWM in above-threshold laser diodes with low or asymmetric facet reflectivities is studied theoretically. We generalize the research of Agrawal to take into account Fabry–Perot cavity effects and, at the same time, incorporate the longitudinal variations of both the nonlinear interactions and the gain distribution in a theoretical description of nearly degenerate FWM in laser diodes. In this way it is possible to obtain a model that is widely applicable and that is, in particular, capable of describing FWM properties in laser diodes in which the longitudinal field and gain distribution are significantly nonuniform. It is shown that enhancement of the conjugate reflectivity and the FWM bandwidth can be achieved in lasers with low-reflectivity facets. It is shown also that the maximum conjugate reflectivities are obtained in lasers with one low-reflective coated facet and one high-reflective coated facet. The importance of incorporating the longitudinal dependence of the nonlinear interaction and the gain is established, especially in lasers with low or highly asymmetric facet reflectivities. The model presented here may also be used to treat multiwave mixing in multisection laser diodes and other devices with longitudinal structural variations.

THEORETICAL MODEL

In this section we present a theoretical model of cavity-enhanced nearly degenerate FWM in above-threshold laser diodes based on a theory proposed by Agrawal,[17] generalized to take into account resonant-cavity effects and longitudinal variations of the nonlinear interaction and the internal gain distribution. The laser is assumed to oscillate in a single transverse and longitudinal mode providing the pump wave at frequency ω_0. A collinear probe wave at frequency ω_1 is injected into the pumped laser through the front facet at $z = 0$, where z is the distance along the longitudinal direction of the laser. A

0740-3224/94/071221-07$06.00

conjugate wave at frequency ω_2 is generated through FWM.

The nonlinear interaction of the field E in the semiconductor laser, assuming that the laser structure supports only the fundamental waveguide TE mode, is described in the scalar approximation by the wave equation

$$\nabla^2 E - \frac{n^2}{c^2}\frac{\partial^2 E}{\partial t^2} = \frac{1}{\epsilon_0 c^2}\frac{\partial^2 P}{\partial t^2}, \tag{1}$$

where n is the refractive index, c is the velocity of light in vacuum, ϵ_0 is the vacuum permittivity, and P is the induced polarization. The field is normalized such that the optical intensity I (in units of watts per square meter) is given by $I = |E|^2$. Using a plane-wave expansion, we write the field E and the induced polarization P as the sum of the Fourier components:

$$E(x,y,z) = U(x,y)\sum_j E_j(z)\exp(-i\omega_j t), \tag{2}$$

$$P(x,y,z) = U(x,y)\sum_j P_j(z)\exp(-i\omega_j t), \tag{3}$$

where $U(x,y)$ is the transverse distribution of the TE mode and $j = 0, 1, 2$ correspond to the pump, the probe, and the conjugate waves, respectively. The frequencies of the various waves obey the relationship

$$\omega_1 - \omega_0 = \omega_0 - \omega_2 = \Omega. \tag{4}$$

We substitute Eqs. (2) and (3) into Eq. (1), multiply by $U^*(x,y)$, and integrate over the transverse dimensions x and y to obtain the one-dimensional wave equation

$$\frac{d^2 E_j}{dz^2} + k_j^2 E_j = -\frac{\Gamma\omega_j^2}{\epsilon_0 c^2}P_j, \tag{5}$$

where $k_j = \bar{n}\omega_j/c$, $\bar{n}$ is the effective-mode index, and Γ is the confinement factor.

The dominant physical mechanism of nearly degenerate FWM in semiconductor lasers was explained by Agrawal to be the modulation of the carrier density at the beat frequency Ω of the pump and the probe waves. The carrier density modulation results in temporal refractive-index and gain modulation, which act as index and gain gratings to the pump and the probe waves. Diffraction of the pump and the probe waves from these dynamic gratings generates the conjugate wave. We can obtain the static carrier density $\bar{N}$ at an injection-current density J and the carrier density modulation ΔN_Ω by solving the carrier rate equation.[17] Because the pump–probe frequency detuning in the nearly degenerate case is much smaller than the gain-spectrum bandwidth, it can be assumed that all waves experience the same gain given by

$$g(N) = a(N - N_0), \tag{6}$$

where N is the carrier density, N_0 is the carrier density at transparency, and a is the gain coefficient. The effect of gain saturation has been reported[18] to reduce the efficiency of FWM interaction, particularly near the relaxation oscillation frequency of the pumped laser. Gain saturation will not, however, change the qualitative effects on phase-conjugate reflectivity arising because of varying laser facet reflectivities. It is these effects that are the focus of the present study.

The field–carrier interaction is governed by the relation

$$P = \epsilon_0 \chi E, \tag{7}$$

where the susceptibility is defined as $\chi(N) = -nc(\beta + i)g(N)/\omega_0$ and β is the linewidth enhancement factor that accounts for the carrier-induced index change. We calculate the induced-polarization components P_j by substituting Eq. (2), together with the gain and the carrier density expressions, into Eq. (7). We then obtain

$$P_0(z) = \epsilon_0 A g(\bar{N}) E_0(z), \tag{8}$$

$$P_1(z) = \epsilon_0 A g(\bar{N})[E_1(z) - \Delta n_\Omega E_0], \tag{9}$$

$$P_2(z) = \epsilon_0 A g(\bar{N})[E_2(z) - \Delta n_\Omega^* E_0], \tag{10}$$

where

$$A = -(nc/\omega_0)(\beta + i), \tag{11}$$

$$\Delta n_\Omega = \frac{-\Delta N_\Omega}{(\bar{N} - N_0)} = \frac{(E_0^* E_1 + E_0 E_2^*)/P_s}{(1 + |E_0|^2/P_s - i\Omega\tau_s)}, \tag{12}$$

$$g(\bar{N}) = a(\bar{N} - N_0) = \frac{(a\tau_s/ed)J - aN_0}{1 + |E_0|^2/P_s}, \tag{13}$$

and where $P_s = \bar{h}\omega_0/(\Gamma a \tau_s)$ is the saturation intensity, $\bar{h}$ is Planck's constant divided by 2π, τ_s is the spontaneous carrier lifetime, e is the electronic charge, and d is the active layer thickness.

CAVITY EFFECTS

To incorporate the effect of the resonant cavity into the analysis, it is necessary to treat both the forward and the reverse propagating waves. In this case, therefore, the z dependence of the fields is assumed to be

$$E_j(z) = \sqrt{P_s}[A_j^+(z)\exp(ik_0 z) + A_j^-(z)\exp(-ik_0 z)], \tag{14}$$

where $A_j^+(z)$ and $A_j^-(z)$ are the normalized complex envelope functions of the forward- and the reverse-propagating waves, respectively. Similarly, the induced polarization at the corresponding frequency is expressed as the sum of the forward- and the reverse-propagating components:

$$P_j(z) = P_j^+(z)\exp(ik_0 z) + P_j^-(z)\exp(-ik_0 z). \tag{15}$$

We substitute Eqs. (14) and (15) into Eq. (5) and apply the slowly varying envelope and the rotating-wave approximations to obtain

$$\frac{dA_0^\pm}{dz} \pm \frac{\alpha_{int}}{2}A_0^\pm = \pm\frac{i\omega_0\Gamma}{2nc\epsilon_0\sqrt{P_s}}P_0^\pm, \tag{16}$$

$$\frac{dA_1^\pm}{dz} \mp \frac{i\bar{n}\Omega}{c}A_1^\pm \pm \frac{\alpha_{int}}{2}A_1^\pm = \pm\frac{i\omega_1\Gamma}{2nc\epsilon_0\sqrt{P_s}}P_1^\pm, \tag{17}$$

$$\frac{dA_2^\pm}{dz} \pm \frac{i\bar{n}\Omega}{c}A_2^\pm \pm \frac{\alpha_{int}}{2}A_2^\pm = \pm\frac{i\omega_2\Gamma}{2nc\epsilon_0\sqrt{P_s}}P_2^\pm, \tag{18}$$

where α_{int} is the internal loss coefficient introduced to take into account all the losses (diffusion, free-carrier absorption, scattering, etc.) other than mirror loss.

Substituting the induced-polarization components from Eqs. (8)–(10) as the source terms into Eqs. (16)–(18), we obtain the coupled-wave equations that describe the evolution of three sets of copropagating and counterpropagating fields along the z direction:

$$\frac{dA_0^{\pm}}{dz} = \pm\alpha_0 A_0^{\pm} \mp \frac{\alpha_{int}}{2} A_0^{\pm}, \tag{19}$$

$$\frac{dA_1^{\pm}}{dz} = \pm\frac{i\bar{n}\Omega}{c} A_1^{\pm} \pm \alpha_0(A_1^{\pm} - \Delta n_\Omega A_0^{\pm}) \mp \frac{\alpha_{int}}{2} A_1^{\pm}, \tag{20}$$

$$\frac{dA_2^{\pm}}{dz} = \mp\frac{i\bar{n}\Omega}{c} A_2^{\pm} \pm \alpha_0(A_2^{\pm} - \Delta n_\Omega^* A_0^{\pm}) \mp \frac{\alpha_{int}}{2} A_2^{\pm}, \tag{21}$$

where

$$\Delta n_\Omega(z) = \frac{A_0^+(A_2^+)^* + (A_0^+)^* A_1^+ + A_0^-(A_2^-)^* + (A_0^-)^* A_1^-}{(1 + P_T - i\Omega\tau_s)}, \tag{22}$$

$$\alpha_0(z) = \frac{g_0(1 - i\beta)}{2[1 + P_T(z)]}, \tag{23}$$

$$P_T(z) = |A_0^+(z)|^2 + |A_0^-(z)|^2, \tag{24}$$

and where $g_0 = \Gamma a N_0(J/J_0 - 1)$ is the small-signal gain and $J_0 = edN_0/\tau_s$ is the transparency current density. Only copropagating wave coupling is taken into account in the equations. Counterpropagating wave beating does not contribute significantly to the nearly degenerate FWM process[3] because spatial gratings created by the counterpropagating fields have periods much shorter than the carrier diffusion length. The z dependence of the normalized intracavity pump intensity P_T is retained in the model. This is of importance when consideration is given to lasers with very low or nonidentical facet reflectivities in which significant nonuniformity in the field distribution is anticipated. We consider the case in which the probe-signal injection is very small so that the effect of probe-induced carrier depletion in the pumped laser is negligible. The intracavity pump signal can thus be assumed to be free running. This assumption is consistent with reported experimental investigations of nearly degenerate FWM in laser diodes in which a very small probe-signal injection power of approximately 0.02 μW was used.[18,20]

The coupled-wave equations must satisfy the boundary conditions at the two laser facets with power reflectivities R_1 and R_2, respectively:

$$A_j^+(z = 0) = \sqrt{1 - R_1}\, E_{in} + \sqrt{R_1}\, A_j^-(z = 0), \tag{25}$$

$$E_{R,j} = \sqrt{1 - R_1}\, A_j^-(z = 0) + \sqrt{R_1}\, E_{in}, \tag{26}$$

$$A_j^-(z = L)\exp(-i\kappa L) = \sqrt{R_2} A_j^+(z = L)\exp(i\kappa L), \tag{27}$$

$$E_{T,j} = \sqrt{1 - R_2}\, A_j^+(z = L)\exp(i\kappa L), \tag{28}$$

where E_{in} is the normalized incident probe-signal amplitude, which is zero for $j = 0, 2$; κ is the wave number in the laser medium; L is the laser cavity length; and $E_{R,j}$ and $E_{T,j}$ are the output fields from the front ($z = 0$) and the rear ($z = L$) facets, respectively, at the corresponding frequency.

We define the probe/conjugate reflectivity $R_{p/c}$ as the ratio of the probe/conjugate output power from the front facet ($z = 0$) to the incident probe power, and we define the probe/conjugate transmittivity $T_{p/c}$ as the ratio of the probe/conjugate output from the rear facet ($z = L$) to the incident probe power, i.e.,

$$R_p = \left|\frac{E_{R,1}}{E_{in}}\right|^2, \quad T_p = \left|\frac{E_{T,1}}{E_{in}}\right|^2, \tag{29}$$

$$R_c = \left|\frac{E_{R,2}}{E_{in}}\right|^2, \quad T_c = \left|\frac{E_{T,2}}{E_{in}}\right|^2. \tag{30}$$

NUMERICAL SOLUTION

The numerical solution of the system of ordinary differential equations (19)–(21) that are subject to the boundary conditions at the laser facets allows the evolution of the various fields and their nonlinear interaction to be computed along the propagation direction z. This z dependence of the fields and hence the gain is of particular importance when the laser has low or asymmetric facet reflectivities, in which case the homogeneous field approximation is no longer valid. In addition, the effects of a Fabry–Perot cavity with different facet reflectivities on the conjugate output can be investigated only by numerical solution of the differential equations.

Because $A_j^{\pm}(z)$ in the coupled-wave equations are complex quantities, we must separate each equation into its real and imaginary parts and solve a total of 12 equations. Although the free-running pump-signal wave equation (19) is independent of Eqs. (20) and (21), numerical solution is required because of the z dependence of the coefficient α_0. An iterative method that uses the piecewise constant inversion population (PCIP) model similar to that of Middlemast *et al.*[21] is used to solve Eq. (19). The model is based on solving the field and carrier density equations self-consistently with the boundary conditions imposed by the two facets. In the model, the longitudinal length of the laser cavity is divided into M segments, in each of which a constant, but as yet unknown, value of the inversion population and thus the gain is assumed. This approach allows an analytical expression for the forward and the reverse propagating pump fields to be obtained in each segment. The average intensity distribution in each segment is then calculated and is used in the charge conservation equation to yield the self-consistent, constant value of the inversion population in each corresponding segment. The procedure is repeated until the boundary conditions are satisfied to a required degree of accuracy. The PCIP model allows the pump wave equations to be solved with considerable reduction in computation time. The probe and the conjugate wave equations are then solved by a library routine for a system of boundary-value ordinary-differential equations in conjunction with the obtained pump waves at each mesh point.

To determine the laser medium wave number κ, we solve the propagation equation (19) by using the PCIP

model in conjunction with the boundary conditions (25) and (27) with $j = 0$ and $E_{in} = 0$. We then obtain the oscillation condition for the free-running laser:

$$\sqrt{R_1 R_2}\exp\left[\left(\frac{1}{M}\sum_{n=1}^{M} g_n - \alpha_{int}\right)L\right]\exp(i\varphi) = 1, \quad (31)$$

where φ is the total phase shift of the pump wave in propagating through the laser cavity in one complete round trip and is given by

$$\varphi = 2\kappa L - \frac{\beta L}{M}\sum_{n=1}^{M} g_n \quad (32)$$

and g_n is the constant gain in the nth segment. The last term in Eq. (32) is the detuning introduced by phase-amplitude coupling as characterized by β. The oscillation condition (31) requires that the total phase shift be some integral multiple of 2π. Equation (32) then becomes

$$2\kappa L = 2m\pi + \frac{\beta L}{M}\sum_{n=1}^{M} g_n, \quad (33)$$

where m is an integer. This defines κ in the boundary conditions. Using initial tests with a variable M, we found that a reasonable degree of accuracy in the solutions of $A_j^{\pm}$ could be obtained with $M = 50$ in the PCIP model.

RESULTS AND DISCUSSIONS

A small probe injection power of $P_{in} = 0.02\,\mu W$ (Refs. 18 and 20) is assumed to be incident at the laser front facet at $z = 0$. The following parameter values appropriate to GaAs–AlGaAs laser diodes are used in the analysis: laser volume $V = (250\,\mu m \times 2.0\,\mu m \times 0.2\,\mu m)$, lasing wavelength $\lambda_0 = 0.83\,\mu m$, $\Gamma = 0.4$, $a = 3 \times 10^{-16}\,cm^2$, $N_0 = 1.1 \times 10^{18}\,cm^{-3}$, $\tau_s = 1\,ns$, and $\alpha_{int} = 20\,cm^{-1}$.

A. Symmetric Laser Diodes

To illustrate how longitudinal variations influence the FWM process in laser diodes, the normalized amplitudes of the carrier density deviation Δn_Ω along the cavity length are plotted in Fig. 1. Significant longitudinal nonuniformity is observed in the carrier density deviation distribution, especially for lasers with highly asymmetric facet reflectivities. Inasmuch as it is the carrier density fluctuations that drive the FWM process, it is to be expected that such carrier variations will influence achievable phase-conjugate reflectivities in these devices. This is shown clearly in Fig. 2.

The evolution of the conjugate-signal intensity along the longitudinal direction of the laser is illustrated in Fig. 2, in which the laser facet reflectivities are $R_1 = R_2 = 0.1$. The solid curves are obtained with the PCIP model. The dashed curves correspond to solutions of the conjugate signal that are obtained with a spatially uniform gain model, in which case one assumes a z-independent normalized average intracavity pump intensity $\overline{P}_T$ given by

$$\overline{P}_T = \frac{1}{L}\int_0^L |A_0^+(z)|^2 + |A_0^-(z)|^2 dz = \frac{g_0}{g_{th}} - 1, \quad (34)$$

$$g_{th} = \alpha_{int} + \frac{1}{2L}\ln\left(\frac{1}{R_1 R_2}\right), \quad (35)$$

where g_{th} is the threshold gain of the laser. Significant differences are observed between the propagation curves of the conjugate intensity computed with the two models when the laser facet reflectivity is small. This is generally true for $R_1 = R_2 \leq 0.3$ and for lasers with highly asymmetric facet reflectivities. Similar differences are also observed in the values of the probe intensity, although the differences between the pump intensities from the two models are less pronounced. Figure 2 also shows that the conjugate intensity along the z axis is highly nonuniform, and thus the homogeneous-field approximation cannot be assumed in lasers with low facet reflectivities. The above results demonstrate that longitudinal variations of the internal gain should be taken into account in discussions of FWM when consideration is given to lasers with low or asymmetric facet reflectivities.

The probe and the conjugate output power at $z = L$ as a function of pump–probe frequency detuning are shown in Figs. 3(a) and 3(b), respectively. The facet reflectivities are $R_1 = R_2 = 0.3$. The solid and the dashed curves correspond to $\beta = 3$ and $\beta = 4$, respectively. Probe and

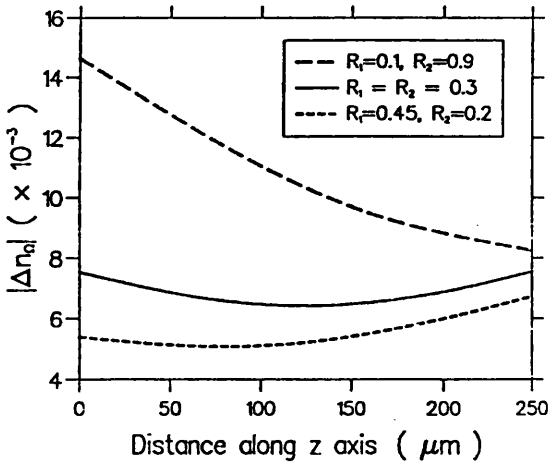

Fig. 1. Amplitudes of normalized carrier density deviation $|\Delta n_\Omega|$ along the longitudinal direction of the laser cavity.

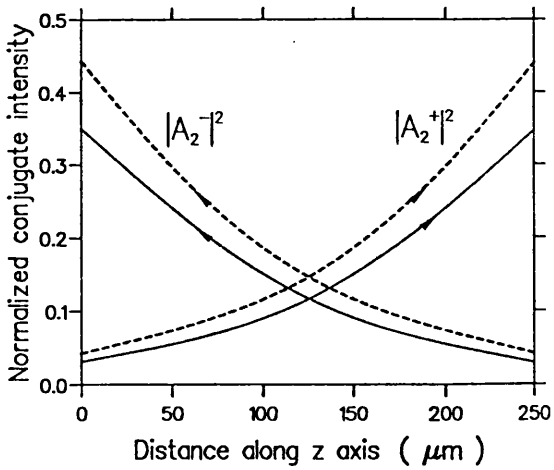

Fig. 2. Evolution of normalized conjugate intensity along the longitudinal direction of the laser cavity. Significant differences are observed between results obtained with the PCIP model (solid curves) and the uniform-gain model (dashed curves).

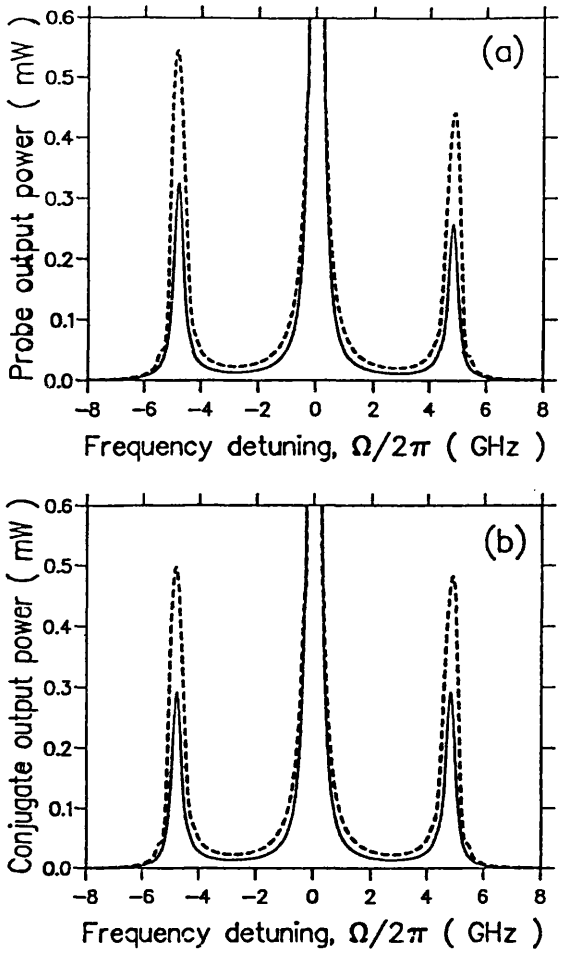

Fig. 3. (a) Probe and (b) conjugate output power versus frequency detuning $\Omega = \omega_1 - \omega_0$ for $\beta = 3$ (solid curve) and $\beta = 4$ (dashed curve). $R = R_1 = R_2 = 0.3$.

conjugate output power peaks are observed at frequency detuning approximately equal to

$$\Omega_R = \left(\frac{g_{th} v_g \overline{P}_T}{\tau_s} \right)^{1/2}, \tag{36}$$

which corresponds to the relaxation oscillation frequency of the pump laser. It is also observed that the conjugate output power curve is symmetric with respect to zero pump–probe frequency detuning, whereas the probe output power curve exhibits strong asymmetry with higher probe output for negative frequency detuning. This agrees well with the experimental results of Simpson and Liu[20] and with observations in semiconductor optical amplifiers.[3,4] Such probe gain asymmetry was theoretically predicted by Bogatov *et al.*[22] and is due to the strong phase-amplitude coupling arising from the gain and the refractive-index dependence on the carrier density.[17,23] This probe output asymmetry is, however, not accounted for by the theoretical treatment and the experimental observation of Mecozzi and co-workers.[18] In addition, Fig. 3 shows that probe and conjugate output power increase for larger values of the linewidth enhancement factor and confirms the significant contribution of the refractive-index grating in the FWM process arising from the large β value in semiconductor lasers.

The transmittivities of the probe T_p and the conjugate T_c waves as a function of frequency detuning are plotted in Figs. 4(a) and 4(b), respectively, for different values of the spontaneous carrier lifetime, τ_s. T_p and T_c in the range of 30–40 dB can be obtained at frequency detunings near the relaxation oscillation frequency for τ_s = 1.0 ns, which agree well with experimental observations.[6]

Because the relaxation oscillation frequency Ω_R is inversely related to τ_s as indicated in Eq. (36), we can see that the bandwidth for positive conjugate transmittivity increases for smaller τ_s. For frequency detunings well above Ω_R, T_p and T_c decrease rapidly with roll-off rates of approximately −20 and −60 dB per frequency decade, respectively, in accordance with the experimental results reported in Ref. 6. In this reference Fabry–Perot cavity effects are indicated as being responsible for the observed roll-off rates. The cavity effect is indeed apparent in Fig. 4, in which, for large frequency detunings, the transmittivities are seen to increase again because of the effect of the adjacent Fabry–Perot resonance.

The conjugate transmittivity characteristics at different output power levels are shown in Fig. 5 for lasers with facet reflectivities $R_1 = R_2 = 0.3$. It is noted that the side transmittivity peaks occur at larger frequency detunings as the output power is increased. This is a direct con-

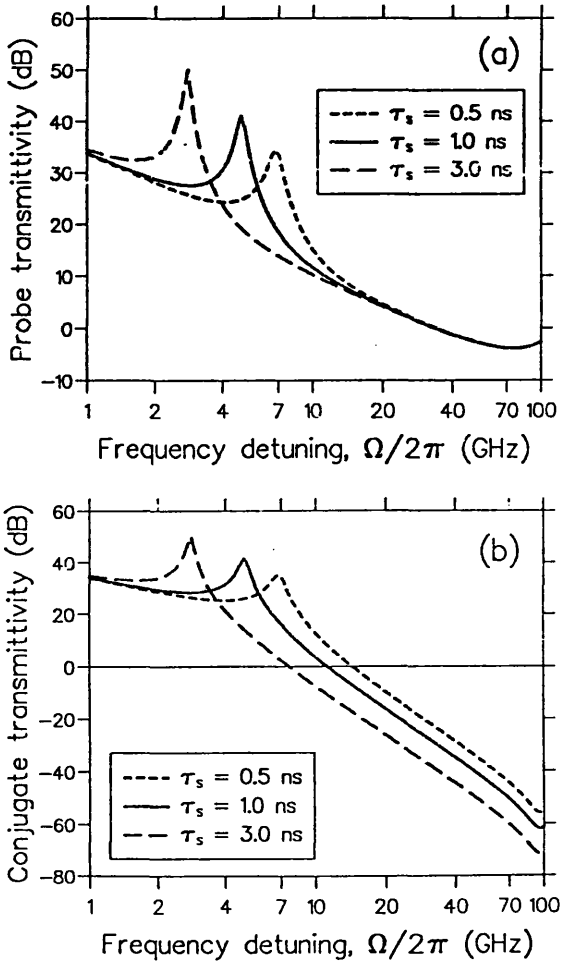

Fig. 4. (a) Probe and (b) conjugate transmittivity as a function of frequency detuning for different τ_s. $R_1 = R_2 = 0.3$ and $\beta = 3.0$.

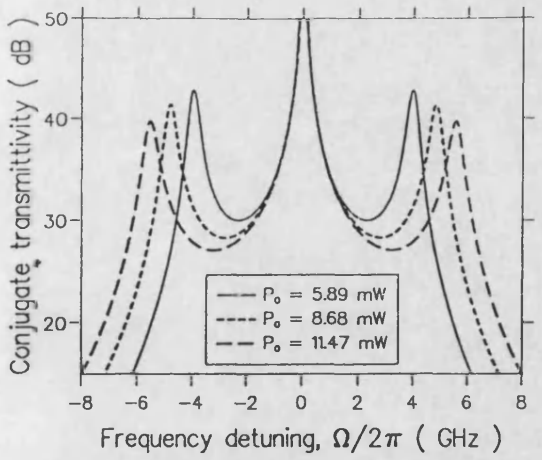

Fig. 5. Conjugate transmittivity T_c, at different output powers P_0 against frequency detuning. $\beta = 3$ and $R = 0.3$. Similar curves are observed for probe transmittivity.

sequence of the dependence of the relaxation oscillation frequency on the optical intensity of the laser.

No change in the above qualitative behaviors is expected, provided that the probe injection power is not too large. Depletion of the gain by the probe and the conjugate signals becomes significant when their powers are comparable with the pump optical power, and in such an operating regime changes in the behavior may occur. The present calculations, however, describe the main features relevant to existing experimental research.[6,18,20] The good agreement between results from the present formalism and available experimental results is a confirmation of the validity of the theoretical model developed in this paper.

B. Conjugate Output Enhancement in Low-Reflectivity Laser Diodes

The effects of varying the facet reflectivity $R = R_1 = R_2$ on conjugate transmittivity at a constant injection-current density, chosen here to be $J/J_0 = 2.45$, are illustrated in Fig. 6. In laser diodes with symmetric facet reflectivity, $R_c = T_c$. For low facet reflectivity, the average intracavity pump intensity is reduced because of high mirror losses. The relaxation oscillation frequency of the laser is correspondingly reduced, resulting in the shift of the side transmittivity peaks to smaller frequency detuning. Lower pump intensity also means that carrier depletion by the pump wave is decreased, thus enhancing the effective gain experienced by the conjugate and the probe waves. Also, at low facet reflectivity, the coupling efficiency of the constant probe injection power into the laser cavity is increased. Both of these effects contribute to higher probe and conjugate transmittivities in laser diodes with low-reflectivity facets. This nontrivial result can be found only by the present technique, in which the coupled-wave equations incorporating the resonant-cavity effects and the z dependence of the nonlinear interaction are numerically integrated subject to the boundary conditions imposed at the laser facets.

It can also be observed from Fig. 6 that the bandwidth for positive conjugate transmittivity increases as the laser facet reflectivity is reduced. This is purely a cavity effect, resulting from the broadening of the Fabry–Perot resonant transmission bandwidth at low facet reflectivities. This explicit dependence of the conjugate transmission bandwidth on laser facet reflectivity can be computed, again, only by use of the present formalism.

The above results show that enhancement of both the conjugate transmittivity and the conjugate transmission bandwidth can be obtained in low-reflectivity laser diodes biased above threshold. Note, however, that a higher injection current is required for obtaining a given level of output power when the laser facet reflectivity is reduced. As a matter of practicality, there is a limit to the injection current that one can apply to the laser and hence a limit to how low the reflectivity of the facet can be with antireflection coating. We have thus shown that the bandwidth of FWM in laser diodes biased above threshold is dependent not only on the spontaneous carrier lifetime, as in traveling-wave amplifiers,[4] but also on the relaxation oscillation frequency and the facet reflectivities of the pumped laser. It is therefore suggested that experimental investigation could be profitably undertaken on FWM effects in low-facet-reflectivity laser diodes with a view to taking advantage of the enhancements of both the conjugate transmittivity and the FWM bandwidth revealed by the present analysis.

C. Asymmetric-Facet-Reflectivity Laser Diodes

The conjugate reflectivity R_c and the conjugate transmittivity T_c, as functions of R_1 (defined as the facet reflectivity at $z = 0$), are shown in Figs. 7(a) and 7(b), respectively. The probe-signal injection is assumed to be tuned to a frequency near the relaxation oscillation frequency of the laser. Each curve in the figure corresponds to a constant product of R_1R_2 and thus to a constant threshold gain g_{th}, assuming the same cavity length and internal loss coefficient. The curves are defined only in the range of R_1 such that $R_2 \leq 1$ sets the limit on the left-hand side of each curve and $R_1 \leq 1$ defines the boundary on the right. The × in each curve represents the point at which $R_1 = R_2$, where $R_c \approx T_c$. For $R_1 < R_2$, we observe that $R_c > T_c$ and vice versa. As the front facet reflectivity is increased, R_c decreases. This is because higher R_1 means that less external injection power is coupled into the laser cavity and less power is emitted from

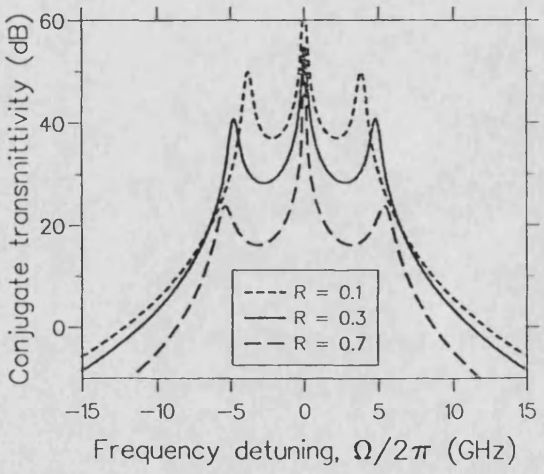

Fig. 6. Effects of varying the facet reflectivity $R = R_1 = R_2$ on conjugate transmittivity. $\beta = 3$. Similar curves are obtained for probe transmittivity.

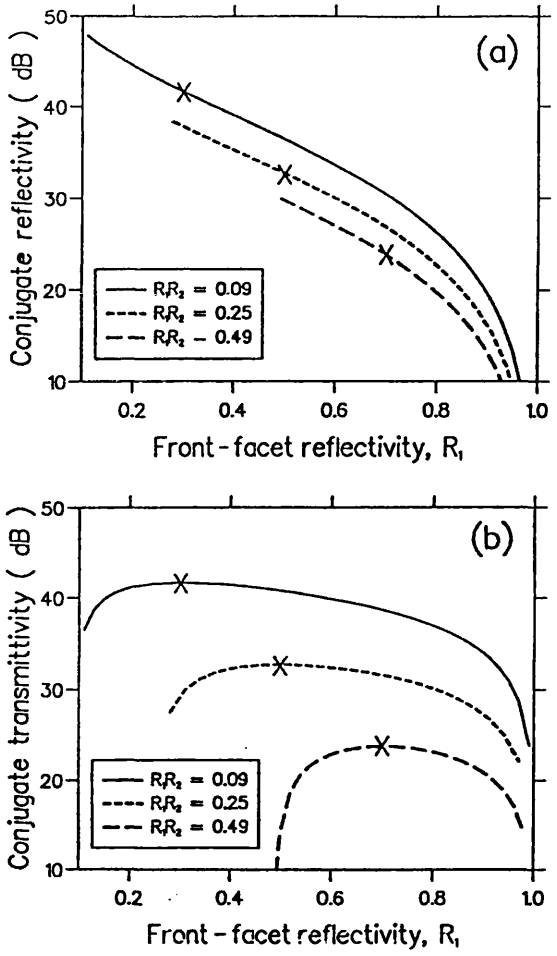

Fig. 7. (a) Conjugate reflectivity R_c and (b) conjugate transmittivity T_c against front-facet reflectivity for lasers with different threshold gain values.

the front facet because of lower front-facet transmittivity. On the other hand, T_c increases up to a maximum, where $R_1 = R_2$, and then decreases as R_1 is increased. It is also found that T_c is the same if R_1 and R_2 are interchanged for a constant product of R_1R_2. This result means that the transmitted conjugate output power is the same at whichever facet the probe signal is incident. However, the reflected conjugate output power does depend on the facet upon which the probe is incident. Figure 7 shows that we can obtain the highest conjugate output power in a laser diode with asymmetric facet reflectivities by injecting the probe signal at the facet with low reflectivity and by deriving the conjugate output from the same facet.

The present study shows that there exist opportunities for enhanced phase-conjugate wave generation by use of highly asymmetric laser diodes. Experimental investigations of such devices will therefore be of some considerable interest.

CONCLUSION

We have theoretically investigated cavity-enhanced nearly degenerate FWM in above-threshold laser diodes with low or asymmetric facet reflectivities. It has been shown that enhancement of both the conjugate output and the FWM bandwidth can be obtained in laser diodes with low facet reflectivities. It has further been shown that maximum conjugate reflectivities can be achieved in lasers with highly asymmetric facet reflectivities. The importance of incorporating the longitudinal variations of the nonlinear interaction and the internal gain distribution in the model has been established. The model developed in this paper has a wide applicability and can be used to study FWM processes in multisection laser diodes. Specifically, the model can be utilized to analyze FWM in laser diodes used for all-optical frequency conversion.

ACKNOWLEDGMENTS

P. Spano, Fondazione Ugo Bordoni, Rome, Italy, is thanked for supplying a copy of Ref. 18. Helpful discussions with J. Sarma and I. Middlemast are gratefully acknowledged.

REFERENCES

1. H. Nakajima and R. Frey, "Collinear nearly degenerate four-wave mixing in intracavity amplifying media," IEEE J. Quantum Electron. QE-22, 1349–1354 (1986).
2. R. Nietzke, P. Panknin, W. Elsässer, and E. O. Göbel, "Four-wave mixing in GaAs/AlGaAs semiconductor lasers," IEEE J. Quantum Electron. 25, 1399–1406 (1989).
3. F. Favre and D. L. Guen, "Four-wave mixing in traveling wave semiconductor laser amplifiers," IEEE J. Quantum Electron. 26, 858–864 (1990).
4. T. Mukai and T. Saitoh, "Detuning characteristics and conversion efficiency of nearly degenerate four-wave mixing in a 1.5 μm traveling-wave semiconductor laser amplifier," IEEE J. Quantum Electron. 26, 865–874 (1990).
5. S. Jiang and M. Dagenais, "Observation of nearly degenerate and cavity-enhanced highly nondegenerate four-wave mixing in semiconductor lasers," Appl. Phys. Lett. 62, 2757–2759 (1993).
6. S. Jiang and M. Dagenais, "Nearly degenerate four-wave mixing in Fabry–Perot semiconductor lasers," Opt. Lett. 18, 1337–1339 (1993).
7. L. F. Tiemeijer, P. I. Kuindersma, P. J. A. Thijs, and G. L. J. Rikken, "Passive FM locking in InGaAsP semiconductor lasers," IEEE J. Quantum Electron. 25, 1385–1391 (1989).
8. K. A. Shore and W. M. Yee, "Theory of self-locking FM operation in semiconductor lasers," Proc. Inst. Electr. Eng. Part J 138, 91–96 (1991).
9. W. M. Yee and K. A. Shore, "Multimode analysis of self-locked FM operation in laser diodes," Proc. Inst. Electr. Eng. Part J 140, 21–25 (1993).
10. L. F. Tiemeijer, "Effects of nonlinear gain on four-wave mixing and asymmetric gain saturation in a semiconductor laser amplifier," Appl. Phys. Lett. 59, 499–501 (1991).
11. S. R. Chinn, "Measurement of nonlinear gain suppression and four-wave mixing in quantum well lasers," Appl. Phys. Lett. 59, 1673–1675 (1991).
12. K. Kikuchi, M. Kakui, C. E. Zah, and T. P. Lee, "Observation of highly nondegenerate four-wave mixing in 1.5 μm traveling-wave semiconductor optical amplifiers and estimation of nonlinear gain coefficient," IEEE J. Quantum Electron. 28, 151–156 (1992).
13. J. Zhou, N. Park, J. W. Dawson, and K. J. Vahala, "Highly nondegenerate four-wave mixing and gain nonlinearity in a strained multiple-quantum-well optical amplifier," Appl. Phys. Lett. 62, 2301–2303 (1993).
14. J. M. Liu and T. B. Simpson, "Characterization of fundamental parameters of a semiconductor laser with an injected optical probe," IEEE Photon. Technol. Lett. 4, 380–382 (1993).
15. N. Schunk, "All-optical frequency conversion in a traveling wave semiconductor laser amplifier," IEEE J. Quantum Electron. 27, 1271–1279 (1991).

16. G. P. Agrawal and I. M. I. Habbab, "Effects of four-wave mixing on multichannel amplification in semiconductor laser amplifiers," IEEE J. Quantum Electron. **26**, 501–505 (1990).
17. G. P. Agrawal, "Population pulsations and nondegenerate four-wave mixing in semiconductor lasers and amplifiers," J. Opt. Soc. Am. B **5**, 147–159 (1988).
18. A. Mecozzi, A. D'Ottavi, and R. Hui, "Nearly degenerate four-wave mixing in distributed feedback semiconductor lasers operating above threshold," IEEE J. Quantum Electron. **29**, 1477–1487 (1993).
19. R. Hui and A. Mecozzi, "Phase noise of four-wave mixing in semiconductor lasers," Appl. Phys. Lett. **60**, 2454–2456 (1992).
20. T. B. Simpson and J. M. Liu, "Phase and amplitude characteristics of nearly degenerate four-wave mixing in Fabry–Perot semiconductor lasers," J. Appl. Phys. **73**, 2587–2589 (1993).
21. I. Middlemast, J. Sarma, K. A. Shore, A. I. Kucharska, E. D. Fletcher, and P. Blood, "Absorptive bistability in inhomogeneously pumped quantum well laser diodes," Proc. Inst. Electr. Eng. Part J **138**, 301–308 (1991).
22. A. P. Bogatov, P. G. Eliseev, and B. N. Sverdlov, "Anomalous interaction of spectral modes in semiconductor laser," IEEE J. Quantum Electron. **QE-11**, 510–515 (1975).
23. M. Yamada, "Theoretical analysis of nonlinear optical phenomena taking into account the beating vibration of the electron density in semiconductor lasers," J. Appl. Phys. **66**, 81–89 (1989).